

**Cavity dynamics of water entry for spheres and
ballistic projectiles**

by

Tadd Trevor Truscott

Submitted to the Department of Mechanical Engineering, Center for
Ocean Engineering

in partial fulfillment of the requirements for the degree of

Doctor of Philosophy of Mechanical and Ocean Engineering

at the

ARCHIVES

MASSACHUSETTS INSTITUTE OF TECHNOLOGY

June 2009

© Massachusetts Institute of Technology 2009. All rights reserved.

Author

Department of Mechanical Engineering, Center for Ocean Engineering

May 21, 2009

Certified by

Alexandra H. Techet

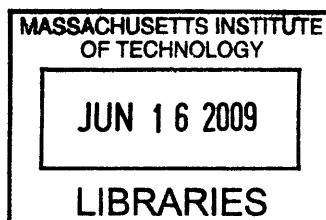
Associate Professor of Mechanical and Ocean Engineering

Thesis Supervisor

Accepted by

David E. Hardt

Chairman, Committee on Graduate Students



Cavity dynamics of water entry for spheres and ballistic projectiles

by

Tadd Trevor Truscott

Submitted to the Department of Mechanical Engineering, Center for Ocean Engineering

on May 21, 2009, in partial fulfillment of the requirements for the degree of

Doctor of Philosophy of Mechanical and Ocean Engineering

Abstract

The free surface impact of solid objects has been investigated for well over a century. This canonical problem has many facets that may be studied: object geometry, surface treatment, and diameter; impact speed and angle; and fluid viscosity and surface tension. The problem is further enriched with the consideration of varying mass ratios and rotational velocities. This thesis uses advanced high-speed imaging and visualization techniques to discover underlying physics and further our understanding of these phenomena through improvements to analytical solutions describing criterion such as cavity formation, depth of deep seal, and trajectory for all impact parameters studied. The topic is extended to the impact of high-speed projectiles or bullets. Through experimentation the trajectory, cavity size, and forces acting on the projectiles are elucidated. Experimentation coupled with improvements to an existing cavitation model lead to an improved bullet design that forms a narrower cavity and achieves higher speeds.

Industrial applications include ship slamming, extreme waves and weather on oil platforms, sprayed adhesives, paint aerosols and ink jet printing. In the field of naval hydrodynamics there is particular interest as these problems relate to the study of the water entry of mines and bullets, and the underwater launching of torpedos and missiles. Physical insight can also be applied to sports performance research relating to the water entry of athletes, reducing drag of swimmers near the free surface, decreasing cavity formation for divers, and the entry and exit of oars in rowing.

This thesis examines the effect of several key parameters on the water entry physics of spheres at relatively low Froude numbers including: hydrophobic vs. hydrophilic surfaces, mass ratio and rotational velocity. Physical models that predict the depth of deep seal and the effect of dynamic and static wetting angle on cavity formation will be discussed. Theories are derived from physical parameters witnessed through high-speed video image sequences using advanced image processing techniques. New phenomena have been witnessed via these techniques including a wedge of fluid that crosses the cavity in the case of transverse rotational velocity. Furthermore, the

images reveal the forces acting on the sphere through the entire trajectory, which adds valuable information for future theoretical models.

The discussion continues with the water entry of bullets, which produce water vapor cavities large enough to engulf the projectile (i.e. supercavitation). The effects of speed, geometry and angle of attack on the formation of the subsurface cavity are analyzed through an improved physical model and full scale experimentation. The analytical model is then used to improve the design of projectile geometry to allow for more efficient travel inside the cavity and experimentally validated.

Thesis Supervisor: Alexandra H. Techet

Title: Associate Professor of Mechanical and Ocean Engineering

Acknowledgments

To my wife: May the fulfillment of the rest of our dreams come a little easier.

To my children: May this work inspire you to live yours.

As all people write, I too would never have completed this goal without the love and support of my family, friends, and colleagues. No matter where I went, whenever I would talk to someone about what I was doing they seemed interested, asked interesting questions I typically couldn't answer, and encouraged me that what I was doing had merit. Perhaps this is a natural instinct in mankind, if it is not I was lucky to always meet people with such trained behavior. The constant support helped me through the clouds of doubt I felt on a weekly basis. I first wish to thank my wife Julie without whom I would never have come here, would never have dreamed of this accomplishment, and would not have had the support I needed to work towards finishing this thesis each day. Thank you for staying with me during the good and the bad, the sleepless nights, all the homework and studying. Thank you for always being happy to see me even if I had been neglectful for months and came home grumpy and insecure. Like a good nights rest, you made everything feel like it was going to be alright... and so I must admit that you were right, it all worked out in the end. Zoë for taking the time to get to know what I do and bragging to her friends about how great the work I am doing is, and for watching over Gus and Sam when I was busy writing. Gus for getting dirty in the lab and wanting to do the experiments right along side of me and for always giving me a smile from across the room. Sam for keeping the crazy and exciting side of life at the surface and for reminding me to calm down when I was frustrated.

I would also like to thank my advisor, Professor Alexandra H. Techet who believed in me before I arrived at MIT and never gave up on me when things got rough. Thank you for pushing me to do my best, trying to understand my circular thoughts and quirky logic, my good and bad habits, my family life, etc. Thank you for not stifling my creative spirit and giving me space and time to finish this work. Thank you

for protecting me from worrying about the small things, and keeping me on track whenever I would panic. I imagine you were worried about my progress on more than one occasion and keeping your game face on despite my fears gave me confidence. Thank you forever for helping me achieve my highest educational goal and aspirations. I will miss being your student but I look forward to working with you as a colleague.

Many thanks to my committee who patiently let me tell them many things that were wrong before I got them right, and for letting me set unreasonable time frames for graduation and then patiently waiting when they never materialized. Professor John W. M. Bush for inspiring me through conversation, lectures, photographs, and articles. Professor Gareth McKinley for asking the right questions and then helping me find the right answers, although I imagine he knew them all along. Dr. David N. Beal for quietly supporting my efforts for four years through regular phone calls, emails, and first-hand practical advice.

Many, many others supported me along the way. Stephen Laverty for helping me finish the project on time, and motivating me to be a good person. Alex Hornstein was an inspirational genius and made the lab so fun I have to mention Marine Man and the terrible tank that flooded our lab. The calm and supportive voice of Jenny Mann made the bad times seem less stressful especially as qualifying exams approached. Melissa Read for listening to me complain for a summer. Jakub Komin for getting the image processing off the ground and having so many clever ideas, thank you so much for building the light bank, I have used it constantly for 4 years. Jason Dahl for staying in the lab with me after hours to debug many codes in early years. Richard Kimball for all the advise, encouragement, and helping me through one of the toughest vector problems I had. Matt Weldon for teaching me the value of finding a place to think. Ashley Cantieny and Libby Palmer for hours of dedicated work doing experiments and processing tedious amounts of data, I still owe you both dinner. Roderick LaFoy for helping me write some of the Matlab codes, helping perfect the art of taking data, for his wonderful eye for good images, and for his useful insight into many problems I encountered. Anna Shih for keeping the lab happy, organized, and moving forward. Jesse Belden for his tireless work on other projects we were

mutually interested in that allowed me to finish in the final months, for teaching me how to focus my efforts on one thing at a time, and for his friendship. Brenden Epps for being a great friend and mentor, for tutoring me patiently on the intricacies of fluid dynamics, for working into the night regularly on difficult problems, and for reminding me to not forget about the rest of my life when I was in the lab late. Jeffrey Aristoff for becoming a great friend and invaluable co-author.

I would like to remember Celeste Fowler, who was my deskmate when I first arrived at MIT. After our first semester she was diagnosed with cancer and never had the opportunity to finish what she started here. Many times I have been on campus late and had her cheerful encouragement from that first year inspire me to keep up the good work. I know she could have done great things here, but imagine she is doing more important things elsewhere, I just wish she would send us a picture.

I also want to thank my best friends Chris Burt and Julie Sampson who drove me to college everyday for a week when my life fell into ruin. Their support helped me realize that I could still do anything I put my mind to even if the path to get there wasn't the one I had intended. And despite the fact that I dropped out a week later, that memory has always given me strength to stick with the rest of my education. The greatest amount of supporting credit goes to my grandparents Tony and Florence Dombrosky for giving me a place to live, getting me a job, and enrolling me in college after a discouraging year, and for all of the wonderful memories and support I felt with them throughout my life. I would like to thank my parents for shoving the importance of getting an education down my throat, but I have to admit it didn't work out the way they sold it to me, but it turned out pretty darn good. A special thanks goes out to Doug and LeiMomi Sampson for their encouragement, financial support, and undying care for me and my family through the past 12 years, you guys are amazing.

As always there are many many other people who should be thanked that I have forgotten here. Please do not take offense, but feel free to give me a hard time the next time we see one another.

THIS PAGE INTENTIONALLY LEFT BLANK

Contents

1	Introduction	23
1.1	Part I: Water entry of spheres with and without spin	26
1.2	Part II: High-speed projectile water-entry	28
I	Water entry of spheres with and without spin	34
2	Experimental details	35
2.1	Overview of facility	35
2.2	Experimental Facility	36
2.2.1	Impact tank	36
2.2.2	Shooting mechanism	37
2.2.3	Positioning mechanism	40
2.2.4	System control	42
2.3	Calibration and reliability	46
2.4	Image acquisition and processing	48
2.4.1	Hardware setup	48
2.4.2	Image acquisition and control	49
2.4.3	Position	51
2.4.4	Rotation	63
2.5	Surface properties	63
2.5.1	Surface roughness	65
2.5.2	Wetting angle	68

3	Unsteady forces on spheres during water entry	73
3.1	Introduction	73
3.2	Experimental study	75
3.2.1	Apparatus	78
3.2.2	Spheres	79
3.2.3	Image processing	81
3.2.4	Post processing	85
3.3	Results	87
3.3.1	Velocity and acceleration	90
3.3.2	Coefficient of drag	93
3.3.3	Non-cavity forming cases	97
3.4	Cavity forming cases	102
3.5	Discussion	106
4	Water entry of spinning spheres	113
4.1	Introduction	114
4.1.1	Water-entry problem	115
4.1.2	Spinning sphere problem	118
4.2	Experimental Details	120
4.3	Results and Discussion	125
4.3.1	Overall cavity dynamics	125
4.3.2	Effect of spin on cavity and splash asymmetry	128
4.3.3	Sphere trajectory	138
4.3.4	Cavity pinch-off	144
4.3.5	Lift and drag forces on the spinning sphere	145
4.4	Conclusions	156
4.5	Acknowledgments	158
5	The dynamic effect of spin and varied surface treatment on cavity formation during water-entry of spheres	163
5.1	Introduction	164

II	High speed projectile water-entry	178
6	Motivation and recent projectile studies	179
7	Determination of the minimum spin rate required to keep a bullet stabilized in air.	189
7.1	Introduction	190
7.2	Gyroscopic Stabilization	191
7.3	Generalized equations of motion for a torque free body	194
7.4	Minimum axial velocity required to balance the aerodynamic pressure force (first order estimate).	196
7.5	Conclusions	199
7.6	Acknowledgments	200
8	Shallow angle bullet entry	201
8.1	Introduction	201
8.2	Experimental details and methods	202
8.2.1	Impact tank	203
8.2.2	Shooting Range	204
8.2.3	Bullets	205
8.2.4	Image Acquisition and Processing	209
8.2.5	Forces and moments	217
8.3	Experimental Results	222
8.3.1	Ricochet and tumbling	222
8.3.2	0.22 standard projectile	224
8.3.3	0.22 modified aluminum projectile	228
8.3.4	0.06 tapered aluminum projectile	232
8.4	Theoretical Cavity Model	241
8.5	Discussion	249
8.6	Acknowledgements	252
9	Summary and conclusions	257

A	A robust method for curve fitting and evaluating derivatives of experimental data using smoothing splines	263
A.1	Introduction	264
A.2	Analytic example	267
A.2.1	Roughness and Error scaling	270
A.2.2	Comparison between csaps and the present method	273
A.2.3	Predictive error	274
A.3	Algorithm	275
A.4	Experimental example	278
A.4.1	Experimental details	279
A.4.2	Application of the present spline fitting method	280
A.4.3	A check for the derivatives $s'(t)$, $s''(t)$, and $s'''(t)$	283
A.5	Conclusions	287
A.6	Appendix	288
A.6.1	Non-dimensional equations	288
B	Bullet designs	291

List of Figures

1-1	Impact of a hydrophobic coated billiard ball with the free surface. . .	24
2-1	Impact tank	38
2-2	Snell's Law illustration	39
2-3	Paintball gun illustration	39
2-4	Photograph of shooting mechanism (isometric)	41
2-5	Photograph of shooting mechanism (front view)	42
2-6	Loading mechanism	43
2-7	Motion control and data aquisition schematic	44
2-8	Loading and firing sequence	47
2-9	X-Stream Vision XS-3 high speed camera	49
2-10	Photograph of steel sphere impact with marked position	53
2-11	Cross correlation image	54
2-12	Gaussian fit to 3 points	55
2-13	Gaussian fit to 5 points	56
2-14	Gaussian fit to 9 points	57
2-15	Gaussian fit to 21 points	58
2-16	Gaussian fits from 3 to 21 compared	59
2-17	Acceleration n=100,1000	60
2-18	Velocity and acceleration estimates using finite difference, windowed least squares, smoothing spline, 3rd and 5th order least squares . . .	62
2-19	Angular displacement images and residuals	64
2-20	Roughness of two glass spheres of equal diameter (9.5 mm)	66

2-21	Roughness of two glass spheres of equal diameter (9.5 mm)	67
2-22	Roughness of two glass spheres of equal diameter one coated one clean	68
2-23	Diagram of receding and advancing contact angles	70
2-24	Raw image of droplet on sphere	71
3-1	Time series of three hydrophobic spheres	76
3-2	Time series of three hydrophilic spheres	77
3-3	Impact tank and spinning drop setup	78
3-4	Wetting angle raw images	81
3-5	Roughness measurement of glass speheres	82
3-6	Cross correlation and gaussian curve fit	83
3-7	Circulation vs. percentage of max vorticity	85
3-8	Velocity and acceleration estimates using finite difference, windowed least squares, smoothing spline, 3rd and 5th order least squares . . .	87
3-9	Trajectory of three hydrophilic and three hydrophobic spheres	91
3-10	Velocity of hydrophilic and hydrophobic spheres	92
3-11	Acceleration of hydrophilic and hydrophobic spheres	93
3-12	Coefficient of drag for six different cases phobic and philic compared for each mass ratio	95
3-13	Coefficient of drag C_D for hydrophilic acrylic case in PIV	98
3-14	Mosaic of PIV from an acrylic hydrophilic sphere impact	100
3-15	Circulation and impulse from PIV of an acrylic hydrophilic sphere impact	101
3-16	Mosaic of PIV from a ceramic hydrophilic sphere impact	103
3-17	Coefficient of drag for hydrophilic ceramic case in figure 3-16	104
3-18	Circulation and impulse from PIV of a ceramic hydrophilic sphere impact	104
3-19	Coefficient of drag for hydrophobic acrylic case in figure 3-20	106
3-20	Mosaic of PIV from an acrylic hydrophobic sphere impact with cavity formation	107
4-1	Images of the cavity and splash formations by (a) non-spinning and (b) spinning sphere	114

4-2	Schematic of the experimental shooting apparatus	121
4-3	A sequence of images depicting the splash and air cavity formed in the wake of a spinning sphere impacting the water	127
4-4	Splash asymmetry due to spin	129
4-5	Raw images of wedge formation and pinch-off	130
4-6	Four water entry cases with increasing spin parameter	132
4-7	A ‘birds-eye’ view of a spinning sphere impacting the water surface at a downward speed of 5.45 m/s ($Fr = 7.3$)	133
4-8	Side and top view for a high spin parameter case	134
4-9	(a) depth of sphere at wedge impact, (b) spin rate decay and (c) spin rate relation time	137
4-10	Five different trajectories of a billiard ball impact with the free surface	139
4-11	Trajectories for three 2.54 cm spheres with increasing mass ratios . .	141
4-12	High speed images of the cavity formation for three different 2.54 cm spheres with increasing mass ratio	143
4-13	(a) Non-dimensional time to pinch-off plotted against Froude number and (b) normalized arc-length-to-pinch-off as a function of Froude number; (c) normalized depth to pinch-off as a function of Froude number and (d) normalized depth to pinch-off as a function of Froude number and mass ratio.	146
4-14	Free body diagram of the forces affecting the sphere after water entry	148
4-15	Position, velocity and acceleration in the x - and y -directions as a function of time	150
4-16	Lift (a) and drag (b) coefficients as a function of instantaneous Reynolds number $R = V(t)d/\nu$	151
4-17	Coefficient of lift versus instantaneous spin parameter, $S(t)$	153
4-18	Coefficient of drag versus instantaneous spin parameter at Reynolds numbers ranging from $1.2 \times 10^5 - 1.8 \times 10^5$	155

5-1	Case I: Water-entry of a hydrophobic (Case I) and hydrophilic (CaseII) billiard ball $V_o = 1.72 \text{ m/s}$ no rotation	165
5-2	Cutaway view of how the water is affected by the surface of the sphere	167
5-3	Impact tank and spinning drop setup	168
5-4	Case III: Water entry of a spinning hydrophobic billiard ball ($\theta = 120^\circ$, $V_o = 1.72 \text{ m/s}$, $\omega = 218 \text{ rad/s}$)	170
5-5	a) Illustration of the distance the wedge must travel to cross the cavity and b) Number of revolutions for wedge to impact cavity wall	171
5-6	Case IV: Water-entry of a spinning hydrophilic billiard ball ($\theta = 68^\circ$, $V_o = 1.72 \text{ m/s}$, $\omega = 192 \text{ rad/s}$)	172
5-7	Case V: Water-entry of a half-hydrophobic half-hydrophilic billiard ball no rotation (half and half: $\theta_{left} = 120^\circ$, $\theta_{right} = 68^\circ$, $V_o = 120 \text{ m/s}$, $\omega = 0 \text{ rad/s}$)	173
5-8	Likelihood of cavity formation as a function of impact velocity and static wetting angle	174
6-1	High speed cavitating projectile unsuccessful entry	180
6-2	Supercavitating torpedo VA-111 Shkval	181
6-3	Projectile bent during underwater testing of supercavitating bullets .	182
6-4	High speed cavitating projectile successful entry	184
6-5	Underwater images of a high speed cavitating projectile	185
6-6	Photograph of testing range at Aberdeen Maryland	186
7-1	Spin rate versus C_{m_α} for $S_g = 1$	193
7-2	Relationship of XYZ and xyz reference frames	194
7-3	Free body diagram of projectile traveling in Z direction	197
7-4	Minimum spin rate required as a function of length to diameter ratio (L/D)	199
8-1	Gun and impact tank set up	203
8-2	Photograph of the experimental setup	204

8-3	Drawing of a standard and modified 22 caliber bullet	206
8-4	0.22 caliber bullet entering the water photographed from the side and above	211
8-5	Timing diagram	213
8-6	Raw image that has been rotated, zoomed and edge detected.	215
8-7	Free body diagram of bullet entry	220
8-8	Tendency of bullet to ricochet off of the free surface	223
8-9	Images of a modified 22 caliber aluminum bullet case number (1,14,2)	225
8-10	Images of a modified 22 caliber aluminum bullet case number (1,14,2) viewed looking at bullet head on	226
8-11	Position, velocity, and accerlation in x and y for projectile impact shown in figure 8-9	227
8-12	Coefficient of drag, lift, and moment for the projectile impact shown in figure 8-9	228
8-13	Time series of a modified 22 caliber aluminum bullet case number (7,14,7)	230
8-14	Images of a modified 22 caliber aluminum bullet case number (7,14,7) viewed looking at bullet head on.	231
8-15	Position, velocity, and accerlation in x and y for projectile impact shown in figure 8-13	233
8-16	Coefficient of drag, lift, and moment for the projectile impact shown in figure 8-13	234
8-17	Time series of a modified 22 caliber aluminum bullet case number (15,14,10)	236
8-18	Images of a modified 22 caliber aluminum bullet case number (15,14,10) viewed looking at bullet head on.	238
8-19	Position, velocity, and accerlation in x and y for projectile impact shown in figure 8-17	239
8-20	Coefficient of drag, lift, and moment for the projectile impact shown in figure 8-17	240
8-21	Physical sketch of control volume of the flow around a disk	242

8-22	Cavity cross section illustrating surfaces CS_1 and CS_2	244
8-23	Cavity outlines for four different theoretical approaches	250
8-24	Sketch of the cavity near the tip of the disc at an angle to incoming flow	251
8-25	Modified Logvinovich model compared to cavity from case (7,14,7) . .	253
8-26	Modified Logvinovich model compared to cavity from case (15,14,10)	254
A-1	Example of analytic function, noisy data, roughness versus error tolerance and selected spline fits to analytic and noisy data	268
A-2	Comparison of the analytic function and spline fit	270
A-3	Example analytic function and noisy data	271
A-4	Roughness versus error tolerance of cubic splines	273
A-5	Predictive error versus error tolerance for quintic and cubic splines . .	274
A-6	A billiard ball falling into a quiescent pool of water	279
A-7	Position of the billiard ball as a function of time and roughness of quintic smoothing spline versus error tolerance	281
A-8	The selected smoothing spline and its derivatives	282
A-9	Force coefficient versus time for the billiard ball water entry experiment	283
A-10	Velocity and acceleration computed by: finite difference; windowed least squares; third-order polynomial; seventh-order polynomial; and the selected smoothing spline	285
B-1	Aluminum 0.12 in tip with 0.22 in angled shoulder.	292
B-2	Steel 0.12 in tip with 0.245 in angled shoulder.	293
B-3	Bronze 0.12 in tip with 0.192 in angled shoulder.	294
B-4	Aluminum 0.13 in modified tip with two steps 0.15 in long.	295
B-5	Steel 0.13 in modified tip with two steps 0.15 in long.	296
B-6	Bronze 0.13 in modified tip with two steps 0.115 in long.	297
B-7	Aluminum 0.15 in tip with 0.22 in shoulder.	298
B-8	Steel 0.15 in tip with 0.21 in shoulder.	299
B-9	Bronze 0.15 in tip with 0.165 in shoulder.	300
B-10	Aluminum 0.22 in tip with no shoulder.	301

B-11	Stee 0.22 in tip with no shoulder.	302
B-12	Bronze 0.22 in tip with no shoulder.	303
B-13	Aluminum 0.06 in tip with no two shoulders.	304
B-14	Bronze 0.06 in tip with shoulder and taper.	305
B-15	Bronze 0.07 in tip with taper only.	306

THIS PAGE INTENTIONALLY LEFT BLANK

List of Tables

2.1	Wheel spacing vs. spin rate	47
2.2	High-speed camera resolution vs. frame rate	50
2.3	Roughness of spheres used in this study	69
3.1	Spheres used in C_D study	80
8.1	Bullet types and their respective tip diameters (d_{tip}), density (ρ), and L/d_{tip} ratios	207
8.2	Outline of method used to uniquely store information about each impact case	218
8.3	Case structure of each data cell	219
A.1	Windowed least squares estimates of the first, second, and third derivatives of noisy data	284

THIS PAGE INTENTIONALLY LEFT BLANK

Chapter 1

Introduction

This two-part thesis looks at the impact of projectiles on the air-water free surface. Part I focuses on spherical projectiles with and without angular velocity, and examines the effect of mass ratio, diameter, surface coating and spin on the cavity formation and projectile dynamics. Part II focuses on the impact of ballistic projectiles with and without axial rotation on the free surface at shallow angles. This work was done in collaboration with the Naval Undersea Warfare Center (NUWC) in Newport, RI.

Free surface water entry has been the subject of scientific investigation for well over a century. The first photographic-based investigations were performed by [36]. Similarly the work of [16], and [5], offered qualitative explanations for the observed cavity shapes. Since then, the beauty and symmetry of spheres entering the water surface has become appealing to many. Figure 1-1(a) shows a symmetric cavity forming in the wake of a hydrophobic sphere. It depicts a large crown of fluid above the free surface that is ejected upward as the sphere passes through the interface. It also shows an hour-glass shaped cavity with the narrowest point being the location at which the cavity will eventually collapse. This event is referred to as deep seal or pinch-off. After pinch-off the cavity is split into two parts, one connected to the free surface, and a smaller air cavity connected to the sphere. Two jets of fluid form at the point of pinch-off, one passing through interior of the upper cavity passing above the free surface and often traveling further above the free surface than the sphere was dropped. The lower cavity also contains a jet that impinges on the top of

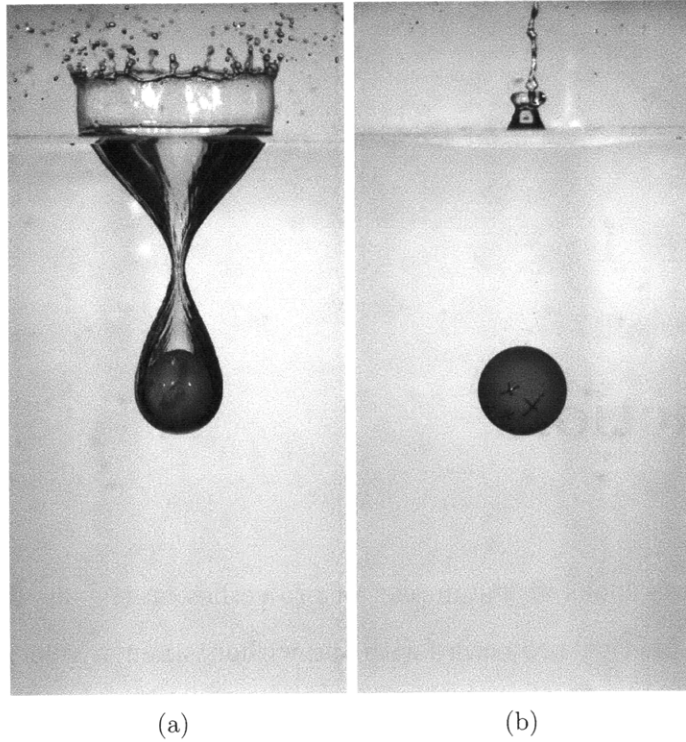


Figure 1-1: Impact of a hydrophobic coated billiard ball with the free surface.

the sphere inside the smaller cavity. Depending on the speed of impact and surface characteristics (hydrophobic or hydrophilic) an impacting sphere can either create an air cavity in its wake (figure 1-1(a)) or no air cavity (figure 1-1(b)) as described by Duez [9].

Many scientists have developed mathematical models to determine the forces at impact and explain the characteristics of splash formation associated with these impacts [15, 18, 28, 24, 4, 2, 33, 20, 22, 13, 37]. Current theoretical models predict the forces of impact up to a half a diameter below the free surface [19], and modern high-speed imaging techniques are discovering phenomenon previously unseen [26]. Many models also address the size and nature of the cavity shape. These models are well developed for relatively slow impact speeds (0 to 20 m/s), but break down at higher velocities [25, 13, 8]. Researchers have explored the changes in cavity shape as a function of atmospheric pressure[11], sphere size [1] and discs rather than spheres[6].

While models that predict the cavity formation and forces on the sphere exist,

very few experiments that measure the forces have been performed. The work of [21] used a force transducer attached to a sphere to experimentally determine the forces of impact up to one radius under the free surface, but force measurements below this depth are lacking in the literature. This thesis attempts to fill this void with detailed experiments. For example, in chapter 3, experimental force data is presented from impact to 12 diameters below the free surface. This data represents the first of its kind and should help improve the models previously developed for times after impact. This thesis also addresses the cases where impact does not form a cavity and gives force data for those cases as well (also in chapter 3).

The problem is generally complicated further by adding a rotational component to the impacting sphere. A full treatment of explaining the effect of rotation is presented in chapter 4 along with a review of the previous literature, which includes the study of sports balls, a topic which inherently includes the study of spinning spheres.

Cavity formation is relevant to many applications including float-plane impact [32], ship slamming [10], stone skipping [23] and drag reduction [30, 3]. Industrial applications include structural interactions with the free surface such, as extreme waves and weather on oil platforms. The application of sprayed adhesives on various surfaces or the coating of objects with dyes and paints can also be related to studies of this nature. Even the sports industry is interested in the water entry of athletes, reducing drag of swimmers [27] near the free surface and the entry and exit of oars in rowing [7]. Dynamic and surface treatment effects on water-entry are of particular relevance to naval hydrodynamics in the areas of torpedo entry [17] and methods for missile deployment [34, 35].

An extension of this research relates to the high-speed, shallow-water entry of projectiles such as military ballistics. Most standardized projectiles are not designed to enter the water, instead they are designed to impart all or most of the kinetic energy they carry into the object they are impacting. This typically results in bullet break up and mushrooming. When these projectiles impact the water at low angles they typically do not enter the water; instead, they either ricochet off the surface or break into many pieces. However, through improved designs, high speed projectiles

can enter the water surface. Results from tests with the NUWC and tests performed at MIT indicate that projectiles with flat noses, tapered sections, and high length to diameter ratios can pierce the surface at low angles, create vaporous cavities, and continue to descend through the water column without ricochet [12], [31] as discussed in Part II.

The following sections give synopses of the chapters contained within this thesis and discuss some of the contributions related to each. References are given in the bibliography of each chapter.

1.1 Part I: Water entry of spheres with and without spin

Part I describes the water entry of spheres with and without spin. The forces exerted on the spheres and the cavity dynamics of impact with the free surface are the main focus. Spin rate, mass ratio, diameter and surface treatment can alter the forces on the sphere and the cavity formation. The specific effects of these parameters are investigated.

Chapter 2 describes the details of the experimental methods in a manner that is accessible to other researchers performing similar work. Details about the equipment used, measurement techniques, and image processing methods are included. Several novel methods were used to determine position with sub-pixel accuracy and to extract the spin rate of the spheres. A method for determining the roughness of a curved object is presented and is now used in the Center for Materials Science and Engineering (CMSE) at MIT. Finally, this chapter includes an introduction to a novel spline fitting method developed specifically for this project; this method is described in detail in Appendix A.

Chapter 3 looks at the forces on the spheres as they descend through the water column with and without cavity formation. This chapter emphasizes the importance of highly resolved data (in space and time) and spline fitting as a means of identifying

forces in the trajectory that affect the sphere. The data shows the unsteady nature of the forces affecting the spheres and represents the first full scale force measurement data of spheres impacting the free surface from 0.5 to 12 diameters below the free surface. Previous studies only look at forces up to 0.5 diameters below the free surface [21, 29]. Fluid forces affect the dynamics of low mass ratio (m^*) spheres (e.g. acrylic, $m^* = 1.2$) more than higher mass ratios (e.g. steel, $m^* = 7.8$). Furthermore, the drag of a non-cavity forming sphere is much higher than the cavity forming counterpart. The surface coating and roughness can affect whether or not a cavity is formed [9].

PIV data presented shows excellent agreement with viscous drag theories in the non-cavity forming cases. In the lower mass ratio cases a vortex ring is shed into the wake and causes the sphere to come to a near halt in its path. In contrast the PIV of the cavity forming cases reveals a potential flow like flow field.

Chapter 4 describes the water entry of spinning spheres and comes directly from a paper that is now published in the *Journal of Fluid Mechanics* [30]. This chapter describes the effect of spin on cavity formation, lift, drag and deep seal. It also highlights a new phenomenon first witnessed by the author in which a wedge of fluid is drawn from one side of the open cavity to another. The cavity is formed when the side of the spinning sphere with the least relative velocity draws water across the cavity due to the no slip boundary condition along the sphere. This study included a comprehensive look at many parameters that could affect deep seal, but concludes that the only parameter that appears to affect deep seal (at these Froude numbers) is the mass ratio. The chapter applies a scaling law that takes into account both Froude number and mass ratio which shows good agreement with experiments.

Chapter 5 illustrates the effect of surface dynamics (transverse rotation of a sphere) and surface treatment on the behavior of cavity formation. Transverse rotation of the sphere or an uneven surface treatment can create altered cavity shapes and affect the trajectory of the spheres. In the rotating cases, the no-slip boundary condition plays a role in allowing fluid to be drawn up and around the cavity along the side of least relative velocity. This formation creates a wedge of fluid that traverses the cavity and bisects the cavity into two parts as mentioned in chapter 4. A theoretical model

that predicts the time for the wedge to cross the cavity is also presented and shows good agreement with experiments. Interestingly, the same behavior can be duplicated using an uneven surface treatment where a sphere is coated half in a hydrophilic and half in a hydrophobic coating.

1.2 Part II: High-speed projectile water-entry

Part II discusses the underwater behavior of bullets designed for air to sub-surface flight. Through collaboration with NUWC it was determined that improvements to the cavity model were needed and an independent study of the cavity shape should be performed. Using the facilities at the MIT Rifle Range, experiments were performed with small projectiles with varying shapes. The theoretical model of [14] was re-derived and improved to account for pitch and yaw inside the cavity. The improved model shows good agreement with experimental data.

Chapter 6 serves as motivation for the high speed projectile study. Tests at Aberdeen, MD are discussed and problems associated with that setup are used as a means to motivate the laboratory study presented in chapter 8. One of the major findings at Aberdeen was that in-air and underwater stability are dissimilar enough to warrant careful consideration of each when designing projectiles that perform in both conditions. In-air stability is accomplished through gyroscopic rotation, fins, flares, etc. Underwater stability is accomplished by intermittent contact with the side walls of the cavity, which require narrow and long projectiles. These long projectiles counteract gyroscopic stabilization, thus requiring fins or flares, however, fins and flares can cause cavity rupture and erratic projectile motion when they come in contact with the cavity wall. Considerations for both in-air and underwater stability are presented here, but they are the topic of on going study.

Chapter 7 is a short discussion in response to the difficulty of using gyroscopic stabilization as a means of stabilizing these projectiles in air and underwater. In particular the equations of motion are used to derive a minimum spin rate required to keep these projectiles stable in air, and it turns out that as the length to diameter

ratio is increased the rate of spin required grows exponentially. In practice the spin rates required for large L/D projectiles is likely not feasible.

Chapter 8 outlines a set of experiments wherein a 0.22 caliber rifle was used to shoot projectiles of varying shape and material. The theoretical model proposed by [14] is presented and small adjustments made to improve the theory. A small-angle pitch/yaw component was added for further improvement. This model matches well with the experimental study presented and could easily be used by future researchers and designers for more accurate underwater cavity estimates. A discussion about the forces and moments acting on the projectiles is also presented and the use of the side-wall as a means of stabilization is validated. This work was recently highlighted in an episode of Time Warp on the Discovery Channel.

Chapter 9 is a conclusion to the entire thesis and outlines the possible extensions of this work in the future. It also outlines a list of contributions this work represents and gives a broader picture of how the presentation fits into the framework of experimental and theoretical hydrodynamics.

The appendix contains a paper written about the spline method used to obtain valid velocity and acceleration data. It also includes a short user guide and set of matlab codes associated with the image processing methods. Finally, a series of engineering drawings representing the designs for the bullets presented in chapter 8 are given.

Bibliography

- [1] J.M. Aristoff and J.W.M. Bush. Water entry of small hydrophobic spheres. *J. Fluid Mech.*, 619:45–78, 2009.
- [2] K. Asfar and S. Moore. Rigid-body water impact at shallow angles of incidence. In *Proceedings of the Sixth (1987) International Offshore Mechanics and Arctic Engineering Symposium.*, volume 2 of *Proceedings of the International Offshore Mechanics and Arctic Engineering Symposium*, pages 105–112, Houston, TX, USA, 1987. Virginia Polytechnic Inst & State Univ, Blacksburg, VA,

USA, ASME, New York, NY, USA. Compilation and indexing terms, Copyright 2005 Elsevier Engineering Information, Inc.

- [3] S. Ashley. Warp drive underwater. *Sci. Amer.*, 284:70–79, 2001.
- [4] H. M. Barkla and L. J. Auchterlonie. The magnus or robins effect on rotating spheres. *Journal of Fluid Mechanics*, 47(3):437–447, 1971.
- [5] G. E. Bell. On the impact of a solid sphere with a fluid surface. *Phil. Mag. J. Sci.*, 48:753–765, 1924.
- [6] R. Bergmann, D. Meer, M. Stijnman, R. Sandtke, A. Prosperetti, and D. Lohse. Giant bubble pinch-off. *Phys. Rev. Lett.*, 96(154505):1–4, 2006.
- [7] Anna Coppel, Trevor Gardner, Nicholas Caplan, and David Hargreaves. Numerical modelling of the flow around rowing oar blades (p71). *The Engineering of Sport 7*, 1:353–361, 2008.
- [8] V. Duclaux, F. Caillé, C. Duez, C. Ybert, L. Bocquet, and C. Clanet. Dynamics of transient cavities. *J. Fluid Mech.*, 591:1–19, 2007.
- [9] Cyril Duez, Christophe Ybert, Christophe Clanet, and Lyderic Bocquet. Making a splash with water repellency. *Nat Phys*, 3:180–183, 2007.
- [10] O. M. Faltinsen. *Sea loads on ships and offshore structures*. Cambridge Univ. Press, 1990.
- [11] David Gilbarg and Robert A. Anderson. Influence of atmospheric pressure on the phenomena accompanying the entry of spheres into water. *Journal of Applied Physics*, 19(2):127–139, 1948.
- [12] Jason T. Gomez and Arun Shukla. Multiple impact penetration of semi-infinite concrete. *International Journal of Impact Engineering*, 25:965–979, 2001.
- [13] M. Lee. On the water-entry-induced cavity closure for a wide range of entry speeds. *Journal of Fluids Engineering, Transactions of the ASME*, 125(5):927–

930, 2003. Compilation and indexing terms, Copyright 2005 Elsevier Engineering Information, Inc.

- [14] Georgii Vladimirovich Logvinovich. *Hydrodynamics of free-boundary flows*. Jerusalem, Israel Program for Scientific Translation; [available from the U.S. Dept. of Commerce, National Technical Information Service, Springfield, Va.], 1972.
- [15] J. W. Maccoll. Aerodynamics of a spinning sphere. *Royal Aeronautical Society – Journal*, 32(213):777–798, 1928.
- [16] A. Mallock. Sounds produced by drops falling on water. *Proc. Roy. Soc. Lond. Ser. A.*, 95:138–143, 1918.
- [17] Albert May and William R. Hoover. A study of the water-entry cavity. Unclassified NOLTR 63-264, United States Naval Ordnance Laboratory, White Oak, Maryland, 1963.
- [18] Albert May and J. C. Woodhull. Drag coefficients of steel spheres entering water vertically. *Journal of Applied Physics*, 19:1109 – 1121, 1948.
- [19] T. Miloh. On the initial-stage slamming of a rigid sphere in a vertical water entry. *Appl. Ocean Res.*, 13:43–48, 1991.
- [20] T. Miloh. On the oblique water-entry problem of a rigid sphere. *Journal of Engineering Mathematics*, 25(1):77–92, 1991.
- [21] M. Moghisi and P. T. Squire. An experimental investigation of the initial force of impact on a sphere striking a liquid surface. *Journal of Fluid Mechanics Digital Archive*, 108(1):133–146, July 1981.
- [22] B. Oesterlo and T. Bui Dinh. Experiments on the lift of a spinning sphere in a range of intermediate reynolds numbers. *Experiments in Fluids*, 25(1):16–22, 06// 1998.

- [23] Lionel Rosellini, Fabien Hersen, Christopher Clanet, and Lyderic Bocquet. Skipping stones. *Journal of Fluid Mechanics*, 543:137 – 146, 2005.
- [24] S. I. Rubinow and J. B. Keller. Transverse force on spinning sphere moving in viscous fluid. *Journal of Fluid Mechanics*, 11(Part 3):447–459, 1961.
- [25] H.-H. Shi and T. Takami. Some progress in the study of the water entry phenomenon. *Experiments in Fluids*, 30(4):475–477, April 2001.
- [26] S. T. Thoroddsen, T. G. Etoh, K. Takehara, and Y. Takano. Impact jetting by a solid sphere. *Journal of Fluid Mechanics*, 499(499):139–148, 2004.
- [27] Huub M. Toussaint, Lex Bruinink, Remco Coster; Michiel De Looze, Bas Van Rossem, Ruurd Van Veenen, and Gert De Groot. Effect of a triathlon wet suit on drag during swimming. *Medicine & Science in Sports & Exercise*, 21(3):325–328, June 1989.
- [28] Leon Trilling. The impact of a body on a water surface at an arbitrary angle. *Journal of Applied Physics*, 21(2):161–170, 1950.
- [29] A. W. Troesch and C.-G. Kang. Hydrodynamic impact loads on three-dimensional bodies. *Proc. 16th Symp. on Naval Hydrodynamics*, pages 537–558, 1987.
- [30] Tadd T. Truscott and Alexandra H. Techet. Water entry of spinning spheres. *J. Fluid Mech.*, 625:135–165, 2009.
- [31] Tadd T. Truscott, Alexandra H. Techet, and David N. Beal. Shallow angle water entry of ballistic projectiles. *61st Annual Meeting of the American Physical Society Division of Fluid Dynamics*, BAPS.2008.DFD.AK.2, November 23 2008.
- [32] T. von Karman. The impact on seaplane floats during landing. Technical Notes 321, National Advisory Committee for Aeronautics, Aerodynamic Institute of the Technical High School, Aachen, October 1929.

- [33] Robert G. Watts and Ricardo Ferrer. The lateral force on a spinning sphere: Aerodynamics of a curveball. *American Journal of Physics*, 55(1):40–44, 1987.
- [34] Chris Weiland, Pavlos Vlachos, and J. Yagla. A novel launcher for cavitating weapons. In *International Symposium on Ballistics*, Vancouver, BC, Canada, Nov 14-18 2005.
- [35] Chris Weiland, Pavlos Vlachos, and J. Yagla. The water piercing missile launcher for launching joint service missiles from submarines. In *American Society of Naval Engineers Day*, Arlington, VA, June 19-21 2006.
- [36] A. M. Worthington, Green Longmans, Co. William Brendon, and Son. *A study of splashes*. London ; New York ; Bombay and Calcutta : Longmans Green and Co. ... ; Plymouth : Printed by William Brendon and Son, Ltd., 1908., 1908 reprinted, The Macmillian Co., New York, 1963.
- [37] A. L. Yarin. Drop impact dynamics: Splashing, spreading, receding, bouncing. *Annual Review of Fluid Mechanics*, 38:159–192, January 2006.

Part I

Water entry of spheres with and without spin

Chapter 2

Experimental details

2.1 Overview of facility

The Impact Laboratory was built as a testing facility for small projectile impacts with the free surface, and as a proof-of-concept online laboratory. The online laboratory has been used several times by researchers outside MIT between 2004 and 2006, but now mainly serves as a research center for free surface impacts and classroom laboratories and demonstrations.

Originally, the impact laboratory was built to showcase the potential of online laboratories to educate students that lack sufficient facilities to complete experiments on their own. Students typically learn more if they are allowed to combine theoretical understanding with experience and visual interaction. Theoretical understanding is most often created in the classroom. Hands on experience and visual stimuli most often come in the laboratory. However, many colleges do not have the same facilities as other campuses. Putting certain laboratories on the world wide web for other college campuses to use as a part of their teaching can help enhance teaching opportunities. Fluid dynamics is an especially difficult field to understand without flow visualization and images of the phenomena being discussed. The free surface impact laboratory was developed with the intent of being used as a model for these types of visualizations for students around the world. Through an interactive website students can perform their own experiments in the impact laboratory. The most basic experiments allow

the user to input the spin rates and drop speeds for the spheres, which are then released into the shooting mechanism and fired at the free surface. Data is then retrieved from the server including: multiple video angles, water temperature, wheel spin rates, etc. Students are then free to process the data as they see fit on their local computers. The experiment was intended to be used both day and night as a resource for students to further expand their experience and understanding through manipulation of the spheres and high-speed video they gather. The laboratory also serves as a jumping point for discussions about the interesting features of the fluid flow formation and as a place for collaboration.

On the MIT campus it serves as a tool for classes in hydrodynamics. The laboratory has been used on a bi-annual basis for a series of labs with topics ranging from added mass to terminal velocity calculations. It is also used by researchers to understand more about the air water interface, and how they interact when an object impacts the free surface. As researchers learn more about this phenomenon they are able to produce more specific models that describe the behavior more accurately. This work is improving the methods of deployment for torpedoes, high-speed projectiles, mines, and even future space mission recovery vehicles. The experimental facility allows researchers to study the unsteady affects of water entry and unexplained phenomenon with the use of high-speed cameras and Particle Image Tracking. These theories becomes more complicated when the objects are spinning and three dimensional effects are considered. These experiments offer experimentalists an opportunity to capture each impact from different view points, thus making these subtle phenomena easier to visualize.

2.2 Experimental Facility

2.2.1 Impact tank

Spherical projectiles are shot into a tank of water 91.4 *cm* (36 *in*) deep, 152.4 *cm* (60 *in*) high, 152.4 *cm* (60 *in*) wide, which holds approximately 2200 *liters* of water

(H_2O). The tank is an acrylic box set into a steel frame. The acrylic box was constructed from 1.27 cm (0.5 in) thick acrylic. The external frame is welded from 5.08 cm (2 in) square extruded steel hollow posts with 6 supporting feet. The weight of the acrylic tank is 133 kg, the frame is 320 kg and the water when full is 2122 kg, together the combined weight is approximately 2575 kg. The outward facing side (front) of the tank has two vertical bars that can be moved if necessary, so as not to obstruct the field of view. The bars prevent the acrylic from bowing out and cracking when the tank is full. In some experiments only one bar is used to increase the viewing area. Figure 3-3 is a photo of the final tank design.

The tank drain is located in the center of the bottom panel. The drain has no lip, and therefore allows all of the water in the tank to be drained when needed. The drain is attached to a standard two-inch pipe, which is then pumped out to the city of Cambridge sewer line. The water that fills the tank is filtered after coming from Cambridge city water by an Everpure E10 with an EC110 prefilter, then by an Everpure K20 with an EC210 filter.

The transparent walls of the acrylic allow for easier video imaging and illumination. Acrylic has an index of refraction of 1.55, which is close to that of water (1.33) though not ideal, as dictated by Snell's Law equation 2.1,

$$N_i \sin(\theta_i) = N_r \sin(\theta_r) \quad (2.1)$$

where N_i is the refractive index of the exiting medium, N_r is the refractive index of the incoming medium, θ_i is the angle normal to the surface interface and the light ray, and θ_r is the refractive angle of the entering light ray normal to the surface interface (see figure 2-2 for clarification). All five sides are transparent to facilitate particle image velocimetry (PIV) experiments, and high speed video acquisition.

2.2.2 Shooting mechanism

Several options were considered initially for the shooting mechanism. A "potato shooter-type" device that required a fuel-air mixture, which is ignited to propel ob-

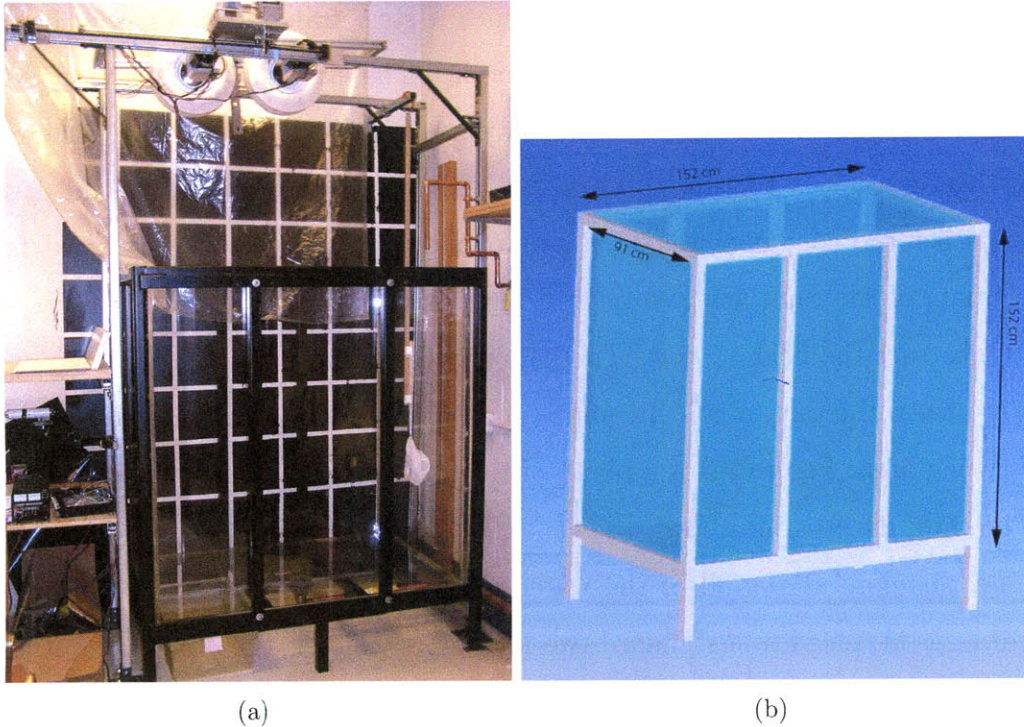


Figure 2-1: Impact tank is made with a steel frame and 1 *in* acrylic. The tank is 91 *cm* \times 152 *cm* \times 152 *cm* and holds 2200 *liters* of water.

jects out of a barrel. Safety concerns and regulations made this high speed option unrealistic. Pneumatic devices, similar to a large paint-ball gun, use pressurized air to launch projectiles. Alternately a slide action device uses a slide or bolt which is pulled back towards the butt of the gun, allowing the projectile to enter the chamber. As the bolt is pulled back it compresses a spring and is finally held in place by a sear gate. The sear gate is released when the trigger is pulled, which also releases the hammer. The hammer then moves towards the back of the chamber and pushes the valve tube into the valve seat. The valve seat forces the cup seal to become unsealed so that the air in the inlet chamber is released into the main chamber and the ball is forced out of the barrel. The process from trigger to firing happens within a few milliseconds. Figure 2-3 illustrates how a paintball gun works.

After some research it became apparent how difficult the precise release of the air would be. Since the Impact Lab design called for the shooting mechanism to be pointed downward it was also difficult to load an object into the chamber without it

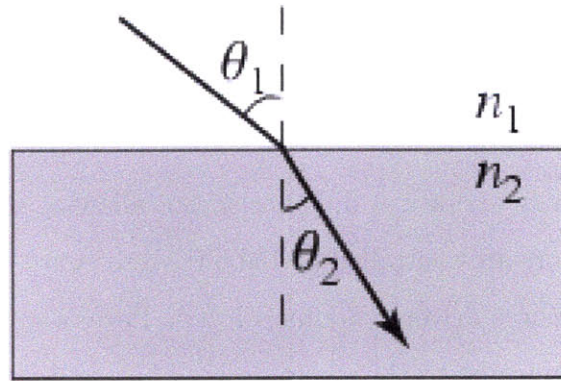


Figure 2-2: Illustration of Snell's Law, refraction of light at the interface of two media with different refractive indices. Photo credit Eric Weisstein <http://scienceworld.wolfram.com/physics/SnellsLaw.html>

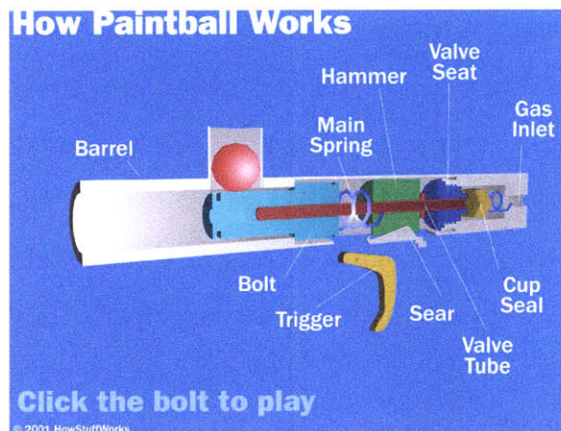


Figure 2-3: Paintball gun illustration. Care of <http://www.howstuffworks.com>

falling out immediately.

The shooting option chosen was a baseball pitching machine. Typically, baseball pitching machines use one or two wheels to propel baseballs at speeds up to 44.7 m/s (100 mph). This type of device could easily be retrofitted with an automatic loader for multiple firings and could shoot objects the size of a baseball very well. However, typical baseball pitching machines do not allow the user to adjust the size of the chamber to fit objects other than baseballs. To allow greater flexibility in choosing object shapes and sizes a modified baseball pitching-style shooter was required. Objects to be studied included wedges that simulate the shape of a ships hull, buoys, torpedos, mines, cylinders, etc. In addition, computer control of shooter speeds are

unavailable in standard consumer models.

The shooting mechanism is composed of two 45.7 *cm* (18 *in*) wheels. They are spun using independent motors (Bodine Electric A/C inverted motors model #42R6BFPP), which can operate at different speeds allowing the user to induce spin if so desired. The motors are controlled by LabVIEW software on the host computer, via their own power source drivers (Bodine Electric Pacesetter model #2703). Each wheel and motor is connected to the structure by a hub and two bearings suspended between a frame of 80/20[®] aluminum. An optical sensor measures the speed of each wheel in revolutions per minute (*rpm*), which is displayed on the users screen. A top view can be seen in figure 2-4, the final assembly can be seen in figure 2-5.

The coordinate system in figure 2-5 represents the generalized coordinates for the shooter itself. The angle θ indicates the angle from which the object was fired. Billiard balls are placed between the wheels for firing by a loading device shown in figure 2-6. The loading device consists of two solenoids (pull-type 24 VDC) which alternate actuation to allow one ball at a time to enter the firing chamber [4]. The plexiglass tubing can hold seven spheres and is connected to the solenoids and shooting mechanism by an aluminum L-bracket. The spheres are released by actuating the solenoids through the LabView interface, which controls the PCI-7342 motion control board, which in turn controls the Grayhill 70RDK8 relay controller.

2.2.3 Positioning mechanism

The positioning mechanism was designed to move the shooting mechanism in a horizontal direction (*x*-direction) and to rotate the shooting mechanism about its center of rotation (θ -direction) as shown in figure 2-5. This added mechanism ensures that the ball will land in the middle of the camera field of view at all angles of impact. The entire shooting assembly is mounted onto two roller bearings that ride on tracks supported by the Unistrut[®] support structure 2-4. The motion of the entire unit is controlled by a stepper motor (Superior Electric model #KML091F07, 2.52 VDC, 3.3 Amps, 200 steps/rev, powered by a Superior Electric SLO-SYN model[®] #SS200MD4 translator drive). This motor is mechanically coupled to a lead screw

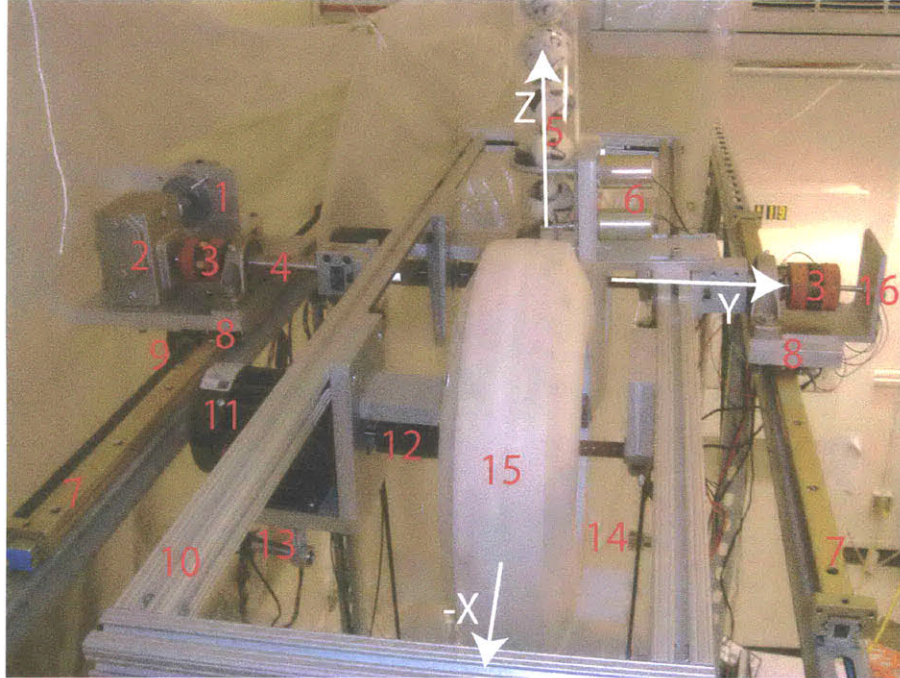


Figure 2-4: Isometric view of shooting mechanism in place. 1) Stepper motor controls rotation (Superior Electric model #KML091F07), 2) Worm gear Grove Gear OE series 130-30 gear reduction of 30:1, 3) Shaft coupling and shaft bearing, 4) Rotational position shaft, 5) Plexiglass loader, 6) Solenoid controlled release of billiard balls, 7) Roller bearing tracks, 8) Roller bearings, 9) Lead screw controls linear position, 10) 80/20[®] aluminum frame, 11) Wheel motors (Bodine Electric A/C inverted motors model #42R6BFPP), 12) Wheel motor to wheel shaft coupling, 13) RPM sensors (Monarch Instruments ROS optical sensor), 14) Break Beam sensors (Monarch Instruments ROS optical sensor), 15) Pitching wheels, 16) Potentiometer (PEM model #KU5011S64) measures angle of attack.

assembly by a 12:1 gear reduction, which controls motion in the x-direction.

The rotation angle is controlled using the same stepper motor configuration as the lead screw assembly. The torque required to rotate the shooting mechanism was greater than the operational limit of the stepper motors coupled to the planetary gear set. Therefore, a worm gear assembly (Grove Gear OE series 130-30 gear reduction of 30:1) is coupled to the system to compensate for the needed holding torque. The National Instruments motion control software controls each stepper motor through the National Instruments[™] motion control board model #PCI-7342.

The support structure is made of Unistrut[®] material. The structure is mounted to the wall in two locations and is supported by six feet on the floor. The frame can

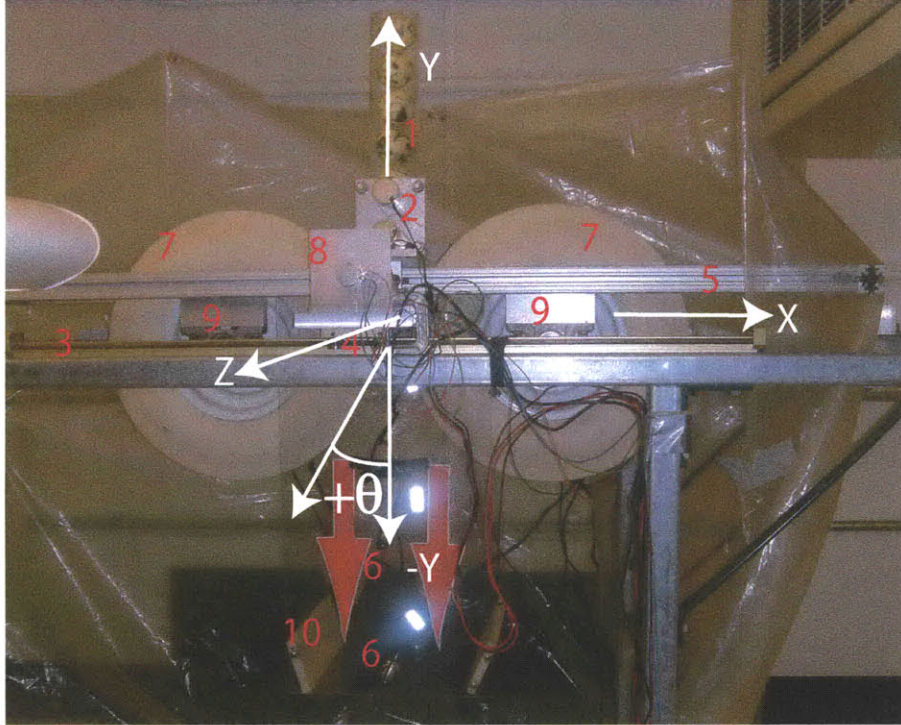


Figure 2-5: Frontal view of shooting mechanism in place. 1) Plexiglass loader, 2) Solenoid controlled release of billiard balls, 3) Roller bearing tracks, 4) Roller bearings, 5) 80/20[®] aluminum frame, 6) Break Beam sensors (Monarch Instruments ROS optical sensor), 7) Pitching wheels, 8) Potentiometer (PEM model#KU5011S64) measures angle of attack, 9) Wheel motor shaft mounting brackets. Note: the two very shiney spots in the picture are the reflective tape used by 6.

be moved if needed and facilitates easy mounting of future equipment. Polyurethane sheeting is connected to the top of the support structure and provides a splash guard to protect electronics and other water sensitive equipment. The structure also serves as a shelf to place electronics off of the floor. A second shelf is sometimes installed to accommodate camera equipment, lighting, etc. A photograph of the final frame with the tank in place can be seen in figure 3-3.

2.2.4 System control

The whole experimental setup is controlled by National Instruments LabView[™] software. The system control works on two levels. The first level is a user interface for those working in the lab to locally control the motors and cameras. The second is a

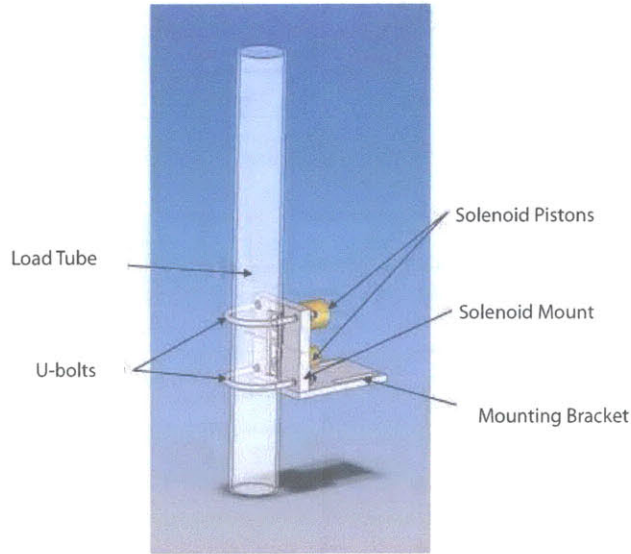


Figure 2-6: Loading mechanism showing the loading tube, u-bolts, solenoids, and mounting bracket.

method for remote users to request operational control by sending a batch file, which allows them to perform experiments and collect data. Both levels control the system in similar ways. The main difference is that from the web, a user sends commands via a batch file, whereas the person in the lab has more real time control over the experimental setup. A flow chart of the mechanical systems and computer control can be seen in figure 2-7. Controlling the system in the lab consists of four inputs, and four outputs. The user can specify the speed of each wheel, the angle of release ($0^\circ - 15^\circ$), and when to fire the projectile. Two outputs come from the RPM sensors, two from the break beams. The angle of impact is converted into an amount of steps needed to turn the shooter to the proper angle, and the amount of steps needed to move the shooter into a safe position for firing. The design intent is for the shots to always land in the center of the tank for safety, but that feature can be overridden if necessary. Each wheel is constrained to spin in such a way that its angular velocity forces the ball downward (ie. the left wheel spins in the $-Z$ direction and the right in the $+Z$ direction.) The motors rotate from $0 - 183 \text{ rad/s}$ ($0 - 1750 \text{ RPM}$) and the drivers can provide 600 steps in that range. The software takes a desired RPM as input and outputs a voltage from $0 - 10 \text{ volts DC}$, which informs the motor driver what speed

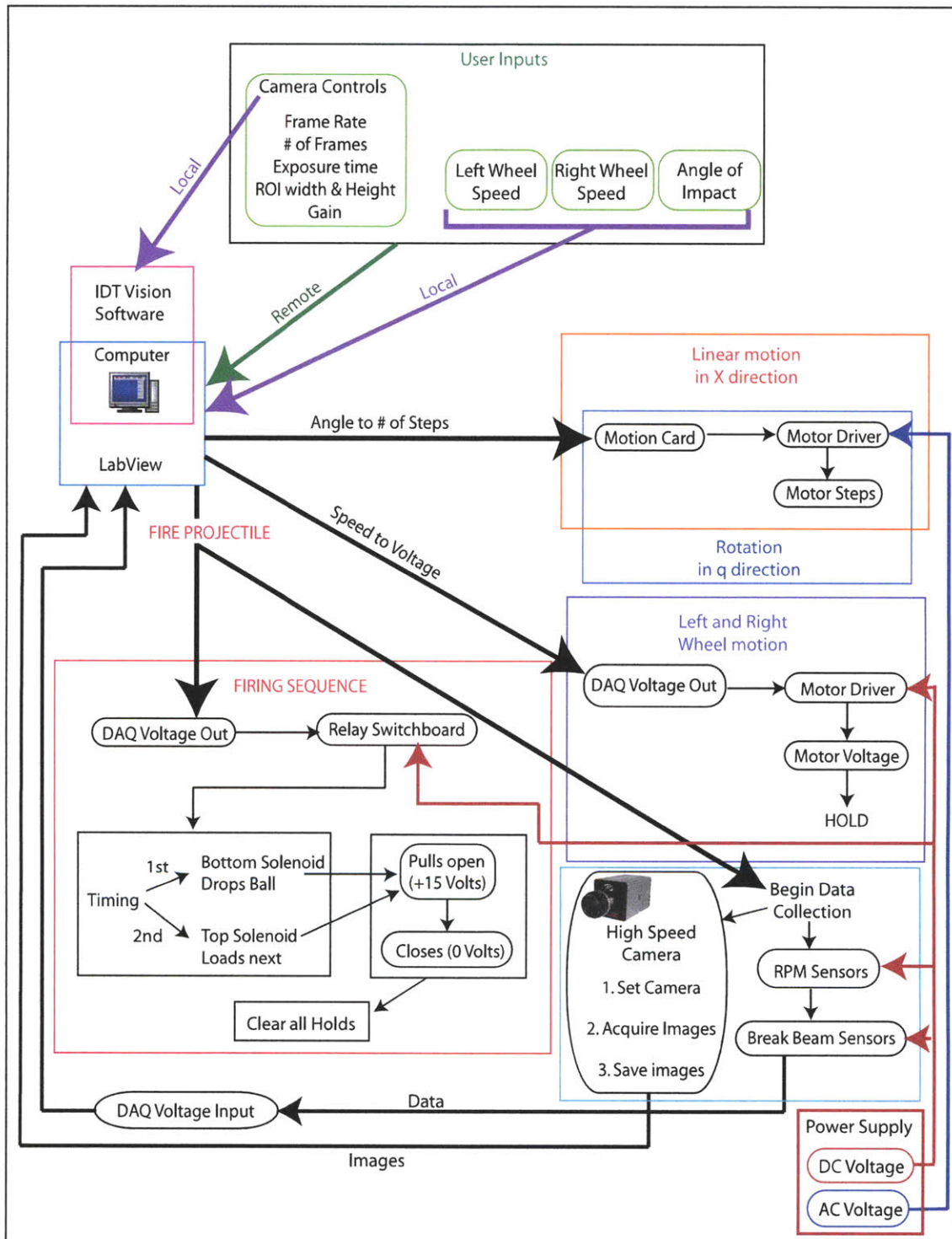


Figure 2-7: Motion control and data acquisition schematic, including differences in local and remote control of experiment.

to spin the motors. The motor driver then supplies the necessary AC voltage to the AC inductive motors and the motors spin. The software then determines how fast the wheels are spinning by looking at the output from the RPM sensors (Monarch Instruments ROS optical sensor). The RPM sensors are optical sensors that create a voltage pulse each time the reflector on the wheel passes by the light beam. The frequency of these occurrences is calculated by the LabVIEW software and output an RPM reading for the user. The break beams are the same sensor as the RPM sensors, yet they work in reverse. The light beams are normally pointed at a reflective tape. The voltage reading is always high until something breaks the light beam. As the ball falls through the light rays the peaks of each break are recorded, the time is measured and the velocity of the sphere is calculated using the known distance between the rays.

The system can be controlled by either a remote user or someone in the lab. The remote user can log into the iMarine website after obtaining a username and password. The user then specifies the parameters for the experiment and submits the job for processing. After submission the commands are sent to the Labview host computer and the request is put into the queue. The computer looks through the queue and waits until an appropriate time to run the experiment. Normally this occurs quickly, unless there are other experiments in progress. The mechanism is positioned according to the inputs and a voltage is sent to the wheels to set them spinning properly. The spheres are then released into the wheels and shot at the free surface. The firing sequence (figure 2-8) begins by sending a voltage to the Grayhill 70RCK8 relay controller. The controller allows 18 volts to pass to the bottom solenoid, which releases the ball into the wheels. Moments later the solenoid is released, then the upper solenoid is held open so the next sphere can be loaded for firing. The upper solenoid is then released to keep the other sphere from falling into the wheels when firing. As the firing sequence begins, a signal is sent to the camera and data acquisition board to begin saving data. This command lasts until the ball is fired and the hold is released. When the holds are released the data from the camera and data acquisition boards is saved to disk. The wheels and positioning mechanism are also

told to return to their resting positions.

The acquired images are sent to the iMarine server for download. This process is done by a secure copy protocol. Once the download is complete, Labview sends an email to the remote user informing him that the information is ready to be downloaded. The user then logs back onto the iMarine website and gathers the data they see relevant to their study. The data can then be stored on the iMarine server for later data mining, and helps create a database of experiments for future work.

If the user is in the lab, the lab user has priority instead of waiting in the queue and simply enters the parameters for the wheels and position separately. When the parameters are entered the computer executes the command immediately. When the user is ready to fire, they simply push the fire button and the sphere is released into the wheels. The user's data remains on the host machine but is not transferred to the iMarine server. The images from the high speed camera are also available for immediate viewing. The main difference in the lab is that the user is in complete control, whereas the remote user must give up some control of the apparatus.

2.3 Calibration and reliability

The diameter of the wheels can increase as the rotation rates increase. This causes the gap where the ball is fired to shrink, which can force the ball out of the firing line in extreme cases. Table 2.1 illustrates the change in size due to spin. The measurements were taken with a camera at each of the various speeds. The images were then read into Matlab and the pixels between the wheels were measured and converted into centimeters.

The wheel size changes proportionally to the wheel speed, therefore billiard balls cannot be shot at all speeds without changing the wheel spacing. The wheel size will be either too narrow or too wide at extreme spin rates. Users will be limited to speeds that will ensure complete ball contact with the wheels. From preliminary testing and use of high-speed video, we infer that the balls can tolerate approximately 0.64cm (0.25inches) of wall flex in the wheels before they are forced out of the firing line.

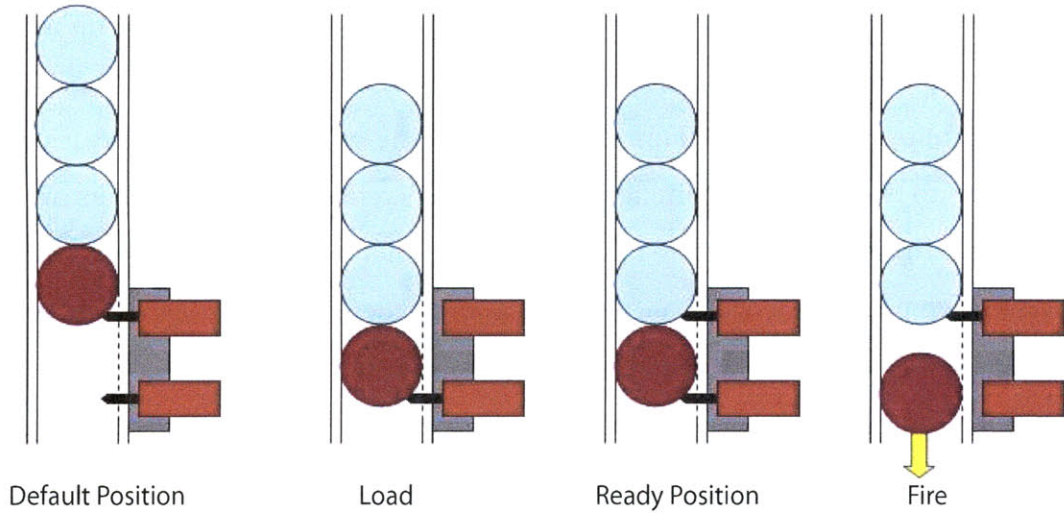


Figure 2-8: Loading mechanism firing and loading sequence [4].

RPM	Distance Apart (cm)
186	5.72
388	5.49
590	5.49
798	5.41
1003	5.28
1215	5.03
1418	4.88
1726	4.60

Table 2.1: Wheel spacing decreases as spin rate increases, which is caused by centripetal forces.

For safety purposes a Plexiglas shield has been installed to protect the camera and users when firing (see figure 2-5).

It is important to calibrate an apparatus like this one after design and implementation. It is fairly easy to parameterize the error involved in returning to an angular and linear position. However, it is more difficult to determine impact angles, spin rate, and impact velocities. This arises because the water in the tank can change height due to evaporation, draining, and filling. Therefore, some parameters are calibrated and the error margins are noted. Others cannot be calibrated but an estimate of values can be made. For instance, it is possible to determine impact velocities from the high speed video images. Making a database of various parameters can help users to pick regions of study and help them to not waste time taking data unnecessarily.

2.4 Image acquisition and processing

2.4.1 Hardware setup

The high speed camera (X-Stream VISION XS-3 model #XS3-000-4) in figure 2-9 is controlled by either LabView or the IDT X-Stream Vision software. When a remote user submits a job for experiment the high speed camera settings and triggering are performed by LabView. This is done by using the IDT X-Stream VI (a subroutine used by LabView to control different parameters of the computer interface) set supplied by IDT . The IDT X-Stream VI set controls the camera and moves the images to the computer by USB. The camera stores up to 4 gigabytes worth of images. When the VI is executed it opens the camera, instructs the camera of the parameters the user has specified, begins acquiring images when the internal trigger is set, and then sends the images back to the computer for storage and data retrieval. Future improvements would include the use of an external trigger (i.e. a light beam being broken, sound triggering, etc.) to begin acquisition.

After the firing sequence begins the camera collects images until the buffer is full. The amount of images collected depends on the size of the image taken. Table 2.2



Figure 2-9: X-Stream Vision XS-3 high speed camera.

shows how many images can be acquired given the pixel size of the image and the related frame rates.

When the setup is run by someone in the laboratory, typically they will use the IDT X-Stream Vision software. This allows the user a little more flexibility in the setup. Since the camera can transfer real time images via the USB cable, the user can check the size, exposure, frame rate, and storage capacity. The user can also capture some data and play it back to see how much of the shot is necessary to keep, and whether the lighting looks right. Unfortunately there is no way for the remote user to have the same advantages. In the future that may change as the IDT X-Stream VI set improves. The laboratory users also use an internal trigger, controlled by the mouse, to tell the camera when to fire. This method is effective, however, an external trigger may be easier to control for some future experiments.

2.4.2 Image acquisition and control

The X-Stream XS-3 can acquire images from 625 *fps* up to 57,000 *fps* by reducing the size of the image (table 2.2). As the image size decreases, the number of lines it has to write becomes less and therefore speeds up the image acquisition. The user can also change the exposure time, which is the main factor in light sensitivity. The amount of light entering the camera can also be changed by the aperture setting on the lens: typically, the user will set the lens to the most open setting available, and then work with the exposure mode. The reason this is done is that the shorter the

Table 2.2: IDT X-Stream XS-3 high speed camera resolution vs. frame rate table.

Image Resolution (Pixels)	Frame Rate (fps)
1280H X 1024V	614
1280H X 640	962
1280H X 320V	1961
1280H X 160V	3910
1280H X 80V	7773
1280H X 40V	15,357
1280H X 20V	29,962
1280H X 10V	57.239

exposure time, the more crisp a fast moving object will appear. Making fast moving objects appear still is usually the goal of high speed photography. The user also has the option to change the gain, number of images aquired, image type (i.e. jpg, tif, avi, mpg, etc.), double or single exposure, and triggering method.

One of the trickiest parts of high speed photography is lighting. Many different effects of the water entry phenomenon can be emphasized by the proper lighting. The best option for water entry is to create an abundance of light and allow the user to step down the exposure time. A decreased exposure time will increase the accuracy and resolution of a particular phenomenon, if the image is well lit. Therefore, two types of light are now employed. The first are halogen bulbs facing the tank on the same side as the camera. These bulbs produce 400 watts of light each and can light the foreground very well if placed correctly. They do not focus the light as well as a spotlight and allow light to scatter to the sides. It is necessary to place these lights strategically to get proper lighting. This can be achieved by setting up the camera in the desired position and then testing the placement of the lights while using the IDT X-Stream Vision software to check that there is enough light. The second method is a backlight, which consists of modular arrays of flourescent bulbs placed behind the tank facing the camera. Each array is made up of 19 T8 series 32 Watt bulbs, supplying a total of 600 Watts of light per panel. Each panel is connected to a track above the water tank by ball bearing rollers. The track and rollers allows easy movement of the lights for maintenance and placement. Normally the lights are

placed between the strengthening crossmembers in the back of the tank. This light is often too strong for the particular shot and can be softened using a white sheet or frosted glass to soften the effect of the backlight. The backlight particularly helps illuminate the splash and cavity formation. When using the back and foreground lighting together the exposure time can often be decreased. This allows the faster and more subtle phenomena to appear less blurred.

In the future, the remote user may want more control of the lighting and camera positioning options. This could be accommodated by allowing the user to control which lights are on, or where the camera and some of the lights are positioned. It would also be advantageous to acquire some high power strobe lighting. This would enable users to sync the cameras with the light and may provide better light than that of the halogen and backlight setup.

2.4.3 Position

It is imperative to determine the trajectory of the spheres as accurately as possible. If this is not done properly then the determination of velocity, acceleration, and forces will be misleading due to the error propagation. Due to the nature of these impacts, the images are the only source of data, making high-precision image processing a necessity. Therefore, it is imperative that the trajectory be determined in a manner that minimizes error and pixel locking.

One method of finding the trajectory involves using a template of the image to be traced and then performing a cross-correlation between the template and the image of interest. If this step is done properly the position of the object can be determined to within ± 1 pixel. This method can be accomplished in a few different ways, here a cross correlation is used between a template (provided by the user) and the next image in the series. The cross correlation returns a matrix of values (-1 to 1) indicating the most likely position of the sphere in the consecutive image. This process can be continued until the position of the sphere in all frames is determined.

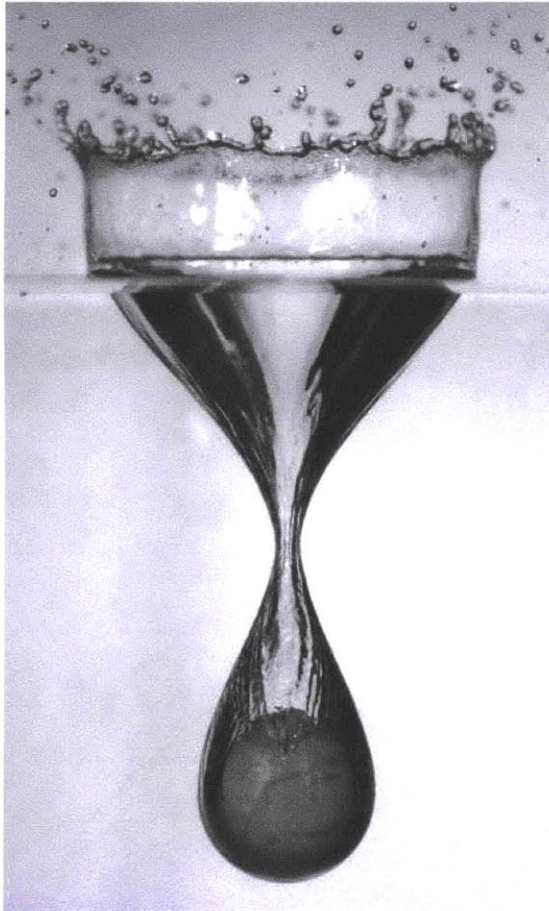
To begin the process the user provides a template by picking the center of the sphere from the first image of interest. Figure 2-10(a) shows an image of the sphere

before any processing is done. The center of the sphere is then marked with a (X) and a circle is drawn around the mark based on the radius in pixels (see figure 2-10(b)). At this point the user can adjust the center of the sphere and the radius to improve the fit. Once the user is finished with the adjustments the image is then cropped as a template. The template is then cross correlated with the next image in the series. The cross correlation produces a new matrix of values from (-1 to 1) where 1 indicates the highest correlation or best estimate of where the sphere occurs in the next image (see figure 3-6). This point is then extracted from the matrix and represents the pixel position of the center of the sphere. Sometimes a large bubble or other common pattern can get a slightly higher correlation than the actual sphere, but in those cases the data can be either thrown out or the user can adjust the error manually.

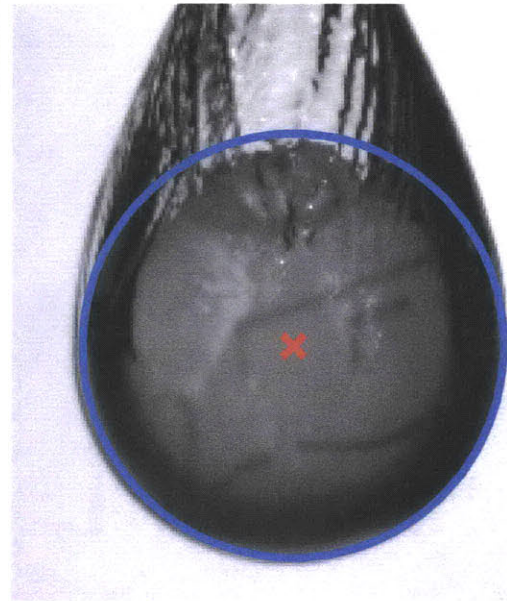
One of the problems with this process is that the images are limited by ± 1 pixel accuracy. This can often lead to pixel locking, where the center of the sphere is actually between two pixels but is interpreted by the program to be on a certain pixel. This can greatly affect the velocity and acceleration when the derivative is involved. One method of overcoming this issue is to fit the data near the point of interest to a Gaussian curve (assuming the cross-correlation peak isn't too steep). This method can give sub-pixel accuracy and greatly improve the acceleration and velocity curves.

This process is accomplished by picking a number of points around the peak from the cross correlation and fitting a Gaussian curve to each row and column of values. Figure 2-11 shows the highest position data obtained by the cross correlation with two points in both directions. The Gaussian fit is applied in both directions and the highest point on the surface is found and marked with an (*).

The next step is to determine the optimum number of points on either side of the peak value to apply to the Gaussian. One can see from figure 2-11 that as one moves away from the peak the values would no longer fit to a Gaussian curve. Using four different fitting values (s=3,5,9,21) it is apparent that using five points for the fit is sufficient and values above 21 become erratic. Figures 2-12 to 2-15 compare these four fitting values. These figures also illustrate the effectiveness of the Gaussian fit on the acceleration curve. Without the fit the acceleration data is almost meaningless.



(a)



(b)

Figure 2-10: Raw image of steel sphere impact with free surface. Sphere is already 3.5 diameters below the free surface. Image from figure 2-10(a) cropped for user to observe center of sphere marked with an 'X', and outline of sphere based on radius marked with a blue circle. User can make adjustments to sphere center and set the proper radius.

The fit shows that the spheres decelerate as a function of frame number (time) with a 2nd or 3rd order decay rate.

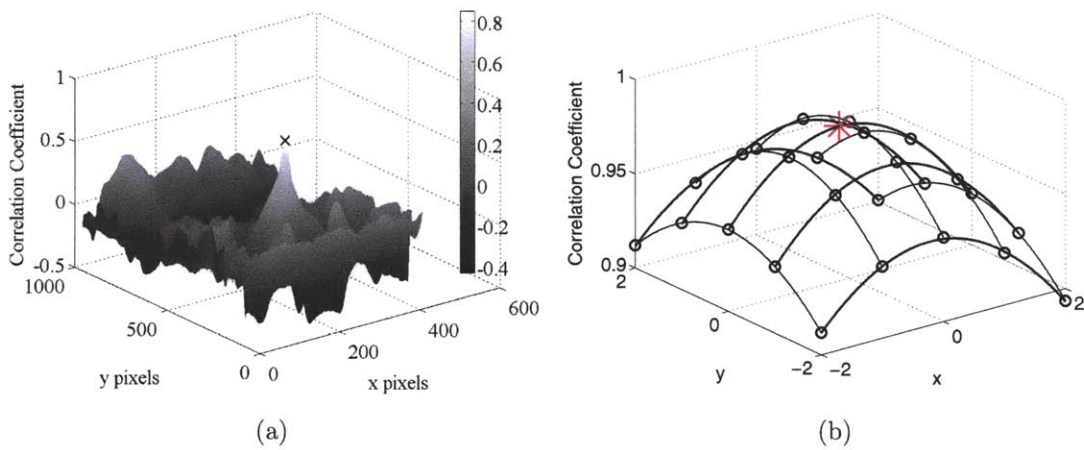


Figure 2-11: Cross correlation of template with next image in series produces a matrix of values from -1 to 1 in which the highest value represents the probable center of the sphere.

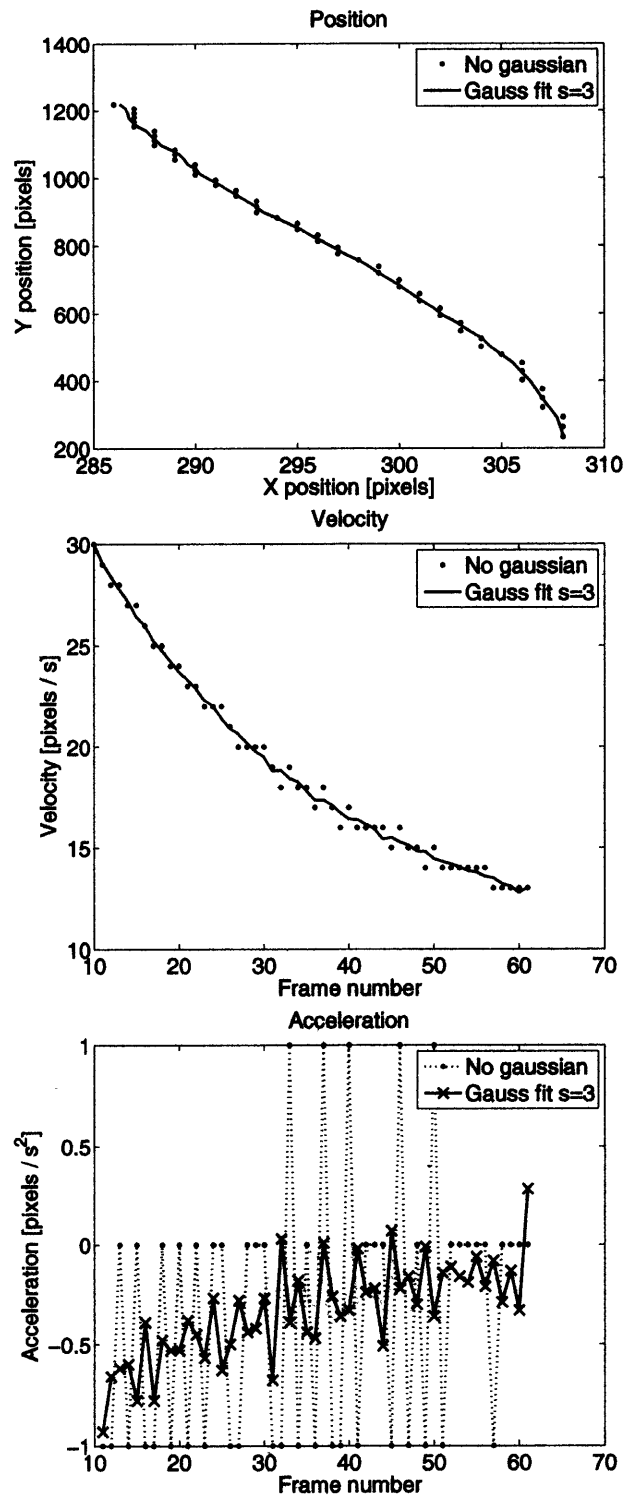


Figure 2-12: Gaussian fit to 3 points compared to no fitting parameter for position, velocity, and acceleration.

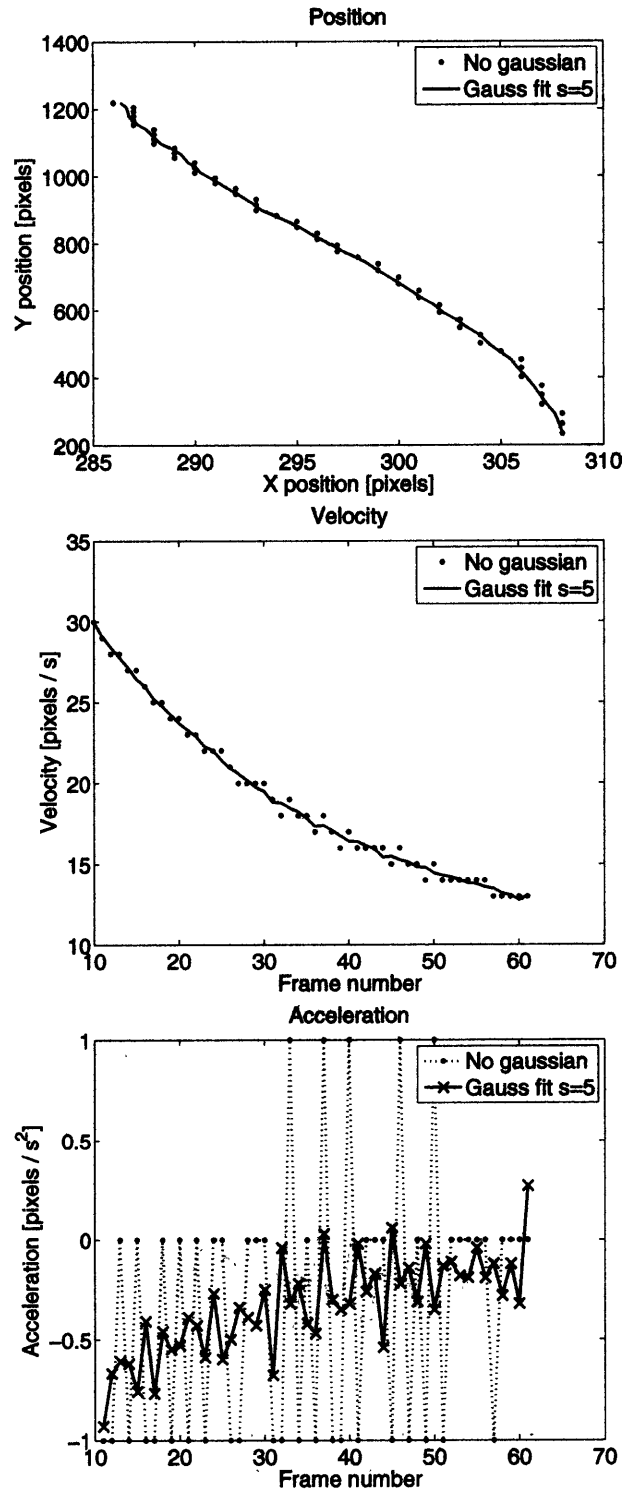


Figure 2-13: Gaussian fit to 5 points compared to no fitting parameter for position, velocity, and acceleration.

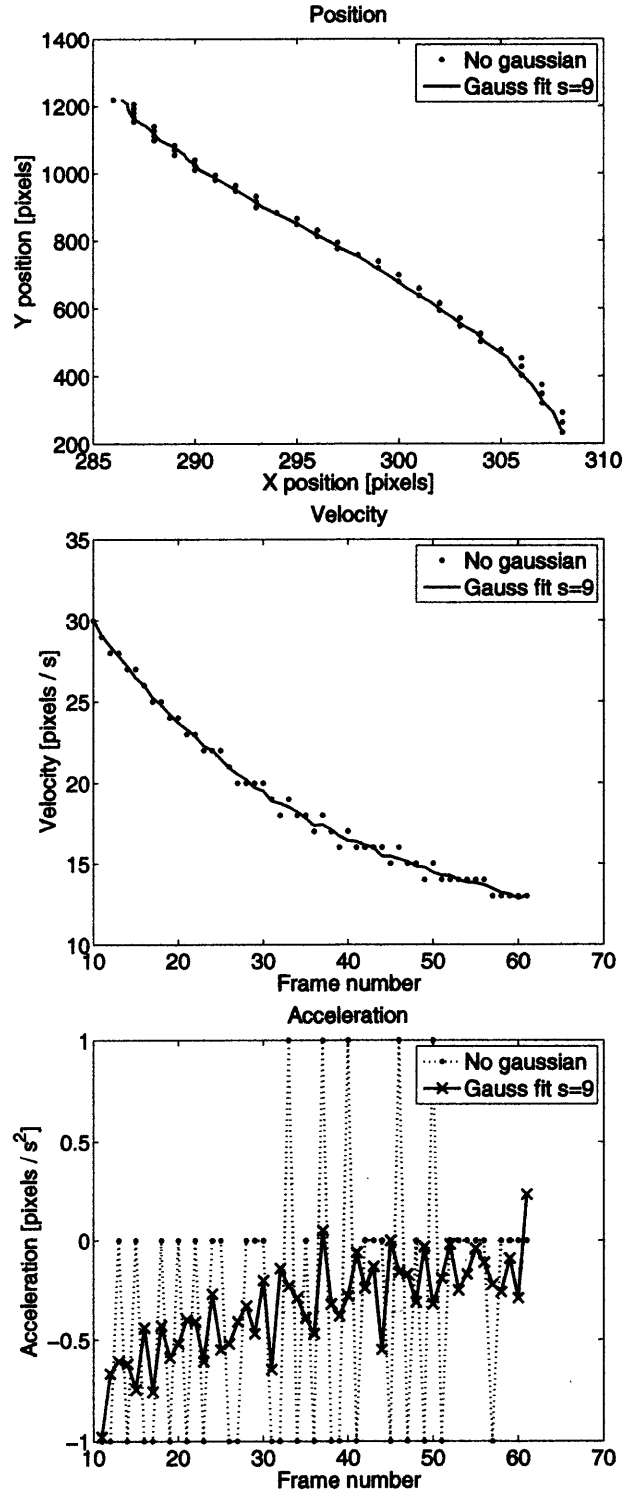


Figure 2-14: Gaussian fit to 9 points compared to no fitting parameter for position, velocity, and acceleration.

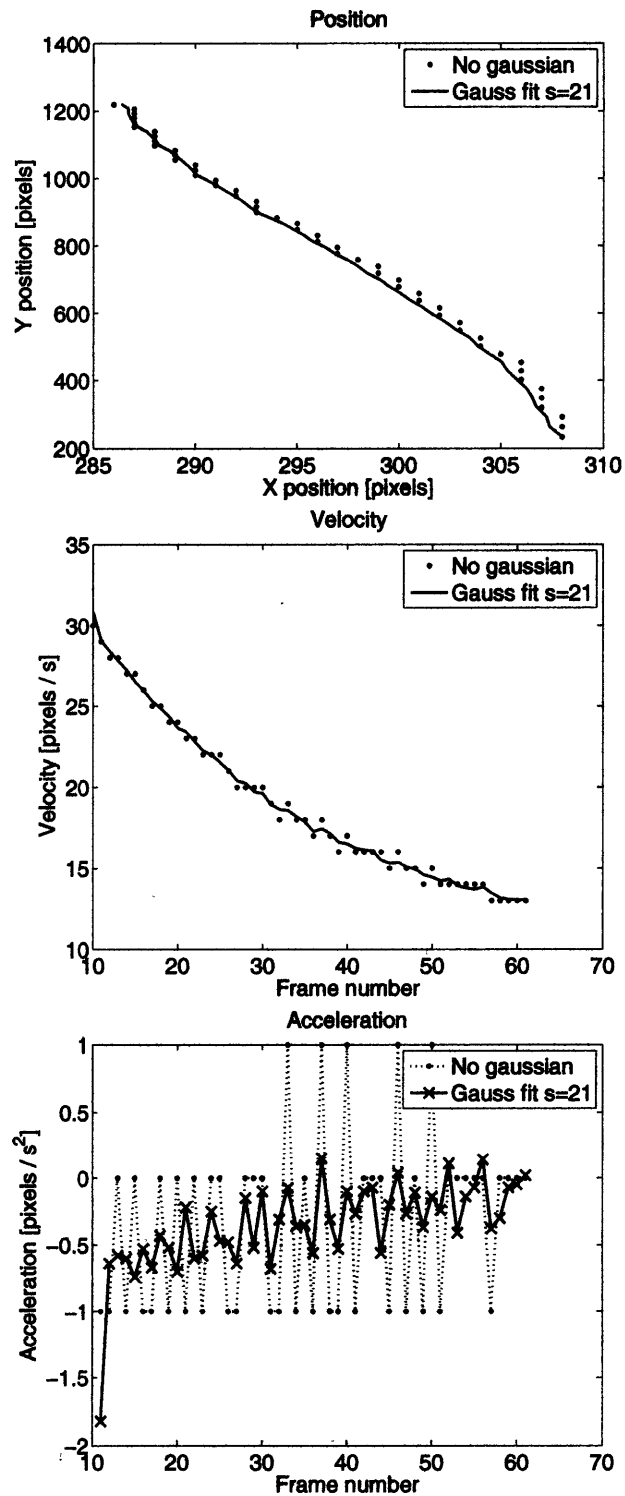


Figure 2-15: Gaussian fit to 21 points compared to no fitting parameter for position, velocity, and acceleration.

If all of the methods are plotted for acceleration one on top of another the inaccuracy of the 21 point fit becomes more obvious. Figure 2-16 shows all of the acceleration data plotted over one another. In general, they all fall on top of one another, emphasizing that increasing the amount of points used to fit the Gaussian curve does not increase the accuracy of the measurement.

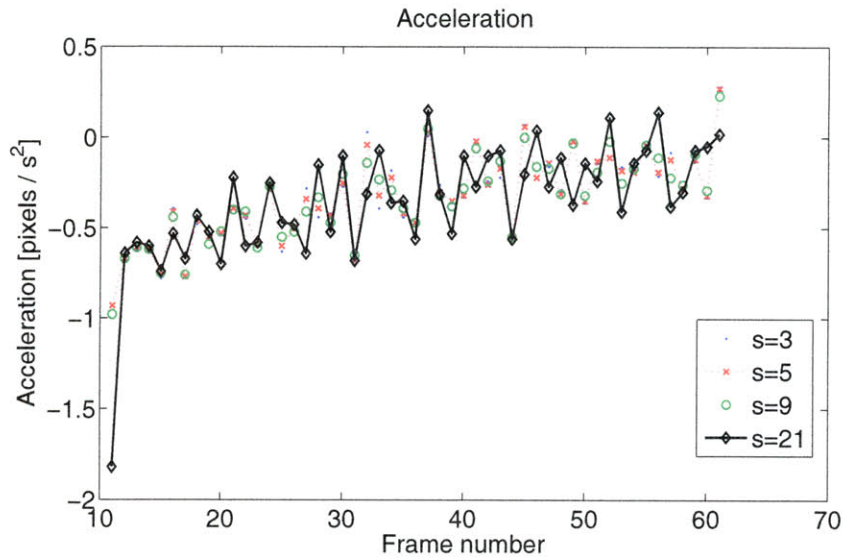


Figure 2-16: Acceleration plots of four different fitting values ($s=3,5,9,21$). Notice that the $s=21$ case appears different than the rest, which is an indication that at 21 points away from the peak value the cross correlation data space is no longer Gaussian as expected.

Now that the number of points needed to fit the Gaussian curve has been determined it is important to determine how increasing the number of points used to define the Gaussian curve itself changes the sub-pixel accuracy of the measurement. Figure 2-17 shows the change in the acceleration curve if 1000 points as opposed to 100 points are used to define the Gaussian fit. It shows that increasing the amount of points along the Gaussian tenfold doesn't seem to affect the outcome enough to justify the time required to run the scripts. Of course, there is a limit to where decreasing the points would be ineffective. Although not plotted here it is reasonable to assume that if the number of points along the Gaussian were reduced to 10 then the effectiveness of the fitting would be in question because the domain space (5 pixels) would only be doubled.

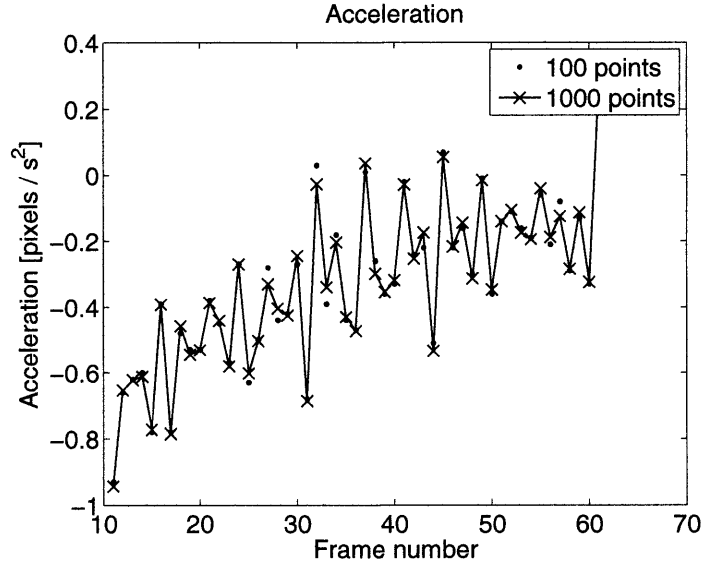


Figure 2-17: Acceleration plot of two different point values ($n=1000,100$) along the same Gaussian curve fit. The case where $n=1000$ is approximately the same as that where $n=100$.

Post Processing

The position data is then normalized by making the free surface the origin of both time and space in the laboratory frame, where the center of the sphere is the origin of the sphere's coordinate system. Thus, when the sphere is centered about the free surface it is said to be at $(x_0, y_0, t_0) = (0, 0, 0)$. A line representing the free surface is used to normalize both the time and spatial data. The easiest method for calibrating the data to a level horizon is to determine the angle of inclination using two points representing the free surface ($\theta = \tan^{-1}(x_{fs2} - x_{fs1}) / (y_{fs1} - y_{fs2})$) and applying a rotational matrix based on this angle to the entire data set given by

$$[x, y] = \begin{pmatrix} \cos \theta & -\sin \theta \\ \sin \theta & \cos \theta \end{pmatrix}. \quad (2.2)$$

The x and y position corresponding to the impact location is then formulated using the new free surface location in y and the nearest frame to impact in x. By subtracting these values to all position data the spatial origin (x_0, y_0, t_0) is now determined.

The actual time of impact is likely not recorded due to the discrete frame rate

of the cameras. Although high speed, the impact event is a finite time and typically happens between frames. To estimate the actual time of impact the frame above (x_a, y_a, t_a) and the frame below (x_b, y_b, t_b) the origin are used to estimate the true impact time as follows,

$$t'_i = t_i + y_a \frac{\Delta t}{\Delta y} \quad (2.3)$$

where $\Delta t = t_b - t_a$ and $\Delta y = y_b - y_a$.

The position data is essentially the only data obtained from experiments like this one. The position data determines all other values including velocity, acceleration and forces. Several methods exist for determining the velocity and acceleration. The first and easiest method is a finite difference. However, this method increases error with each difference and can lead to erroneous results when the accelerations are determined.

Another method is to fit a polynomial of order n to the data, then the velocity and acceleration can be determined simply by taking the first and second derivative of the polynomial. Using a polynomial can lead to accurate results if the trajectories are smooth, continuous, and predictable. However, as the trajectories are altered by viscous diffusion, cavity formation, and impact with the free surface, the ability of the curves to accurately determine the deceleration diminishes.

The accuracy of polynomial approximation can be improved by windowing the data or analyzing only a localized set of data. At a given point $y(t)$, we fit a line $(a_1 t + a_2)$ from t_{i-w} to t_{i+w} for all points along $y(t)$. Using this method, each of the lines along $y(t)$ represents a portion of the position versus time data. The first derivative of the estimate in time is the velocity, the second derivative is acceleration, etc., where the derivatives are applied at the center of each localized set. This method yields much more accurate data in the first and second derivatives. However, it results in the data not being smooth and data near the ends becomes lost.

One way of mitigating these problems is to employ a smoothing spline. A smoothing spline is a continuous, smooth piecewise polynomial of order n that has $n-1$ continuous derivatives at each piecewise dislocation. If the piecewise polynomial is of the

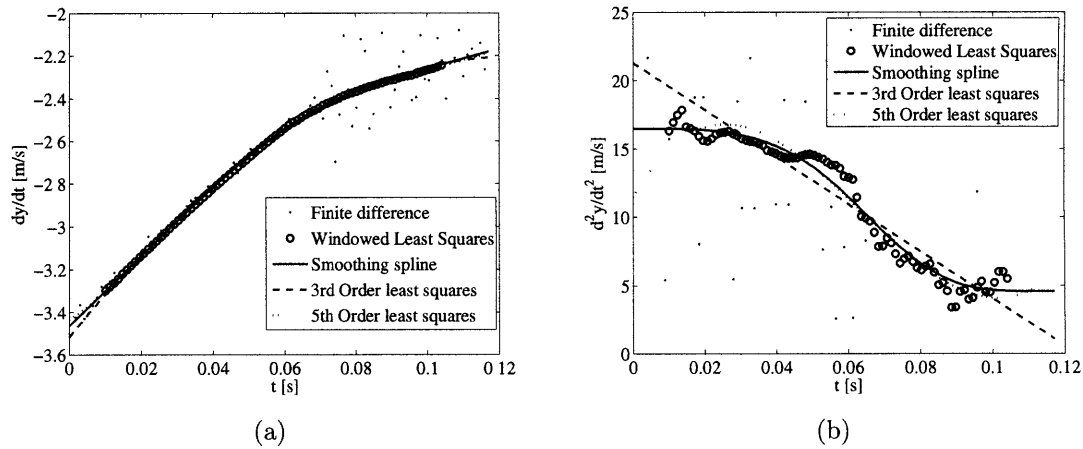


Figure 2-18: Velocity and acceleration for $m^* = 3.9$ and $\theta = 120^\circ$ for a sphere with $U_0 = 3.43$ m/s, computed by finite difference, windowed least squares, smoothing spline, 3rd order least squares, and 5th order least squares. The order of the least squares estimates is the order of the polynomial fitted to the position-time data.

order of the number of points in the data set then the spline represents every point in the data set exactly. Here we use a 5th order spline ($n = 5$) to maintain a continuous second derivative, and apply a novel method for finding the best spline proposed in appendix A.

This method yields excellent results. Figure 3-8 presents a comparison of the finite difference, windowed least squares, smoothing spline, 3rd order least squares, and 5th order least squares methods. The position data (not shown) for all five methods is in excellent agreement. The velocity data shows good agreement for all but the finite difference method. Furthermore, the acceleration (second derivative) illustrates the large discrepancies between all but two of the methods. The best fit that maintains a derivative that is smooth, continuous, has an exact solution and has reasonable end points is the smoothing spline.

The accelerations and velocities from this method can now be used to determine the forces acting on the body. In chapter 4 a force model is used to determine the coefficients of drag and lift. In chapter 3 the force model is applied to elucidate the unsteady nature of the drag coefficient with spheres of varying masses and surface treatments.

2.4.4 Rotation

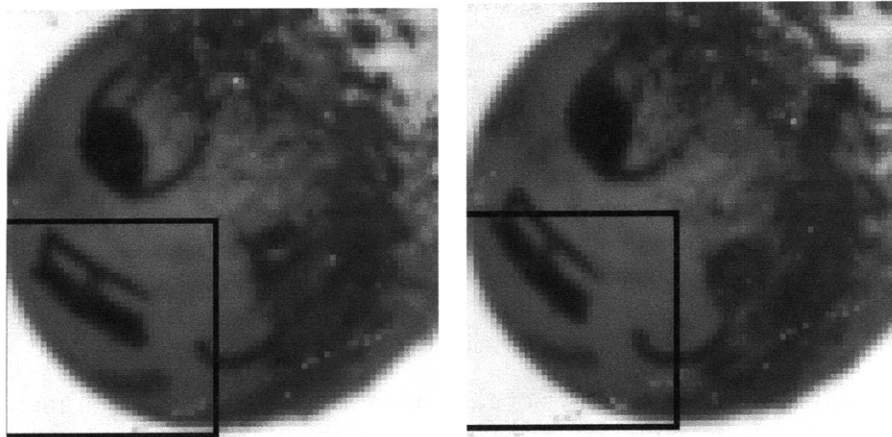
In chapter 4 the effect of spin on the water entry of a cavity forming sphere is presented. In that work it was necessary to determine the rotational velocity of the spheres as a function of time. To do this the position was found as noted above and then an algorithm was developed to determine the angular displacement between frames.

The method begins by cropping everything but the portion of the sphere that is not visually disturbed by the index of refraction changes associated with the cavity (e.g. portion underwater). For the cases presented in chapter 4 the spheres were cropped in the lower left quadrant of the sphere. Two consecutive images were compared by calculating the residual of their difference. One of the images was rotated about the (experimentally determined) center of the sphere from 0 to $\pi/4$ rad in increments of $\pi/1800$ rad and then they were compared again. The result is a minimum in residual where the best estimate of rotation occurs. Figure 2-19 shows an images of a sphere in two consecutive images and plots the residuals for that particular case. The best estimate for rotation is thus $\theta = 11.8^\circ$. In practice, non-uniform markings were placed on the spheres with indelible marker so that the rotational correlations would remain accurate through each time step.

The angular position can be found through a summation of these angular displacements. Spin rate, $\Omega(t)$ rad/s, can be calculated from the first derivative of a second order polynomial fit to the angular position data. The sensitivity of the measurement to accurate position data was calculated by determining the minimum residual of angular displacement for the sphere at its central point and two points on either side. The mean spin rate and standard deviation were then applied to a Student's-t distribution outlined by [3], which revealed error estimates of 4% to 9%.

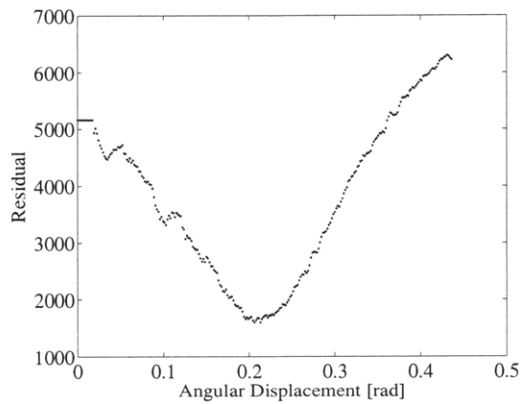
2.5 Surface properties

Projectiles used underwater must be smooth and water resistant, therefore a baseball was not the most desirable object for these experiments. Tennis balls are similar in



(a) image 116

(b) image 117



(c)

Figure 2-19: Two images depicting the angular displacement between them. a) is of image 116 in the series and shows where the program would crop the image to compare to image 117 b). The program outputs the residual of their subtraction in c) and shows that in this case the lowest value (highest correlation) is at 0.2059 rad or 11.8°.

size, but aren't as dense as water and therefore float. Billiard balls and baseballs are both 5.71 *cm* (2.25 *in*) in diameter and weigh 0.17 kg (6 *oz*). Billiard balls are also smooth and water resistant, therefore a billiard ball is a perfect match for an experiment like this one.

2.5.1 Surface roughness

Surface roughness can affect the interaction between the fluid and the sphere. Often surface roughness plays a role in how the surface is wetted. The roughness of the spheres was determined using a profilometer. A model Tencor P-10 Surface Profilometer was used to take the measurements. Raw data was obtained for all types of spheres used in this study. Figure 2-20 shows a typical raw output for both a smooth glass sphere and a glass sphere coated with WX2100 by Cytonix Corp.

The data indicates how dramatic a change can occur with a thin coating like this one. It also illustrates the problem with curved surfaces. Typically, measurements for roughness are done by coating flat surfaces. Here the curvature of the smooth glass surface is obvious. The coated surface is also curved, however, the roughness of the coating masks the curved effect enough to make the measurement appear non-curved. Furthermore, if a simple root mean square (rms) value is taken from either set of data the result is nearly the same. This is because the roughness to curvature ratio is on the same order. The measurement that is desired is one in which the actual roughness is quantified by some numerical value that distinguishes the rough surface from the smooth one. In other words, it would be nice to remove the curvature of the sphere from the measurement to make the surface appear flat.

Typically a high pass filter is used to remove the curvature of the sample. However, it is less than ideal if the wavelength of the curvature is orders of magnitude larger than the sample size. Therefore, this technique is not particularly well suited for use on the surface of spheres.

Another method for determining this is to fit the data to the curvature of a sphere with the same diameter as that of the sample. To do this an assumption is made that the profilometer has been placed so that it passes through the highest point on

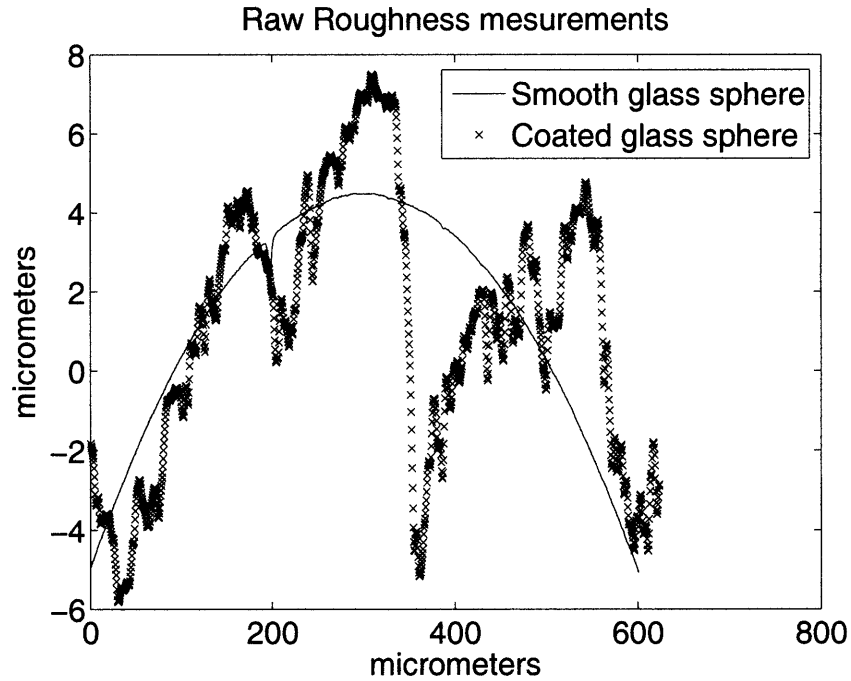


Figure 2-20: Roughness of two glass spheres of equal diameter (9.5 mm). The non-smooth glass sphere was coated with WX2100. Raw data shows the curvature of the sphere, as well as the dramatic difference between the coated and uncoated spheres.

the sphere. Without this assumption it would be difficult to know which radius to use to remove the curvature from the measurement. The user can find the highest point of the sphere by making multiple passes with the profilometer along the sphere in linear directions. By observing the high point on each pass and watching the camera view of the surface the highest point can be determined. If necessary all of the passes can be saved and processed to find the roughness over a larger statistical range. Once the highest point of the sphere is determined, the profilometer can be set to pass through this point and set as the zero point in the measurement. In the case presented here that was done at 100 micrometers. A circle of radius equal to the sample is then made using $R = \sqrt{(y^2 + x^2)}$; and only that portion equal to the sample length is used compared to the measured data. The coordinate systems are then lined up using the point of contact where the profilometer was zeroed. The raw data is then subtracted from the curve and the rms is taken.

Figure 2-21 shows how effective this process can be at flattening the raw data.

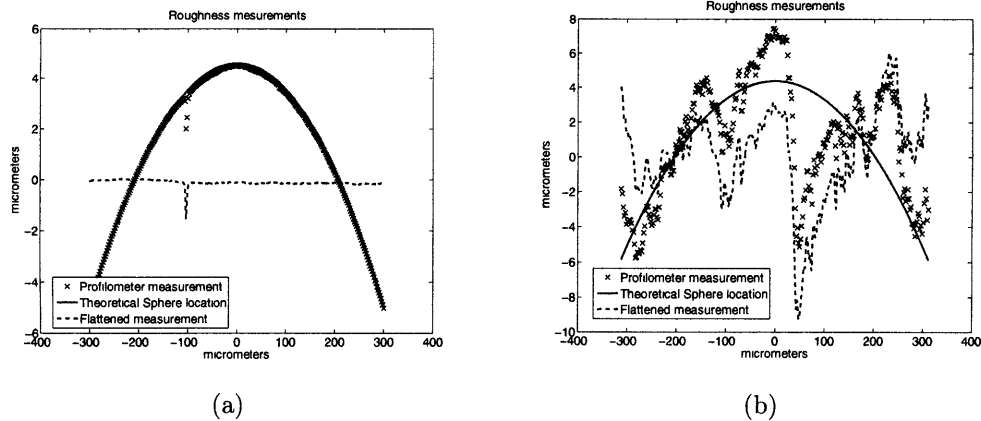


Figure 2-21: Roughness of two glass spheres of equal diameter (9.5 mm). The non-smooth glass sphere was coated with WX2100. 3-5(a) Uncoated sphere and 3-5(b) coated sphere both showing the raw measurement, theoretical data and subtracted difference.

The smooth glass spheres now appear flat and have an rms value of 0.158 compared to 3.108, while the coated glass sphere now has an rms value of 2.692 compared to 3.558. It is clear that this is one method for finding a relative roughness between two curved surfaces of similar mean height.

This method does well at removing the curvature, however, the requirement that the measurement to be taken at the highest point along the sample is time consuming, because one must find the highest point of the sample by performing the measurement several times. The best way of accomplishing this is to estimate where the high spot is on the sample and move it into position manually. Multiple passes are taken to find the highest spot on the sample. Often, multiple rounds of multiple passes are necessary to find the true high spot. Each round can take up to 20 minutes, which makes this method both time consuming and frustrating. Once the data is acquired the entire surface made from the pass can be subtracted from the surface of a theoretically smooth sphere and used for statistical analysis, but this is still inefficient.

A more practical method is to fit the data to a quadratic polynomial. The polynomial can be approximated from the equation of a circle $x^2 + y^2 = R^2$. Rearranging and applying a Taylor series expansion for small x $y = R - \frac{x^2}{2R}$. Therefore, a quadratic

fit to the surface data is a reasonable approximation of the actual sphere surface. The curvature can be removed by subtracting the polynomial from the measured data and the more realistic rms values determined. Figure 2.5.1 shows the polynomial fit and subtraction similar to figure 2-21 for a ceramic sphere. It can be seen from the figure that the rms values are similar to the curvature approach, however the approach is much more simple.

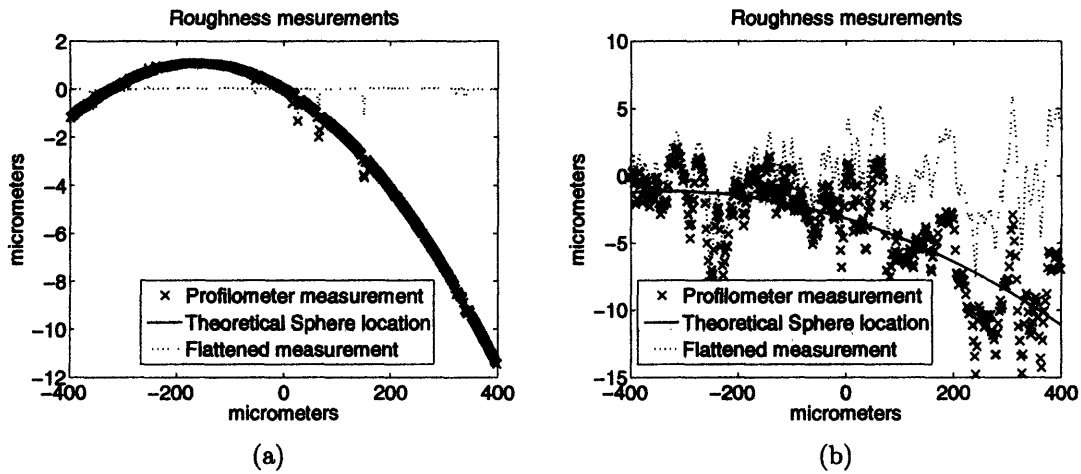


Figure 2-22: Roughness of two glass spheres of equal diameter (9.5 mm). The non-smooth glass sphere was coated with WX2100. 2-22(a) Uncoated sphere and 2-22(b) coated sphere both showing the raw measurement, theoretical data and subtracted difference.

Further data in table 2.3 shows that although the curvature of the spheres is different the general values for roughness remain the same for similar materials. This method was used to determine the roughness of all spheres used in this study and is summarized in table 2.3.

2.5.2 Wetting angle

The wetting angle of the spheres plays an important role in determining whether they will create a subsurface cavity or not. The work of Duez [2] has shown that for sufficiently high impact velocities there is a critical velocity based on wetting angle above which the spheres will create cavities. In general, for spheres with wetting

Table 2.3: Roughness of spheres used in this study. Spheres coated with WX2100 to make them hydrophobic and non-coated spheres are presented for each material.

Material	Diameter [mm]	Coating	Roughness rms	Adv. Contact Angle [deg]
Phenolic	57	Coated	1.69	122
Phenolic	57	Uncoated	0.09	79
Phenolic	35	Uncoated	0.37	79
Acrylic	25	Coated	2.73	100
Acrylic	25	Uncoated	0.29	69
Ceramic	25	Coated	2.42	118
Ceramic	25	Uncoated	0.11	57
Steel	25	Coated	2.40	122
Steel	25	Uncoated	0.01	70
Delrin	38	Coated	1.59	83
Delrin	38	Uncoated	1.99	122

angles above 90° cavities form with decreasing velocity, eventually reaching a critical regime, where spheres with wetting angles above $\sim 160^\circ$ form cavities at all velocities. Whereas, spheres with wetting angles below 90° form cavities above a critical velocity near 7 m/s.

The cavity formation is dependent on wetting angle as it relates to air entrainment. When a sphere has a large wetting angle, air is entrained behind the sphere as it falls through the free surface such that the cavity near the sphere moves outward. The cavity grows outward until some distance underwater when the surrounding hydrostatic pressure causes collapse. Thus, the wetting angle has an important role in cavity formation and should be considered when performing experiments of this type and should be measured accordingly.

The wetting angle of many materials is well known. Typically an engineer can look up this information in a table or chart. The wetting angle may be measured in many ways and typically on flat objects. Spheres are obviously curved, and the materials we used can have variable wetting angles depending on the manufacturer. Therefore, it was important to measure the wetting angle under the laboratory conditions. To do so the sessile drop method was employed. This method is accomplished on a

spherical surface by the following. The sphere is placed between the camera and a diffuser with a bank of florescent bulbs behind. A 105 mm micro Nikkor lens is used to get an approximately 4 cm² viewing window. A 0.5 μ L pipette was used to add a small droplet, a photo was taken, and then another drop added and so on until four droplets had been added to the sphere. The pipette flow direction was then reversed to remove approximately one droplet at a time until the water is gone. This allowed for the measurement of an advancing contact angle and a receding contact angle. Figure 2-23 shows a diagram of the receding and advancing contact angles.

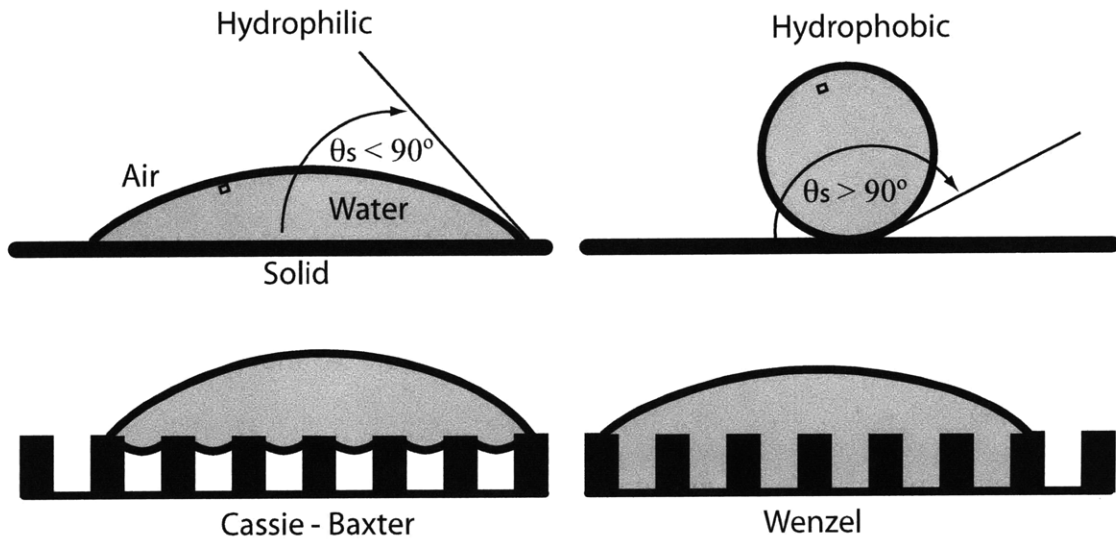


Figure 2-23: Diagram of a droplet on a hydrophilic and hydrophobic surface [1]. Below the effect of the surface shape and chemistry on the droplet can create either a Cassie-Baxter state in which the liquid remains suspended between the valleys in the solid. In the Wenzel state the water penetrates into the valleys. In the case of the spheres when a droplet is added the advancing contact line appears much like the hydrophobic case, whereas when a droplet is removed it appears to spread and looks more like the hydrophilic state.

The images are then processed to determine the contact angle of the droplet with the sphere. The program finds the sphere and the droplet using an edge detection algorithm (Canny method). A circle is fit to the sphere and the droplet. The droplet is slightly deformed so the approximated circle is a best fit. The two circles intersect at two locations where their intercepts are then used to calculate the wetting angle.

Another circle is fitted to only 200 points near each of the intercepts. These two circles approximate the curvature of the droplet more closely depending on the orientation of the droplet. Figure 2-24 shows a droplet on a sphere and illustrates how each side of the droplet appears to have a slightly different wetting angle. Some of this difference is due to surface energy and some is due to the non-horizontal curved surface. This method gives a rough estimate with an accuracy of approximately $\pm 10^\circ$.

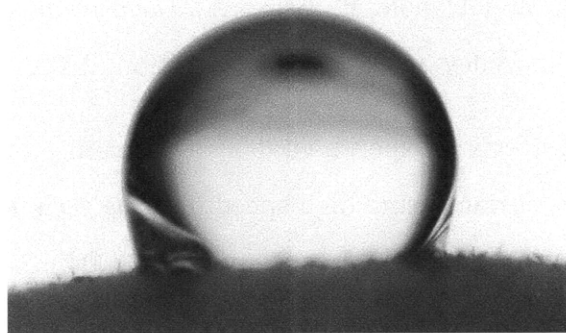


Figure 2-24: A raw image of a droplet on the surface of a hollow polypropylene sphere 0.0254 cm in diameter. Notice how each side of the droplet has a slightly different wetting angle.

The advancing contact angle is the most commonly used measurement for the falling spheres. In chapter 4 these angles will be altered by rotating the spheres. Where applicable the wetting angle is reported and was calculated using this method.

Bibliography

- [1] P. G. de Gennes, F. Brochard-Wyart, and D. Quere. *Capillarity and Wetting Phenomena*. Springer, 2004.
- [2] Cyril Duetz, Christophe Ybert, Christophe Clanet, and Lyderic Bocquet. Making a splash with water repellency. *Nat Phys*, 3:180–183, 2007.
- [3] Richard S. Figliola and Donald E. Beasley. *Theory and design for mechanical measurements*. John Wiley and Sons Inc., 3 edition, 2000.
- [4] Stephen Michael Laverty. Experimental hydrodynamics of spherical projectiles impacting on a free surface using high speed imaging techniques. Master's thesis, Massachusetts Institute of Technology, September 2004.

Chapter 3

Unsteady forces on spheres during water entry

Abstract

We present a study of the dynamics of water entry for spheres of varying masses, diameters, and surface treatments. As in past results we show that the formation of a cavity in the wake of a falling sphere is conditional upon impact speed and surface treatment. We go on to show that the mass of the sphere affects both the deep seal location, shape of the cavity, acceleration, and trajectory of the spheres. We also present a scaling law for determining the location of the sphere at deep seal based on impact speed, diameter, and mass ratio, given that a cavity is formed. This investigation also notes that for small mass ratios oscillatory motion is observed in the sphere's descent.

3.1 Introduction

The impact of a solid sphere with the free surface can create an air cavity or no air cavity depending on the initial conditions and surface treatment. The forces the sphere experiences, particularly at shallow depths, depends upon whether or not this cavity is formed. The measurement of these forces has been experimentally difficult until now and the subtleties of these differences difficult to pinpoint. Through the use of high speed-video, sub-pixel accuracy, novel smoothing techniques, and manipulation of the mass ratio of the spheres we elucidate the forces these two types

of impact produce.

The impacting the free surface has enamored the scientific community with its symmetry, beauty, and complexity for centuries. The first images of this phenomenon were recorded by [25], while more recent studies include the parameters required for cavity formation [6] and a full characterization of the cavity dynamics ([1] and [5]). This problem also provides a broader set of smaller problems on a smaller scale. The small scale effects can be witnessed and characterized through observation and analytical modeling such as the initially small but fast jet that is ejected at the moment of impact with the free surface [22], the cavity ripples associated with the portion of the cavity that descends with the sphere after deep seal [12] and the altered cavity shape and lift forces due to the addition of spin [23]. The hydrodynamic observations and measurements obtained from all of these studies can be applied to various industries from naval hydrodynamics such as the water entry of mines to the underwater launching of torpedos. Early studies focused on the impact of float planes on the water surface [14], torpedo water entry [18], and general impact [24] recently reviewed by Korobkin [15]. Industrial applications include structural interactions with the free surface such as ship slamming, extreme waves and weather on oil platforms, sprayed adhesives, and ink jet printing. Even the sporting industry is interested in the water entry of athletes, reducing drag of swimmers near the free surface and the entry and exit of oars in rowing.

Typically, the studies that focus on the dynamics of entry have chosen to keep all parameters constant while varying the impact speed [18], atmospheric pressure [10], impact angle [2], or surface treatment [6]. Most studies have focused on the growth of the cavity and the pinch-off location [4], [11], [17] and [3] for both spheres and disks. We present an experimental setup that allows us to study the variability of these findings when multiple parameters are changed. In particular we show the change in behavior of the spheres when surface coating is altered along with mass ratio. This study goes on to show the differences in drag forces associated with these two different wake features, and discusses the effect these features have as a function of mass.

By way of introduction to these subtle differences six cases are presented in figures 3-1 and 3-2. Although all six sets of impacts have the same water entry speed the spheres in figure 3-1 create a large cavity in their wake while those of figure 3-2 do not. The spheres in both figures have three different mass ratios which obviously has an effect on the cavity size, trajectory, and descent rate. This paper will examine these differences and highlight areas where these changes cause significant alterations to the behavior of this phenomenon.

This study was accomplished with the use of a high speed digital method of gathering and analyzing data and emphasizes the need to resolve the position data to sub-pixel accuracy and apply smoothing splines before deriving velocities and accelerations. The results give a truer estimation of the forces resulting in a coefficient of drag that varies in time. These varying forces come from different sources. In the cavity forming case the unsteadiness is based upon the expanding and contracting cavity, which alters the pressure field around the sphere and alters the forces acting on it over time. The non cavity forming case is forced unsteadily by the vortices it naturally sheds in its wake. Through the use of high speed Particle Image Velocimetry and a theoretical force model the source and magnitude of this forcing is elucidated. This work represents the only drag data available for distances greater than $1/2$ a diameter below the free surface. The methods used herein could be applied to past and future studies to gather force data for comparison.

3.2 Experimental study

This experiment consists of dropping different types of spheres from varying heights into a large tank of water. The size, mass, and surface makeup of each sphere was recorded before being dropped and each impact with the water surface was recorded by a high-speed video camera. Details of the apparatus, spheres, image processing, and method of finding velocity and deceleration are presented in this section.



Figure 3-1: Three different spheres of the same diameter ($D = 0.0254$ m) dropped from the same height ($h = 60$ cm), coated with the same surface treatment (advancing contact angle $\theta = 120^\circ$) but all have different mass ratios $m^* = \rho_s/\rho$ as indicated. The time between images is 7.1 ms and the impact speed is $V_i = 3.43$ ms⁻¹ yielding the same Froude number $F = V_i/\sqrt{gD} = 6.87$ for all cases.

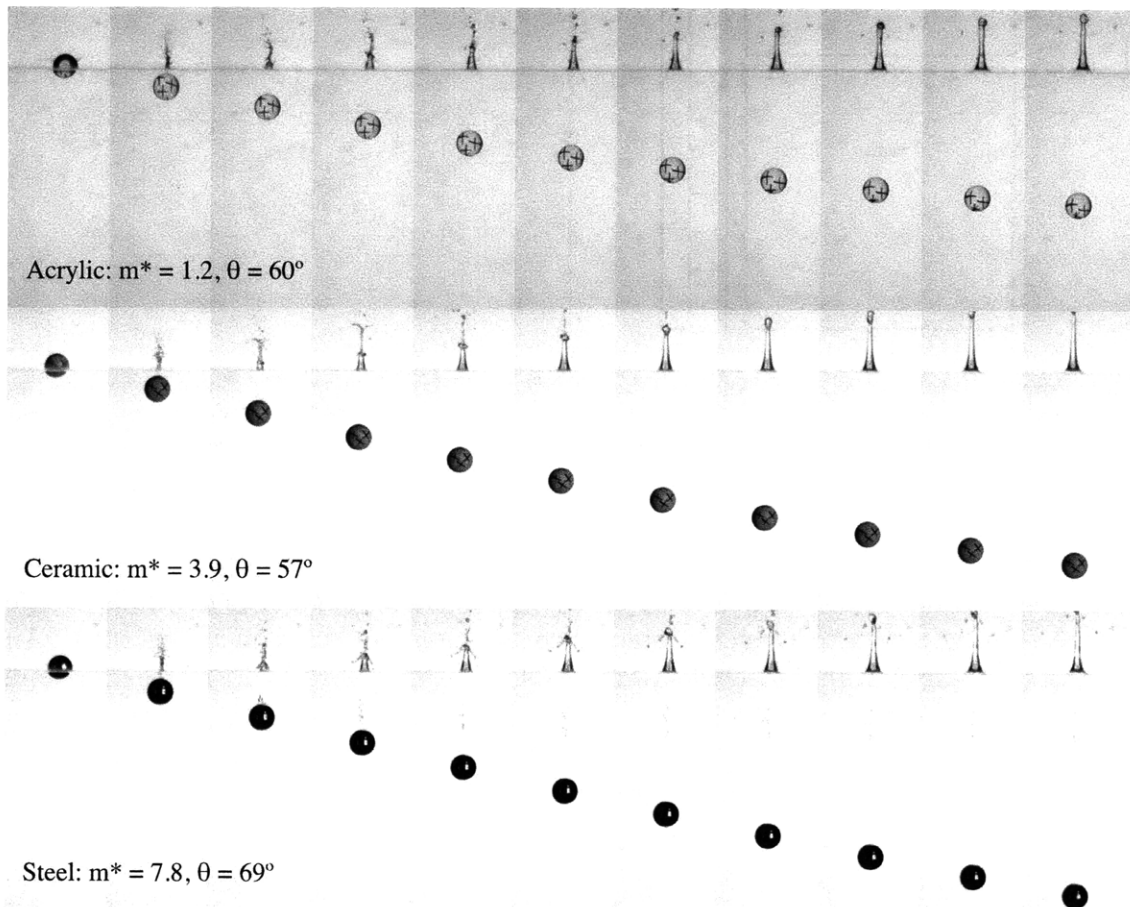


Figure 3-2: Three different spheres of the same diameter ($D = 0.0254$ m) dropped from the same height ($h = 60$ cm), cleaned in the same manner (advancing contact angle θ above) but all have different mass ratios $m^* = \rho_s/\rho$ as indicated. The time between images is 7.1 ms and the impact speed is $V_i = 3.43$ ms $^{-1}$ yielding the same Froude number for all cases $F = V_i/\sqrt{gD} = 6.87$.

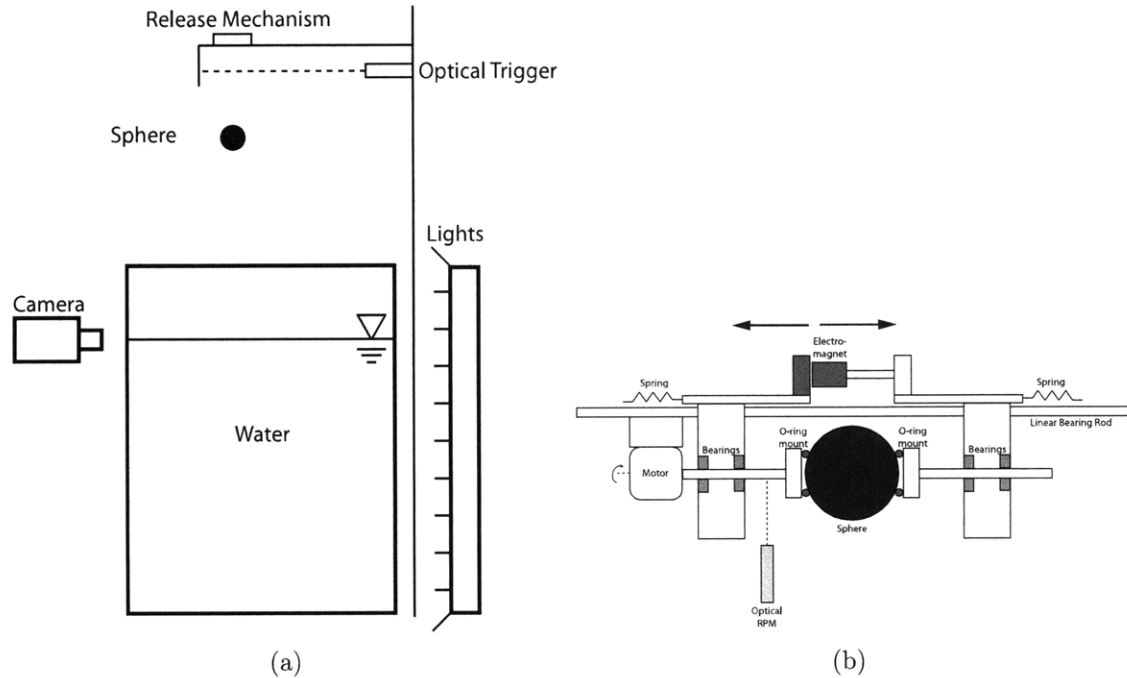


Figure 3-3: a) Impact tank is made with a steel frame and 1 in acrylic. The tank is $91\text{ cm} \times 152\text{ cm} \times 152\text{ cm}$ and holds 2200 liters of water. b) Secondary device used to drop the spheres. The sphere is held above the water surface by two brackets that are attached to a set of o-rings. The brackets are attached to a set of bearings allowing the sphere to rotate out of the plane of the illustration. A motor is attached to one of the bearing shafts to induce a prescribed rotation (not used in this study). An optical rpm sensor is mounted separately to detect the spin rate of the sphere before release. An electromagnet holds the two halves of the device apart until the dropping time at which point the electromagnet is turned off and the springs draw the device apart allowing the sphere to fall freely into the tank of water.

3.2.1 Apparatus

The experimental apparatus consists of two different tanks of water and two different methods of dropping the spheres. The largest tank is $91.4 \times 152.4 \times 152.4\text{ cm}^3$ and holds approximately 2200 liters of water and is made of acrylic (1.27 cm thick) set into an external steel frame. The frame is welded from 5.08 cm square extruded steel hollow posts with 6 supporting feet. The combined weight when full is approximately 2575 kg. Figure 3-3 shows the largest tank and the supporting equipment. The smaller tank is a typical glass aquarium $30 \times 50 \times 60\text{ cm}^3$ and was used in conjunction with the smaller sphere diameters.

Two different methods for dropping the spheres into water were used. The method

for dropping spheres into the smaller tank of water was to place the spheres a distance z above the free surface in a small manual aperture, similar to an aperture in a camera. The aperture was then opened and the sphere allowed to fall into the water. The method for dropping the spheres into the larger tank was to place them between two small circular plates fitted with o-rings mounted to a device held closed by an electromagnet (see figure 3-3). The electro-magnet was then released and a spring forced the circular plates away from the sphere letting it fall freely towards the water surface. This more complicated device was developed to allow the spheres to spin before being dropped, but they were not allowed to spin for this study. The majority of the data presented here used the larger tank setup.

A high speed camera (IDT XS-3 CCD) was used to record each of the falling spheres at 840 frames/s (fps). The image resolution was 756×1260 pixels and the field of view was 28.66×47.77 cm yielding a 26.4 px/cm magnification. Image data was stored as tiff images and post processed using image processing techniques developed on the Matlab software platform.

3.2.2 Spheres

These experiments involve the use of many different spheres to determine the effects of density, diameter, and surface treatment on entry behavior. The effect of any of these three parameters was under investigation, therefore, multiple diameters of varying density were used. Each unique diameter and density was either cleaned to enhance the natural contact angle of the spheres, or coated with a hydrophobic coating to induce a similar hydrophobic effect between all sphere types. The roughness and wetting angle of each type of sphere and coating was then measured.

Table 3.1 shows all of the spheres tested in this study and their relevant parameters. The various densities were achieved by altering the material properties of the spheres. The surface treatment was accomplished by cleaning or coating the spheres. Cleaning was performed under a chemical hood with the operator wearing protective eye and hand equipment. The cleaning was done by hand and the spheres were 1) sprayed with Acetone and then wiped with KIM wipes, 2) rinsed with alcohol and

Table 3.1: Spheres used in this study. Advancing contact angles are given with error in the measurement of $\pm 10^\circ$. Roughness measurements are also given in μm with the error in the actual measurement of $\pm 0.01\mu\text{m}$.

Material	Density [kg m^{-3}]	Diameters [mm]	Advancing Contact Angle / Roughness rms
Nylon	1.1	4.76, 9.53, 15.9, 25.4	81/2.14, 122/1.28
Acrylic	1.2	25.4	69/0.29, 100/2.73
Phenolic	1.9	25.4	79/0.8, 122/1.95
Glass	2.4	4.76, 9.53	50/0.03, 122/2.53
Ceramic	3.9	25.4	57/0.11, 118/2.42
Steel	7.8	1.59, 4.76, 9.53, 15.9, 25.4	70/0.01, 122/2.40

allowed to partially dry and 3) rinsed with Ethanol and allowed to thoroughly dry in the hood. The spheres were then placed in a container that had been cleaned in a similar manner and covered with clean sheet of aluminum foil. If the spheres were left unused for more than 20 minutes they were cleaned again.

The spheres that are treated with a hydrophobic coating are coated in a slightly different manner. First they are cleaned as prescribed above, then they are set on a small railing where they are in contact with the rail at two points. The spray coating (WX2100) is then applied gently by spraying away from the sphere and drawing the nozzle past the sphere for just a brief moment. This process is repeated on the opposite side. In order to insure even coating the sphere is allowed to dry for 2 hours and then it is rotated and sprayed again. It is allowed to dry again for two hours and is coated one last time after rotation. This seems to provide a thin even coating without extra equipment requirements.

The coating produces both a new wetting angle and an associated roughness. Wetting angles were measured using the static sessile drop method. Spheres were placed on table and a drop of water placed on the top surface. Photographs were taken using a Canon 20D SLR camera with backlighting provided behind the sphere through a diffuser. A droplet was placed on the sphere with a pipette then a photograph was taken. Another droplet was then added to the first and another photograph taken. This was done until three droplets were added to the top of the sphere and photographs taken. Then each of the droplets was removed using a Pasteur Pipette.

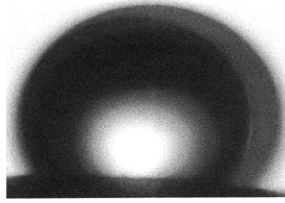


Figure 3-4: Four images overlaid to show the addition of each droplet on the surface of a hydrophobic sphere. The advancing contact line can be deduced by measuring the angle between the sphere and each droplet.

This yielded both an advancing contact angle and a receding contact angle. Only the advancing contact angles are reported in table 3.1. Images of this process can be seen in figure 3-4.

The coating alters the surface roughness of the spheres. Roughness measurements were measured by using a Tencor P-10 Surface Profilometer. The profilometer data determined surface profile of the spheres. The surface profile includes both the surface roughness and in this case it also includes the curvature. The curvature is removed from the data by subtracting a curve proportional to the radius of the sphere from the data. The result is a true roughness measurement (see figure 3-5). The rms of the roughness is then taken and reported in table 3.1. This same technique was used to determine the roughness of both the coated and uncoated spheres. Spheres smaller than 9.53 mm were not measured but instead assumed to be of the same roughness as the larger diameter spheres in the material family.

3.2.3 Image processing

It is imperative to determine the trajectory of the spheres as accurately as possible. If this is not done properly or accurately then the determination of velocity, acceleration, and forces will be misleading due to the error propagation. Due to the nature of these experiments the images are the only source of data, which makes validation important and increases the need for image processing to be done accurately. Therefore, it is imperative that the trajectory be determined in a manner that minimizes error and pixel locking.

One method of finding the trajectory involves using a template of the image to be

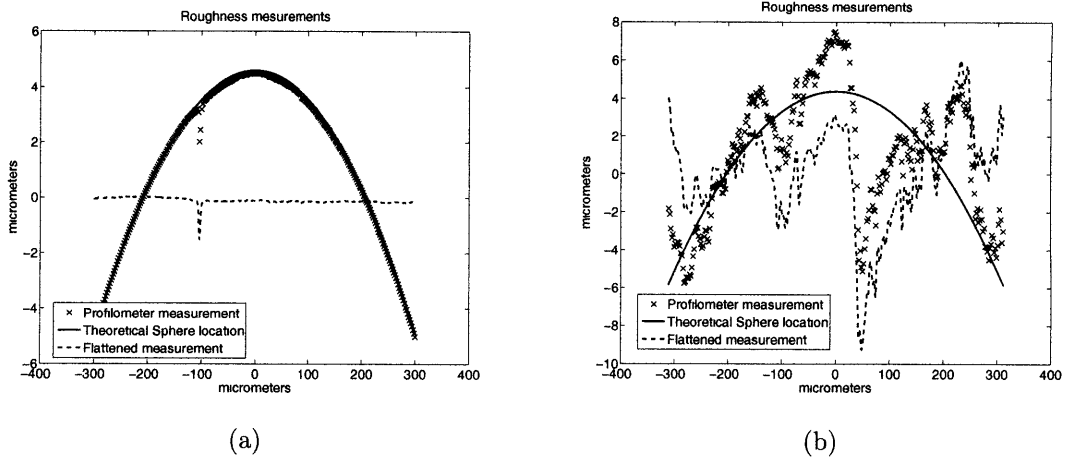


Figure 3-5: Roughness measurement of two glass spheres of equal (diameter = 9.5 mm). 3-5(a) uncoated sphere and 3-5(b) coated sphere both showing the raw measurement, theoretical curvature and subtracted difference. The roughened glass sphere was coated with WX2100.

traced and then performing a cross-correlation between the template and the image of interest. If this step is done properly the position of the object can be determined to within ± 1 pixel. Here a cross correlation is used between a template (provided by the user from the most applicable image in the series) and the rest of the images in the series. The cross correlation returns a matrix of values (-1 to 1) indicating the most likely position of the sphere in the consecutive image (see figure 3-6). This process can be continued until the position of the sphere in all frames is determined.

One of the problems with this process is that the images are limited by ± 1 pixel accuracy. This can often lead to pixel locking, where the center of the sphere is actually between two pixels but is interpreted as a particular pixel. This can greatly affect the velocity and acceleration when the derivative is involved. To overcome this issue the data near the point of interest is fit to a Gaussian curve (assuming the cross-correlation peak isn't too steep). This method is similar to the method used in [20] and can give sub-pixel accuracy and greatly improve the acceleration and velocity curves.

This process is accomplished by picking a number of points around the peak from the cross correlation and fitting a Gaussian curve to each row and column of values.

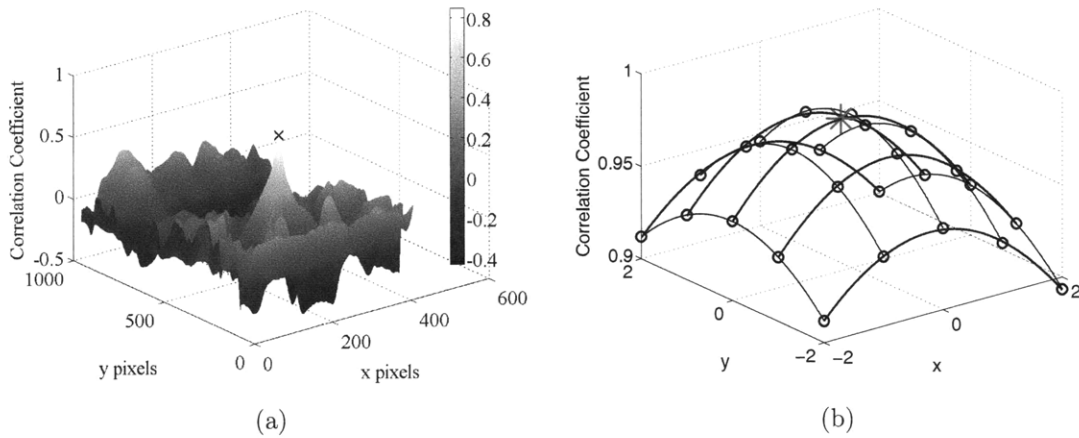


Figure 3-6: a) Cross correlation of template with an image in the series produces a matrix of values from -1 to 1 in which the highest value represents the probable center of the sphere. b) Gaussian curve fitted in both x and y directions around peak value. This plot shows the curve fitting to each row and column as well as the sub-pixel position of the sphere (*).

Figure 3-6(b) shows the highest position data obtained by the cross correlation with two points in both directions. The Gaussian fit is applied in both directions and the highest point on the surface is the new center location. One can see from figure 3-6(a) that as one moves away from the peak the values would no longer fit to a Gaussian curve, thus an optimal amount of points around the peak must be used to apply this fitting parameter. Similar to the method of determining the best correlation in Particle Image Velocimetry (PIV), the best fit occurs when the fit is applied from 1 to 2 points on either side of the peak. In this study 2 points on either side of the peak value were used to apply the fitting parameter. This method improved the accuracy by two orders of magnitude to ± 0.025 pixels (0.00005 cm).

The increased accuracy of the acceleration data reveals an unsteady forcing on the sphere as a function of time. Two different techniques were employed in order to determine the unsteady forces. The first technique is used for the spheres that form cavities. This technique traces the cavity as a function of time. This is done using a Canny edge finding image processing technique, which detects the highly contrasted edges of the cavity as viewed in figure 3-1.

The second technique uses a high speed implementation of Particle Image Ve-

locimetry (PIV) [19] to gather information about the cavity and non-cavity forming flow fields. The setup is similar to that of the previous section (see figure 3-3) but instead of using the fluorescent back lighting a laser plane illuminated a plane along the axis of the falling sphere perpendicular to the camera. The tank was seeded with 50 μm polyamide neutrally buoyant particles, which were illuminated by the 2.2 W Laser (LaVision) at 532 nm, which was fitted with an optical lens that produced a 20° fan of light. The IDT XS-3 camera was again used but this time the resolution was 404×1280 with a field of view of 8.14×25.80 cm yielding a 49.61 px/cm magnification. PIV data was collected and processed using the LaVision DaVis 7.2 software package. A multi-pass, cross-correlation processing algorithm, with a final interrogation window size of 16×16 pixels and 50% overlap was used for processing all of the images. The output was a velocity field with an output of 160×50 vectors. The data was further processed in Matlab to determine the moment when vortices are shed into the wake of the sphere by evaluating the instantaneous impulse at each time step in a manner similar to [7]. Circulation was computed using the Stokes theorem at each time step

$$\Gamma = \sum_{ij} \omega_{ij} \delta A \quad (3.1)$$

where the ω_{ij} is the curl of the velocity field at a point (i,j) and $\delta A = (8 \text{ px})^2 = 0.163 \text{ cm}^2$ is the box size. The circulation depends upon the velocity in the flow field and the area of the circulation. Determination of the area that the circulation affects can be difficult. Gharib [9] resolved this problem by defining a line of isovorticity of a fixed amount to prescribe the area of vorticity to consider. Here we use the same technique and apply an isovorticity line equivalent to 25% of the the maximum circulation for each vortex. Figure 3-7 shows an example of the circulation calculated at frame 231 or $t = 86.3$ ms after impact as viewed in the 15th image in the sequence of figure 3-15. This value yielded the most effective results for all times given our field of view and PIV spatial resolution. Further discussion can be found in § 3.3.3.

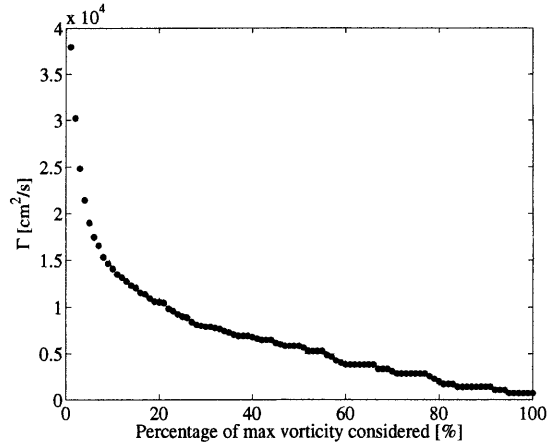


Figure 3-7: Circulation as a function of the percentage of maximum vorticity. The percentage of maximum vorticity defines the area used by the circulation (see equation (3.1)). Circulation is calculated at $t = 86.3$ ms after the center of the sphere passed through the free surface as shown in figure 3-15 (15th image). The hydrophilic acrylic sphere in this case was 0.0254 cm in diameter dropped from 60 cm.

3.2.4 Post processing

The position and cavity data was normalized with the free surface making the free surface the origin of both time and space, where the center of the sphere is the origin of the sphere fixed coordinate system. Thus, when the sphere is centered about the free surface it is said to be at $(x_0, y_0, t_0) = (0, 0, 0)$. A line representing the free surface is used to normalize both the time and spatial data. The easiest method for calibrating the data to a level horizon is to determine the angle of inclination using two points representing the free surface ($\theta = \tan^{-1}(x_{fs2} - x_{fs1}) / (y_{fs1} - y_{fs2})$) and applying a rotational matrix based on this angle to the entire data set given by

$$[x, y] = \begin{pmatrix} \cos \theta & -\sin \theta \\ \sin \theta & \cos \theta \end{pmatrix}. \quad (3.2)$$

The x and y position corresponding to the impact location is then formulated using the new free surface location in y and the nearest frame to impact in x. By subtracting these values to all position data the spatial origin (x_0, y_0, t_0) is now determined.

The actual time of impact is likely not recorded due to the discrete frame rate of the cameras. Although high speed, the impact event is a finite time and typically

happens between frames. To estimate the actual time of impact the frame above (x_a, y_a, t_a) and the frame below (x_b, y_b, t_b) , the origin is used to estimate the true impact time as follows,

$$t'_i = t_i + y_a \frac{\Delta t}{\Delta y} \quad (3.3)$$

where $\Delta t = t_b - t_a$ and $\Delta y = y_b - y_a$. The position data is essentially the only data obtained from experiments like this one. The position data determines all other values including velocity, acceleration and forces. Several methods exist for determining the velocity and acceleration. The first and easiest method is a finite difference. However, this method increases error with each difference and can lead to erroneous results when the accelerations are determined.

Another method is to fit a polynomial of order n to the data, then the velocity and acceleration can be determined simply by taking the first and second derivative of the polynomial. Using a polynomial can lead to accurate results if the trajectories are smooth, continuous, and predictable. However, the sphere is influenced by the unsteady and nearly instantaneous forcing from impact with the free surface and near the point of pinch-off, thus the ability of the curves to accurately determine the deceleration diminishes when the relative magnitude of these forces is on the order of the force of the sphere.

The accuracy of the polynomial approximation can be improved by windowing the data or analyzing only a localized set of data. At a given point $y(t)$ fit a line $(a_1 t + a_2)$ from t_{i-w} to t_{i+w} for all points along $y(t)$. Using this method, each of the lines along $y(t)$ represents a portion of the position vs. time data. The first derivative of the estimate in time is the velocity, the second derivative is acceleration, etc., where the derivatives are applied at the center of each localized set. This method yields much more accurate data in the first and second derivatives. However, it results in the data not being smooth and data near the ends being lost.

One way of mitigating these problems is to employ a smoothing spline. A smoothing spline is a continuous and smooth piecewise polynomial of order n that has $n-1$ continuous derivatives at each piecewise dislocation. If the piecewise polynomial is

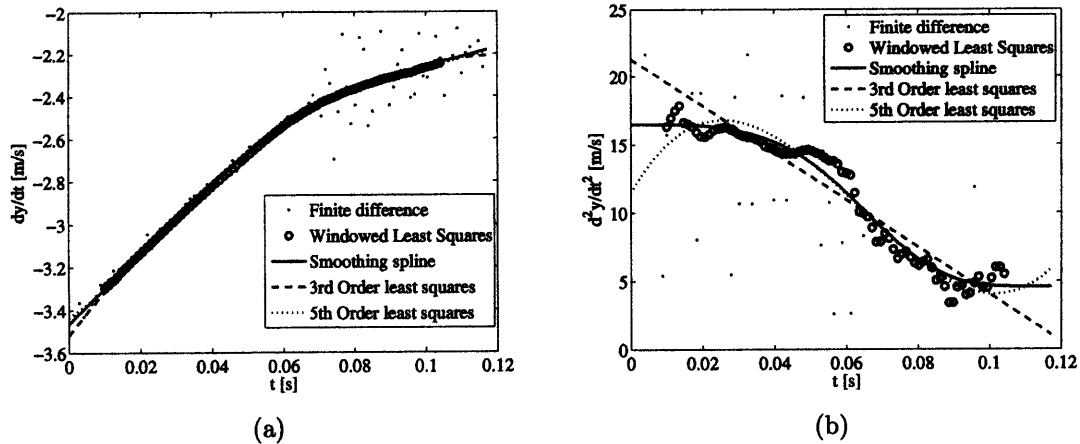


Figure 3-8: Velocity and acceleration for $m^* = 3.9$ and $\theta = 120^\circ$ as seen in figure 3-1b, computed by finite difference, windowed least squares, smoothing spline, 3rd order least squares, and 5th order least squares. The order of the least squares estimates is the order of the polynomial fitted to the position-time data.

of the order of the number of points in the data set then the spline represents every point in the data set exactly. Here we use a 5th order spline ($n = 5$) to maintain a continuous second derivative, and apply a novel method for finding the best spline proposed by [8].

This method yields excellent results. Figure 3-8 shows a comparison of the finite difference, windowed least squares, smoothing spline, 3rd order least squares, and 5th order least squares methods. The position data (not shown) for all five methods shows excellent agreement. The velocity data shows good agreement for all but the finite difference method. Furthermore, the acceleration (second derivative) shows large discrepancies between all of the methods. The best fit that maintains a derivative that is smooth, continuous, has an exact solution and has reasonable end points is the smoothing spline.

3.3 Results

The impact of a sphere that creates a subsurface air cavity is characterized by a few distinct features. Figure 3-1 shows a time series for three different sphere densities. In each case the moments near impact are characterized by an outward radial jet of

fluid and the formation of a thin sheet of fluid ejected away from the sphere. These images begin after the moment of impact in which a cavity has already formed in the wake of the sphere, and the cavities appear to be attached near the equatorial region. As the sphere descends the cavity is created by the force the sphere exerts on the fluid in the radial direction. This force causes the fluid to move outward radially with some inertia until the momentum of the growing cavity is completely dissipated in the fluid. By the time the fluid has lost its radial momentum the sphere has descended some distance downward in the z direction. This outward momentum has created a cavity which now is opposed by the hydrostatic force of the water at the given depth. The hydrostatic force then acts in opposition to the direction the cavity formed and moves the cavity inward, beginning the collapse event.

The collapsing event increases in velocity up until the moment of collapse where two cavities are formed. This moment of collapse is called deep seal or pinch-off. The top cavity is connected to the free surface and as it collapses a large jet is formed at the point of pinch-off. The jet grows as the cavity collapses further and ascends above the free surface well above the initial drop height of the sphere. The bottom cavity remains attached to the sphere for a period of time. This cavity also has a jet of smaller magnitude that forms at the point of pinch-off but descends towards the sphere eventually impacting the sphere. For larger mass ratios the cavity remains attached for longer times and exhibits cavity rippling [12] before the cavity is released from the sphere and water fills in behind it. For smaller densities the cavity remains attached for very short times and does not appear to exhibit the same cavity rippling phenomenon.

The most obvious difference between the three mass ratios in figure 3-1 is the trajectories. The heaviest sphere (steel) has descended the most of the three cases at the moment of pinch-off, while the lightest sphere (acrylic) has descended the least. This is mainly due to the differences in inertia. Because the lighter sphere has a smaller mass it has a reduced inertial mass even though it has fallen from the same height as the heavier spheres. The force of drag due to cavity formation and hydrostatic forces can be assumed to be on the same order of magnitude for all three

cases. Thus a reduced mass will result in a greater percentage of the inertia being dissipated by the hydrostatic forces, resulting in a shallower trajectory.

Another major difference is the depth of deep seal. The depth at which this phenomenon occurs changes dramatically as a function of mass ratio. As the mass ratio increases so does the depth at which deep seal occurs. However, the non-dimensional time to deep seal ($\tau = t_{ds}(g/r)^{0.5}$) remains constant despite increasing mass or changing diameter, where r is the radius and g is the gravitational constant. Many authors have noted this agreement, here, deep seal occurred at $\tau = 1.78 \pm 0.0752$, which is slightly larger than that reported by Gilbarg [10] ($\tau = 1.74$) and Truscott [23] ($\tau = 1.726 \pm 0.0688$).

In the non cavity forming case of figure3-2 the entry is visually much less dramatic. The fluid is unimpeded to travel up and around the sides of the sphere and does not entrain air behind it, thus no cavity is formed. This phenomenon was first witnessed by Worthington [25] when clean glass spheres were dropped in water and theoretically explained for smooth spheres by Duez [6]. As the sphere passes through the free surface the water it has displaced comes back together at the top of the sphere, creating a large jet that ascends above the free surface as seen in figure 3-2. The jet is characterized by a somewhat messy top portion that has more velocity to ascend above the free surface to higher heights, while a more organized and slower growing bottom layer produces a radially symmetric column of fluid that begins to neck and form a droplet near at the top of the jet. The sphere continues its descent and in the case of the acrylic sphere comes to a nearly complete stop near the last frame. The ceramic and steel cases continue to fall through the fluid but the steel sphere has a greater descent rate compared to the ceramic case.

The trajectory of each sphere is presented in Figure 3-9 which shows the traces of the six impacts shown previously in figures 3-1 & 3-2. The most dramatic difference in the figure is the erratic behavior of the hydrophilic acrylic sphere ($m^* = 1.2$, $\theta = 69^\circ$), which nearly comes to a complete stop in the y-direction as it descends. The kink in the trajectory indicates the position where the sphere changed direction. This sudden change is due to vortex shedding around the sphere as discussed in the rising

and falling of spheres with mass ratios from 0.08 to 1.41 in [13]. Further evidence is presented in the preliminary PIV results of § 3.3.3. All of the hydrophilic spheres have some deviation from vertical descent. The acrylic and ceramic spheres have the greatest deviation, however, the steel spheres ($m^*=7.8$) also display this behavior, which is consistent with the results of [13]. Horowitz concluded that spheres falling with a mass ratio of 1.41 or rising with a mass ratio of 0.41 would follow an oblique rectilinear path, meaning that they would tend to fall vertically with some nearly constant horizontal displacement in x , which is consistent with the data presented in figure 3-9. However, spheres with mass ratios of 0.11 or less would always vibrate in a single vertical plane. Here we find oblique rectilinear agreement with spheres of ratios higher than 1.4, but spheres with mass ratios below 1.2 also seem to vibrate as they descend, at least for the 12 diameters below water entry presented in figure 3-9.

The hydrophobic cases do not deviate from the horizontal as strongly. The cavities that they produce act to prevent vortex shedding in the wake until the moment of deep seal, where vortex shedding can then occur. Deep seal is marked in figure 3-9 by a horizontal line. All cases have the same time to deep seal similar to the results of [11] and [23]. Although out of the field of view of these images, it appears that below the point of deep seal the spheres begin to exhibit similar behavior to the hydrophilic cases and take on trajectories that drift to one side.

3.3.1 Velocity and acceleration

The velocity of each sphere as a function of time was calculated in figure 3-10. Each of the six spheres presented is dropped from the same height and has an impact speed of $V_o = 3.4 \text{ ms}^{-1}$. The velocity shown in figure 3-10 is the velocity of the sphere beginning with the first frame after the sphere is submerged one radius. Thus, the data does not lie exactly on the $t=0$ axis. The acrylic sphere already experiences a deceleration compared to the larger mass ratios due to its smaller mass. The terminal velocity of each sphere can be calculated by a force balance around the sphere assuming that the acceleration of the sphere is zero. Lumping the hydrodynamic forces into a known

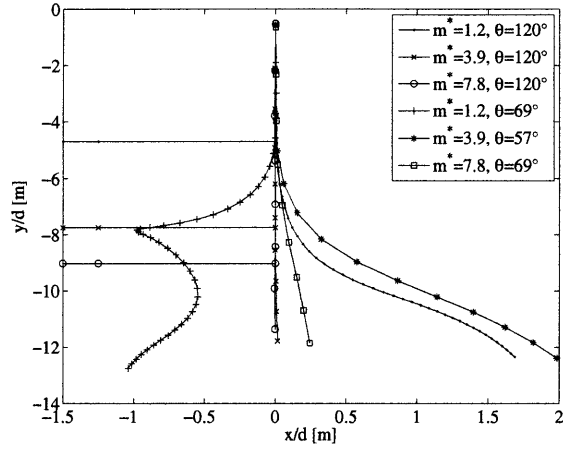


Figure 3-9: Trajectory of spheres for six different impact cases. The hydrophobic cases ($\theta = 120^\circ$) correspond to figure 3-1 while the hydrophilic cases relate to figure 3-2. All spheres were dropped from the same height and all had a diameter of $d = 0.0254$ cm. Every tenth data point is plotted.

drag coefficient ($C_D=0.5$) the terminal velocity becomes,

$$V_f = \sqrt{\frac{8}{3} \frac{gR}{C_D} (m^* - 1)}. \quad (3.4)$$

Figure 3-10 shows the terminal velocity for each of the different spheres. For both the hydrophilic and hydrophobic acrylic cases it appears that the spheres are approaching the terminal velocity, however they approach them at different rates. The hydrophilic spheres approach the terminal velocity faster than the hydrophobic cases indicating that there is some force reducing the velocity of the hydrophilic cases more quickly. One might think that the large cavity created by the hydrophobic cases would increase drag and slow these spheres more quickly than the non-cavity forming counterparts, however, it appears that the cavities formed by the hydrophobic spheres act to mitigate the pressure drag, thus the hydrophilic spheres decelerate more quickly. It will be shown in § 3.4 that this is indeed the case.

The accelerations of the spheres are plotted in figure 3-11 and positive values indicate deceleration. The difference in deceleration between the cavity forming and non-cavity forming spheres is dramatic. The hydrophobic cases show a smooth deceleration until a few moments after the deep seal phenomenon, after which the acrylic

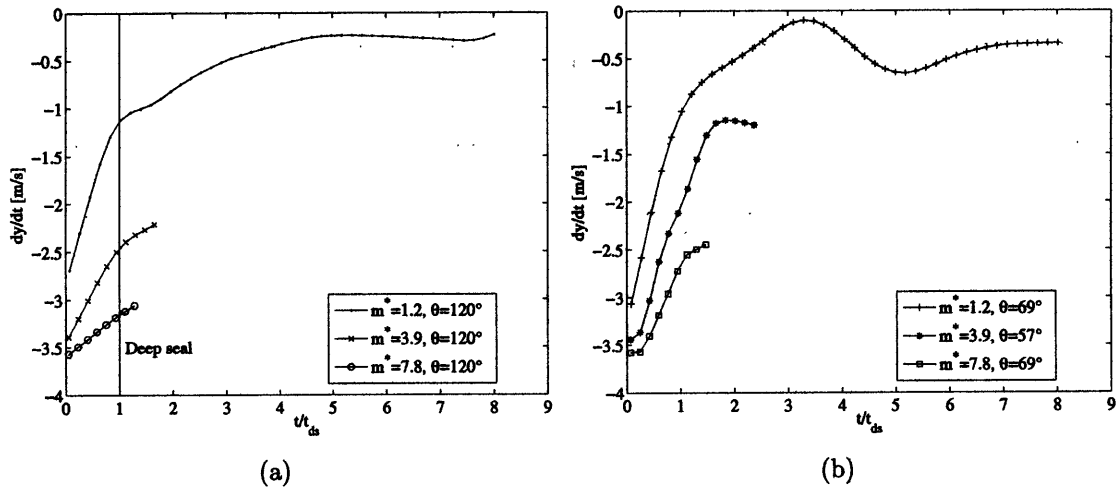


Figure 3-10: The velocity of the spheres presented in figures 3-1, 3-2 & 3-9. Velocities are plotted versus time and non-dimensionalized by the time to deep seal (t_{ds}) for each mass ratio whether hydrophilic or hydrophobic. Terminal velocity for each sphere is compared (\dots). The time of deep seal for the hydrophobic cases (a) is indicated at ($t/t_{ds} = 1$).

case displays a bit more erratic behavior. The steel and ceramic cases have very little data after this point (out of field of view). The deep seal phenomenon does not occur at the moment of least deceleration, indicating that these spheres are still decelerating after deep seal.

The hydrophilic cases appear to have much greater decelerations overall. They also appear to have some oscillatory forcing making their decelerations appear unsteady in time. This is likely due to vortex shedding in the wake and more evidence of this phenomenon will be shown in § 3.3.3. All of these figures indicate that the deceleration of these spheres is neither constant nor linear, and indicates that theories approximating these types of impact with second or third order models may miss some of the more subtle forcing experienced by the sphere as it descends through the water column.

The oscillatory motion of the hydrophilic acrylic sphere can also be seen in figure 3-10(b). The smaller mass of the acrylic spheres allows the vortices in the wake to affect the trajectory of the sphere in a more pronounced manner. Both the ceramic and acrylic spheres in the hydrophilic cases appear to slow to velocities smaller than their

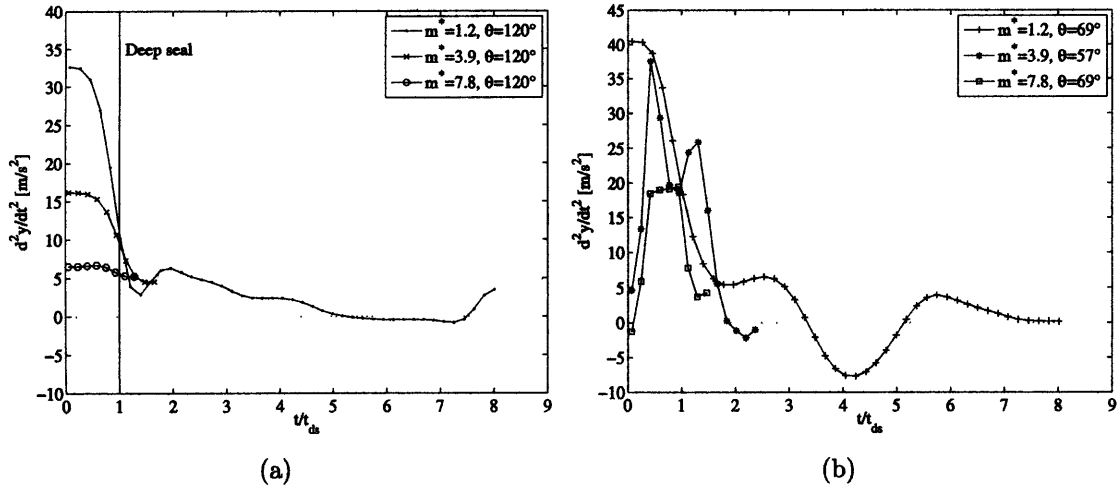


Figure 3-11: The Acceleration of the spheres presented in figures 3-1, 3-2 & 3-9. Accelerations are plotted versus time and non-dimensionalized by the time to deep seal (t_{ds}) for each mass ratio whether hydrophilic or hydrophobic. The time of deep seal for the hydrophobic cases (a) is indicated at ($t/t_{ds} = 1$).

theoretical limit. This is mainly due to the unsteady nature of the drag force. One can determine the unsteady frequency of this behavior by analyzing the frequency of shedding via the Strouhal number ($S_t = fD/V(t)$). For spheres in a uniform flow with Reynolds numbers between $800 < Re < 200,000$ the Strouhal number should be about 0.2. Here the instantaneous Reynolds number is $12,500 < Re < 87,500$. The frequency of shedding can be calculated as $f = 0.2V(t)/D$. The acrylic case has an average velocity around $V(t) \approx 0.5$. Thus, the shedding frequency should be about 4 Hz, which is approximately what the frequency of oscillation is for this case. For the ceramic sphere the shedding frequency should be approximately 12 Hz, which indicates a higher frequency of oscillation, however, the field of view for these cases is not large enough to gather evidence that this is indeed the case, as the sphere falls through the field of view too quickly to observe this frequency.

3.3.2 Coefficient of drag

The data can also be analyzed to determine the forces affecting the descent of the sphere.

The net force on the ball in the y direction, $\hat{\mathbf{k}}$ (positive upwards), is

$$m\ddot{y} = -mg + \int p(-\hat{\mathbf{n}} \cdot \hat{\mathbf{k}})dS + \int \hat{\mathbf{n}} \cdot \mathbf{T} \cdot \hat{\mathbf{k}}dS + 2\pi r\sigma \cos \varphi \quad (3.5)$$

where $\hat{\mathbf{n}}$ is the unit normal vector directed *out* of the ball and \mathbf{T} is the viscous stress tensor. The viscous force scales like $\rho U^2 \pi R^2 \text{Re}^{-\frac{1}{2}}$, which is quite small, since the Reynolds numbers of these experiments is on the order of 10^4 . The surface tension force is also quite small; comparing surface tension to gravity, we have $\frac{2\pi R\sigma \cos \varphi}{mg} \sim \frac{\rho_s \frac{\sigma}{\rho g R^2}}{\rho_s \frac{\sigma}{\rho g R^2}} \sim 10^{-3}$ for these experiments. Thus, the net hydrodynamic force on the ball is dominated by the pressure force on the ball.

The pressure forces are more formally decomposed in the coming sections, but let us make an estimate of the drag coefficient by normalizing the two forces that are well defined by the velocity squared as follows

$$C_D = \frac{2m(\dot{y} + g)}{\rho V(t)^2 \pi R^2}. \quad (3.6)$$

The coefficients of drag are computed for each sphere and presented in figure 3-12.

The data indicates that the drag forces are unsteady and complex. Looking first at the comparison between hydrophobic and hydrophilic acrylic cases (figure 3-12(a)) one notices that the coefficients of drag are similar up to about $0.5 t/t_{ds}$ (see inset). The hydrophobic case continues to rise and then suddenly falls before deep seal and continues to decrease for a short time afterwards. The hydrophilic case has a steady even exponential rise up to a non-dimensional time of about $3 t/t_{ds}$. This is the time at which the sphere virtually stops in the y direction and changes its course in the x direction as noted in figure 3-9. After this event the drag coefficient diminishes as quickly as it rose and reaches a minimum near $4.5 t/t_{ds}$.

The ceramic cases also exhibit increased drag in the case of the hydrophilic spheres. Some argument can be made that hydrophilic spheres have longer slip lengths and thus a higher frictional drag coefficient, but the scaling argument reminds one that this term is much smaller than the overall effect witnessed here. The hydrophobic sphere has a maximum drag coefficient some time before deep seal, similar to the

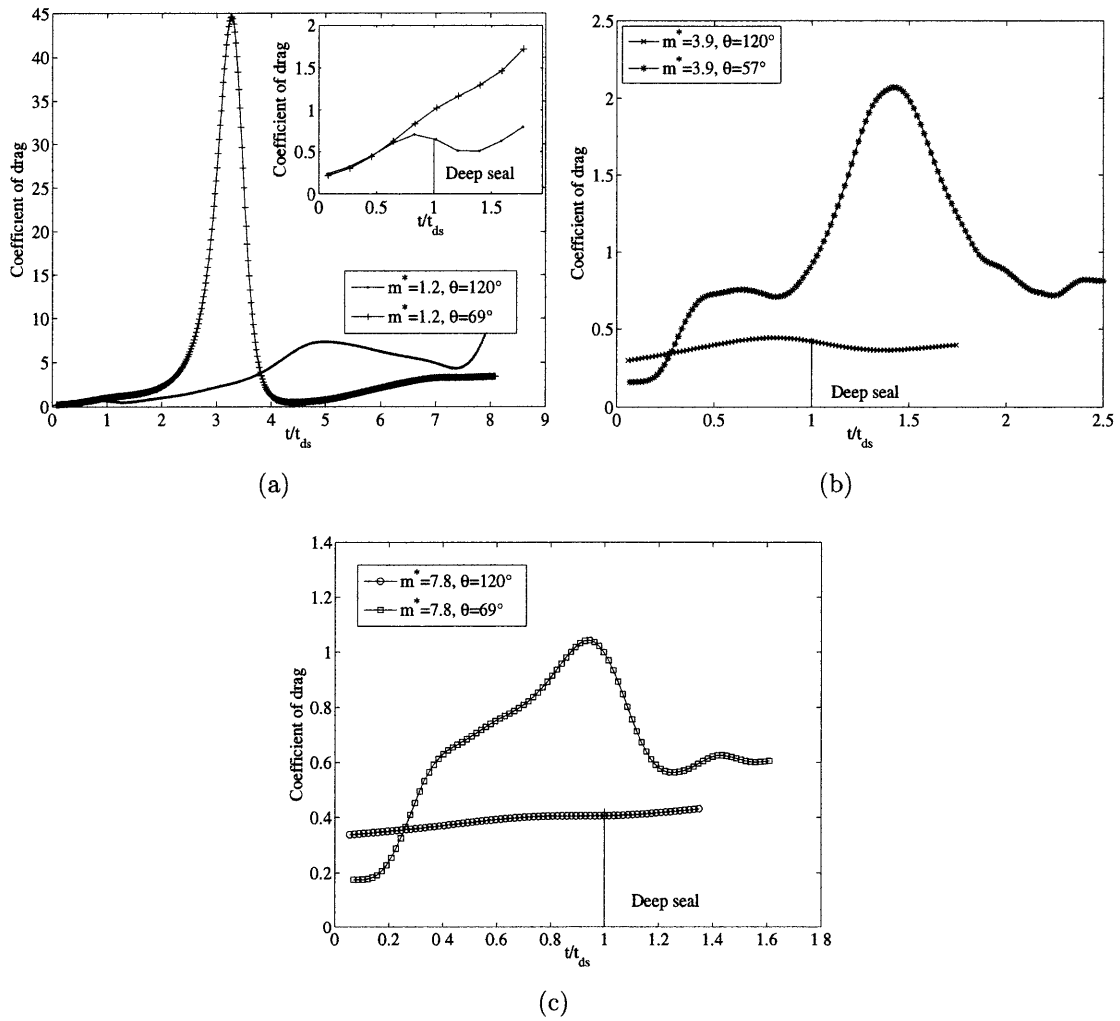


Figure 3-12: Coefficient of drag for the spheres presented in figures 3-1 & 3-2 & 3-9. Legends in figure correspond to legend in figure 3-9. The higher wetting angles $\sim 120^\circ$ tend to have lower drag coefficients.

acrylic case, and a minimum sometime after. This leads one to wonder why the deep seal event is not the maximum or minimum measurement in either of these cases (see § 3.4). As the mass ratio increases, the effect of the unsteady forcing becomes progressively less apparent as the inertial term ($m\ddot{y}$) plays an increasing role in dampening out the visible measurement of these forces. In the case of the ceramic sphere the drag coefficient for the cavity forming case appears to be nearly constant, leading one to wonder if this isn't a remnant of error in the measurement or simply an overlooked (yet simple) force. It is only upon inspection of the smaller mass ratios that one discovers that these unsteady forces can be explained.

The ceramic hydrophilic case (figure 3-12(b)) has generally increasing drag coefficient but there are two interesting points along the way to the maximum $1.47 t/t_{ds}$. The first rise and then plateau occurs around $0.4 t/t_{ds}$ and then C_D dips slightly around $0.8 t/t_{ds}$. These two curious points can only be explained by examining the fluid structure interaction further through PIV. The steel cases also exhibit more drag in the hydrophilic spheres (figure 3-12(c)). The nearly constant drag coefficient for steel explains why nearly all of the previous cavity forming studies accurately predict the drag force using linear deceleration models.

In most of the past cavity forming studies steel spheres were used to perform experiments. This explains why most models assume a constant drag coefficient as shown figure 3-12. The contrast between the steel and acrylic cases emphasizes the importance of these findings. Using only data from steel could be misleading and ignore important dynamics of the cavity due to the large inertial component dominating this case. Although the steel spheres seem to have very small deviations ($C_d = 0.2$ to 0.3) they nonetheless experience the same forcing, but are less influenced by its magnitude than the acrylic spheres. The maximum occurs again at about $0.8 t/t_{ds}$ and then decreases after deep seal to some minimum value. Here, there is a slightly upsetting wobble in the data set around $1.15 t/t_{ds}$. This discrepancy is due to the strangely shaped bubble attached to the sphere. Since the steel spheres appear nearly black in all images despite the lighting angle, the cavity bubble has a few moments where it is able to alter the overall appearance of the steel sphere

enough to move the correlation peak a few pixels upward. Instead of altering these data points by hand they are left here to show how important image processing is to these types of studies.

Overall this data indicates that the spheres without cavities tend to have higher drag coefficients than their cavity forming counterparts due to pressure recovery in the wake. Furthermore, they show a non-constant drag coefficients for all cases. The accelerations, in particular, indicate that decelerating spheres are neither constant nor linear, when measured carefully. This leads to questions about the nature of the forces acting on the spheres. In order to understand the forces at work on the sphere as it descends we will consider two approaches. The first approach will consider the effect of vortices shed in the wake of the non-cavity forming cases. Through the use of PIV we can calculate these effects and correlate them to the rise and fall of the drag coefficients. The second approach also uses PIV to show the nearly potential flow associated with the cavity forming cases. In these cases the cavity acts to mitigate the growth of vortices in the wake allowing the flow fields to resemble a potential flow argument with subtle differences that account for the expansion and contraction of the cavity.

3.3.3 Non-cavity forming cases

The drag coefficient leads to a number of questions that can only be answered by analyzing the flow around the spheres. For now let us consider the non-cavity forming sphere cases. Using standard PIV techniques the flow field around the spheres can be identified and the magnitudes of the forces exerted on the wake can be measured and correlated to the times at which these events occur.

The hydrophilic acrylic spheres have the greatest decelerations and are associated with a very large change in the drag coefficient. Similar to the formulation of drag in equation (3.6), figure 3-13 shows the drag coefficient for the acrylic sphere presented in figure 3-15. The coefficient of drag shown in figure 3-13(b) indicates a maximum drag coefficient at $t = 173$ ms, similar to the results in figure 3-12(a).

In this study we took PIV and position data for the spheres up to a time of

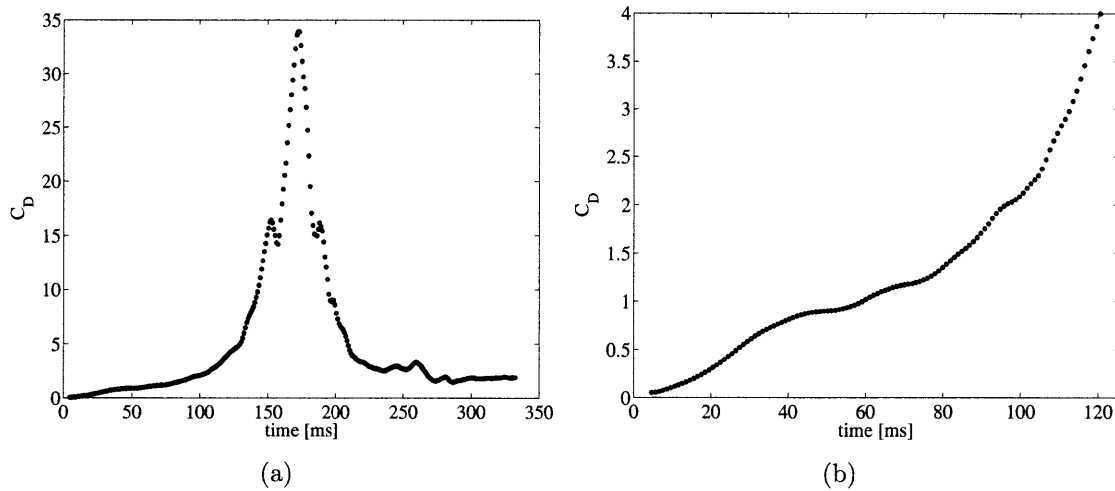


Figure 3-13: Coefficient of drag for an acrylic sphere with $d = 0.0254$ cm and an impact speed of $V_0 = 3.43$ m/s. a) coefficient of drag for all time, b) zoomed in C_D for comparison with PIV results.

$t = 0.3324$ s, however, the PIV data becomes difficult to interpret once the first vortex ring is shed from the sphere for two reasons. The first is that a shadow from the sphere blocking some of the laser light makes data difficult to gather as the vortex ring passes by the sphere on the right. In figure 3-15 the laser comes in from the left and the shadow appears to the right of the sphere. Therefore, we desired that the spheres drift to the right so that the vortex on the left would be most visible. However, the spheres are three dimensional and the shedding of these vortices in the wake is randomly distributed. Therefore, multiple drops were required to gather data where the spheres fell to the right. The second difficulty is that as the sphere slows its descent the vortex ring expands, causing the ring to go out of the laser plane as it passes by the sphere. Nonetheless we are interested in the formation and release of this vortex ring, therefore, we present a close-up view of the drag coefficient up to $t = 0.08$ s in figure 3-13(b), which is beyond the point where the vortex is shed into the wake.

A qualitative understanding of the vortex formation can be seen in figure 3-15. As the sphere descends the fluid along the body is moving faster than the surrounding fluid causing it to wrap up into a vortical structure as it passes towards the back of the

sphere. On the right hand side of the sphere the circulation is counter-clockwise while the left hand side is clockwise. As the sphere continues its descent a small amount of circulation is left in the wake between $10.1 < t < 51.7$ ms. Two larger vortices continue to grow in strength up until $t = 74$ ms where the diameter of the vortex ring begins to grow outward. This outward growth is dominated by the negative vortex (left side) moving further to the left, while the positive vortex moves out of plane as it attempts to navigate its way past the sphere $75.4 < t < 119.0$ ms.

As the vortex grows out and away from the sphere the positive vortex motion on the sphere causes the sphere to move outward to the right in figure 3-15. The positive vortex on the right has a counter-clockwise flow. When the sphere is in the center of the vortex ring the flow field motion is downward, however, as the sphere moves to the right the counter-clockwise rotation begins to cause the sphere to move right and upward. This causes the sphere to slow even more and allows the vortex ring to pass by the sphere! This phenomenon is interesting. A flow field created by the sphere has enough force to move the sphere out of the way so that the vortex can overtake the spheres descent. Eventually, the vortex ring moves ahead of the sphere and the positive vortex has some influence on the sphere, moving it back to the left and down. This motion moves the sphere somewhat back into the path it was previously in, as can be seen in the trajectory of the acrylic case of figure 3-9.

The growth of the vortex ring beyond the diameter of the sphere indicates that it has now become detached from the sphere and that its circulation is no longer fed by the interaction of the sphere with the fluid. The circulation of the sphere can be calculated by (3.1) and is presented in figure 3-15(a). Though the circulation is a bit scattered the data shows that circulation generally increases until approximately $t = 74$ ms, which can also be seen in figure 3-15 from $70.0 < t < 80.9$ ms.

Using the circulation data we can also determine the overall change in momentum of the fluid by determining the impulse force of the vortex ring. Using classical theory for a toroidal vortex moving steadily forward [21] we have

$$I(t) = \rho\Gamma\frac{\pi D^2}{4}\left[1 + \frac{3}{4}\frac{d^2}{D^2}\right] \quad (3.7)$$

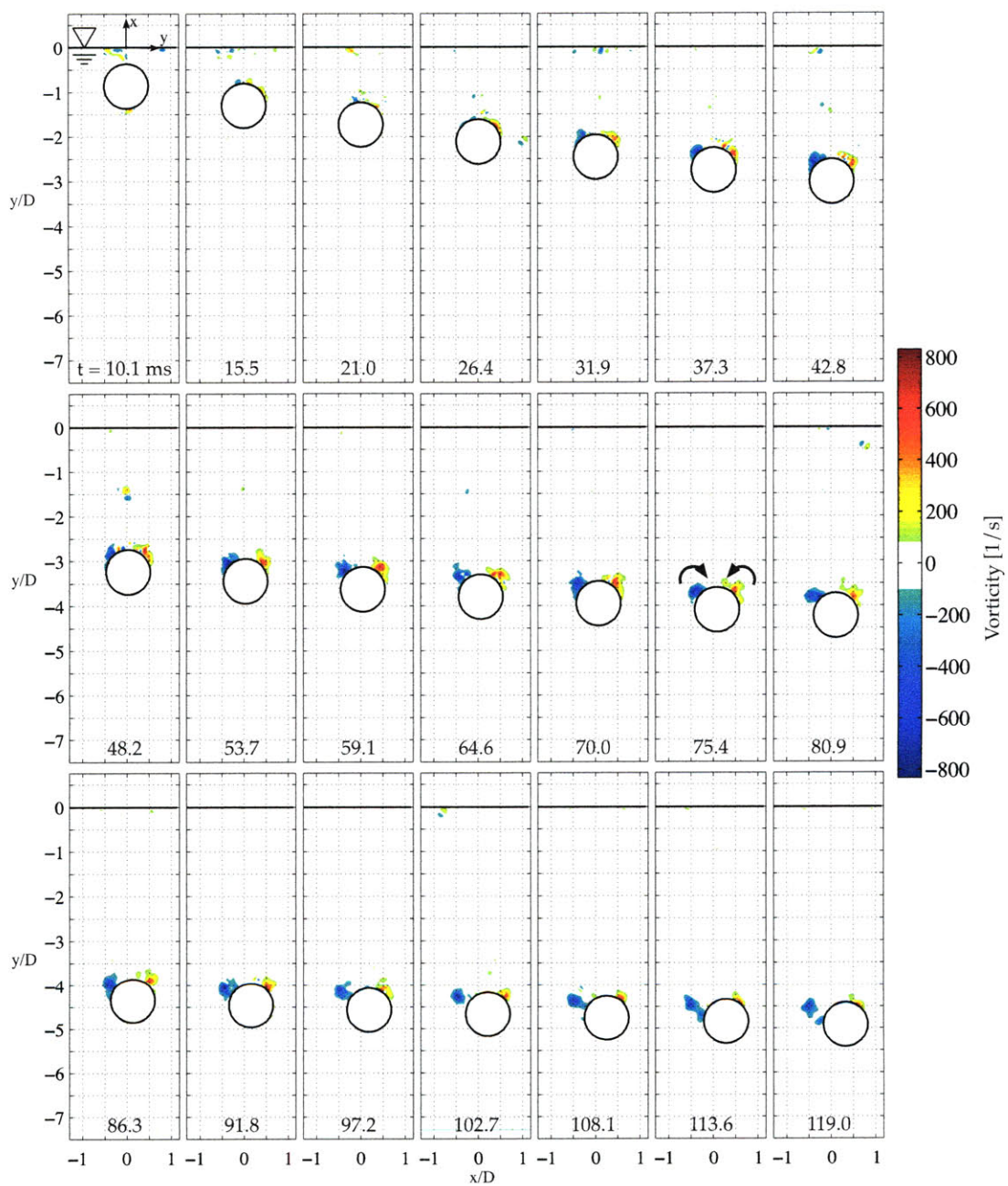


Figure 3-14: Vorticity contours for several steps in time of an acrylic sphere impact. This acrylic sphere is considered hydrophilic and does not form a cavity. The sphere has a diameter of $d = 0.0254$ cm and an impact speed of 3.43 m/s.

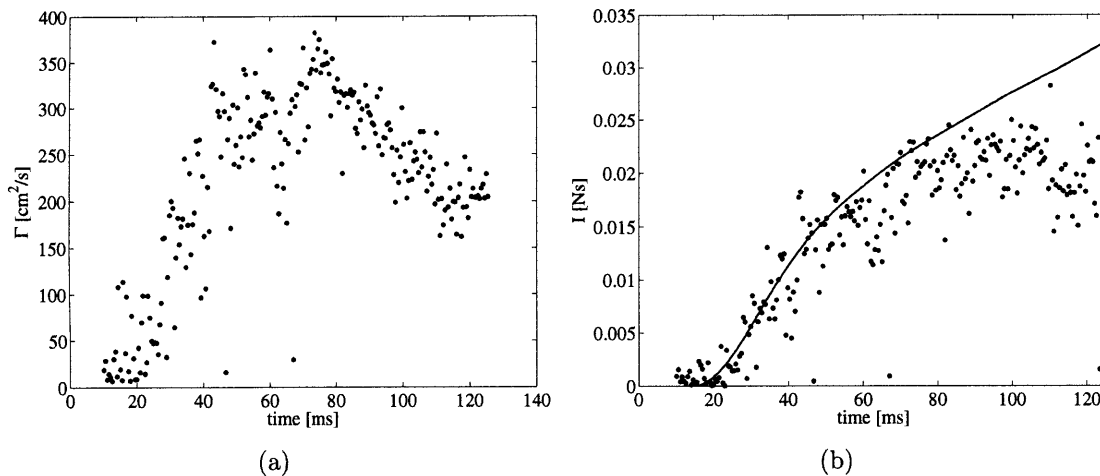


Figure 3-15: Circulation and impulse from PIV for the sphere presented in figure 3-15.

where d is the diameter of the vortex core, Γ is the circulation (3.1), D is the diameter of the toroid from core to core. Figure 3-15(b) shows the result and indicates a rise in impulse force as expected.

We can now determine if this force in the fluid is what we expect. Modeling the forces on the sphere similar to § 3.3.2 we formulate the forces acting on the sphere as

$$m\ddot{y} = -mg - m_a\ddot{y} + \frac{dI}{dt} + \frac{1}{2}\rho V(t)^2 c_d \pi R^2 \quad (3.8)$$

where $m_a = 2/3\pi R^3 \rho$ is the added mass, dI/dt is the impulse force from the vortex ring and $c_d = 0.2$ is the estimated drag coefficient due to form drag. Although we see from figure 3-13 that the drag coefficient is not constant, we can use this constant value to estimate the unsteady nature of the vortex in the wake. Solving for dI/dt and integrating gives the theoretical line in figure 3-15(b). The theory fits accurately up to $t \approx 80$ ms where the vortex ring is beginning to shed from sphere, as seen in the expansion between the positive and negative vortices in figure 3-15 $t > 75.4$ ms. Up to this point the theoretical estimate does an accurate job of determining the impulse force, indicating that this model works well up to this point. After $t \approx 80$ ms the shedding of the vortex indicates that the vortex no longer interacts with the sphere in the same manner as we assumed and therefore the theoretical estimate no longer captures the impulse force accurately beyond this time.

The drag coefficient of a smooth sphere in a uniform cross flow is typically $c_d = 0.5$ for spheres at this Reynolds number ($Re = 8e10^4$) [16]. In our formulation of the impulse acting on the sphere body we used $c_d = 0.2$. The choice of c_d gives us the best theoretical estimation of the impulse force for this acrylic case. We present a second PIV case where a ceramic sphere is dropped from the same height as the acrylic sphere in figure 3-16. As a means of visualizing the differences in the two cases figure 3-16 is presented to show the increasing circulation in the sphere's wake. The circulation in the wake of the ceramic sphere is formed in a slightly different way than in the acrylic case. Here the accumulation of circulation forms more slowly but eventually grows to larger proportions. The vortex is never shed from the sphere and the magnitude of the circulation continues to increase for all times as the sphere descends through the fluid (figure 3-18(a)).

In this second case the best fit for finding the impulse force is $c_d = 0$. This zero coefficient means that we can neglect this portion of equation (4.2) and realize that the impulse force in this case captures all of the drag experience by the sphere as it descends through the fluid.

3.4 Cavity forming cases

The cavity forming spheres also exhibit an unsteady drag coefficient. The hydrophobic acrylic sphere exhibits the greatest change in drag when compared to the higher density ratio spheres and shall be the subject of analysis in this section. Once again standard PIV techniques will elucidate the flow field around the cavity. The cavity radius will also be analyzed in an effort to determine the forces exerted on the fluid at each depth (z).

Using equation (3.6) the drag coefficient is calculated and presented in figure 3-19 and reveals the unsteady behavior of these types of water entry. As the sphere descends through the fluid a large increase in the drag coefficient is experienced. This is an expected behavior as the depth of the sphere is linearly related to the hydrostatic pressure ρgz . However, just before deep seal ($t = 64$ ms) the drag coefficient decreases.

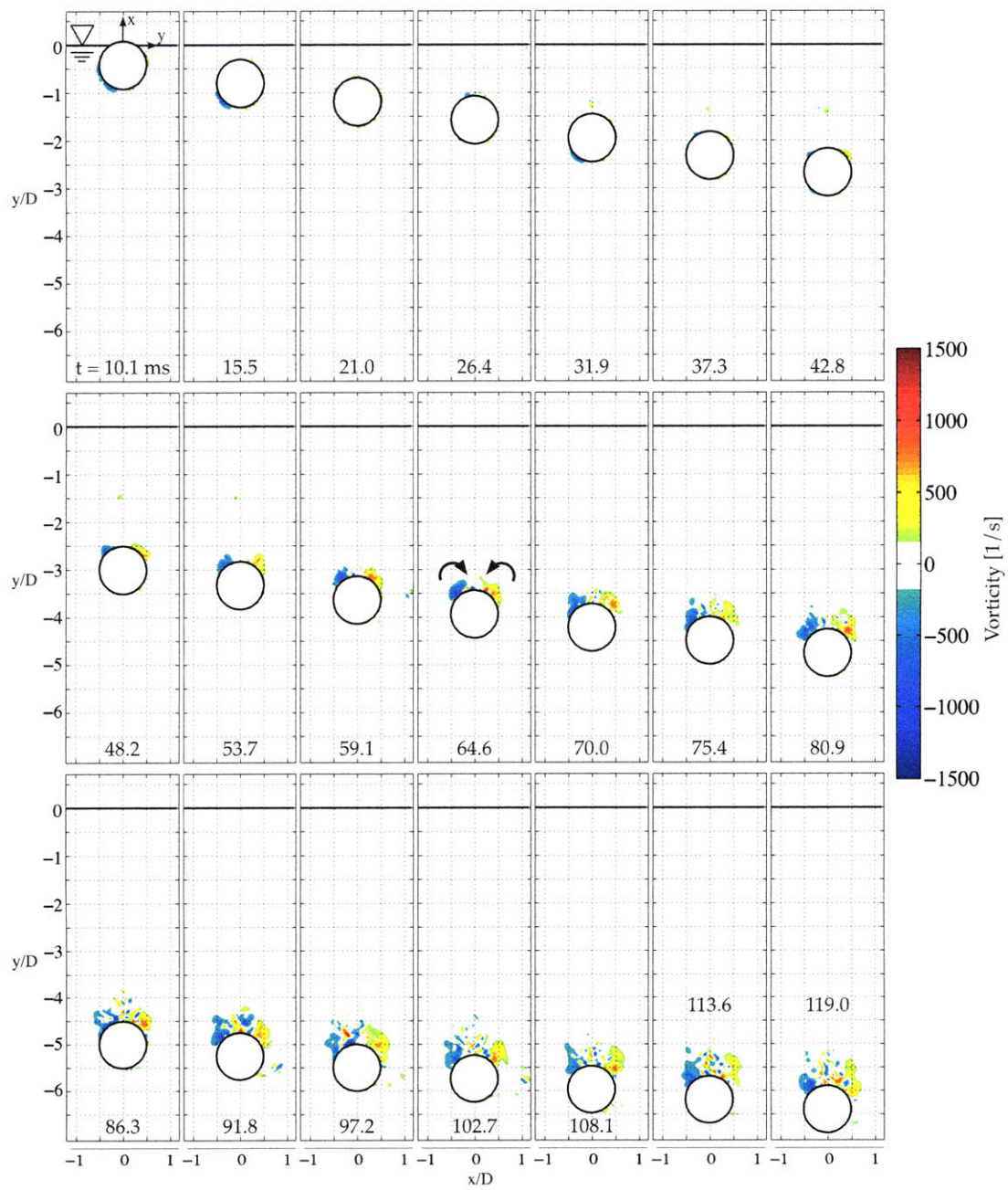


Figure 3-16: Vorticity contours for several steps in time of a ceramic sphere impact. This ceramic sphere is considered hydrophilic and does not form a cavity. The sphere has a diameter of $d = 0.0254$ cm and an impact speed of 3.43 m/s.

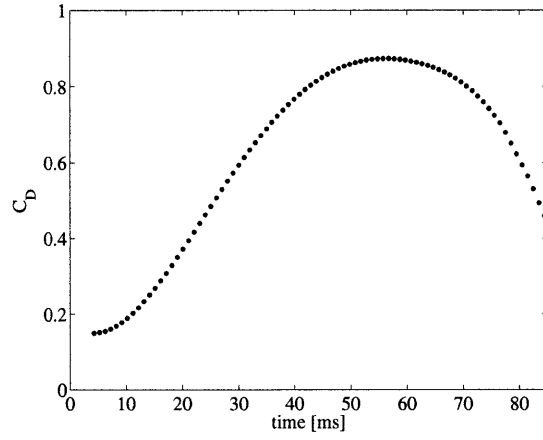


Figure 3-17: Coefficient of drag for an acrylic sphere with $d = 0.0254$ cm, impact height $h = 60$ cm, and an impact speed of 3.43 m/s from figure 3-16.

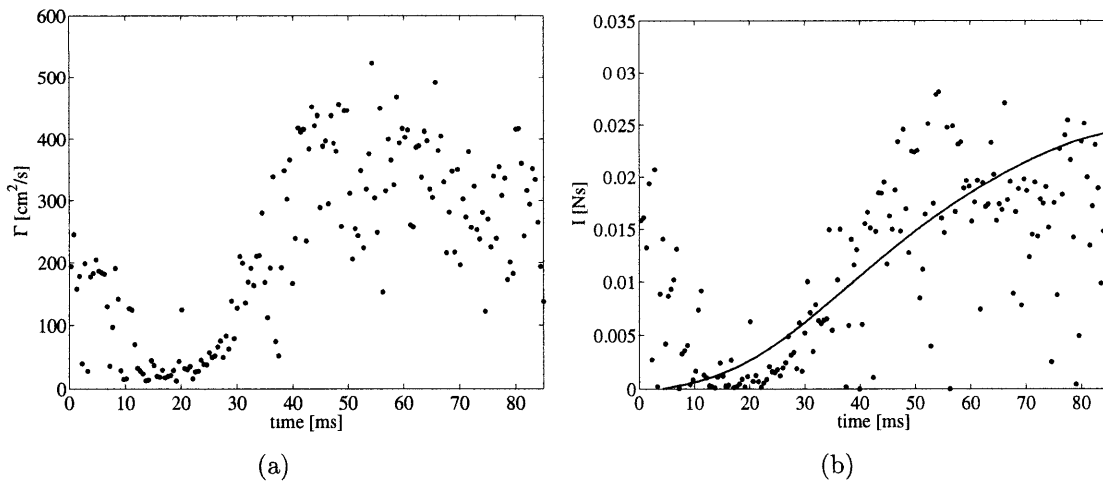


Figure 3-18: Circulation and impulse for a ceramic hydrophilic sphere in figure 3-16.

This decrease continues through deep seal and beyond until the breaks up and water fills in behind the sphere at $t = 77$ ms. After this time the drag coefficient increases similar to the case presented in figure 3-12(a).

The cavity forming cases exhibit less vorticity in the flow, and much less organized structures in their wakes. Figure 3-20 shows these behaviors. The vorticity measurements emphasize the low amounts of vorticity in the flow and the disorganized nature when compared to the previous PIV results. Here the vorticity that is seen in the wake does not roll up into vortex rings emphasizing that cavity formation inhibits the growth of vortices in the wake, thus decreasing the viscous drag of these types of impact. This is one of the major reasons that the cavity forming cases have lower drag coefficients.

The velocity vectors are plotted in Figure 3-20 as arrows in the flow field. These velocities show a very potential flow like nature with very little rotational flow being formed. They also show that the flow moves out and away from the sphere as it passes through and that the cavity keeps the flow moving outward to some extent. As the cavity begins to collapse the flow moves back inward and begins to fill in behind the sphere. This change in momentum occurs between $t = 34.7$ to 39.7 ms. This corresponds to a C_D that increases in slope in figure 3-19. As the drag increases the inward flow near the pinch-off location increases until it becomes nearly the same magnitude as the flow moving down and outward near the sphere itself at $t = 54.5$ ms. This is near the location where the drag curve reaches a maximum $t = 55.0$ ms. When the flow behind the sphere moves inward as quickly as it is moved outward in front of the sphere it appears that is the maximum coefficient of drag. As the inward flow now continues to increase in magnitude as the cavity reaches pinch-off the flow behind the sphere increases in magnitude but also exhibits a slightly downward velocity as the cavity begins to collapse. This downward component of velocity above the sphere continues past pinch-off until the cavity breaks up and water flows in behind the sphere. After this point the flow around the sphere behaves more like the case presented in figure 3-15.

Figure 3-20 also shows the maximum cavity radius at any given depth (shown in

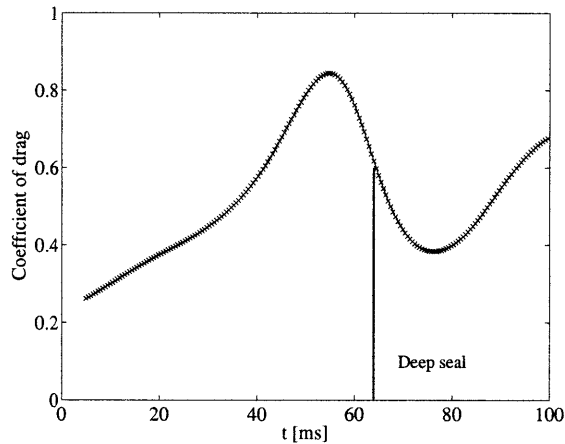


Figure 3-19: Coefficient of drag for an acrylic sphere with $d = 0.0254$ cm, impact height $h = 60$ cm, and an impact speed of 3.43 m/s from figure 3-20.

red on the right side of each cavity). The maximum cavity radius at the point of pinch-off occurs when cavity begins inward collapse at $t = 34.7$ to 39.7 ms. Above pinch-off the cavity continues to grow outward even after cavity collapse near the free surface, whereas below pinch-off the maximum cavity radius is roughly equal to the radius of the sphere.

These PIV measurements emphasize the potential flow like nature of the cavity forming cases, and show that the cavity mitigate the growth of vorticies in the wake, thus decreasing the drag of these types of entry when compared to the non-cavity forming cases.

3.5 Discussion

This paper presents the most fully resolved forces affecting the water entry of spheres after impact to date. This study shows that the water entry of spheres is very unsteady and that the trajectory assumptions appropriate for higher mass ratio spheres cannot be treated in the same manner as the mass ratio decreases. In the case of cavity formation, mass ratio affects the depth of deep seal, and the drag coefficient, but does not affect the time to deep seal, which remains constant for all spheres regardless of diameter or mass ratio. In the case where no cavity is formed, the mass ratio affects

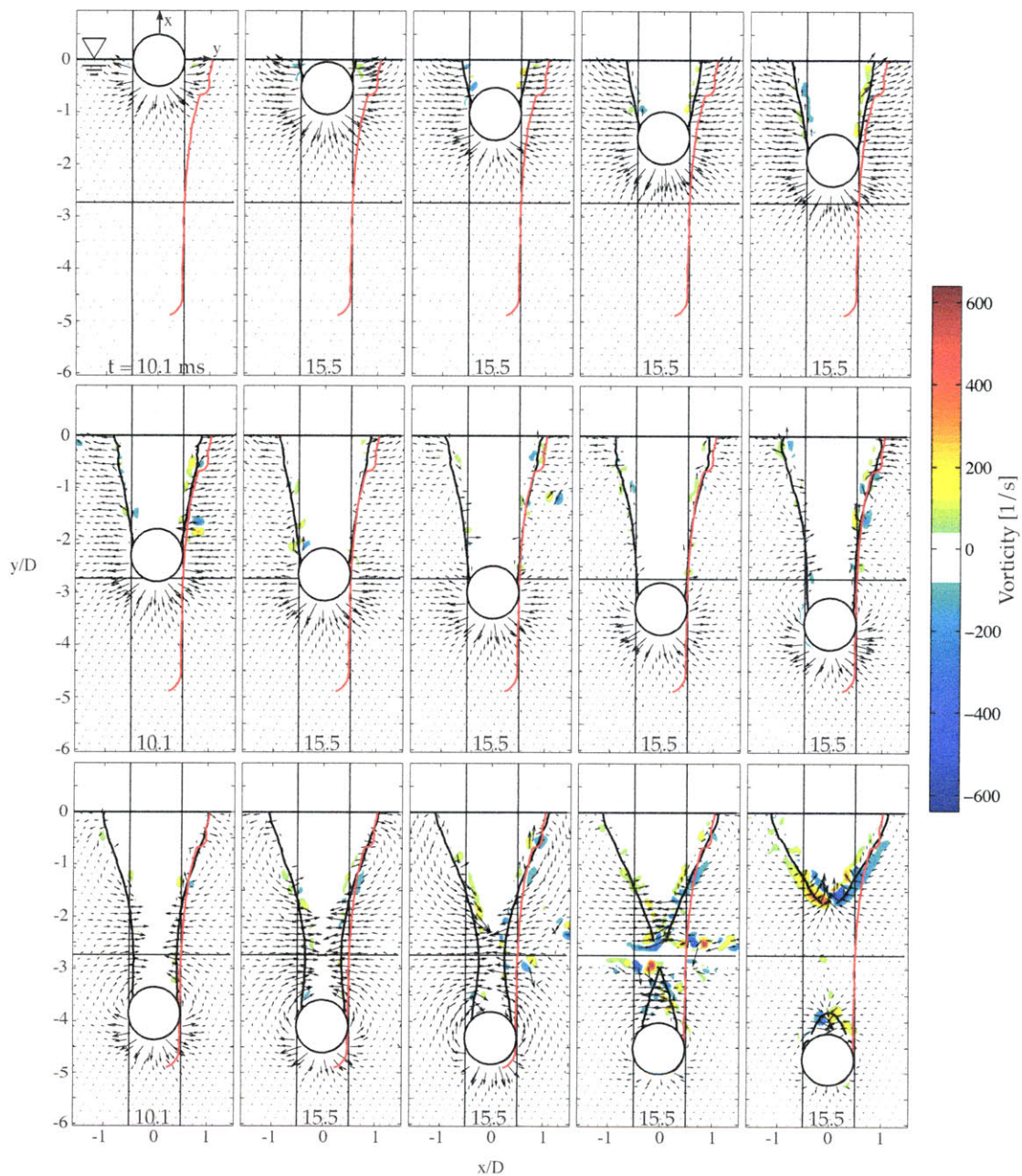


Figure 3-20: Vorticity contours for several steps in time of an acrylic sphere impact. This acrylic sphere is considered hydrophobic and forms a cavity. The sphere has a diameter of $d = 0.0254$ cm and an impact speed of 3.43 m/s, similar to the acrylic case in figure 3-1. The cavity is marked in black along with the free surface and sphere diameter. The red line on the right of each image is the maximum cavity radius at the particular depth (z) below the free surface. Time after impact (when sphere is $1/2$ submerged) is marked below each image. Vorticity is shown in the color and velocity vectors are presented as the arrowed lines in each image.

the drag coefficient and trajectory of the spheres. We have also shown that the unsteadiness in both the cavity forming and non-cavity forming cases is a result of both vortex shedding and cavity formation. In the cavity forming case the cavity acts to mitigate the formation of vortices, which allows the cavity forming spheres to maintain higher velocities after impact. However, this same cavity has an unsteady effect of its own that becomes more noticeable as the mass ratio is decreased. We note that the maximum drag coefficient occurs for when the magnitude of the velocities near deep seal are on the same order of magnitude as those near the sphere. We also note that as the cavity collapses these inward velocities give rise to some downward motion, which seems to aid in decreasing the drag coefficient past deep seal.

In the non-cavity forming cases (hydrophilic spheres) we note that the maximum drag coefficients are much larger than their cavity forming counterparts and that their maximums occur when the first vortex is shed in the wake. Vortex shedding was estimated by calculating the circulation in the flow field over time through PIV and then correlating to the maximum drag coefficient. This work emphasizes the need to account for unsteady effects in modeling the impact of spheres, especially as the mass ratios approach unity.

Acknowledgments A. H. T. gratefully acknowledges funding from the Office of Naval Research University Laboratory Initiative grant # N00014-06-1-0445 for funding T. T. T. We thank Roderick La Foy, Johanna Gentils, Anna Shih, Ashley Cantieny, Libby Palmer and Jesse Belden in helping with the acquisition, processing and general support of this project. Discussions with Jeffrey Aristoff, John Bush, and Gareth McKinley were also very helpful. Especially my co-author, Brenden Epps for working extremely hard on the theoretical modeling and for the spline tool and PIV circulation tools that made this work possible.

Bibliography

- [1] ARISTOFF, J. M. & BUSH, J. W. M. 2009 Water entry of small hydrophobic

- spheres. *Journal of Fluid Mechanics* **619**, 45–78.
- [2] ASFAR, K. & MOORE, S. 1987 Rigid-body water impact at shallow angles of incidence. In *Proceedings of the Sixth International Offshore Mechanics and Arctic Engineering Symposium*, , vol. 2, pp. 105–112. Virginia Polytechnic Inst. State Univ, Blacksburg, VA, USA: ASME, New York, NY, USA.
- [3] BERGMANN, R., VAN DER MEER, D., GEKLE, S., VAN DER BOS, A. & LOHSE, D. 2009 Controlled impact of a disk on a water surface: cavity dynamics. *J. Fluid Mech.* In press.
- [4] BIRKHOFF, G. & ISAACS, R. 1951 Transient cavities in air-water entry. *Tech. Rep.* 1490. Navord Rep.
- [5] DUCLAUX, V., CAILLÉ, F., DUEZ, C., YBERT, C., BOCQUET, L. & CLANET, C. 2007 Dynamics of transient cavities. *J. Fluid Mech.* **591**, 1–19.
- [6] DUEZ, C., YBERT, C., CLANET, C. & BOCQUET, L. 2007 Making a splash with water repellency. *Nat Phys* **3**, 180–183.
- [7] EPPS, B. P. & TECHET, A. H. 2007 Impulse generated during unsteady maneuvering of swimming fish. *Experiments in Fluids* **43** (5), 691–700.
- [8] EPPS, B. P., TRUSCOTT, T. T. & TECHET, A. H. 2009 A robust method for curve fitting and evaluating derivatives of experimental data using smoothing splines. *Submitted to Measurement Science and Technology* .
- [9] GHARIB, M., RAMBOD, E. & SHARIFF, K. 1998 A universal time scale for vortex ring formation. *Journal of Fluid Mechanics* **360** (-1), 121–140.
- [10] GILBARG, D. & ANDERSON, R. A. 1948 Influence of atmospheric pressure on the phenomena accompanying the entry of spheres into water. *Journal of Applied Physics* **19** (2), 127–139.
- [11] GLASHEEN, J. W. & MCMAHON, T. A. 1996 Vertical water entry of disks at low froude numbers. *Physics of Fluids* **8** (8), 2078–2083.

- [12] GRUMSTRUP, T., KELLER, J. B. & BELMONTE, A. 2007 Cavity ripples observed during the impact of solid objects into liquids. *Physical Review Letters* **99**, 114502.
- [13] HOROWITZ, M. & WILLIAMSON, C. H. K. 2008 Critical mass and a new periodic four-ring vortex wake mode for freely rising and falling spheres. *Physics of Fluids* **20** (101701), 1–4.
- [14] VON KARMAN, T. 1929 The impact on seaplane floats during landing. Technical Notes 321. National Advisory Committee for Aeronautics, Aerodynamic Institute of the Technical High School, Aachen.
- [15] KOROBKIN, A. A. & PUKHNACHOV, V. V. 1988 Initial stage of water impact. *An. Rev. of Fluid Mech.* **20**, 159–185.
- [16] KUNDU, P. K. & COHEN, I. M. 2004 *Fluid Mechanics*, 3rd edn. Elsevier Academic Press.
- [17] LEE, M., LONGORIA, R. G. & WILSON, D. E. 1997 Cavity dynamics in high-speed water entry. *Phys. Fluids* **9**, 540–550.
- [18] MAY, A. & HOOVER, W. R. 1963 A study of the water-entry cavity. Unclassified NOLTR 63-264. United States Naval Ordnance Laboratory, White Oak, Maryland.
- [19] RAFFEL, M., WILLERT, C. & KOMPENHANS, J. 2002 *Particle image velocimetry: a practical guide..* Springer, New York.
- [20] RAFFEL, M., WILLERT, C., WILLERT, C. E. & KOMPENHANS, S. 1998 *Particle image velocimetry.* Springer.
- [21] SAFFMAN, P. 1995 *Vortex Dynamics.* Cambridge: Cambridge University Press.
- [22] THORODDSEN, S. T., ETOH, T. G., TAKEHARA, K. & TAKANO, Y. 2004 Impact jetting by a solid sphere. *Journal of Fluid Mechanics* **499** (499), 139–148.

- [23] TRUSCOTT, T. T. & TECHET, A. H. 2009 Water entry of spinning spheres. *Journal of Fluid Mechanics* **623**, 135–165.
- [24] WAGNER, H. 1932 Phenomena associated with impacts and sliding on liquid surfaces. *ZAMM* **12**, 193–235.
- [25] WORTHINGTON, A. M. 1908 reprinted, The Macmillian Co., New York, 1963 *A study of splashes*. Longmans Green and Co., Plymouth : Printed by William Brendon and Son, Ltd., 1908.

THIS PAGE INTENTIONALLY LEFT BLANK

Chapter 4

Water entry of spinning spheres

This chapter appears as: T. T. Truscott and A. H. Techet, Water entry of spinning spheres, *J. Fluid Mech.* 625, pp 135-165.

Abstract

The complex hydrodynamics of water entry by a spinning sphere are investigated experimentally for low Froude numbers. Standard billiard balls are shot down at the free surface with controlled spin around one horizontal axis. High speed digital video sequences reveal unique hydrodynamic phenomena which vary with spin rate and impact velocity. As anticipated, the spinning motion induces a lift force on the sphere and thus causes significant curvature in the trajectory of the object along its descent, similar to a curve ball pitch in baseball. However, the splash and cavity dynamics are highly altered for the spinning case compared to impact of a sphere without spin. As spin rate increases the splash curtain and cavity form and collapse asymmetrically with a persistent wedge of fluid emerging across the center of the cavity. The wedge is formed as the sphere drags fluid along the surface, due to the no-slip condition; the wedge crosses the cavity in the same time it takes the sphere to rotate one half a revolution. The spin rate relaxation time plateaus to a constant for tangential velocities above half the translational velocity of the sphere. Non-dimensional time to pinch off scales with Froude number as does the depth of pinch-off; however a clear mass ratio dependence is noted in the depth to pinch off data. A force model is used to evaluate the lift and drag forces on the sphere after impact; resulting forces follow similar trends to those found for spinning spheres in oncoming flow, but are altered as a result of the subsurface air cavity. Images of the cavity and splash evolution, as well as force data, are presented for a range of spin rates and impact speeds; the influence of sphere density and diameter are also considered.

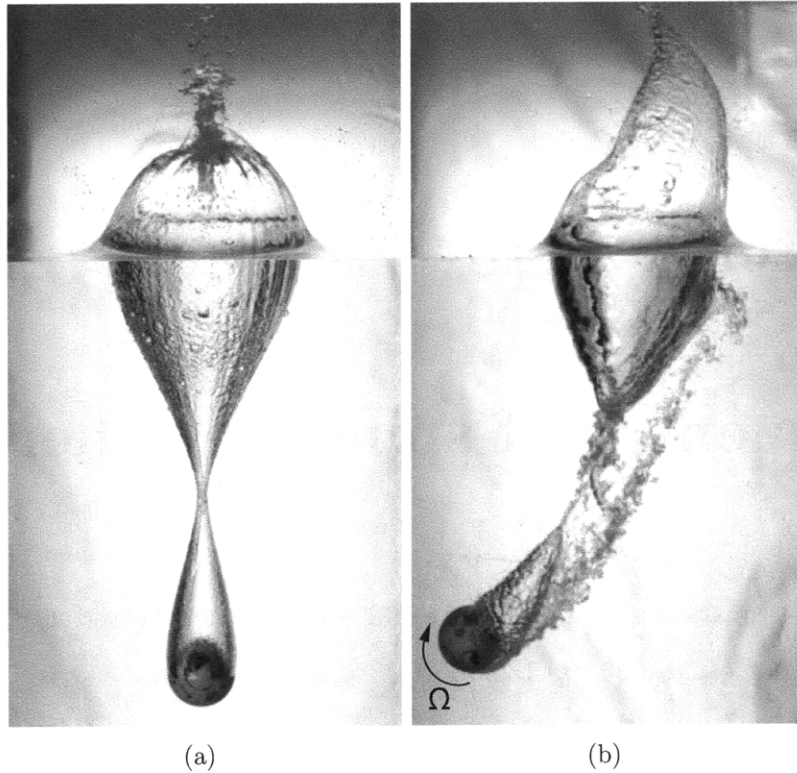


Figure 4-1: Images of the cavity and splash formations by (a) non-spinning and (b) spinning sphere ($d = 0.057\text{ m}$) after impact into water. Impact speeds are $V(a) = 5.95\text{ m/s}$ ($Fr = 7.9$) and $V(b) = 5.45\text{ m/s}$ ($Fr = 7.3$). Case (b) has a spin rate at impact of 251 rad/sec , in the clockwise direction. Both images are taken at the same time after impact ($t = 102\text{ ms}$).

4.1 Introduction

The water-entry problem, by itself, is directly relevant to many different applications: from ballistics [24] and ship slamming [11] to skipping stones [35] and the dynamics of Basilisk lizards [14]. One of the most geometrically simple objects that can be studied is the sphere. This canonical shape impacting on the free surface does not, however, yield simple hydrodynamic results, and the results are even more complex when spin is introduced [40]. An experimental study of the impact of a sphere, spinning transverse to its velocity, on a water surface is presented herein, offering a first look into how spin can affect water-entry behavior.

Figure 4-1 shows a comparison of the non-spinning (a) and spinning (b) impact of

a standard billiard ball on the free surface. The air cavity and splash formed by the spinning sphere vary distinctly from the axisymmetric cavity formed with no spin. The subsurface air-cavity bends along the trajectory of the spinning sphere, and the splash curtain grows vertically and collapses asymmetrically. For the spinning water-entry problem, valuable insight into the physics can be drawn from both water-entry and spinning sphere research.

4.1.1 Water-entry problem

Numerous experiments on water-entry of bodies seek to qualitatively and quantitatively characterize the hydrodynamic phenomena generated by, and forces acting, on the impacting object. Among the first to study such phenomena, Karman [17] investigated the forces exerted on a sea plane float during landing. Subsequent, early impact studies typically focus on ballistics investigations in military laboratories. The experiments of May [24] are some of the most extensive studies of free surface impact for naval ordinance applications. His research focuses on the formation of the air cavity in the wake of spherical projectiles with high impact velocities.

High speed imaging techniques are critical for capturing the rapidly evolving stages of impact hydrodynamics and have been used since early water-entry tests. [42] present some of the earliest images of the splash cavity created by falling objects, which were captured using single spark photography. Today, digital high-speed cameras are widely used for imaging water-entry hydrodynamics. Extensive experimental investigations of water entry by spheres and projectiles are presented in [5], [33], [26, 27], [25], [22], and [1].

Investigations by [23] of the vertical entry of missiles (steel spheres) into water indicate that Froude scaling is a good first approximation to use when describing cavity behaviors such as deep closure. Several other researchers assert, however, that the instantaneous Reynolds number is a better description of the cavity hydrodynamics than the impact Froude number (eg. [13]).

The effect of fore- and aft-body shape on the impact is also of interest to researchers in the area of naval ballistics. [26] conclude that the cavity shape is not

dependent on the nose shape of the projectile for a given drag force. [36] image bullets shot vertically into a tank at 342 m/s, qualitatively considering the bullets' supercavitating behavior; they find that for blunt leading edge projectiles, the afterbody shape can significantly affect the splash formation.

Atmospheric pressure can also be considered a factor affecting the impact problem. Gilbarg [13], at the Naval Ordnance Laboratory, investigate the dependence of the cavity formation on atmospheric pressure. They conclude that surface closure, defined when the splash crown domes over and closes, is the most important event in the development of the water cavity and greatly influences later cavity growth, and note that time to surface closure is inversely proportional to pressure. Deep closure, when the cavity pinches-off below the free surface, is a function of surface closure only for early closure times up to ~ 70 ms after impact [13].

Even biologists are fascinated by the problem of impact. A biological air-water impact study, modeled after the Basilisk lizard, is performed by [14]. Disks, representing the lizard's feet, are shot into water at low speeds (compared to most ballistics studies); high-speed video and load cells measure the forces during impact. Their results also indicate that the time between impact and cavity closure is given by a single value of dimensionless time. Surface closure and cavity pinch-off have also been numerically investigated in detail for circular disks impacting the surface by [12] and [6].

[19] employ a two-dimensional model, based on experimental observations, for cavity formation and collapse taking into account the energy transfer between projectile and cavity wall. Their work considers relatively low impact velocities, where both a surface closure and later a deep-closure, or pinch-off, occur. Data indicate that the time to deep closure, after surface closure, is approximately constant and not a function of the impact speed for any given sphere diameter. The location of deep closure, however, seems to have only a weak dependence on impact velocity, and thus, Froude number was not a good scaling parameter for the range of impact speeds that they investigated [19]; the velocities and Froude numbers in [19] were considerably higher than those considered in the present study. [13] also report, for low Froude numbers,

that surface closure dominates cavity formation, and note that Froude number is not a useful parameter in characterizing cavity growth and collapse.

In general, research has shown that there are a few key mechanisms driving surface closure, the most important of which are Bernoulli pressure and surface tension [7, 19]. As the cavity grows, air flows in through the splash curtain, and for low-speed impact, the local under-pressure inside the cavity is approximately $\frac{1}{2}\rho_{air}V_o^2$. After the splash curtain domes over and closes (i.e. surface closure), the cavity continues to expand due to inertial effects of the ball moving through the fluid. Assuming the process is isentropic [19], the pressure inside the cavity decreases. Eventually, deep closure (i.e. pinch-off) occurs when the cavity stops expanding radially and the hydrostatic pressure of the surrounding fluid is greater than the internal cavity pressure [13, 23, 19].

For impact cases where the impact velocity is sufficiently high, a small, axisymmetric, horizontal jet is ejected at great velocity radially outward from the point of contact between the sphere and the liquid surface. The jet emanates horizontally at first and can travel radially outward at speeds up to thirty times impact velocity. The initial jet forms between 10 and 100 μs after impact, for water solutions of up to 90% glycerin [39]. Thoroddsen *et al.* [39] also report that surface tension and compressibility appear to have little effect on this initial jet formation. The introduction of spin also causes a similar horizontal jet to form, albeit asymmetrically. The effect of spin on the initial stages of impact will be discussed in subsequent sections of this paper.

[43] reviews experimental and theoretical work on droplet impact onto thin liquid layers and dry surfaces, focusing on the splash crown formation and initial jetting. He notes that jetting and crowning originate from the same point irrespective of surface shape, as a result of a sharp kinematic discontinuity. Typically the velocity of the initial horizontal jet is significantly higher than the impact velocity and the formation time is very small. These results are verified by [38] for liquid drops and are similar for solid spheres impacting on the surface [39].

[30] measure the forces during impact using a load cell up to a depth of one-eighth

of the sphere diameter. They report that for impact velocities between one and three meters per second, $1 < V_o < 3 \text{ m/s}$, a maximum force occurs very quickly after impact, at times as short as 1.5 ms or between one tenth and one fifth of the radius below the surface. [29] conclude that the dependence of drag coefficient on Reynolds numbers, between $0.05 < Re < 5 \times 10^3$, resembles that of a sphere in a homogenous fluid. Their work, like much of the existing theoretical work done to determine the force at impact, only considers impact up to a maximum penetration depth of half a sphere diameter. [26, 27] note that the drag coefficient declines gradually towards a value between 0.25 and 0.3 when cavity is formed; the precise shape of the curve appears to depends on the specific gravity of the impacting object.

Direct force measurements are not easily obtained for water-entry experiments. [33] and [26, 27] derive force components using force balance equations and position-time curves, taken from high-speed video after the sphere is fully submerged. [18] offers a review of these force models derived from experimental data. A similar force balance model for determining forces is developed in this study on spinning spheres, and data is presented in section 4.3.

4.1.2 Spinning sphere problem

Spin, by itself, imposed on a sphere in flow, acts to induce lift and alter the flight path of an unconstrained sphere. Newton [31] first remarks on the distinct change in the flight path of spinning tennis balls, noting their tendency toward the side that is moving the fastest. Later, Robbins [34], interested in this problem from his experimental observations of canon ball ballistics, shows that a spinning sphere suspended as a pendulum experiences a lateral aerodynamic force. A similar force is seen for spinning cylinders; this force due to rotation is widely credited as the “Magnus Effect” [3].

The subject of spinning spheres is of special interest to many sports fans, especially soccer, baseball, cricket and golf enthusiasts. Baseball pitchers can break their curve balls at just the right time, or throw a knuckleball, without spin, to drop at the last minute over the plate. Golfers hoping to gain loft, or fade or hook their shots, or

avoid hooking their shots, rely on small spinning balls riddled with tiny dimples. A comprehensive review of sports ball aerodynamics is presented in Mehta [28].

Attempts to predict the behavior of spinning sports balls drive experimentalists to perform lift and drag tests, as well as flow visualization experiments on spinning spheres. Much of the experimental force data for spinning spheres is compiled in [2]. Researchers studying cricket and baseball report that, for pre-critical Reynolds numbers, asymmetric boundary layer separation, due to tripping by the seams on the balls, results in increased lateral forces [28]. Spin induced effects also lead to asymmetrical boundary layer transition flow on one side of the sphere, which causes large lateral forces, for example in baseball curveballs [28, 2] and golf-ball flight [4].

Interestingly, for sub-critical Reynolds numbers, experimental measurements of the lateral forces on spinning smooth spheres in flow, by [21] and [9], show that the lift coefficient, C_L , can be negative for small values of non-dimensional spin parameter, $S = r\Omega/V$, where r is the radius of the sphere, Ω is the spin rate in radians per second, and V is the flight velocity. [21] shows that above spin parameter values of $S = 0.35$ to 0.50 , for subcritical flow around smooth spheres, the coefficient of lift becomes positive and increases steadily up to $S = 1.0$, above which the lift coefficient appears to level off. The negative lift coefficients for low spin numbers ($S < 0.4$) have never been seen for roughened or dimpled spheres, or those with seams (e.g. Bearman & Harvey [4], Watts & Ferrer [41], Smits & Smith [37], Alaways & Hubbard [2]).

Davies [9] presents a plausible explanation for the negative lift force as a result of an asymmetric transition from laminar to turbulent flow. As the velocity of the incoming flow approaches the limit of transition away from laminar flow, only slight perturbations are necessary to trip the flow to turbulent. Since the sphere is spinning, one side of the sphere experiences a higher relative velocity than the other, and could trip before the side with a lower relative velocity thus inducing lift in the opposite direction than anticipated. This would only be plausible for low spin parameters, above which the force of lift from circulation is greater than the imbalance due to asymmetric transition. Davies [9] acknowledges that this explanation only works for very specific critical parameters and any changes in turbulence levels or velocity could

reverse the effect. He cautions that further measurements of pressure or flows around spinning spheres are needed in this negative lift regime.

Results from [4], for a dimpled sphere, show that the lift coefficient is proportional to the spin parameter, S , and thus the lift force is proportional to Ωr , the tangential velocity. [37] measure the forces on golf balls (dimpled spheres), along with the spin decay rate, in a wind tunnel. Their results suggest that the lift coefficient has some Reynolds number (Re) dependence only up to Reynolds number 100,000. Above this value there appears to be little, if any, dependence of the lift coefficient on Reynolds number. This lack of dependence at $Re > 100,000$ is reinforced by data in Always & Hubbard [2], who present an extensive compilation of published data for spinning spheres.

In the current investigation, spheres with nominal roughness heights of $k/(2r) = 1.4 \times 10^{-5}$ are considered. While not the main focus, nor presented herein, results from our own preliminary investigations in a water tunnel show good agreement with [21] data for the lift and drag spinning, smooth spheres above spin parameter $S \approx 0.35$. The forces determined using the sphere trajectories are also similar to wind and water tunnel experiments. The effect of spin rate on the physics of the cavity dynamics, splash formation and collapse, and the forces acting on the sphere are addressed in the following sections.

4.2 Experimental Details

Experiments on water entry of spinning spheres were performed using standard billiard balls (diameter, $d = 5.72$ cm; mass, $m = 0.17$ kg) shot vertically into a tank of quiescent water. The steel-reinforced, clear acrylic tank was 1.5 m long, 0.9 m wide, and 1.5 m deep. A shooting apparatus, modeled after a baseball-style pitching machine with two rotating wheels (diameter, $d_w = 0.46$ m), was mounted above the tank. The spheres were released out of the loading tube and dropped between the two wheels, which fired the spheres into the water (figure 4-2). The ball exited the launch mechanism, with initial downward launch velocity and spin, at a height of

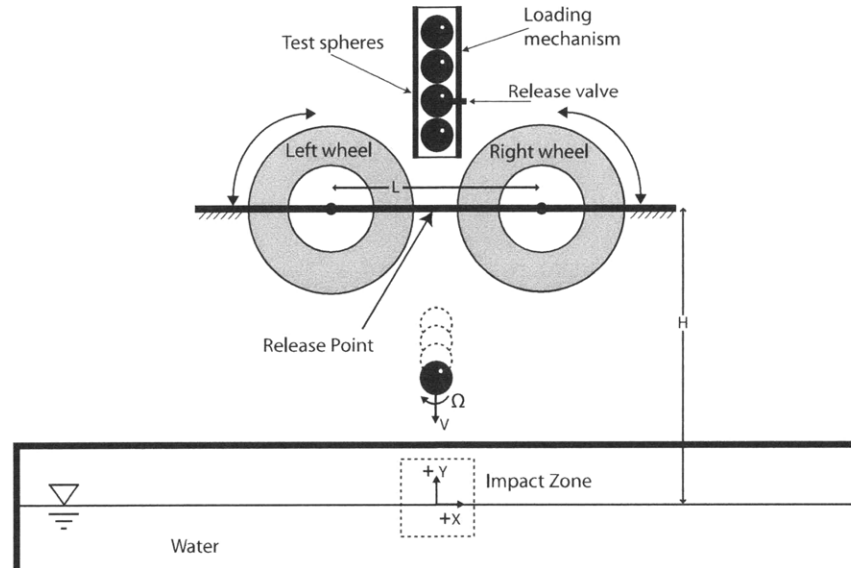


Figure 4-2: Schematic of the experimental shooting apparatus. Spheres are released from the loading mechanism, dropping between the two spinning wheels, which shoot the spheres into the tank below. The speed of each wheel was independently controlled in order to change the impact and spinning speed of the projectiles. (Figure is not to scale.)

1.40 *m* above the surface of the water; this maximum distance above the free surface was constrained only by the laboratory ceiling height. The wheels of the shooting mechanism imparted spin to the sphere by rotating at different speeds. Both initial impact velocity, V_o , and initial spin rate, Ω_o were varied by altering the spinning rate of wheels of the shooting mechanism. The wheel speed and ball release timing were controlled using a personal computer and a National Instruments LabView interface, which also controlled the video recording system to ensure accurate, synchronized timing.

High-speed video images of the sphere's trajectory were used to calculate the instantaneous velocity of the sphere in the *x*- and *y*-directions. Two high-speed video systems were used: camera #1 for the top view was an IDT X-StreamVision XS-3 camera and camera #2 for the side view was a Redlake Motion Pro X3. It was not physically possible to place a camera directly above the impact zone, as the shooting mechanism obstructed the field of view. Thus, camera #1 was positioned

adjacent to the wheels looking down at a slight oblique angle to the free surface. Camera #2 was positioned such that it captured the motion of the sphere at least one diameter above the water, as well as along its descent through the water, allowing the velocity just before and after impact to be determined.

Both cameras had a maximum resolution of 1280(V) x 1024(H) pixels, however, camera #1 had a maximum frame rate of 625 frames per second (*fps*) at maximum resolution, whereas camera #2 could reach 1000 *fps* at maximum resolution. When the resolution of camera #1 was reduced in one direction, the frame rate could be increased, and thus both cameras could record at 1000 *fps*. At 1000 *fps*, camera #1 recorded images at 480(H) x 1108(V) pixels and camera #2 recorded at full pixel resolution; the exposure time was 234 μs per frame for both cameras. A 28 mm, *f*/2.8 lens with a fully open aperture was used and a fixed field of view (FOV) was maintained on both cameras for all experiments. The cameras were synched in time with the ball release mechanism through the LabView interface.

Sufficient lighting is crucial for quality high-speed video, thus lights were placed both in front of and behind the tank. For back-lighting, thirty-six, standard, 32 W, fluorescent bulbs were aligned vertically in a large bank that was positioned directly behind the impact zone, outside of the tank, and projected light directly towards the cameras. The bank of bare bulbs was 0.5 m wide x 1.6 m high. Nine separate, out-of-phase, ballasting units minimized the 60 Hz flickering effect generated by the fluorescent lights. A white sheet placed between the light bank and the impact zone diffused the back light and created a more uniform backdrop. The front illumination used six 400 W, halogen lights, positioned outside the tank and focused towards the impact region. These six light were used to illuminate the front side of the cavity. Three of the halogen lights were mounted vertically near the water surface in an arc around the region of interest, which focused the light towards the impact zone. Three more lights, also outside the tank, were stationed approximately one meter below the surface level, and focused towards the lower half of the sphere's trajectory, again in an arc around impact the zone. The lights in front of the tank were positioned around the camera such that there was minimal glare off the tank wall and the sphere

trajectory was sufficiently lit for the image processing algorithm to detect the sphere consistently.

The impact velocity and spin rate were calculated by analyzing the high-speed video data. Impact speeds and initial non-zero spin rates ranged from $|V_o| = 1.9$ to 9.9 m/s and $|\Omega_o| = 13$ to 394 rad/sec , respectively. For comparison, several test cases had zero spin; these cases were performed at impact velocities of $|V_o| = 1.9$ to 7.5 m/s . The horizontal velocity at impact was less than 2-4% of the vertical velocity for both spinning and non-spinning cases.

The effect of spin is considered in terms of the non-dimensional ratio between tangential velocity, Ωr , where $r = d/2$, and the magnitude of the velocity of the sphere, V . The spin parameter, defined following the nomenclature of Maccoll [21] as $S = \Omega r/V$, is akin to a Strouhal number and used in this paper to ensure consistency with previously reported data in the field of spinning spheres. Using the shooting mechanism described herein, it was possible to obtain initial, impact spin parameters, $S_o = \Omega_o r/V_o$, between 0 and 2.25, using the spin rate and velocity at impact, Ω_o and V_o . Data for cases with $S_o < 1.4$ are presented herein. After impact, spin parameter also changed, in time, as a result of the changing instantaneous velocity and spin rate, such that $S(t) = \Omega(t)r/V(t)$.

Froude number, $Fr = V_o/\sqrt{gd}$, was used to categorize the initial impact velocity of the ball, and is only given in terms of initial impact velocity. Froude numbers considered range from 2 to 13; however, most of the data and images presented herein were obtained at $Fr = 7.3 \pm 0.2$, unless otherwise specified. After impact, once the ball was fully submerged, Reynolds number was used as a non-dimensional parameter to characterize cavity and sphere trajectory behavior. Reynolds number was defined *instantaneously* along the sphere trajectory as $Re = V_i d/\nu$, where $V_i = V(t)$ is the instantaneous velocity of the ball in time, t , and ν is the kinematic viscosity of the fluid.

The sphere's position in time was found using standard image processing cross-correlation techniques on the whole sphere (74 pixel window size). A five point gaussian peak-fit was used to find the location of the maximum correlation peak,

and thus determine the displacement of the sphere with subpixel accuracy. The peak fitting implementation was similar to that employed in Particle Imaging Velocimetry processing algorithms (e.g. [32]). Using cross-correlation with peak-fitting, the position of the sphere was determined accurate to within ± 0.025 *pixels*. Conversion from pixels to meters yields an uncertainty of $\pm 1.93 \times 10^{-5}$ *m* (0.0193 *mm*) in *x*- and *y*-positions.

Measurement error for *x*- and *y*-position was affected predominately by image resolution and video acquisition rate: e.g. higher resolution, or more pixels per meter, would have given higher accuracy. The velocity and acceleration were determined by taking the first and second derivatives of a polynomial fit to the position data. The lowest order curve fit to both *x*- and *y*-positions was chosen such that higher order polynomials yielded nearly identical results for both velocity and acceleration, minimizing the error. This corresponded to a seventh order polynomial fit, with an R^2 value of 0.99. Error estimates were between 2-4% in velocity, 5-10% in acceleration, and 5-15% in lift and drag.

The rotation of the sphere was determined using an iterative, rotating cross-correlation routine, which determined the mean and standard deviation of the angular position from the video sequences. Random, non-uniform markings were drawn on the sphere with indelible marker to enhance the correlation algorithm. The correlation algorithm isolates one quadrant of the sphere in two sequential images and directly compares these isolated regions of interest, thus eliminating the need to shift the entire image. The quadrant from image two is rotated through a maximum rotation of $\pi/4$ *rad*, in increments of $\pi/1800$ *rad*. The incremental angular displacement between time steps corresponds to the angle where maximum correlation is found between image one and the rotated image two. The angular position data is found by summing the incremental angular displacement over time. Spin rate, $\Omega(t)$ *rad/s*, was found from the first derivative of a second order polynomial fit to the angular position data. The mean spin rate and standard deviation were applied to a Student's-*t* distribution, which revealed error estimates of 4 – 9% for $\Omega(t)$.

The spheres used in the bulk of this study were standard billiard balls made from

phenolic resin with a mass ratio, $m^* = m_{sphere}/m_{fluid} = 1.74$. The surface roughness of the spheres was determined using model Tencor P-10 Surface Profilometer, sensitive to roughness of $\pm 0.01 \mu m$. The size of the spheres was large compared to the profilometer's measurement range precluding measurement over the entire sphere surface, so only a fraction of the sphere could be tested at any given time. The theoretical smooth surface location is subtracted from the profilometer curves to determine RMS values. The RMS value for the phenolic resin spheres is $0.8 \pm 0.4 \mu m$; the roughness to diameter ratio was $k/d = 1.4 \times 10^{-5}$. The static contact angle made by a drop of fluid with the surface of the phenolic resin spheres was $90^\circ \pm 10^\circ$. The random markings on the spheres did not locally alter the average roughness or contact angle.

Additional materials and sizes of spheres were also tested to determine the effect of density and diameter on the splash and cavity physics. These spheres included small ($d = 2.54 \text{ cm}$) acrylic, ceramic, and steel spheres. The mass ratios of the 2.54 cm spheres were $m^* = \{1.2, 3.9, 7.8\}$, for the acrylic, ceramic, and steel spheres, respectively. The spheres were coated with a hydrophobic coating (Cytonics Corporation's WX2100TM) to have uniform surface properties; the RMS surface roughness for all 2.54 cm spheres was $k = 2.4 \mu m$, and the static contact angle was $\theta_c = 120^\circ \pm 10^\circ$. The data from these tests with the smaller projectiles are not the main focus of this paper, and therefore unless explicitly expressed, data and images presented in the following sections are for the standard billiard balls.

4.3 Results and Discussion

4.3.1 Overall cavity dynamics

Following the discussions of [24], we consider the impact problem in five distinct stages: (1) the moment of contact, (2) the flow forming stage, (3) the open cavity and splash growth stage, (4) the closed cavity and pinch-off stage, and (5) the collapsing cavity stage. While the details of each stage may vary with impact parameters, these five distinct stages persist for the case of the sphere impacting with spin.

Fundamentally, the initial stages of high-speed impact of any object on the free surface, with or without spin, are dominated by inertial effects. Figure 4-3 shows a sequence of images taken for a standard billiard ball spinning with $\Omega_o = 199 \text{ rad/s}$ ($S_o = 1.1$) and impacting the free surface with an initial velocity of $V_o = 5.45 \text{ m/s}$ ($Fr = 7.3$). Each image in the sequence is separated by $\Delta t = 10 \text{ ms}$. The first image (a) is taken 1 ms after impact. The sphere is already moving beyond stage one into stage two in figure 4-3(a).

An initial horizontal jet of fluid forms as the sphere impacts the free surface; this jet continues to extend radially outward as the sphere descends into the fluid. The jet transitions from outward to upward growth during stage 2 when the sphere is submerged approximately one quarter of its diameter. A thin layer of fluid is driven around the lower surface of the sphere until it nears the equator, where it separates from the sphere to form the splash crown. Below a critical impact velocity and critical wetting angle, the flow remains attached until it surrounds the sphere completely and meets at the top, causing a jet of fluid to form upward without the presence of an air-cavity [10]. For the spinning sphere, in the range of impact speeds considered for the standard billiard balls, the splash curtain appears to form symmetrically below $S \approx 0.30$, but above this value asymmetric growth of the splash curtain can be seen in the high speed video sequences.

In stage three of the impact sequence (figure 4-3(c-f)) the entire ball passes below the ambient free surface and an open air-cavity begins to form in its wake. The splash crown base, connected to the free-surface, grows in diameter, with the top of the subsurface air cavity, and grows in height forming a vertical curtain. The subsurface air cavity both elongates vertically and grows radially outward as the ball descends. At this stage the cavity is conical in shape, similar to the non-spinning case, but curved because of the spinning motion of the sphere which induces a lift force perpendicular to the ball trajectory.

During stage three, the sphere continues along its curved trajectory, bending the air cavity further. The sub-surface air cavity is still open to the atmosphere and air flows in through the splash curtain resulting in a reduced pressure, which acts

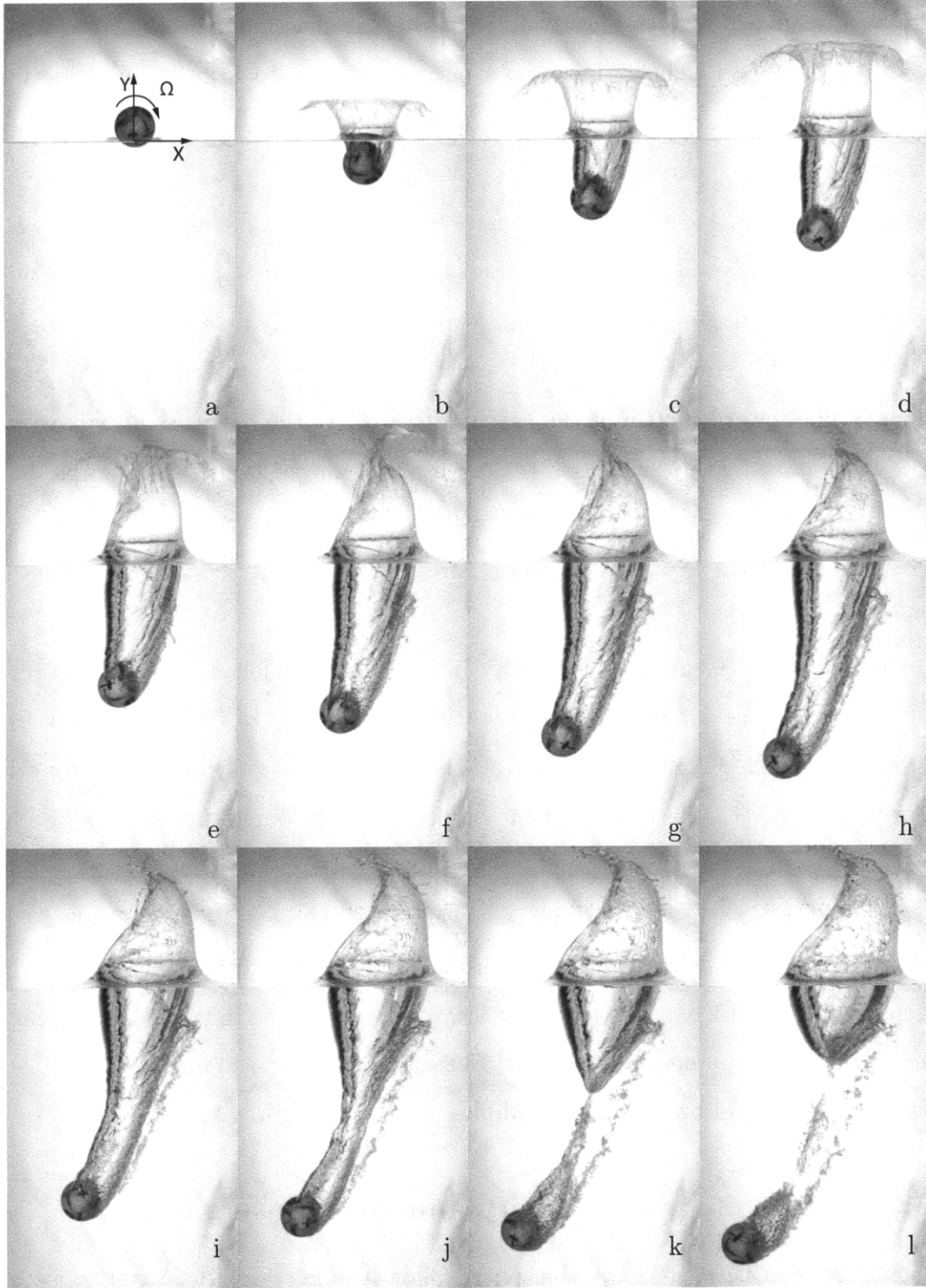


Figure 4-3: A sequence of images depicting the splash and air cavity formed in the wake of a spinning sphere impacting the water. The initial impact velocity is $V_o = 5.4 \text{ m/s}$ ($Fr = 7.3$), and the initial spin parameter is $S = 1.1$. The first frame (a) is 1 ms after impact; subsequent frames are 10 ms apart. (Digital video is available online for both side and top views of this run.)

to draw the splash curtain inward as it reaches its maximum height. The splash curtain continues to collapse inwards, eventually closing to form a dome (between figures 4-3(g-h)).

In stage four the splash curtain is closed and no more air can flow into the cavity; however, the subsurface air cavity continues to stretch and curve under the movement of the spinning sphere. The cavity collapse for the case of the spinning sphere is similar to that of a non-spinning projectile as described in [19]. Hydrostatic pressure of the surrounding fluid retards the outward growth of the cavity and initiates the cavity collapse. The inward inertia of the cavity forces it to neck down into a curved, yet bottle-like shape, reaching pinch-off (deep-closure or deep seal) between figures 4-3(j) and 4-3(k). At pinch-off the cavity splits into two distinct, closed cavities: a lower cavity still fully attached to the sphere, and an upper cavity connected to the free surface.

After pinch-off (stage five) the cavity begins a rapid, violent collapse (figures 4-3(j-k)). In both the lower and upper cavities, distinct jets of fluid eject away from the point of pinch-off in opposite directions similar to what is also seen by other researchers (e.g. [42, 20]). The jet in the upper cavity bursts up through the free surface with significant velocity, pulling the upper cavity almost inside-out. The jet attached to the lower cavity is directed towards the sphere without an immediately obvious effect on the sphere's motion. The smaller, lower cavity remains attached to the sphere (figure 4-3(l)). Ripples in the lower cavity are seen in the video sequences, comparable to those reported by [16]. Eventually vortex shedding begins and the lower cavity starts to break up into bubbles that ascend to the surface.

4.3.2 Effect of spin on cavity and splash asymmetry

As spin rate increases from zero, the sphere follows an increasingly curved trajectory. The symmetry seen in the non-spinning cases gives way to asymmetric cavity and splash growth in the spinning cases. Asymmetry, due to spin, develops even for relatively low spin parameters and at early stages of splash formation. For example, the growth of the initial axial jet (at $t < 1 \text{ ms}$) is already asymmetric as it rises

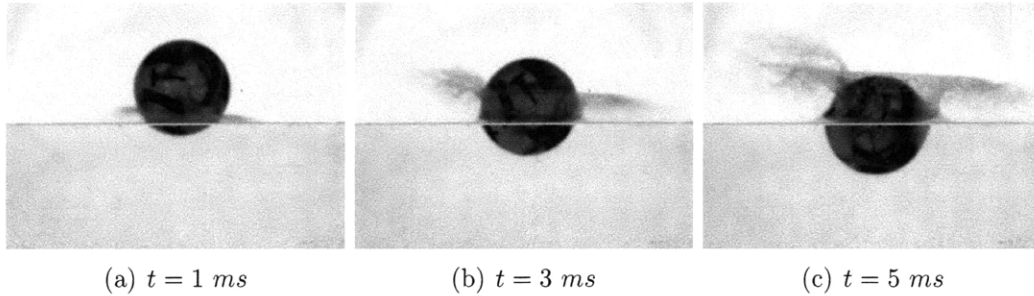


Figure 4-4: Splash asymmetry is already beginning to form due to spin 1 ms after impact (a); the splash continues to grow in (b) and (c), leading to an asymmetric splash crown and dome. Sequence of images taken $\Delta t = 2\text{ ms}$ apart, for a clockwise spinning sphere with initial impact parameters: $S = 2.25$ and $Fr = 7.0$.

faster on the left-side of the sphere, which is rotating out of the water, than the jet on the right-side of the sphere. This is more evident in higher spin rate cases (figure 4-4).

As the splash curtain develops further, the left-to-right asymmetries persist (figure 4-3(a-d)) and are most evident when the curtain ceases to grow radially and starts its inward collapse. At this point (figure 4-3(e-h)) the splash curtain appears to collapse earlier on the left side of the crown. The asymmetry of the splash dome is further exaggerated, as spin rate increases, and no outward splash is formed on the left side of the cavity for spin parameters above a critical value of $S \approx 1.0$.

A clear line of bubbles can be seen ejecting out the right side of the cavity after surface closure and prior to deep closure (pinch-off). These bubbles persist for several frames and do not appear to have an effect on the overall cavity behavior (figure 4-5). Upon close investigation it becomes clear that these bubbles are generated by a thin wedge of fluid which has traveled from left to right inside of the cavity and has impacted the cavity wall, thus forcing air out along the line of impact. From the side view, the presence of a wedge is indicated by a dark, diagonal line rooted near the free surface on the left side of the cavity and extending down to the right inside of the cavity; this line is the top of the fluid wedge (figure 4-5(a)).

The fluid wedge formation and bubble ejection are not persistent across all spin parameters. Figure 4-6 shows images taken at four distinct impact spin parameters, $S_o = \{0.3, 0.75, 1.1, 1.4\}$. The top two image rows are synchronized in time and

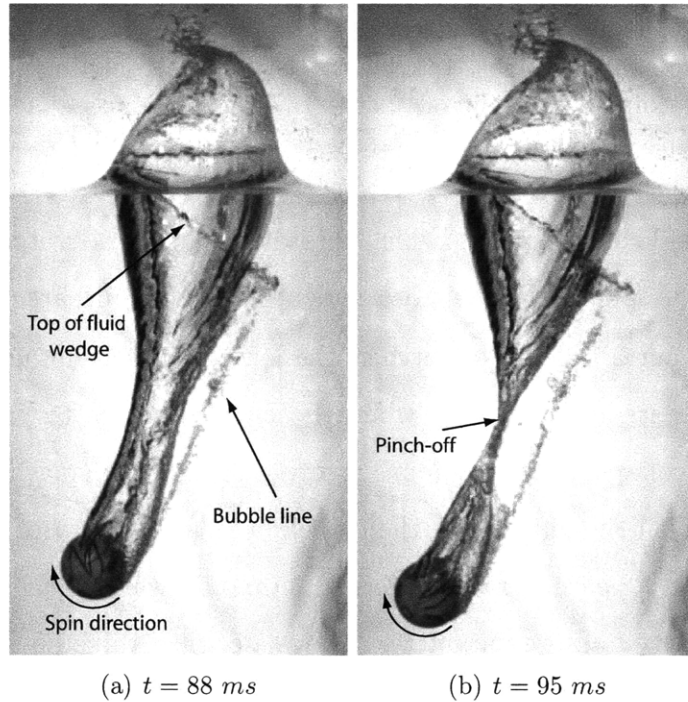


Figure 4-5: Two images taken at $t = 88 \text{ ms}$ (a) and $t = 95 \text{ ms}$ (b) after impact respectively, for initial impact parameters: $S = 0.75$ and $Fr = 7.5$. In figure (a) the top of the fluid wedge can be seen through the cavity as a grey line descending from the upper-left free surface to the lower right. A line of bubbles is ejected out of the right side of the cavity. Image (b) is captured at the moment of pinch-off (deep closure); after pinch-off two separate air cavities form.

illustrate how the wedge formation varies from low to high spin parameters. Looking into the cavity from above the top of the sphere is moving to the right and a small triangular wedge of fluid can be seen growing into the cavity. As the sphere spins it carries fluid, drawn from the cavity walls, along its equator into the cavity. The extruded fluid resembles a thin wedge, or sheet, that is anchored, at the top, on the left side of the cavity and extends down the length of the cavity attaching, at the lower end, to the sphere surface. For the lowest spin parameter presented ($S_o = 0.30$, figure 4-6(a)), the wedge formation is weak and does not fully extend across the cavity as it does in higher spin cases. In cases where spin parameters are less than $S_o \approx 0.30$ a distinct wedge of fluid is not formed; however, for all spin rates, images taken from the top reveal that the fluid is clearly drawn across the cavity in contact with the sphere, thus satisfying the no-slip condition.

At a later instant in time ($t = 99 \text{ ms}$ after impact) the side views of the cavity reveal greater splash dome asymmetries with increasing spin parameter. The increase in spin causes the wedge to form earlier and travel at a faster velocity across the cavity. The progression of the fluid wedge from inception to the time at which the top of the wedge impacts the far cavity wall, is illustrated in figure 4-7 for the case $S = 1.1$. The first image in this ‘birds-eye’ sequence shows vertical striations on the left wall of the cavity, which continue to grow into the cavity to form the wedge as the sphere descends. Even the early splash crown and air cavity opening, at $t = 10 \text{ ms}$, are slightly asymmetric. The shape of the cavity cross-section eventually evolves into a cardioid as the wedge extends across the cavity (figure 4-7(d)). At the higher spin rates the volume of fluid pulled from the left wall of the cavity increases, detracting from growth of the splash crown and affecting the cross-sectional shape of the cavity (figure 4-8). The splash crown growth and collapse are increasingly asymmetric at higher spin rates. For sufficiently high spin rates, no outward splash occurs on the left side of the cavity; this behavior is linked to the dynamic wetting angle and pinned contact line on the sphere as it both translates and rotates, and is the subject of ongoing investigation.

Just moments after impact, as the sphere continues to descend through the fluid,

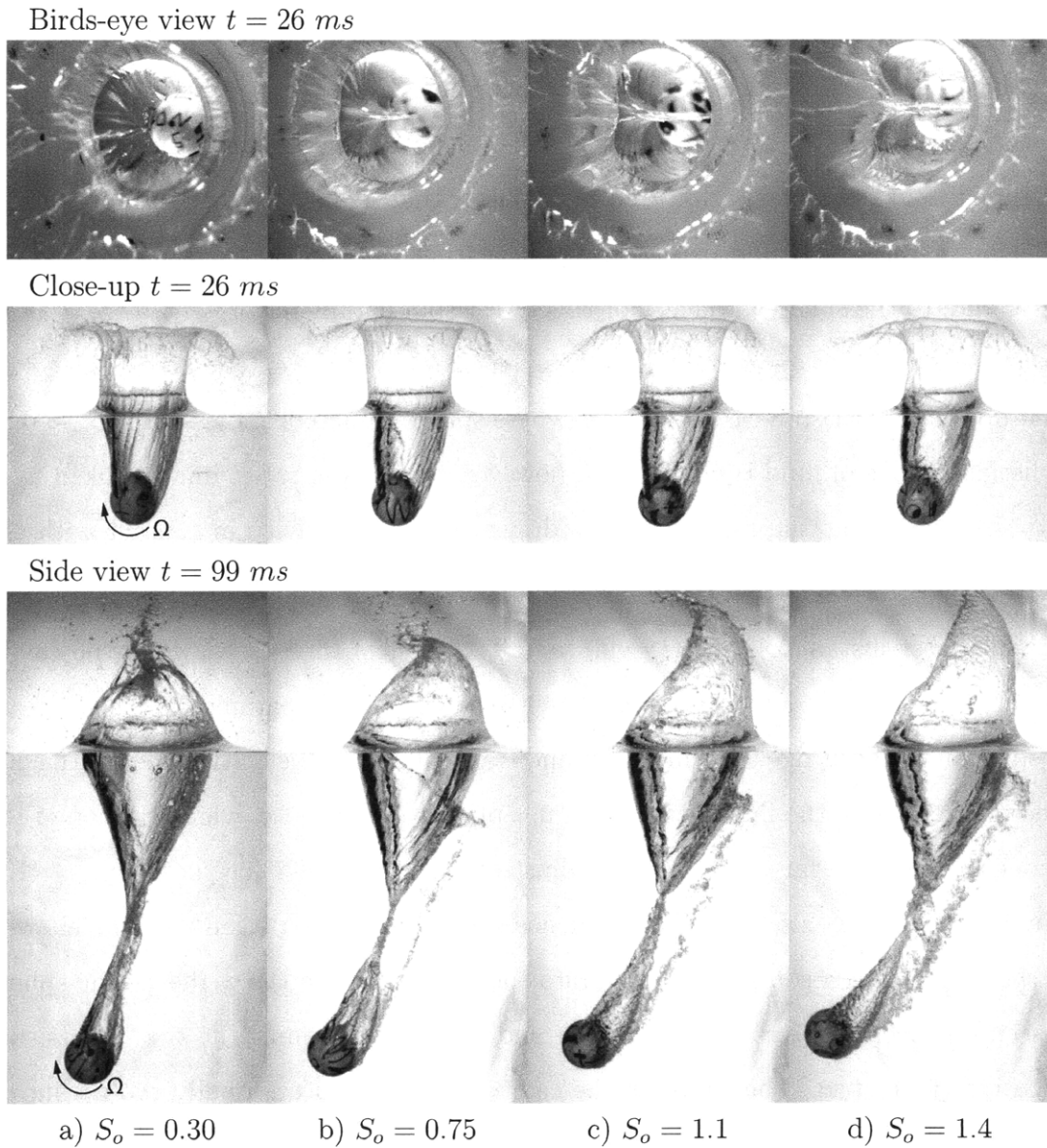


Figure 4-6: Four water entry cases with increasing spin parameter (left to right). The ‘birds-eye’ view (off-axis viewed from above) images in the top row are captured in synch with the images in the middle row; these images are taken at $t = 26 \text{ ms}$ after impact. The bottom row captures the cavity at $t = 99 \text{ ms}$ after impact, near the moment of pinch-off, showing the extent of the wedge formation for the four cases and pinch-off behavior. Increased spin rate affects both the shape of the cavity cross section and the overall splash symmetry. The spheres are spinning clockwise in the side views and the top of the sphere is moving left to right in the ‘bird’s-eye’ view, drawing fluid across the cavity in the same direction. Froude number is $Fr = 7.3 \pm 0.2$ for all cases presented.

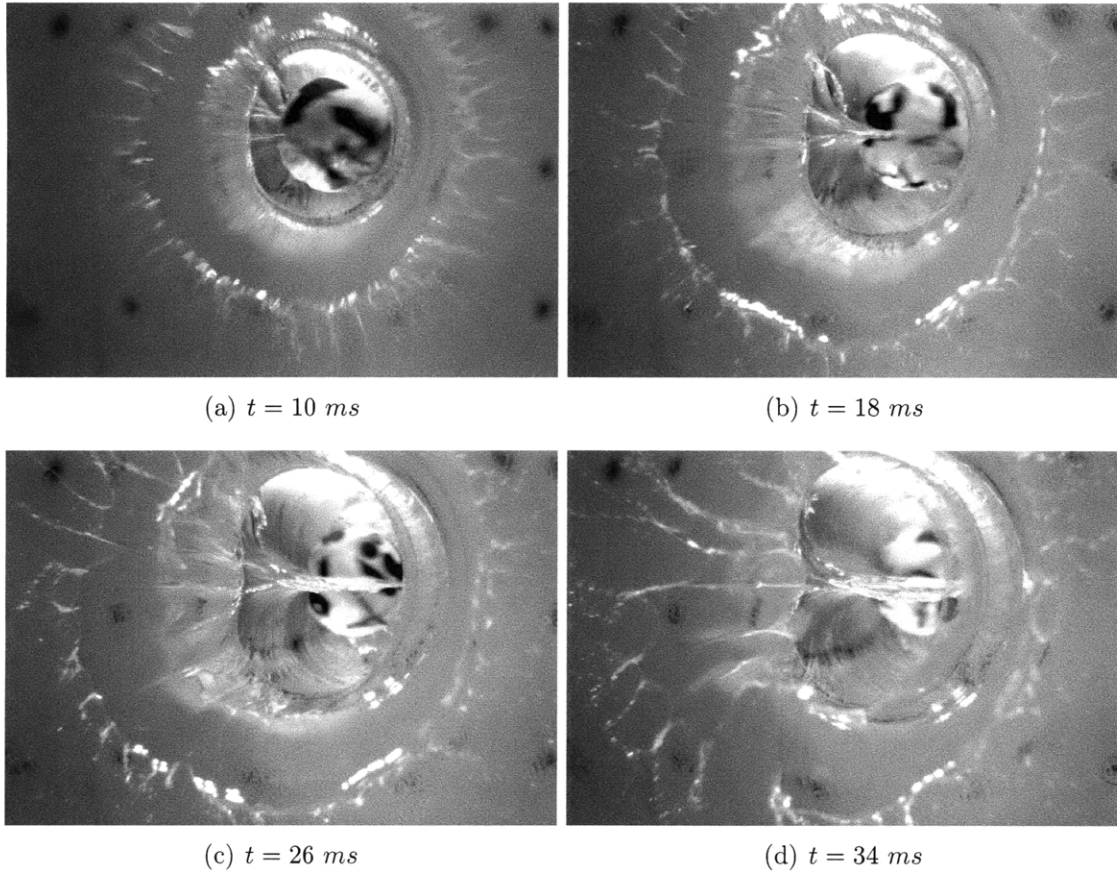


Figure 4-7: A ‘birds-eye’ view of a spinning sphere impacting the water surface at a downward speed of 5.45 m/s ($Fr = 7.3$). The top of the sphere moves to the right with spin parameter $S_o = 1.1$. Images are taken 8 ms apart. The rotation of the sphere draws fluid in from the left wall of the cavity (a) towards the right, forming a wedge. The wedge increases in size as water continues to be brought in from the left (18 ms) (b), and thins along the equator of the sphere forming a sheet of water (26 ms) (c), which eventually impacts the right hand side of the cavity (34 ms) in (d).

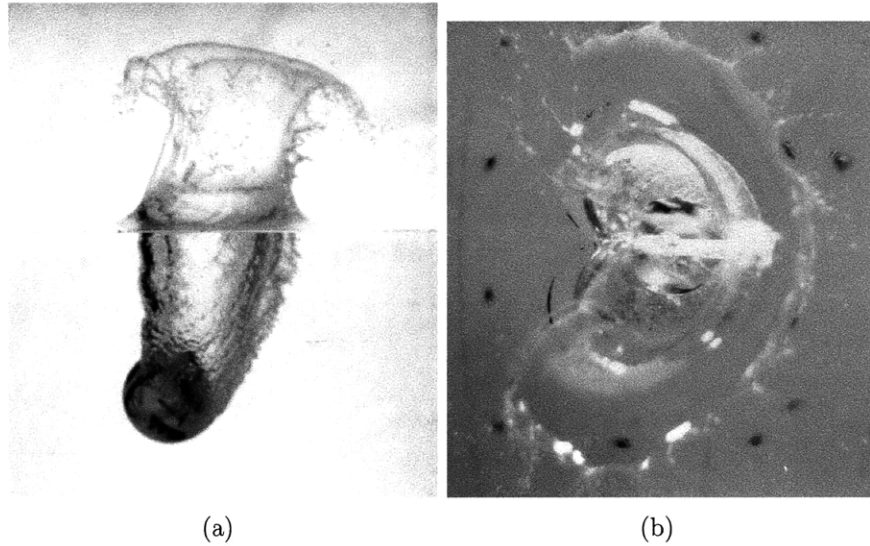


Figure 4-8: Side and top view for a high spin parameter case, $S_o = 2.25$, for $Fr = 7.0$, taken 26 ms after impact. The synched images show that the wedge has already crossed the cavity impacting the opposite cavity wall ejecting a line of bubbles on the right hand side of figure (a). Figure (a) also shows the asymmetry of the splash curtain at this early stage of impact. Figure (b) from above shows a distinct cardioid shaped cavity and shows the wedge bisecting the cavity into two distinct halves. The spin parameter is sufficient enough to cause no splash to occur on the left hand side of the splash curtain as witnessed in figure (b).

the spinning motion forces an already wetted section of the sphere to move upward, dragging fluid along the surface of the sphere and into the cavity. Due to the rotational forces the fluid is drawn to the equatorial region. Assuming no-slip, the time the sphere takes to turn one half of a full rotation, or π radians, should be coincident with the time at which the wedge first impacts the cavity wall, such that $t_\pi = \pi/\Omega_o$. During the time t_π , the sphere will have traveled some number of diameters, αd , below the free surface. Assuming that the sphere's forward velocity changes only minimally in this short time, then $\alpha d = V_o t_\pi$, such that

$$\alpha = \frac{V_o \pi}{\Omega_o d} = \frac{\pi}{2S_o}. \quad (4.1)$$

If the sphere is located at some depth, y_w , when the wedge impacts the wall then $\alpha = y_w/d$.

Plotting y_w/d as a function of $V_o \pi / \Omega_o d$, reveals a linear relationship (figure 4-9(a)). However, the slope of the data is not equal to -1 as expected from equation 4.1. Instead the slope of the data is closer to -1.3, indicating that the depth of the sphere at the moment of wedge impact, y_w is over-estimated. y_w is determined by looking closely at the video sequences taken from the side view (camera #2), and choosing the frame at which the bubbles first eject from the cavity near the sphere. There is a slight lag between the time that the leading edge of the wetted surface reaches the far wall and the time when a sufficient mass of fluid from the wedge hits the wall, causing air to eject from the cavity, which leads to an over estimation of y_w . For very low spin rates relative to impact velocity, it is possible that the wedge will not even reach the opposite side of the cavity before pinch-off, which is the case for data shown at $Fr = 7.3$ and $S \leq 0.3$.

Since the ratio of spin rate to downward velocity strongly affects the wedge formation, the top of the fluid wedge forms a shallower angle to the free surface as spin rate increases; the top of the fluid wedge is illustrated clearly in figure 4-5(a). The leading, top corner of the wedge traverses across the cavity at approximately 60% of the tangential velocity, $\Omega_o r$, of the sphere. As the cavity grows radially outward and

then begins collapsing, the distance the wedge must travel across the cavity grows and shrinks. It appears that the wedge is traversing the cavity at a nearly constant rate, however, the oscillation of the cavity wall makes the relative velocity between the wedge and opposing wall non-uniform. For cases where $S \gg 1$ the wedge impacts the side of the cavity early and violently, typically causing a line of bubbles, almost the length of the entire cavity, to eject from the cavity at nearly the same moment in time, not just one particular impact site (figure 4-8). For lower spin parameters the initial wedge impact zone is typically near the top of the sphere, at the bottom of the cavity, and progresses up the cavity wall towards the free surface.

As a result of the no-slip condition at the solid boundary, the fluid velocity at the sphere surface must match the sphere surface normal and tangential velocities, and thus fluid is dragged along the surface of the sphere as it rotates. Frictional, viscous forces on the surface of the sphere act to reduce the spin rate of the spheres along the trajectory by causing a viscous torque that opposes rotation. Figure 4-9(b) plots the spin rate, $\Omega(t)$, as a function of time, for four cases, normalized by the spin rate at impact. Ultimately, if allowed to travel in an infinite viscous fluid, the spheres would cease to spin due to the viscous torque opposing the rotation of the sphere. The rate of decay appears to have a dependency on spin parameter, increasing with increasing initial spin parameter, S_o .

Based on figure 4-9(b), it would be expected that the time that it would take a sphere to cease spinning, $t|_{\Omega(t)=0}$, would decrease with increasing initial spin parameters. Figure 4-9(c) shows $t|_{\Omega(t)=0}$, given the linear decay rates extracted from figure 4-9(b), as a function of initial spin parameter, S_o ; this spin relaxation time is found by extrapolating the lines in figure 4-9(b) to the zero-crossing point on the time axis. Plotted as a function of impact spin parameter, the data reveal an asymptote beyond $S_o \approx 0.5$, where the relaxation time tends towards a value of $t|_{\Omega(t)=0} \approx 0.3 \pm 0.1$ seconds.

The decrease in relaxation time, or increase in spin decay rate, as a function of increasing spin parameter is not wholly unexpected. As the spin parameter increases, so does the relative velocity on the surface of the sphere on the side where the tangen-

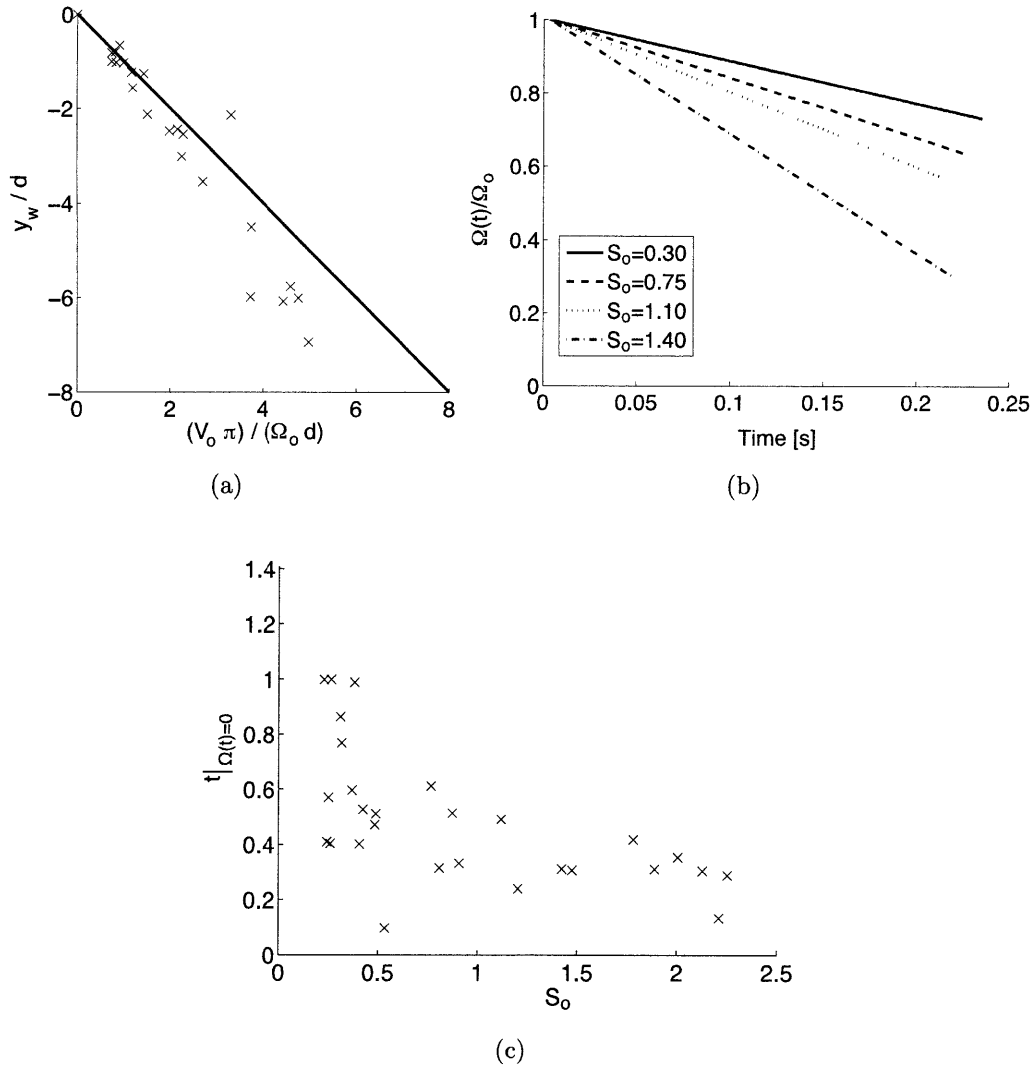


Figure 4-9: (a) The normalized depth of the sphere at which the wedge first impacts the opposite cavity wall as a function of the dimensionless parameter $V_o \pi / \Omega_o d$. Symbols are for experimental data, and solid line represents theoretical line with slope -1, from equation 4.1. (b) The decay of spin rate, normalized by the impact spin rate, as a function of time for the four spinning cases from the standard billiard balls at $Fr = 7.3$. The highest spin rates see the largest reduction of spin in time. (c) The relaxation time, at which the spin rate would decay to zero, is found by extrapolating the data from (b) down to the point at which the line crosses the horizontal axis.

tial velocity due to rotation is additive with the sphere's forward motion. This acts to trip the boundary layer sooner on the side of the sphere with the highest relative velocity, thus transitioning it to a turbulent regime with higher viscous boundary layer drag. This increased viscous drag leads to a higher viscous torque that opposes the rotation and acts to slow the sphere at a faster rate than the spheres with a slower initial spin rate.

4.3.3 Sphere trajectory

The most obvious and anticipated change in behavior of the spinning sphere, compared to the non-spinning case, is the curvature in its trajectory. The lift force induced by the rotating motion, coupled with forward velocity, moves the sphere along a curved path. Sphere trajectories for five different spin parameters, $S_o = \{0, 0.3, 0.75, 1.1, 1.4\}$, are plotted in figure 4-10, for one impact velocity ($V_0 = 5.6 \pm 0.4$ m/s); only position data after impact are presented. The x and y positions are normalized by the diameter of the sphere, d , and the free surface corresponds to a value of $y/d = 0$.

The zero spin case shows a straight descent until after pinch-off. In figure 4-10, below $y/d \approx -7$, the sphere moves to the left; all non-spinning spheres tended to move away from their vertical trajectories at some time after pinch-off. This is most likely due to vortex induced forces. Data in Govardhan & Williamson [15] indicates that tethered spheres, without spin, tend to present a sinusoidally oscillating motion in the axial direction due to vortices being shed in the wake. Before pinch-off, the cavity attached to the sphere retards classical vortex shedding from the sphere; thus it is only after pinch-off that the effects of vortex shedding would become noticeable.

The lift force significantly increases with spin, in the range of spin rates investigated, and results in greater curvature of the sphere trajectory (figure 4-10). Path curvature is evident for all cases, indicating positive lifting force even at lower spin parameters (e.g. $S = 0.30$). If spin parameter is held constant but Froude number increased, for a constant diameter sphere, the trajectories, x/d versus y/d , are very similar for each increasing Froude number (not shown). Differences in trajectories for

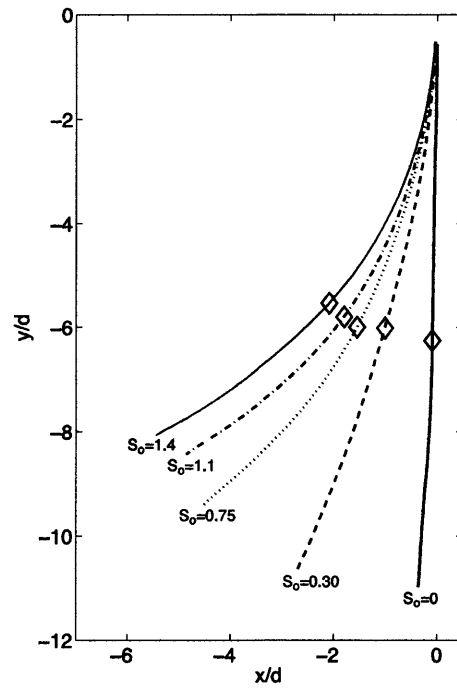


Figure 4-10: Five different trajectories of a billiard ball impact with the free surface. Each trajectory is marked by its corresponding spin parameter ($S_o = \Omega_o r / V_o$) at impact. Froude number at impact was $Fr = 7.3 \pm 0.2$. The diamond marks the location of the sphere when pinch-off occurs for each case.

increasing impact velocity are seen in the position as a function of time, as higher Froude number spheres reach deeper depths, and further horizontal excursions, earlier in time than cases with lower impact velocities. Since gravity plays a significant role in the motion of the sphere, the mass of the sphere should also be considered. Lower mass ratios should yield greater curvature assuming that the lift force results from increased circulation around the sphere. The mass ratio of the billiard ball used here is quite high, $m^* = 1.74$, yet the curvature is still significant.

For the same impact parameters, S_o and Fr , lower mass ratios experience greater lateral excursion due to lift. The force of lift is expected to be similar for a given diameter, velocity and spin rate, but as the sphere travels along a curved trajectory the force of gravity tends to stretch the trajectory downwards and thwarts lateral movement; the gravitational force is greater for increasing body mass. Mass effects are considered using three different spheres, with constant diameter but varying mass ratios. Figure 4-11 shows the trajectories, x/d versus y/d , at $Fr = 6.7$ and $S_o = 0.65$, for the three different types of spheres. The lighter spheres (acrylic) tend to have more curvature in their trajectories than the heavier spheres (ceramic and steel). After the sphere leaves the camera's field of view, the acrylic sphere moves almost exclusively in a horizontal direction, whereas the heaviest spheres always have some downward motion. For low mass ratios, m^* , inertial forces are diminished compared to hydrodynamic forces, and added mass and lift forces become more significant. For m^* near unity, e.g. acrylic spheres, lift force has a considerable effect on the sphere's trajectory and velocity in the horizontal direction. For high m^* , e.g. steel spheres, the inertial forces dominate and spin has little effect on the overall trajectory of the sphere.

Video images from the 'birds-eye' view and the side view for the acrylic, ceramic, and steel spheres, captured at $t = 21 \text{ ms}$ after impact for $Fr = 6.7$ and $S_o = 0.65$, are shown in figure 4-12. These images were obtained just prior to the time that the top two rows of images were acquired in figure 4-6. The top-view images in figure 4-12(a-c) show a distinct difference in cavity cross-section for the three materials despite the identical impact parameters. No outward splash is generated on the left side of

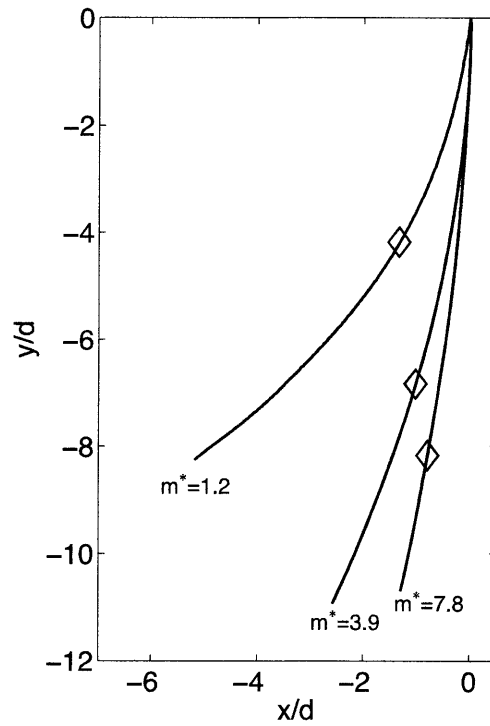


Figure 4-11: Trajectories for three 2.54 cm spheres with increasing mass ratios: acrylic ($m^* = 1.2$), ceramic ($m^* = 3.9$), and steel ($m^* = 7.8$). The three spheres impact the water at the same Froude number ($Fr = 6.7$) and the same spin parameter ($S_o = 0.65$). The diamond markers indicate the depth of cavity pinch-off.

the cavity for the steel spheres resulting in a distinct cardioid cross-sectional cavity shape, compared to the rounder cross section of the acrylic and ceramic spheres. The spheres all have the same surface roughness, $k = 2.4 \mu m$, thus we should expect a similar frictional force to drag the fluid around as the sphere rotates. However, since wedge formation is dependent on the ratio of tangential velocity to downward velocity (figure 4-9(a)), the qualitative difference in wedge formation makes sense. After impact, the acrylic spheres experience a more rapid deceleration compared to the ceramic and steel spheres, since inertial effects are not as large, and thus have lower instantaneous velocities compared to the ceramic and steel spheres. The higher deceleration of the acrylic spheres is seen in the side view images in figure 4-12(d-f); the steel sphere is deeper in the water than the acrylic sphere at the same time after impact.

The heavier the sphere, the higher its kinetic energy is upon impact. The energy transferred to the fluid upon impact affects the splash and cavity formation. In the acrylic spheres a clean, almost vertical splash is formed; this is similar for the ceramic spheres, but in figure 4-12(e) the splash crown is just beginning to collapse. However, for the steel sphere the splash has already begun to dome over. The bubble line, resulting from the wedge impacting the far wall of the cavity, can also be seen on the right side of the cavity for the steel sphere in figure 4-12(f). No outward splash is seen on the left side of the cavity for the steel spheres in either the ‘birds-eye’ or side views resulting in a distinct cardioid cross-sectional cavity shape.

The diamond markers in figure 4-11 indicate that the depth of the sphere at the moment of pinch-off increases dramatically as mass ratio increases. The depth of pinch-off for the steel sphere is deeper than that of the ceramic and acrylic spheres. These trajectory plots do not reveal information about the velocity of the spheres’ descent, but qualitative velocity differences are seen in the images in figure 4-12. As a result of the differences in velocities after impact, the time at which each sphere reaches a certain depth, e.g. pinch-off, changes dramatically between materials. Thus, to further investigate the effect of mass on pinch-off, or cavity collapse, looking at the time to pinch-off is warranted.

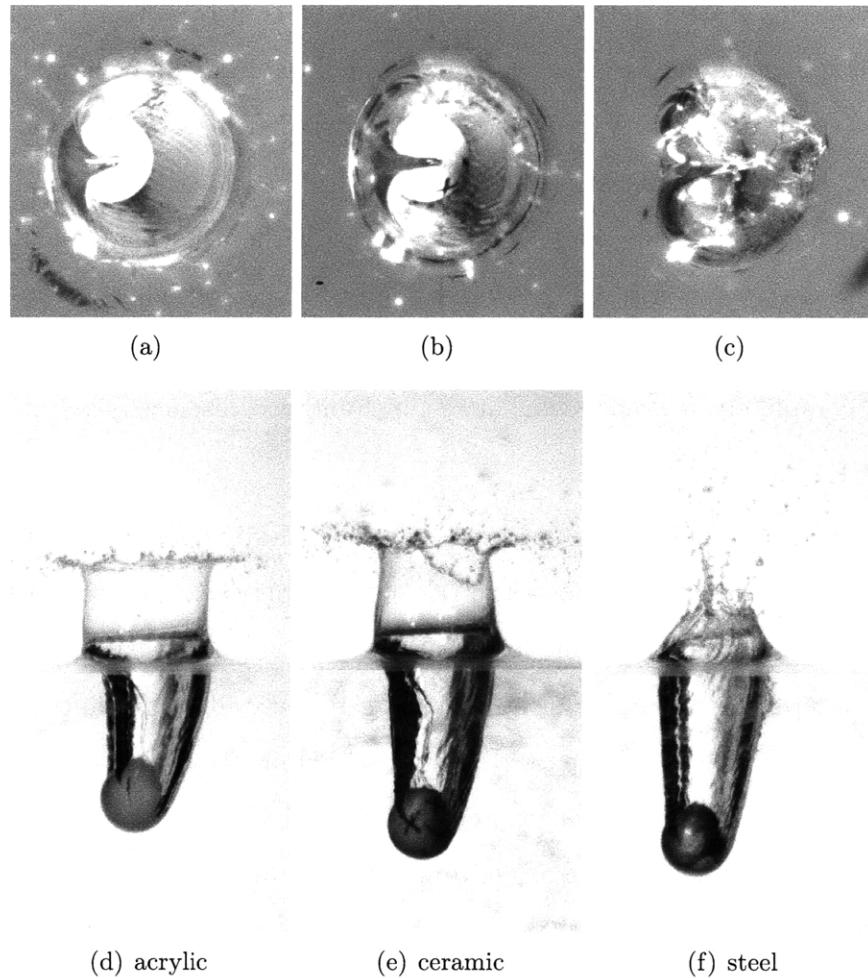


Figure 4-12: High speed images of the cavity formation for three different 2.54 cm spheres with increasing mass ratio: acrylic ($m^* = 1.2$), ceramic ($m^* = 3.9$), and steel ($m^* = 7.8$). The spheres all impact the water at the same Froude number ($Fr = 6.7$) and the same spin parameter ($S_o = 0.65$). Images of the 'birds-eye' view in the top row (a-c) correspond to images of the side view in the bottom row (d-f) and are captured at the same instant in time ($t = 21\text{ ms}$). In images (a-c) the equatorial line of the spheres is moving to the right and the spheres are rotating in a clockwise direction in images (d-f).

4.3.4 Cavity pinch-off

Cavity deep seal is initiated by an imbalance in pressure inside and outside of the sub-surface cavity. After surface closure the cavity continues to expand for some time as the sphere descends. Since air no longer flows into the cavity, the pressure inside must decrease if cavity expansion is considered to be an adiabatic isentropic process [19]. Hydrostatic pressure outside the cavity grows with depth and the radial expansion of the cavity slows, and eventually stops, without new energy added to the system. The cavity starts to collapse and finally pinches off when it can no longer resist external pressures. The moment of pinch-off is taken when the subsurface air cavity has completely necked down; after pinch-off two distinct, separated cavities form.

To find a scaling relationship for deep seal, the non-dimensional time to deep seal is considered. Figure 4-13(a) shows the relationship between non-dimensional time, $t^* = V_o t/d$ versus Froude number, and that data for all mass ratios, diameters and spin rates collapse onto one line. The slope of the linear fit to the data reveals that $t^* = 5/4 Fr$, over the range of mass ratios tested herein. However, in this figure the initial impact velocity dominates for both the x- and y-axes, making t^* a less than ideal scaling parameter. [13] use a non-dimensional time scaling for deep seal using small spherical projectiles under varied atmospheric conditions, at Froude numbers much higher than those considered here. [14] propose a single value of dimensionless time, $\tau = t\sqrt{g/r}$, for which deep seal reduces to a single number for all impact speeds and disk diameters. Data obtained herein reveals that $\tau = 1.726 \pm 0.0688$ ($\bar{x} \pm \sigma$; $n = 118$ trials), over the range of impact velocities and sphere diameters tested. This is similar to $\tau = 1.74$ for spheres as reported by [13], and can be contrasted with $\tau = 2.285 \pm 0.0653$ ($n = 47$ trials) for disks as reported by [14].

The location of the sphere at the time of pinch-off is indicated in figure 4-10 by the diamond-shaped marker. The sphere's location at pinch-off is clearly affected by initial velocity and mass, but not spin. For constant Froude numbers, but increasing spin parameters, the depth, y/d , of pinch-off increases only slightly, and the distance

traveled by the sphere along its trajectory before pinch-off remains nearly constant. The distance traveled along the trajectory is the arc-length-to-pinch-off distance, $\bar{s}/d = \sum ds/d$, where ds is an elemental length along the trajectory path, s .

For higher impact velocities and mass ratios, both the depth of pinch-off and arc-length-to-pinch-off distances increase due to larger inertial effects and greater energy available to feed cavity growth. Both \bar{s}/d and y/d are plotted as functions of Froude number in figure 4-13(b) and 4-13(c). The data plotted in these figures also include, in addition to the standard billiard ball data, data obtained from three different one-inch ($d = 0.025\text{ m}$) spheres: acrylic ($m^* = 1.2$), ceramic ($m^* = 3.9$) and steel ($m^* = 7.8$). Data plotted includes *all* spin rate cases for each Froude number considered, including the non-spinning cases, revealing a minimal effect of spin on the deep seal phenomenon. While each specific mass ratio reveals a linear trend with Froude number, the data show that mass ratio is an important parameter affecting the depth and arc length at which pinch off occurs. Taking into consideration the mass ratio effect, the normalized depth of pinch off collapses neatly as a function of Froude number times the square root of the mass ratio (figure 4-13(d)).

4.3.5 Lift and drag forces on the spinning sphere

Force model

Lift and drag forces on the standard billiard balls are calculated using the position data acquired from the video sequences. The coefficients of lift (C_L) and drag (C_D) are found by normalizing the forces by $\frac{1}{2}\rho V_o^2 \pi r^2$. A force balance on the sphere is written in vector form based on the free body diagram in figure 4-14(a). The hydrodynamic forces (\vec{F}_H) acting on the sphere are balanced by gravitational forces, added mass forces and surface tension:

$$\vec{F}_H = m\vec{g} + (m + m_a)\vec{a} - \vec{F}_B - \vec{F}_\sigma \quad (4.2)$$

where m is the mass of the sphere, \vec{g} is gravity, m_a is the sphere added mass, \vec{a} is the acceleration of the sphere, and \vec{F}_B is the buoyancy force. The force due to

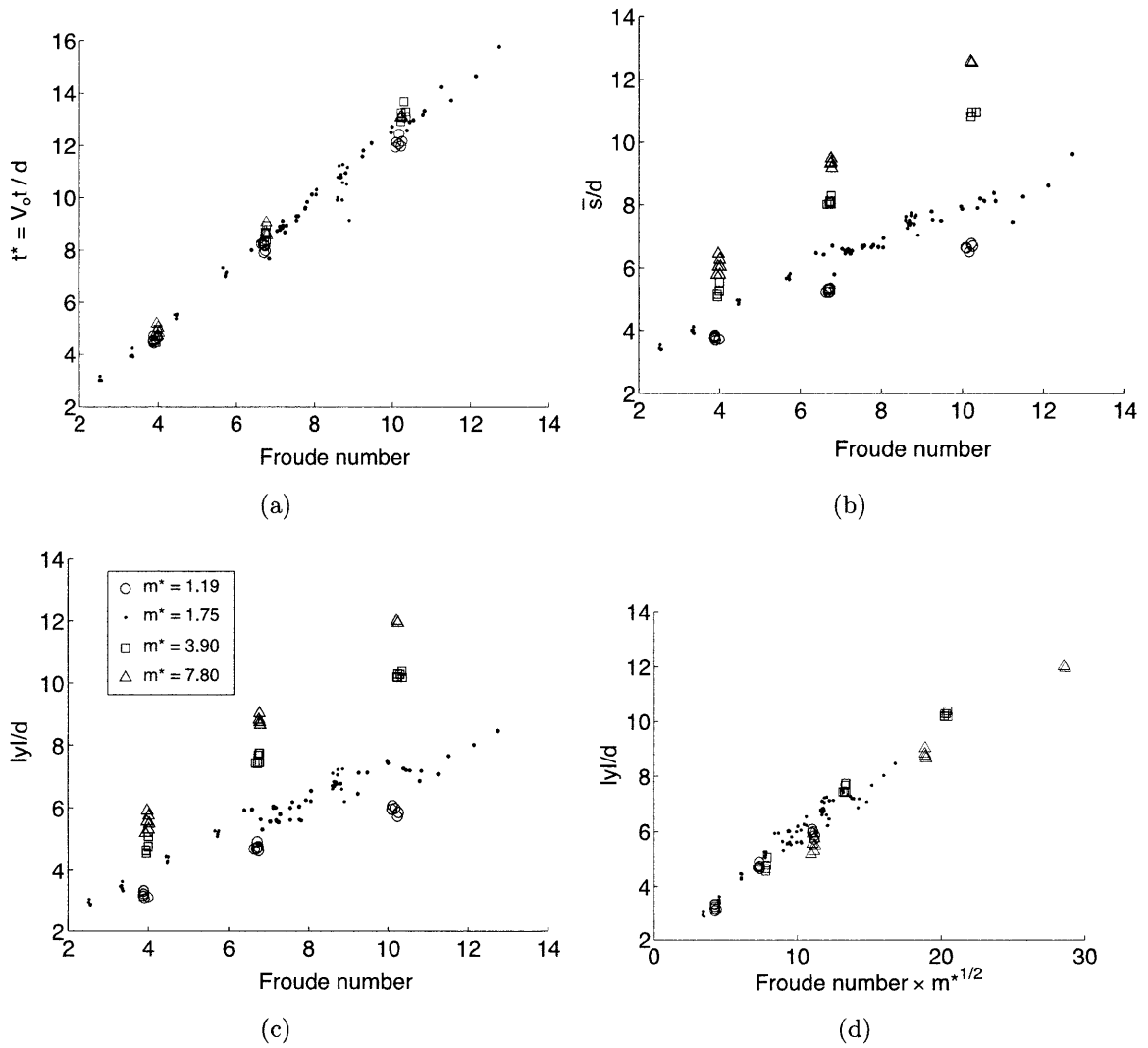


Figure 4-13: (a) Non-dimensional time to pinch-off plotted against Froude number and (b) normalized arc-length-to-pinch-off as a function of Froude number; (c) normalized depth to pinch-off as a function of Froude number and (d) normalized depth to pinch-off as a function of Froude number and mass ratio. Data includes tests from standard billiard balls (\cdot), 2.54 cm acrylic spheres (\circ), 2.54 cm ceramic spheres (\square), and 2.54 cm steel spheres (\triangle). Each material has a different mass ratio; m^* is indicated in the legend for figure (a).

surface tension, \vec{F}_σ , can be neglected as it is less than 1% of the gravitational force for the standard billiard balls. The buoyancy force $\vec{F}_B = \rho g \forall \hat{j}$, where \forall is the sphere volume, and the added mass is found from $m_a = C_m \rho \forall$, where C_m is the added mass coefficient. For this study C_m was chosen to be constant over the entire run, $C_m = 0.5$. C_m likely changes over the course of the run, depending on how much of the sphere is submerged in water. Running the force model with a constant drag coefficient ($C_D = 0.4$) for the non-spinning case, shows that after the sphere is fully submerged, added mass coefficient could vary from as low as 0.2, just after the cavity is formed, to as high 0.5, after pinch-off. Choosing an added mass coefficient $C_m = 0.25$, a 50% reduction in added mass, reduces the results for C_D and C_L by 8-10%, well within the error bounds of this study. For a mass ratio closer to unity ($m^* \approx 1$) the added mass term will play a larger role and the choice of C_m will be more critical. Force data is presented only for the standard billiard balls and assumes $C_m = 0.5$.

To determine the lift and drag components of the forces, equation 4.2 can be broken into cartesian vector components in the x and y directions

$$F_H \hat{i} + F_H \hat{j} = mg \hat{j} + (m + m_a)(\ddot{y} \hat{j} + \ddot{x} \hat{i}) - F_B \hat{j} \quad (4.3)$$

where \hat{i} and \hat{j} are unit vectors in x and y respectively. Rewriting equation 4.3 in the reference frame of the sphere makes determining lift and drag forces along the curved trajectory more straightforward. The unit vector tangent to the sphere trajectory, \hat{s} , is written in terms of the x and y components of instantaneous velocity, V_i ,

$$\hat{s} = \frac{\vec{V}_i}{|\vec{V}_i|} = \frac{V_x}{|\vec{V}|} \hat{i} + \frac{V_y}{|\vec{V}|} \hat{j}. \quad (4.4)$$

The unit normal vector, \hat{n} , is defined as the cross product of the unit tangent vector with the unit vector in the z direction, \hat{k} :

$$\hat{n} = \hat{s} \times \hat{k}. \quad (4.5)$$

The forces of lift (transverse), \vec{F}_L , and drag (in-line), \vec{F}_D , can be determined from

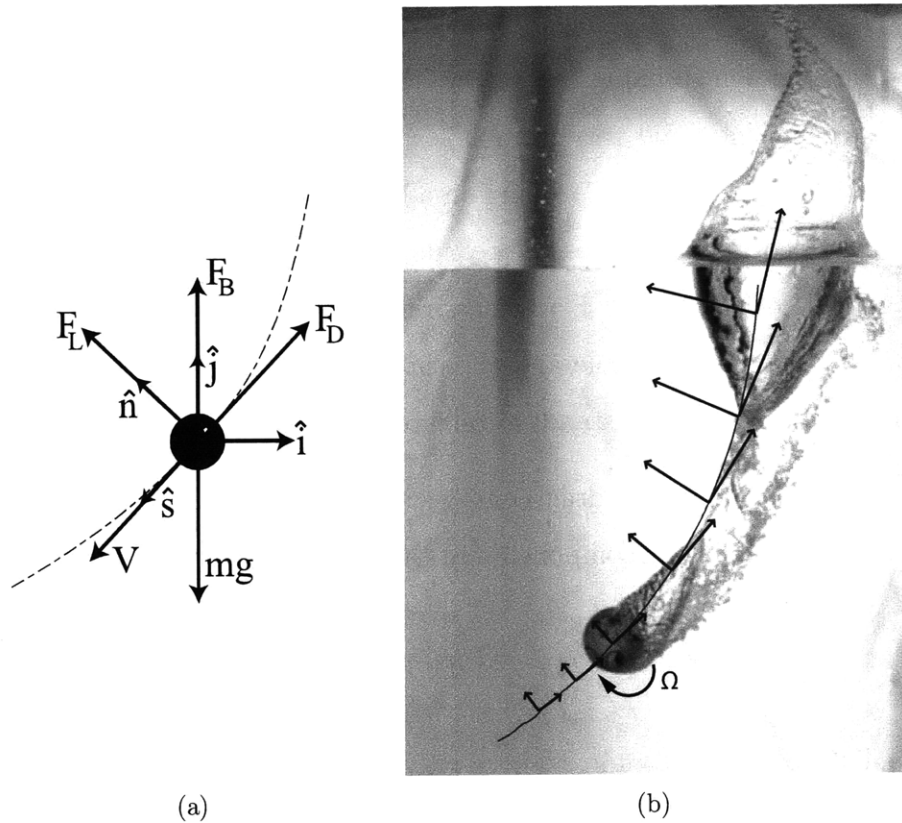


Figure 4-14: Free body diagram of the forces affecting the sphere after water entry is drawn in figure (a). The dashed curve represents the sphere's trajectory. Figure (b) illustrates the changing magnitude of the lift and drag force components in time along the trajectory superimposed on one image taken from the same video sequence, $t = 141 \text{ ms}$ after impact. The vector origins correspond to the location of the center of the sphere along the trajectory at the same time step when the forces were calculated. Impact parameters for this case are $S_o = 1.4$ and $Fr = 7.3$.

equation 4.2, in terms of unit vectors from equations 4.4 and 4.5 as

$$\vec{F}_L = (\vec{F}_H \cdot \hat{n})\hat{n} \quad (4.6)$$

and

$$\vec{F}_D = (\vec{F}_H \cdot \hat{s})\hat{s}, \quad (4.7)$$

respectively. Lift is considered positive in the $+\hat{n}$ direction and causes curvature to the left in the images presented herein (the sphere is spinning in a clockwise direction).

The acceleration of the sphere is necessary to determine the force of lift (\vec{F}_L) and drag (\vec{F}_D). Directly differentiating the raw data does not result in accurate acceleration data and presents significant scatter and error. Thus a polynomial curve is fit to both the x and y data. A 7th order polynomial fit was chosen for both the x - and y - position data; this was the lowest order to ensure convergence in acceleration for all cases. The R^2 values for the position fits are 0.99. The acceleration in the x - and y - directions is calculated from the second derivative of the polynomial fits to position. Similarly velocity is obtained by taking the first derivative of the polynomial fit. The x - and y - positions, velocities and accelerations are plotted in figure 4-15 as a function of time for the five cases considered here.

Forces acting on the sphere change along the sphere's trajectory with changing velocity and acceleration. The coefficients of lift (C_L) and drag (C_D) are found by normalizing the forces by $\frac{1}{2}\rho V_o^2 \pi r^2$. Figure 4-14(b) shows a sphere at time $t = 141 \text{ ms}$ after impact ($S_o = 1.4$, $Fr = 7.3$). The sphere's trajectory is indicated by the curved line through the cavity. Superimposed on this line are pairs of orthogonal vectors representing the lift (normal) and drag (inline) forces; the length of the vector arrows indicate the relative magnitude of the forces on the sphere when it was located at the origin of the force vector pairs. As the sphere descends through the fluid column the forces of lift and drag decrease. Figure 4-14(b) also illustrates the asymmetry of the cavity formation around the sphere trajectory, with greater growth in the negative \hat{n} direction than in the positive \hat{n} direction.

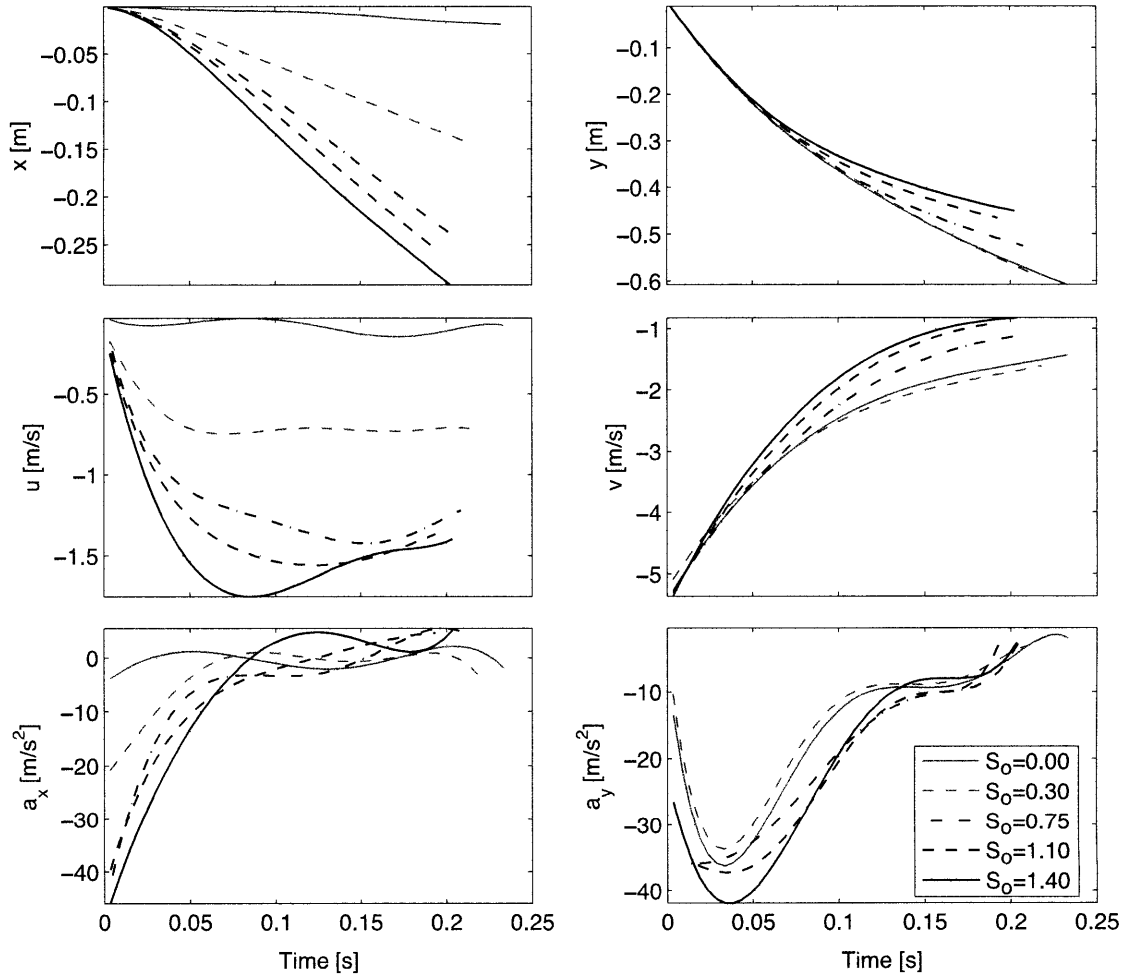
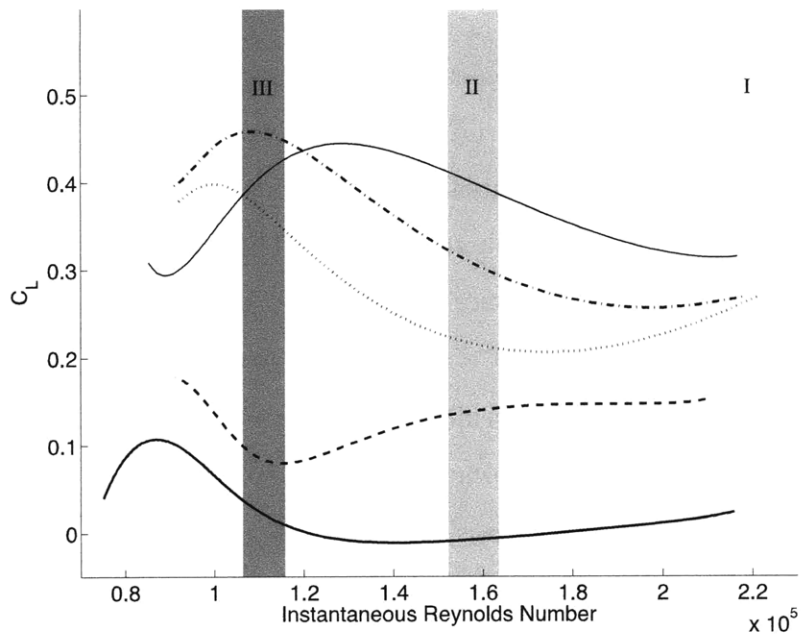
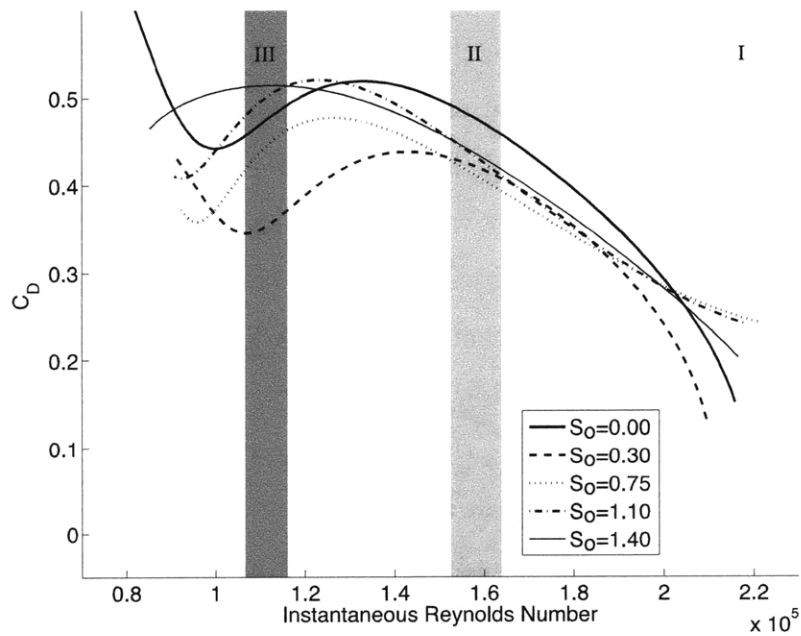


Figure 4-15: Position, velocity and acceleration in the x - and y -directions as a function of time, resulting from a 7th order polynomial fit to the raw position data for standard billiard balls with $Fr = 7.3$. Impact spin parameters are $S_o = \{0.0, 0.3, 0.75, 1.1, 1.4\}$; legend for a_y is valid for all plots.



(a)



(b)

Figure 4-16: Lift (a) and drag (b) coefficients determined using the force model as a function of instantaneous Reynolds number $R = V(t)d/\nu$. Impact conditions for the five cases are: $S_o = \{0.0, 0.3, 0.75, 1.1, 1.4\}$ for $Fr = 7.3 \pm 0.2$. The legend in figure (b) also corresponds with figure (a).

Forces as a function of Reynolds number

Calculated values for lift and drag coefficients are plotted in figure 4-16 as a function of instantaneous Reynolds number ($R = V_i d / \nu$), for the five cases presented in figure 4-6. The Reynolds number is greatest at the moment of impact and varies with instantaneous velocity along the sphere's descent. The impact region is identified by the Roman numeral I. Surface closure is marked by a vertical grey band (region II) around Reynolds number of $R \approx 1.6 \times 10^5$. The range of Reynolds numbers, at which the five cases reach pinch-off and form two distinct cavities, is marked by the second, darker vertical band (region III) around $R \approx 1.1 \times 10^5$.

For increasing spin rates, the overall lift coefficient increases with the circulation around the sphere. Looking at the two higher spin parameters, $S_o = 1.1$ and 1.4 , it appears that there may be a maximum possible amount of lift that can be gained by increasing spin; a plateau in lift coefficient is seen above $S \approx 1.5$ in the data for smooth spinning spheres reported by [21]. Over the course of the sphere's decent the lift coefficients rise to a maximum at or near the point of pinch-off, in similar fashion to the drag coefficient. Drag coefficients, just after impact, are on par with the measured drag coefficient for a fully wetted sphere in flows at comparable Reynolds numbers (see figure 4-18). In the absence of vortex shedding, while the cavity is still fully intact, it might be expected that the drag coefficient would be lower than the fully submerged sphere at similar Reynolds numbers. Choosing a lower coefficient of added mass, e.g. $C_m = 0.25$, reduces the overall drag coefficient to a value lower than published values for similarly rough, but fully submerged, spheres in the range of Reynolds numbers considered. The choice of added mass coefficient $C_m = 0.5$ could account for the drag coefficient after impact being near to that of a fully submerged sphere.

Forces as a function of spin parameter

To further investigate the effect of spin on the forces incurred by the sphere, the coefficients of lift and drag are plotted as functions of instantaneous spin parameter,

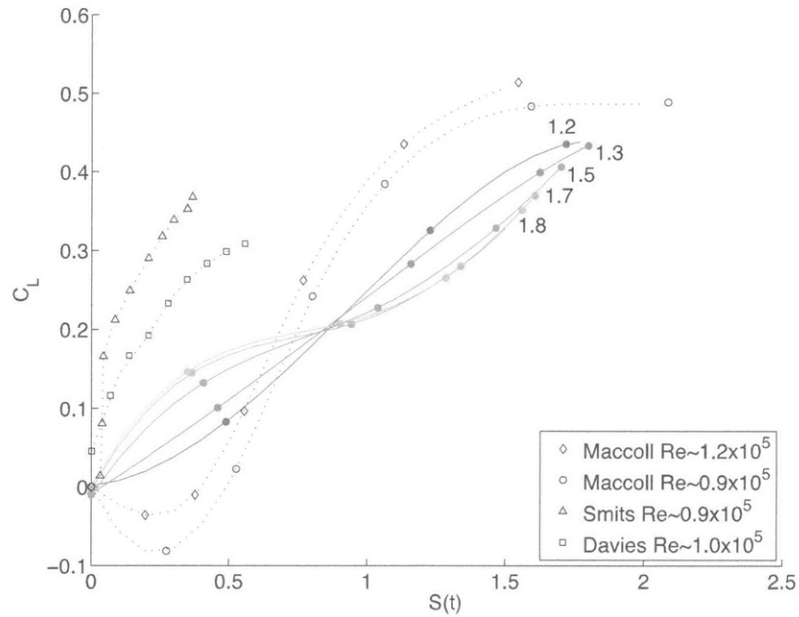


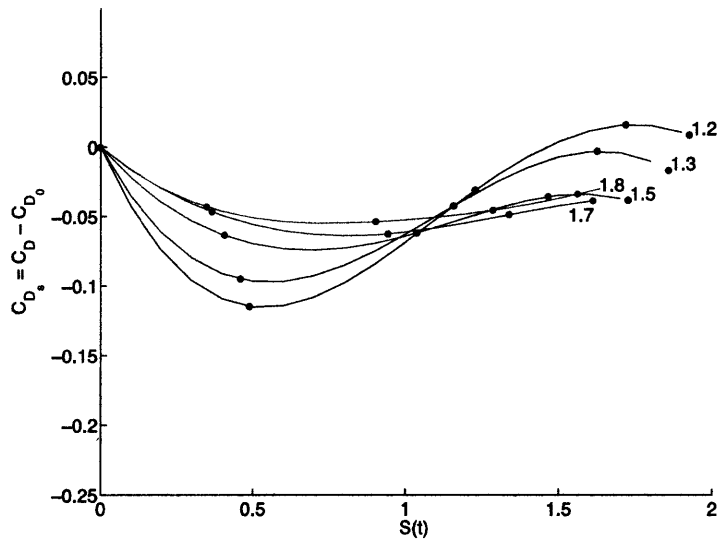
Figure 4-17: Coefficient of lift versus instantaneous spin parameter, $S(t)$. Data for the spinning sphere impacting the free surface is plotted for five instantaneous Reynolds numbers between $R = 1.2 \times 10^5$ and 1.8×10^5 . These Reynolds numbers are taken from cases with different initial spin parameters but the same impact velocity, and correspond to the instantaneous, and changing, Reynolds number of the sphere along the trajectory. The number at the right of each curve is the corresponding Reynolds number divided by 10^5 . For comparison, data for dimpled spheres from Smits and Smith (1994) and Davies (1949) are plotted along with data from Maccoll (1928) for smooth spheres.

$S(t)$, in figures 4-17 and 4-18 respectively. Figure 4-17 presents lift coefficient as a function of instantaneous spin parameter for five instantaneous Reynolds numbers, using data from figure 4-16(a). Data from smooth spheres measured by [21] and dimpled spheres (golf balls) measured by [37] and [9] are plotted for comparison.

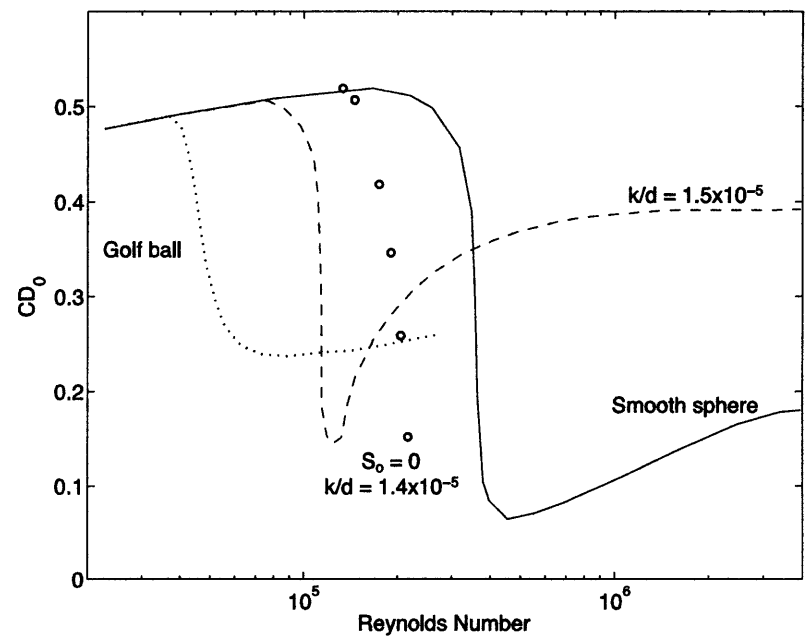
Data show that the lift coefficient increases to a local maximum value of $C_L \approx 0.46$ at spin parameter $S(t) = 1.8$ for Reynolds number $R(t) \approx 1.08 \times 10^5$; this instantaneous Reynolds number corresponds to the speed of the sphere near the time of pinch-off, but no obvious plateau has been reached. Data for higher instantaneous spin parameters were not obtainable for any given case, thus an overall maximum was not obtained. The trend in lift coefficient is similar at higher Reynolds numbers, but the maximum coefficient is diminished with increasing Reynolds number. Higher Reynolds number curves in figure 4-17 correspond to points along the trajectory where the cavity is still intact and growing. The curvature of the trajectories increases as the sphere continues along its path, indicating that the lift forces due to spin could be more dominant, compared to cavity effects, as the sphere and cavity growth slows.

Lift coefficients obtained here follow similar trends, as a function of instantaneous spin parameter, to those found by [21], however it is unclear whether this similarity continues above spin rate $S \approx 2.0$. In [21], negative lift coefficients were observed at very low spin parameters, below $S = 0.35$ to 0.45 . Negative lift was not witnessed in this study, nor in the golf ball studies done by other researchers, but was verified by [9] for very smooth spheres. [13] noted that the average measured drag coefficients of the projectiles in their study were independent of cavity shape. Data presented here indicate that changes in cavity shape due to spin do affect drag; however variable added mass forces should also be considered in future studies.

Drag coefficients as a function of spin rate are plotted in figure 4-18, for the same five instantaneous Reynolds numbers used in figure 4-17. The value for drag coefficient in the non-spinning case, C_{D_o} , is calculated at each instantaneous Reynolds number using the force model from section 4.3.5. C_{D_o} is subtracted from each curve in figure 4-18, such that each curve has zero drag at $S = 0$. Thus figure 4-18 closer represents the spin-induced drag forces on the sphere, C_{D_s} , without cavity effects.



(a)



(b)

Figure 4-18: Coefficient of drag versus instantaneous spin parameter at Reynolds numbers ranging from $1.2 \times 10^5 - 1.8 \times 10^5$. Figure (a) shows the contribution due to spin only (C_{D_s}); the numbers to the right of the data curves are instantaneous Reynolds number divided by 10^5 . Figure (b) plots the drag coefficient (C_{D_0}) for the zero-spin water entry case with identical impact velocity as the spinning cases (circles). Standard drag coefficient data for smooth, roughened and dimpled spheres taken from Blevins (1984) is plotted for comparison.

The total drag coefficient acting on the sphere is the sum of the zero-spin drag and the spin-induced drag: $C_D = C_{D_o} + C_{D_s}$. A negative C_{D_s} represents a reduction in drag coefficient due to spin. The effect of spin appears to decrease the drag coefficient over the course of a run compared to a non-spinning case, above an instantaneous Reynolds number $R \approx 1.2 \times 10^5$ and $S(t) \approx 1.5$.

Figure 4-18(b) presents the coefficient of drag calculated for the zero spin case, C_{D_o} at $S_o = 0$. Data are plotted along with standard drag curves for smooth and roughened spheres taken in flow tunnels taken from [8]. The cases investigated herein fall in the laminar-turbulent transition region, and figure 4-18(b) illustrates how the introduction of spin can easily tip the balance in favor of turbulent flow.

4.4 Conclusions

The effects of spin on the flight path of a sphere impacting into water are not ultimately surprising. However, high speed video reveals the formation of unique and elegant splash and cavity morphologies when spin is introduced. As the spin rate of the sphere is increased, for a constant impact speed, the sphere's trajectory exhibits greater curvature, in a similar fashion to curve-balls in sports like golf, cricket and baseball. The trajectories of higher mass projectiles are not as affected by spin as their lower mass counterparts. The bent cavity for the spinning case holds a similar, albeit curved, form compared to the non-spinning case, and the splash formation and collapse and the cavity pinch-off behaviors are fundamentally similar.

Unique to this problem, however, is the nature of the sub-surface air cavity, and the formation of a secondary fluid feature, namely the fluid wedge, that forms in the cavity. Since there is no slip between the sphere surface and the fluid, fluid is drawn along with the sphere, which is fully wetted after one half a rotation, and the wedge is extruded into the cavity as the sphere descends. Data show that the ratio of spin rate to downward velocity strongly affects the wedge formation. If allowed to travel in an infinite viscous fluid, the spheres would cease to spin due to the viscous torque opposing the rotation of the sphere. The rate of spin decay increases with

increasing spin parameter, up to about $S_o \approx 0.5$, after which the spin relaxation time appears to plateau. The effect of mass ratio on wedge formation is played out in the instantaneous downward speed of the sphere. Since the lighter spheres decelerate more rapidly than the heavier spheres, the instantaneous spin parameter for the light spheres is lower for the same impact velocity and the wedge formation is not as obvious.

Spin appears to have minimal effect on cavity pinch-off and collapse, compared to Froude number. The depth and arc-length to pinch-off do not scale well with Froude number when mass effects are considered, yet scale well with Froude number times the square root of the mass ratio. Dimensionless time does collapse the pinch-off data as a linear function of Froude number, for all mass ratios; data for non-spinning cases collapse in an identical fashion to the data for spinning cases.

Several distinct regimes can be identified within the range of spin parameters studied. First, at zero spin rates the traditional water impact behaviors are identified. Using a force balance equation, the drag coefficient is found to increase for decreasing instantaneous Reynolds number, along the trajectory of the sphere, up to the point of pinch-off where the sphere separates from the large cavity. The cavity and splash formation and collapse are symmetric in the absence of spin and the calculated lift coefficients are zero.

For very low spin parameters ($0 < S < 0.35$), where [21] notes negative lift coefficients, the spinning spheres studied here do not show negative lift, but instead tend to bend in the direction of positive lift, yielding the lowest calculated values for C_L . The drag coefficients calculated for the $S = 0.30$ case were also the lowest of all the spin parameter cases run. Already at this low range of spin parameter, asymmetric splash and cavity formation and collapse are notable. No distinct wedge formation grows into the cavity, but the visible striations associated with wedge formation are evident (figure 4-6a; top row). Close observations of the ‘birds-eye’ videos indicate that there is no-slip between the fluid and the sphere at any spin rate.

As spin parameter increases ($0.35 < S < 0.7$), the lift data from [21] transitions to positive and the data recorded herein show a local minimum in drag coefficients for

spin parameters between 0.5 and 0.6, yet lift coefficient shows a steady increase in this region. The asymmetry in cavity and splash formation and collapse is exaggerated with increasing spin parameter, and a fully formed fluid wedge traverses across the cavity. Despite the wedge formation the cavity is still relatively round in cross-section at lower spin parameters, compared to spin parameters above $S_o \approx 0.7$. At the highest spin parameters $S_o > 1.0$, the splash crown formation is significantly altered by spin. Minimal outward splash arises from the left side of the impact region (as seen in the ‘bird’s-eye’ images) and the cavity has a distinct and elegant cardioid shape and a dominant wedge that fully transects the cavity from surface all the way down to pinch-off.

Overall, the fundamental nature of water entry is not destroyed when spin is introduced, but instead altered in a unique fashion. Splash crown and sub-surface air cavity do form and collapse in similar stages, but a new fluid wedge is formed that can dissect the cavity in half in the presence of spin. Preliminary tests show that static surface contact angles can affect the formation of the splash crown, as well as the fluid wedge; these effects warrant further investigation.

4.5 Acknowledgments

Funding for this work was provided through the ONR ULI (University Laboratory Initiative) grant number N00014-06-1-0445 by Theresa McMullen (ONR Code 333).

Bibliography

- [1] ABELSON, H. I. 1970 Pressure measurements in the water-entry cavity. *Journal of Fluid Mechanics Digital Archive* **44** (01), 129–144.
- [2] ALAWAYS, L. W. & HUBBARD, M. 2001 Experimental determination of baseball spin and lift. *Journal of Sports Sciences* **19**, 349 – 358.

- [3] BARKLA, H. M. & AUCHTERLONIE, L. J. 1971 The magnus or robins effect on rotating spheres. *Journal of Fluid Mechanics* **47** (3), 437–447.
- [4] BEARMAN, P. W. & HARVEY, J. K. 1976 Golf ball aerodynamics. *Aeronautical Quarterly* **27** (pt 2), 112 – 122.
- [5] BELL, G. E. 1924 On the impact of a solid sphere with a fluid surface. *Philosophical Magazine* **48** (287), 753–764.
- [6] BERGMANN, R., VAN DER MEER, D., STIJNMAN, M., SANDTKE, M., PROSPERETTI, A. & LOHSE, D. 2006 Giant bubble pinch-off. *Physical Review Letters* **96** (15), 154505–4.
- [7] BIRKHOFF, G. & ISAACS, R. 1951 Transient cavities in air-water entry. *Naval Ordinance Report No. 1490* .
- [8] BLEVINS, R. D. 1984 *Applied Fluid Dynamics Handbook*. New York, NY: Van Nostrand Reinhold Co.
- [9] DAVIES, J. M. 1949 The aerodynamics of golf balls. *Journal of Applied Physics* **20** (9), 821–828.
- [10] DUEZ, C., YBERT, C., CLANET, C. & BOCQUET, L. 2007 Making a splash with water repellency. *Nat Phys* **3**, 180–183.
- [11] FALTINSEN, O. M. & ZHAO, R. 1997 Water entry of ship sections and axisymmetric bodies. *AGARD FDP and Ukraine Institute of Hydromechanics Workshop on HighSpeed Body Motion in Water* **24**, 11.
- [12] GAUDET, S. 1998 Numerical simulation of circular disks entering the free surface of a fluid. *Physics of Fluids* **10** (10), 2489–2499.
- [13] GILBARG, D. & ANDERSON, R. A. 1948 Influence of atmospheric pressure on the phenomena accompanying the entry of spheres into water. *Journal of Applied Physics* **19** (2), 127–139.

- [14] GLASHEEN, J. W. & MCMAHON, T. A. 1996 Vertical water entry of disks at low Froude numbers. *Physics of Fluids* **8** (8), 2078–2083.
- [15] GOVARDHAN, R. & WILLIAMSON, C. 2005 Vortex-induced vibrations of a sphere. *Journal of Fluid Mechanics* **531**, 11 – 47.
- [16] GRUMSTRUP, T., KELLER, J. B. & BELMONTE, A. 2007 Cavity ripples observed during the impact of solid objects into liquids. *Physical Review Letters* **99** (114502).
- [17] VON KARMAN, T. 1929 The impact on seaplane floats during landing. Technical Notes 321. National Advisory Committee for Aeronautics, Aerodynamic Institute of the Technical High School, Aachen.
- [18] KORNHAUSER, M. 1964 *Structural effects of impact, Chapter 2: Entry into water*. Sartan Books, Inc.
- [19] LEE, M., LONGORIA, R. G. & WILSON, D. E. 1997 Cavity dynamics in high-speed water entry. *Physics of Fluids* **9** (3), 540.
- [20] LOHSE, D., BERGMANN, R., MIKKELSEN, R., ZEILSTRA, C., VAN DER MEER, D., VERSLUIS, M., VAN DER WEELE, K., VAN DER HOEF, M. & KUIPERS, H. 2004 Impact on soft sand: Void collapse and jet formation. *Phys. Rev. Lett.* **93** (19), 198003.
- [21] MACCOLL, J. W. 1928 Aerodynamics of a spinning sphere. *Royal Aeronautical Society – Journal* **32** (213), 777–798.
- [22] MAY, A. 1951 Effect of surface condition of a sphere on its water-entry cavity. *Journal of Applied Physics* **22** (10), 1219–1222.
- [23] MAY, A. 1952 Vertical entry of missiles into water. *Journal of Applied Physics* **23** (12), 1362–1372.
- [24] MAY, A. 1975 Water entry and the cavity-running behavior of missiles. *Tech. Rep.* 20910. Naval Surface Weapons Center White Oak Laboratory.

- [25] MAY, A. & HOOVER, W. R. 1963 A study of the water-entry cavity. Unclassified NOLTR 63-264. United States Naval Ordnance Laboratory, White Oak, Maryland.
- [26] MAY, A. & WOODHULL, J. C. 1948 Drag coefficients of steel spheres entering water vertically. *Journal of Applied Physics* **19**, 1109 – 1121.
- [27] MAY, A. & WOODHULL, J. C. 1950 The virtual mass of a sphere entering water vertically. *Journal of Applied Physics* **21** (12), 1285–1289.
- [28] MEHTA, R. D. 1985 Aerodynamics of sports balls. *Annual Review of Fluid Mechanics* **17**, 151–189.
- [29] MOGHISI, M. & SQUIRE, P. T. 1980 An absolute impulsive method for the calibration of force transducers. *J. Phys. E: Sci, Instrum.* **13**, 1090–1092.
- [30] MOGHISI, M. & SQUIRE, P. T. 1981 An experimental investigation of the initial force of impact on a sphere striking a liquid surface. *Journal of Fluid Mechanics Digital Archive* **108** (1), 133–146.
- [31] NEWTON, I. 1671 New theory about light and colors. *Philisophical Transactions of the Royal Society* **6**, 3078.
- [32] RAFFEL, M., WILLERT, C., WILLERT, C. E. & KOMPENHANS, S. 1998 *Particle image velocimetry*. Springer.
- [33] RICHARDSON, E. G. 1948 The impact of a solid on a liquid surface. *Proc. Phys. Soc.* **4**, 352–367.
- [34] ROBBINS, B. 1742 *New Principles of Gunnery*. Richmond UK: Republished by Richmond Publishing in 1972, first printed by ed. Hutton.
- [35] ROSELLINI, L., HERSEN, F., CLANET, C. & BOCQUET, L. 2005 Skipping stones. *Journal of Fluid Mechanics* **543**, 137 – 146.

- [36] SHI, H.-H., ITOH, M. & TAKAMI, T. 2000 Optical observation of the supercavitation induced by high-speed water entry. *Journal of Fluids Engineering* **122** (4), 806–810.
- [37] SMITS, A. J. & SMITH, D. R. 1994 *A new aerodynamic model of a golf ball in flight*. E. and F.N. Spon, London.
- [38] THORODDSEN, S. T. 2002 The ejecta sheet generated by the impact of a drop. *Journal of Fluid Mechanics* **451**, 373–381.
- [39] THORODDSEN, S. T., ETOH, T. G., TAKEHARA, K. & TAKANO, Y. 2004 Impact jetting by a solid sphere. *Journal of Fluid Mechanics* **499** (499), 139–148.
- [40] TRUSCOTT, T. T. & TECHET, A. H. 2006 Cavity formation in the wake of a spinning sphere impacting the free surface. *Physics of Fluids* **18** (9).
- [41] WATTS, R. G. & FERRER, R. 1987 The lateral force on a spinning sphere: Aerodynamics of a curveball. *American Journal of Physics* **55** (1), 40–44.
- [42] WORTHINGTON, A. M. & COLE, R. S. 1897 Impact with a liquid surface, studied by the aid of instantaneous photography. *Philosophical Transactions of the Royal Society of London. Series A, Containing Papers of a Mathematical or Physical Character* **189**, 137–148.
- [43] YARIN, A. L. 2006 Drop impact dynamics: Splashing, spreading, receding, bouncing. *Annual Review of Fluid Mechanics* **38**, 159–192.

Chapter 5

The dynamic effect of spin and varied surface treatment on cavity formation during water-entry of spheres

Abstract

Air cavities formed in the wake of falling spheres are affected by impact velocity and wetting angle, but can be further altered through dynamic effects, mainly transverse rotation (θ). The rotating sphere alters the position of the contact line by moving it up and around the sphere from the side of least relative velocity to the side of greatest relative velocity ($\vec{V} = V_0\hat{e}_z + \dot{\theta}R\cos(\phi)\hat{e}_\theta$). This forms a wedge of fluid that crosses the cavity bisecting it into two separate cavities attached to the sphere. Eventually, both of the cavities collapse in an event known as deep seal. These phenomenon can occur for both hydrophobic and hydrophilic spheres of sufficient impact velocity. In the case of hydrophilic spheres that typically do not form cavities, if the rotational velocity is sufficient a cavity is formed on the side of greatest relative velocity. The rotating spheres have a lift force due in part to the coupling of the rotational and forward motion. The most interesting result, however, is that the same behavior can be replicated by coating the spheres half in a hydrophobic coating and half in a hydrophilic.

5.1 Introduction

The impact of a spherical object upon the free surface can create a sub-surface air cavity much larger than the sphere's volume (figure 5-1). At low enough velocities the formation of this cavity is dependent upon many factors including impact velocity, surface properties, and viscous effects [1]. We present the additional importance of dynamic motion upon the shape of the cavity formed. In particular, we demonstrate that manipulation of this phenomenon can produce irregularly shaped cavities through both dynamic means such as rotational velocity and surface properties such as wetting angle. Qualitatively, the effects of both cases are similar. The trajectory of the sphere moves towards the side of the most wettable surface and away from the side of least wettable surface for both rotating and non-rotating spheres.

Cavity formation is relevant to many applications including float plane impact [2], ship slamming [3], stone skipping [4] and drag reduction [5, 6]. Industrial applications include structural interactions with the free surface such as ship slamming, extreme waves and weather on oil platforms, sprayed adhesives, and ink jet printing. Even the sporting industry is interested in the water entry of athletes, reducing drag of swimmers near the free surface and the entry and exit of oars in rowing. Dynamic and surface treatment effects on water-entry are of particular relevance to naval hydrodynamics in the areas of torpedo entry [7] and methods for missile deployment [8, 9].

The impact of spheres and droplets on the surface of water has been studied extensively for over 100 years [10]. One of the main features of these types of impacts is the development of an underwater air cavity. [10] observed that when an already wetted sphere was dropped into a pool of water no underwater cavity was formed. He also noted that when the spheres were coated with soot (residue from a carbon based fire) the spheres made more definite cavities. Recently, [1] characterized the nature of this phenomenon and explained the behavior based on the wetting angle inherent to the sphere surface. Their study noted that for clean, smooth spheres there was a critical velocity $U^* > 7 \text{ m/s}$, above which all surface coatings created

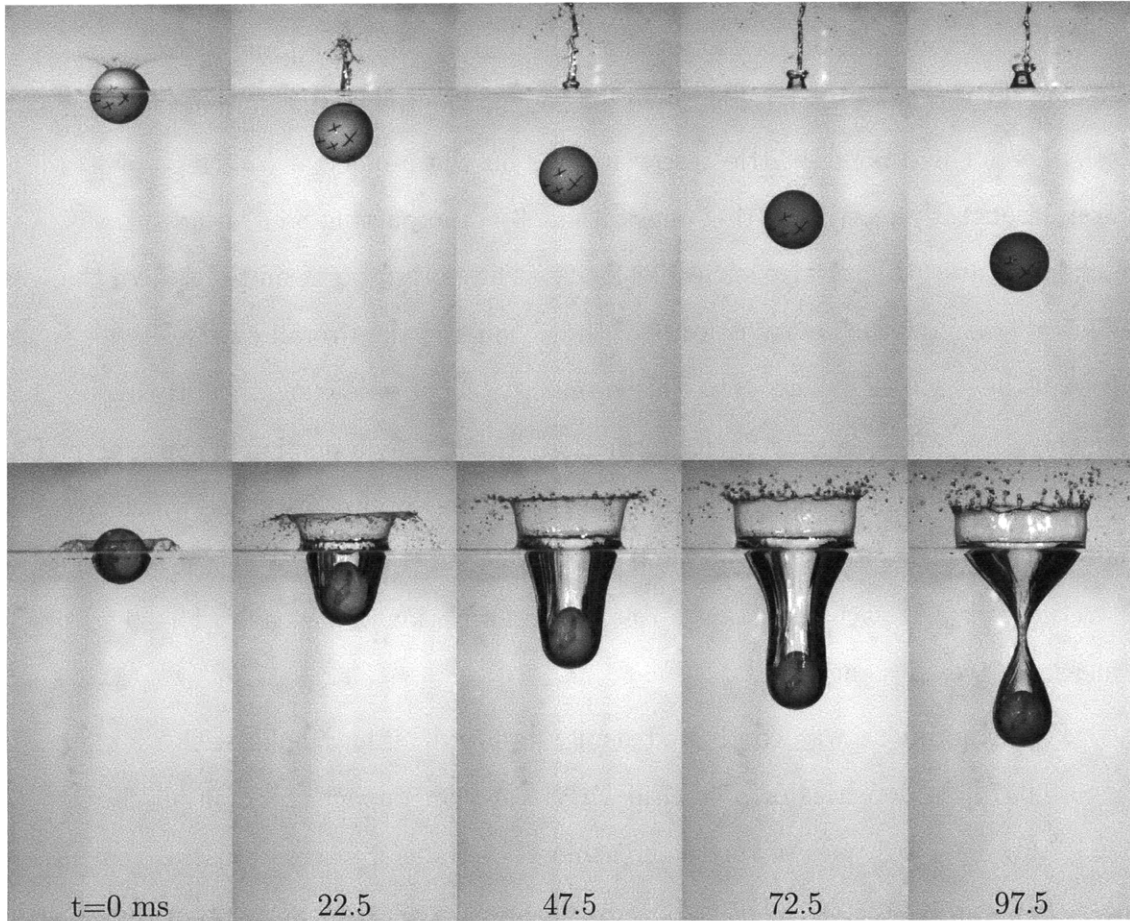


Figure 5-1: Case I (top): The water-entry of a hydrophilic billiard ball ($\theta = 67^\circ$) impacting at $V_o = 1.72 \text{ m/s}$. A large vertical jet is formed in the wake of this non-cavity forming case. Case II (bottom): The water-entry of a hydrophobic billiard ball ($\theta = 120^\circ$) impacting at $V_o = 1.72 \text{ m/s}$. The sphere is completely encased in a thin layer of air, a large cavity is formed in the wake, and the splash crown is uniquely vertical.

a cavity. More importantly their theoretical model couples two predictable values (impact velocity and statically measured contact angle) with the occurrence of this dynamic phenomenon. This extraordinary finding makes the phenomenon appear easy to understand despite the century of work by many ([10, 11, 12, 13, 14, 15, 7, 16, 17, 18, 19, 20] and others).

The phenomenon becomes more complicated by simply adding a rotational component. Although a large body of work exists on the free surface impact phenomenon of spheres there is very little research done on the impact of rotating spheres [21]. Spin alters the effective wetting angle of an object impacting on a liquid surface. As a sphere rotates, the relative surface velocity at any given point on the sphere changes. This affects how the cavity is formed, thus changing the overall cavity shape. In the case of the spinning sphere, the relative velocity on one side is significantly higher than on the other, often causing cavity formation around only a portion of the sphere. Figure 5-2 illustrates this effect, the sphere is rotating counterclockwise which becomes an added velocity on the right hand side and a subtracted one on the left. The altered speed of impact now plays a role in the formation of the cavity for all statically measured wetting angles.

The experiment was conducted using standard billiard balls with diameters of $d = 0.0572\text{ m}$, densities of $\rho = 1740\text{ kg/m}^3$ and an impact speed in all cases of $U_0 = 1.72\text{ m/s}$. Two types of surface treatments were used to create useful wetting angles. Hydrophobic spheres ($\theta = 120^\circ \pm 10^\circ$) were created by spraying a thin coating of a chemical treatment known as WX2100 by Cytonix Corp. Hydrophilic spheres ($\theta = 68^\circ \pm 10^\circ$) were created by cleaning the spheres with acetone, isopropyl alcohol, ethanol, respectively and then allowing them to dry thoroughly. The roughness to diameter ratio of the hydrophobic coating was $k/d = 1.96 \times 10^{-5}$, whereas the uncoated spheres had values of $k/d = 0.80 \times 10^{-5}$.

Experiments were performed using an apparatus that could both spin the spheres and drop them from a given distance above the free surface (figure 5-3). The sphere is held above the free surface by between two plates connected to two shafts supported by bearings and held together with an electro-magnet. A motor attached to the

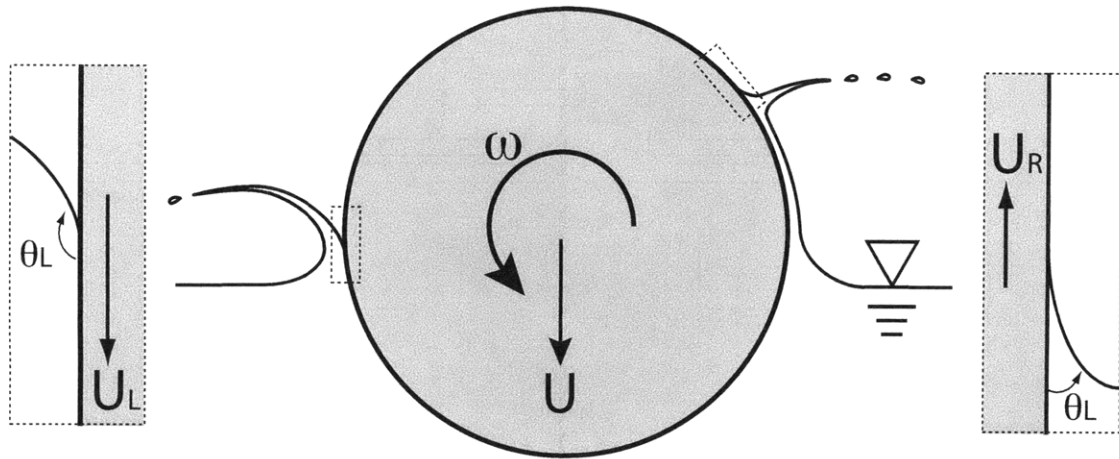


Figure 5-2: Cutaway view of how the water is affected by the surface of the sphere. On the left, the increased relative velocity creates an advancing contact line, increasing the dynamic wetting angle, thus allowing air entrainment and cavity formation. On the right, the relative velocity is actually in the upward direction creating a receding contact line, thus keeping the fluid in contact with the spheres surface.

shafts prescribes the rotation, which is monitored via an optical sensor. When the electro-magnet is turned off the mechanism opens and the sphere is free to fall with a prescribed initial spin rate. For the non-spinning cases the motor is not used, thus no rotational component of velocity is induced.

Four distinct cases are presented where cavity formation is clearly dependant on the wetting-angle driven air-entrainment of cavity formation. Cases I and II show the effect of hydrophobic and hydrophilic spheres with evenly coated surface treatments and no rotational velocity. They are similar to the results shown by a myriad of previous authors. The wetting angle is dynamically altered in cases III and IV by a dynamic effect (counter-clockwise rotational velocity), and by surface treatment only in case V. The velocity of impact for all cases presented is $V_o = 1.72 \pm 0.1 \text{ m/s}$.

Case I is presented in figure 5-1(top) and shows a hydrophilic sphere impacting the free surface without rotation. The images show how the sphere enters the fluid column and does not make a cavity in the wake, but does form a large jet at the free surface.

Case II is presented in figure 5-1(bottom) and shows a hydrophobic sphere impact-

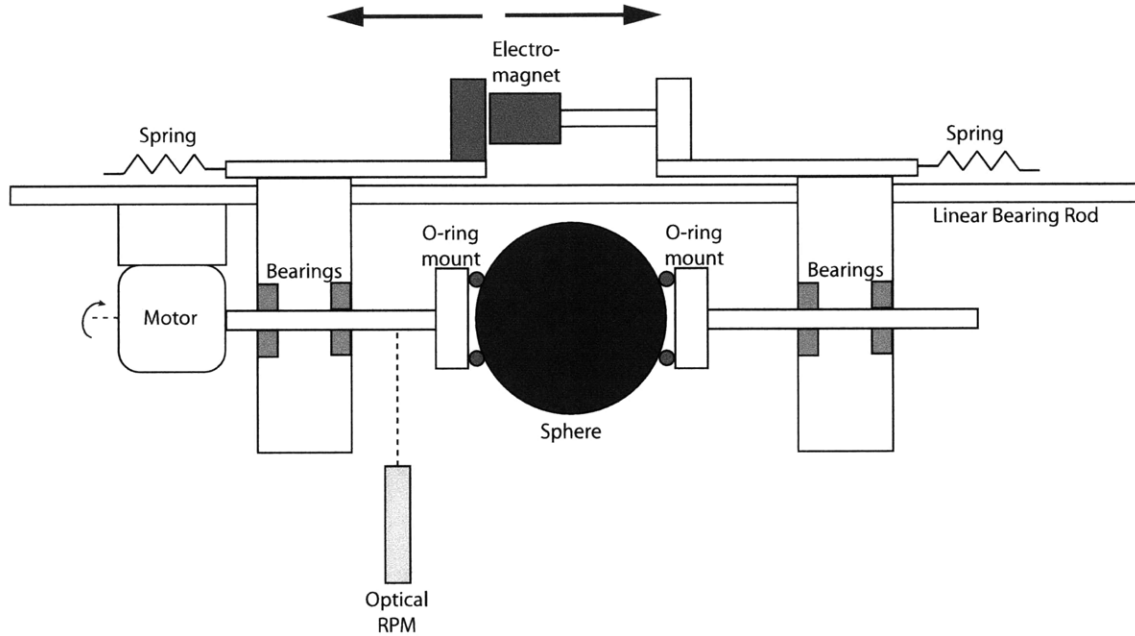


Figure 5-3: Device used to drop the spheres. The sphere is held above the water surface by two brackets that are attached to a set of o-rings. The brackets are attached to a set of bearings allowing the sphere to rotate out of the plane of the illustration. A motor is attached to one of the bearing shafts to induce a prescribed rotation (not used in this study). An optical rpm sensor is mounted separately to detect the spin rate of the sphere before release. An electromagnet holds the two halves of the device apart until the dropping time at which point the electromagnet is turned off and the springs draw the device apart allowing the sphere to fall freely into the tank of water.

ing the free surface without rotation. The figure shows the classic cavity formation and splash growth that occurs. The hydrophobic nature of the coating allows the sphere to be coated in a thin layer of air over most of its surface as it enters the water. The tendency for the sphere to remain non-wetted allows air to become entrained in its wake, thus opening a cavity in the water column. The cavity grows as the sphere descends, eventually collapsing some distance above the sphere. The collapse of the cavity begins when the momentum imparted by the sphere on the fluid is halted by the surrounding hydrostatic pressure, which then acts to close the cavity. The cavity collapses at the narrowest cavity radius (pinch-off) and two distinct cavities are formed, one attached to the sphere, and one connected to the free surface. After collapse two jets are also formed at the pinch-off point, one that ejects up beyond the free surface, and the other that passes through the cavity attached to

the sphere, impacting the sphere from above.

By comparison, case III (figure 5-4) illustrates the effect of rotation on a similar impact. The top images are taken from directly above the sphere, allowing us to look into the cavity, and the lower images are taken from the side to view the profile. The rotation rate of this impact is $\omega = 218 \text{ rad/s}$, which yields a spin parameter of $S = \omega_o r / V_o = 3.6$). The spin parameter is an indicator of the magnitude of the rotational velocity to the impact velocity. In the non-spinning case the sphere has the same relative velocity compared to the free-surface at all points on the sphere. In the spinning cases these speeds differ depending on the location along the sphere in cylindrical coordinates as

$$\vec{V} = V_o \hat{e}_z + \dot{\theta} R \cos(\phi) \hat{e}_\theta. \quad (5.1)$$

Any one given point on the sphere will have a changing relative velocity in z at all times, except the two points that lie on the z -axis. Figure 5-2 shows the differences in velocities along the equatorial line. For spin parameters equal to one ($S = 1$), the left hand side of the sphere has a velocity equal to twice the impact velocity, whereas the right hand side has no relative velocity. For spin parameters greater than one ($S > 1$), the left hand side of the sphere has a velocity greater than twice the impact speed, and the right hand side has an upward velocity. The left hand side of the sphere in contact with the water becomes an advancing angle, while the right hand side becomes a receding angle. The antisymmetric nature of the two sides creates an altered cavity shape. Typically, as seen in figure 5-1 the sphere has an axially symmetric circular cavity. The altered velocities along the surface in figure 5-4 form a wedge along the equatorial line of the sphere. This wedge is drawn in and across the cavity due to both the no slip condition at the surface and the receding nature of the wetted surface along the right hand side of the sphere.

Looking down into the cavity from the top reveals the formation of the wedge more clearly. In figure 5-4, the wedge is formed by the line of fluid in contact with the sphere that is drawn up and around the sphere through the no-slip boundary

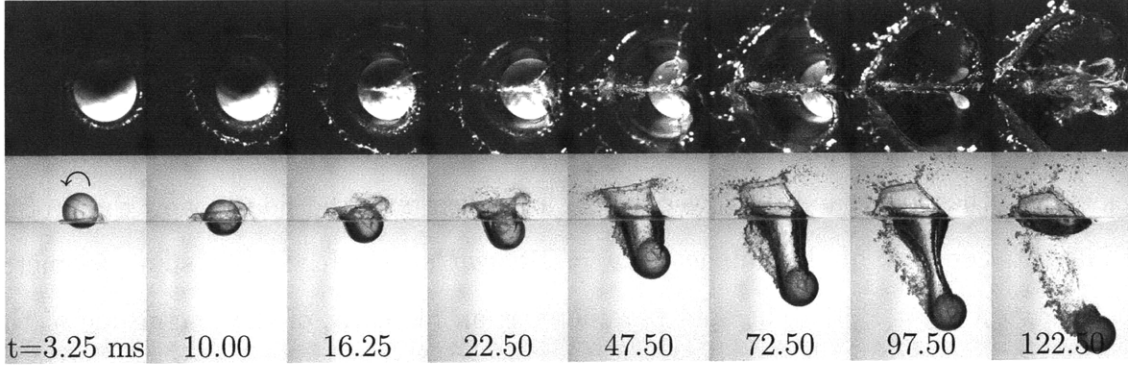


Figure 5-4: Case III (hydrophobic: $\theta = 120^\circ$, $V_o = 1.72 \text{ m/s}$, $\omega = 218 \text{ rad/s}$): Top and side views of a spinning billiard ball with hydrophobic coating. Viewed from above, the sphere creates a cardioid shaped splash curtain and subsurface air cavity as it descends in the fluid. The dynamic wetting angle is high on the left side of the sphere due to an advancing contact line forming a large outward splash. On the right, the relative velocity is upward, creating a receding contact line which inhibits splash growth and helps to draw a wedge of fluid across the cavity, bisecting it into two separate cavities. Note that the first four images are spaced by $t = 6.25 \text{ ms}$ while the next four are spaced by 25 ms .

condition. The out of plane component of velocity is reduced by $\cos(\phi)$. The images illustrate that indeed the greatest amount of fluid is drawn along the equator with less fluid being drawn into the cavity as one moves towards the polar regions. We can estimate the number of revolutions it will take the wedge to cross the cavity with a simple model. Using figure 5-5(b) we assume that at t_o the sphere is just now in contact with the fluid along the mid-horizontal line of the sphere. At $t_{1/4}$ the sphere has rotated $\pi/2$ radians. At this point the wedge of fluid not in contact with the sphere must cross the cavity, however, the cavity is growing with a rate of U_c . The time of impact is denoted by t_β . The wedge will travel with a speed $\omega_o R$ from $t_{1/4}$ to t_β and traverse a distance $U_c t_\beta + R$. This produces the following relationship

$$\omega R(t_\beta - t_{1/4}) = U_c t_\beta + R \quad (5.2)$$

which can be simplified to

$$t_\beta = \frac{R + \omega_o R t_{1/4}}{\omega_o R - U_c} \quad (5.3)$$

letting t_β equal to the time to rotate β revolutions gives $t_\beta = \beta \frac{2\pi}{\omega}$ and the time to

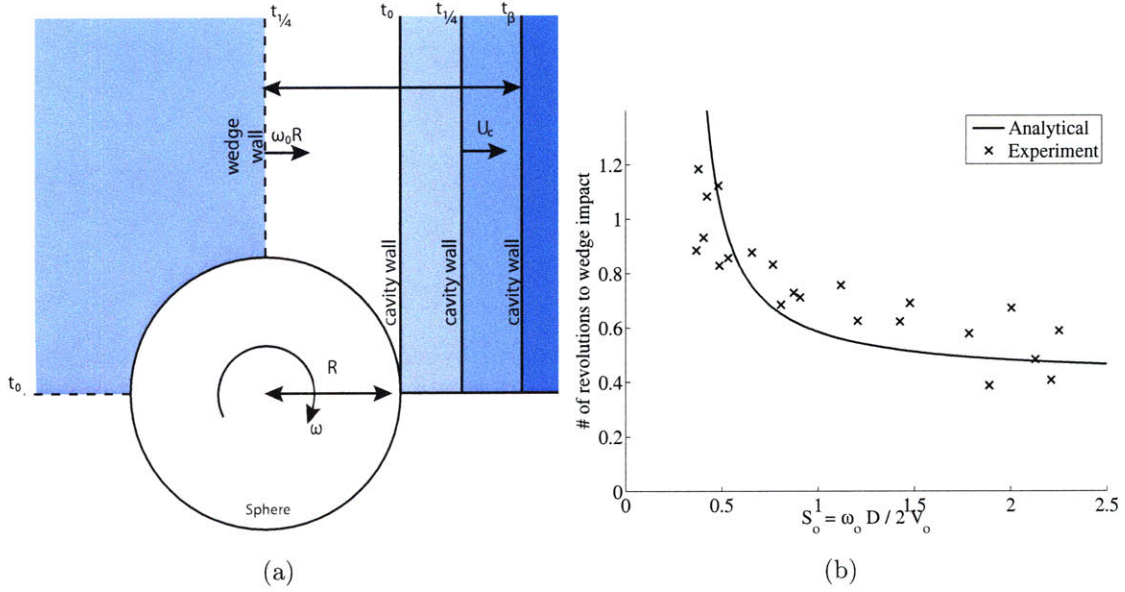


Figure 5-5: a) Illustration of the distance the wedge must travel to cross the cavity and its relationship to the expanding cavity. b) Number of revolutions from when the sphere is half way submerged in the water to when the wedge of fluid impacts the opposite cavity wall measured by the first frame in which a deformation in the cavity wall appears as a function of spin parameter ($S = \omega_o r / V_o$).

travel 1/4th a revolution $t_{1/4} = \frac{\pi}{2\omega_o}$. Thus, simplifying this relationship to a useful format to find the number of revolutions to impact we have

$$\beta = \left(\frac{1}{2\pi} + \frac{1}{4} \right) \frac{1}{1 - \frac{1}{S_o} \frac{U_c}{V_o}}. \quad (5.4)$$

This estimate is plotted in relation to the experimental data in figure 5-5(b). The only term we are not sure of is the value of U_c , which is the expansion rate of the cavity. This value can be calculated by analyzing the cavities. The entire value $\frac{U_c}{V_o}$ is simply the rate of expansion of the cavity versus the velocity of the sphere. This is the rate of energy transferred from the sphere to the fluid, which seems necessary in calculating the wedge formation. It can be assumed that $\frac{U_c}{V_o} = 0.3$ by noting that β should go to infinity as the spin parameter approaches $S = 0.3$.

Wedge formation occurs for both hydrophobic and hydrophilic rotating spheres. In fact, for hydrophilic rotating cases a cavity can be formed on the left hand side

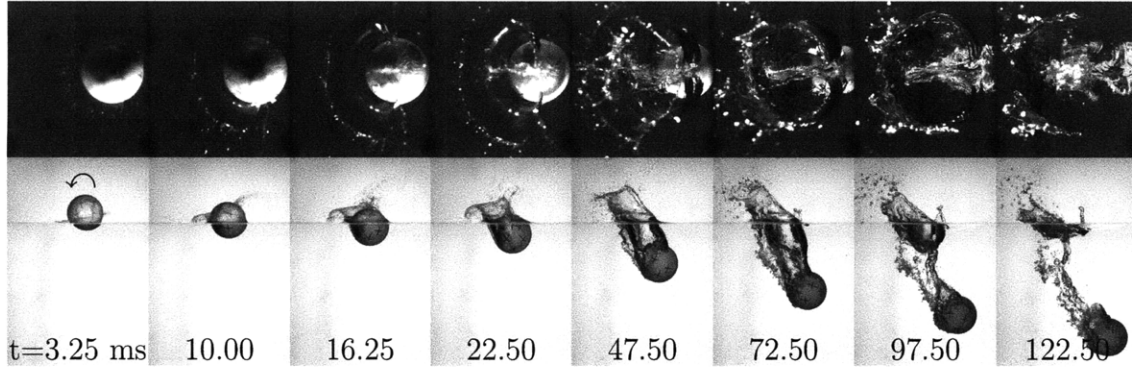


Figure 5-6: Case IV (hydrophilic: $\theta = 68^\circ$, $V_o = 1.72 \text{ m/s}$, $\omega = 192 \text{ rad/s}$): Top and side views of a hydrophilic spinning billiard ball. This case has the same impact speed and nearly the same rotation rate as Case III, however the top view reveals a less pronounced cardioid cavity shape, but still divides the cavity into two halves before pinch-off. Due to the lower wetting angle of the hydrophilic sphere, the splash radiates outward only from the left half of the sphere. In contrast, the splash forms around almost two-thirds of the sphere in Case III. Note that the first four images are spaced by $t = 6.25 \text{ ms}$ while the next four are spaced by 25 ms .

of the sphere, whereas a similar non-spinning sphere would normally not create a subsurface cavity. Case IV (figure 5-6) shows a spinning hydrophilic sphere, which exhibits similar behavior to case III. However, the subsurface cavity is not as large and the wetting nature of the sphere's surface has a tendency to draw more fluid along the surface than for the hydrophobic counterpart. Thus, the subsurface cavity is much less pronounced and the above surface splash formation is more dramatically altered. Indeed, the splash crown is only formed on the left hand side of the initial impact point as fluid ejected from the right hand side is quickly moved upward and leftward, leaving the right hand side of the splash curtain missing. This is similar to the non-spinning hydrophilic case I, where no cavity is formed. Here the cavity is formed on the left hand side due the high relative velocity, while the right hand side remains wetted due to the upward velocity and low static wetting angle, which both act to inhibit air entrainment. Fluid is also pulled across the cavity to form a wedge like structure similar to case II, however, this wedge appears wider in this case.

The most interesting part of this study is that these dynamic effects can be nearly duplicated by simply coating a non-spinning sphere half in a hydrophobic coating and leaving half hydrophilic. Figure 5-7 shows a half hydrophobic (left half), half

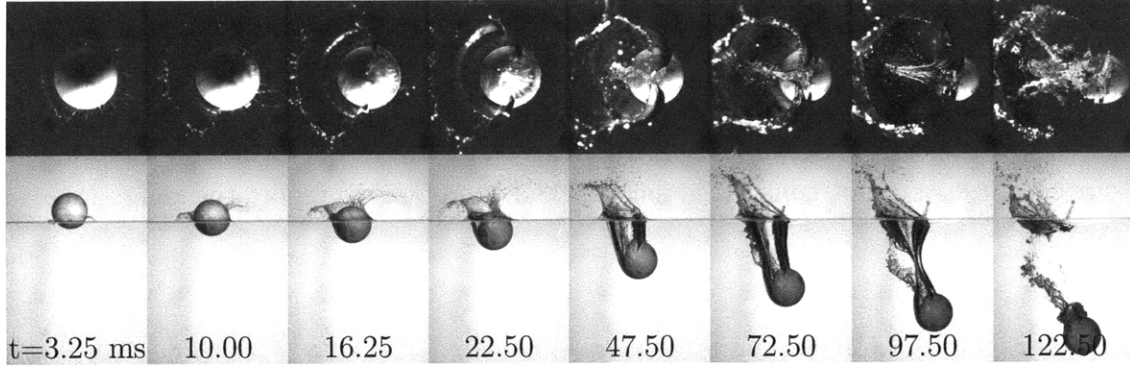


Figure 5-7: Case V (half hydrophobic and half hydrophilic: $\theta_{left} = 120^\circ$, $\theta_{right} = 68^\circ$, $V_o = 120 \text{ m/s}$, $\omega = 0 \text{ rad/s}$): Top and side views of a non-spinning billiard ball half coated with a hydrophobic coating and half hydrophilic. The hydrophobic surface coating encourages air entrainment in the wake, forming a cavity on the left hand side. The hydrophilic nature of the right hand side inhibits cavity formation, allowing fluid to be driven up around the sphere, funneling it to the left and inward, toward the equator of the sphere forming a fluid wedge. Amazingly, a cardioid shaped cavity, similar to the spinning cases, is formed for this non-spinning case and the sphere moves to the right as it descends despite having no initial horizontal velocity or spin rate. Note that the first four images are spaced by $t = 6.25 \text{ ms}$ while the next four are spaced by 25 ms .

hydrophilic (right half) sphere entering the water with the same impact velocity as cases I, II and III ($V_o = 1.72 \pm 0.1 \text{ m/s}$). The sphere enters the water and the right hand side draws water up along the hydrophilic surface, creating a sheet of fluid that converges toward the upper most part of the sphere, however, the left hand side has created an air cavity allowing air entrainment. Since the left hand side of the cavity is moving outward there is nothing to stop the sheet from the right hand side from converging and crossing the cavity, thus forming a fluid wedge similar to the one in cases III and IV. The altered cavity shape forces the sphere to the right similar to the spinning cases, but after pinch-off the effect of lift is diminished and the sphere falls downward more vertically than the spinning cases as the lifting effect becomes negligible (not shown).

Using the theoretical estimates for impact velocity V_0 as presented in [1], figure 5-8 shows how each of the cases presented here fits into the general picture for how cavities are formed. The figure shows cavity formation as a function of velocity and statically measured wetting angle. The dashed lines depict the predicted values above

which cavities should form. All of the cases herein have an initial impact velocity of $V_o = 1.72 \pm 0.1 \text{ m/s}$. In our study we noticed that our hydrophobic coating allowed the spheres to create cavities at lower impact velocities than in previous studies, however, our coatings were not considered smooth and therefore we report the roughness (see above).

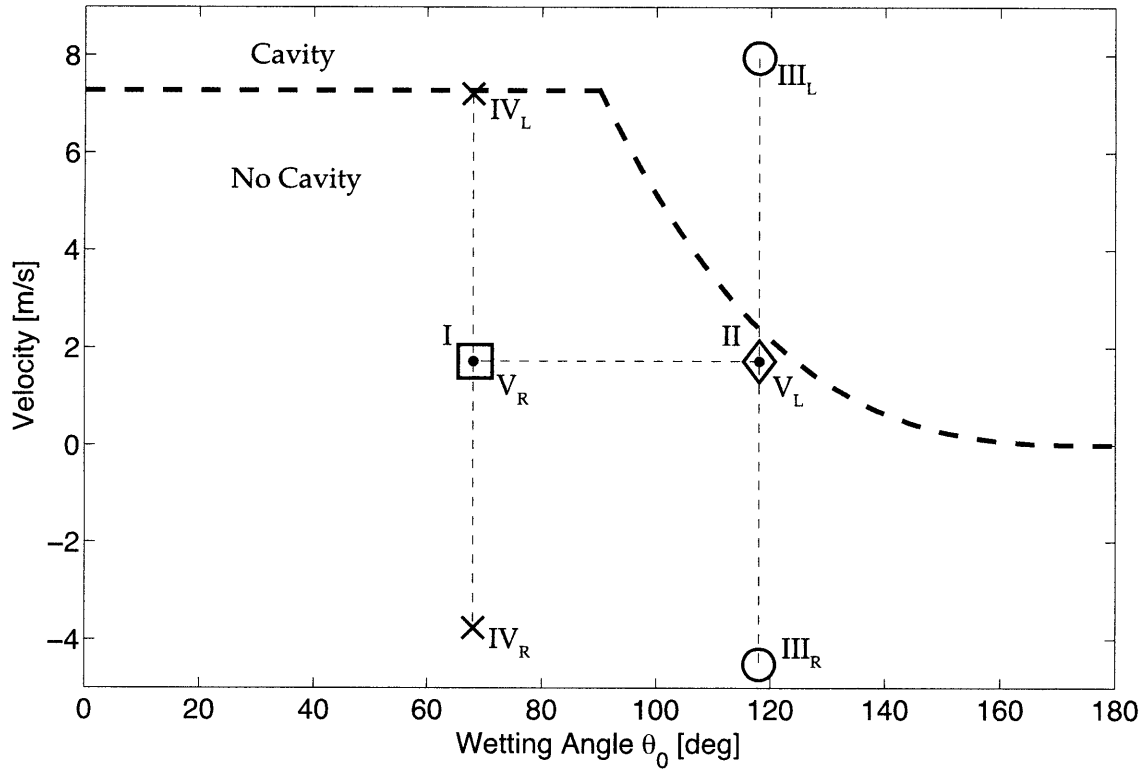


Figure 5-8: Likelihood of cavity formation as a function of impact velocity (\vec{V}_0) and static wetting angle (θ). Case I(\square) and II(\diamond) have constant velocities for all points on the sphere. Case III (\circ hydrophobic) and Case IV (\times hydrophilic) have a rotational velocity that span a vertical portion of the chart. Case V (\cdot) is coated half in hydrophilic and half hydrophobic, spanning the chart horizontally. The dashed line is the theory proposed by [1], above the line a cavity is formed, below no-cavity.

The trajectory of the sphere is affected as well as the cavity shape and splash crown. Here we do not elucidate the altered trajectory for spinning spheres but one can read more about this effect in [21]. We would like to point out, however, that cases III, IV and V are very similar and that the lift force seems to have approximately the same effect on the non-spinning case before pinch-off, which could be of interest in the work of cavity guided missile technology [8, 9].

The altered velocities (\vec{V}_0) of the sphere span the theory presented by [1]. Figure 5-8 shows the theoretical line of cavity formation (dashed) and the cases presented here. The figure shows cavity formation as a function of velocity and statically measured wetting angle. The dashed lines depict the predicted values above which cavities should form. Cases I and II are represented by merely points on the plot and show good agreement that case II should form a cavity whereas case I does not. Cases III and IV span the chart vertically based on their respective coatings. Case III is clearly cavity forming at its greatest surface velocity at (III_L) and clearly non-cavity forming where its surface velocity is negative (III_R). Case IV just enters the cavity forming behavior where its greatest surface velocity is marked by (IV_L) while its negative surface velocity obviously falls in the non-cavity forming regime. Finally, Case V spans the figure horizontally and shows good agreement that the hydrophobic side should form a cavity while the hydrophilic side should not.

In conclusion, this study has shown that air cavities formed in the wake of spheres can be altered in a similar manner through surface treatment and the dynamic effects of relative surface velocity. In the case of cavity forming spheres that are rotating in the transverse direction a wedge of fluid is formed which traverses the cavity from the side of least relative velocity to greatest relative velocity and bisects the cavity into two halves. A method of determining the time it takes for this fluid body to cross the cavity is presented. This effect can be replicated for both hydrophobic and hydrophilic spheres when the critical relative velocity (\vec{V}_0) is exceeded (figure 5-8). Furthermore, these effects can be duplicated without rotating the spheres by coating the spheres half in a hydrophobic and half hydrophilic coating. This simple yet elegant extension of the work of [1] has applications to many naval hydrodynamics problems and should be taken into consideration when trajectory and/or cavity shape are important factors in engineering applications.

Acknowledgements T. T. T and A. H. T. gratefully acknowledge funding from the Office of Naval Research University Laboratory Initiative grant # N00014-06-1-0445 for funding T. T. T. We thank Brenden Epps, Ashley Cantieny, Mike Smith-

Bronstein, Libby Palmer, and Jesse Belden in helping with the acquisition, processing and general support of this project. And Gustav Truscott for showing us all that 7 year olds can perform experiments like this one!

Bibliography

- [1] C. Duez, C. Ybert, C. Clanet, and L. Bocquet, *Nat Phys* **3**, 180 (2007).
- [2] T. von Karman, Technical Notes 321, National Advisory Committee for Aeronautics, Aerodynamic Institute of the Technical High School, Aachen (1929).
- [3] O. M. Faltinsen, *Sea loads on ships and offshore structures* (Cambridge Univ. Press, 1990).
- [4] L. Rosellini, F. Hersen, C. Clanet, and L. Bocquet, *Journal of Fluid Mechanics* **543**, 137 (2005), ISSN 0022-1120, URL <http://dx.doi.org/10.1017/S0022112005006373>.
- [5] T. T. Truscott, B. P. Epps, and A. H. Techet, *Journal of Fluid Mechanics* (Submitted 2009).
- [6] S. Ashley, *Sci. Amer.* **284**, 70 (2001).
- [7] A. May and W. R. Hoover, Unclassified NOLTR 63-264, United States Naval Ordnance Laboratory, White Oak, Maryland (1963).
- [8] C. Weiland, P. Vlachos, and J. Yagla, in *International Symposium on Ballistics* (Vancouver, BC, Canada, 2005).
- [9] C. Weiland, P. Vlachos, and J. Yagla, in *American Society of Naval Engineers Day* (Arlington, VA, 2006).
- [10] A. M. Worthington, *A study of splashes* (Longmans Green and Co., Plymouth : Printed by William Brendon and Son, Ltd., 1908, 1908 reprinted, The Macmillian Co., New York, 1963).

- [11] A. Mallock, Proc. Roy. Soc. Lond. Ser. A. **95**, 138 (1918).
- [12] G. E. Bell, Philisophical Magazine **48**, 753 (1924).
- [13] D. Gilbarg and R. A. Anderson, Journal of Applied Physics **19**, 127 (1948).
- [14] E. G. Richardson, Proc. Phys. Soc. **4**, 352 (1948).
- [15] G. Birkhoff and R. Isaacs, Tech. Rep. 1490, Navord Rep. (1951).
- [16] H. I. Abelson, Journal of Fluid Mechanics Digital Archive **44**, 129 (1970).
- [17] J. W. Glasheen and T. A. McMahon, Physics of Fluids **8**, 2078 (1996), URL <http://link.aip.org/link/?PHF/8/2078/1>.
- [18] M. Lee, R. G. Longoria, and D. E. Wilson, Phys. Fluids **9**, 540 (1997).
- [19] S. Gaudet, Physics of Fluids **10**, 2489 (1998), URL <http://link.aip.org/link/?PHF/10/2489/1>.
- [20] R. Bergmann, D. van der Meer, S. Gekle, A. van der Bos, and D. Lohse, J. Fluid Mech. (2009), in press.
- [21] T. T. Truscott and A. H. Techet, Journal of Fluid Mechanics **625**, 135 (2009).

Part II

High speed projectile water-entry

Chapter 6

Motivation and recent projectile studies

Until recently, naval underwater combat consisted of slow moving torpedoes traveling with speeds that allowed ships to respond with countermeasures and evasive maneuvering. Today new threats to ocean-going vessels include underwater supercavitating torpedos that travel hundreds of meters per second, thus greatly decreasing the time surface ships have to respond defensively. These torpedos are characterized by small flat tips that form vaporous cavities in their wake. Near the tip, ventilation ducts add gas to the liquid vapor cavity allowing the torpedos to travel inside an underwater air column, thus ensuring a greatly reduced drag. Figure 6-2(a) shows a supercavitating torpedo known as a VA-111 Shkval torpedo; notice the round disk-like tip and nearby vents. The vents serve as an opening for gas to be released into the wake of the disc and envelop the torpedo in gas [1].

Systems similar to those used in ground-to-air missile defense could counter these increased underwater threats. When missiles attack ships from the air, a computer controlled gunner fires thousands of bullets at the missile in an effort to destroy it before it reaches the ship. In a similar manner, projectiles shot underwater from the deck of a ship could destroy the supercavitating threats as well as conventional torpedos.

An extension of the research presented in Part I is the high-speed, shallow-water

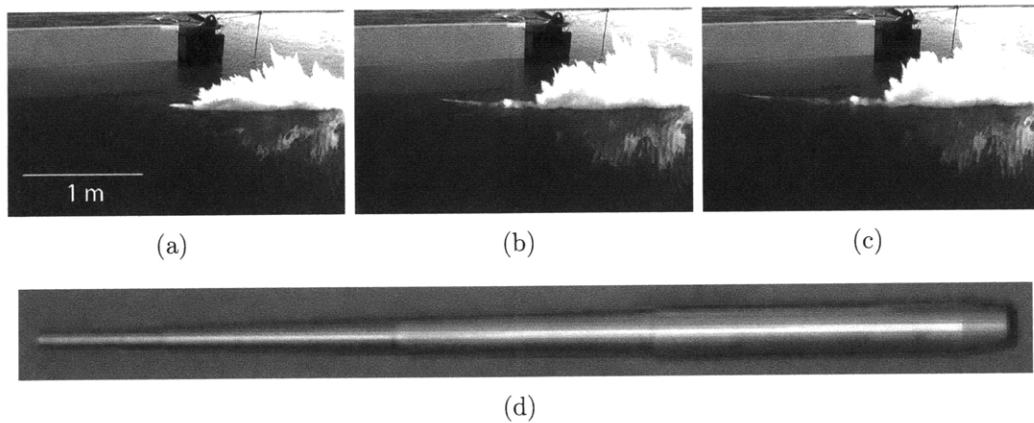


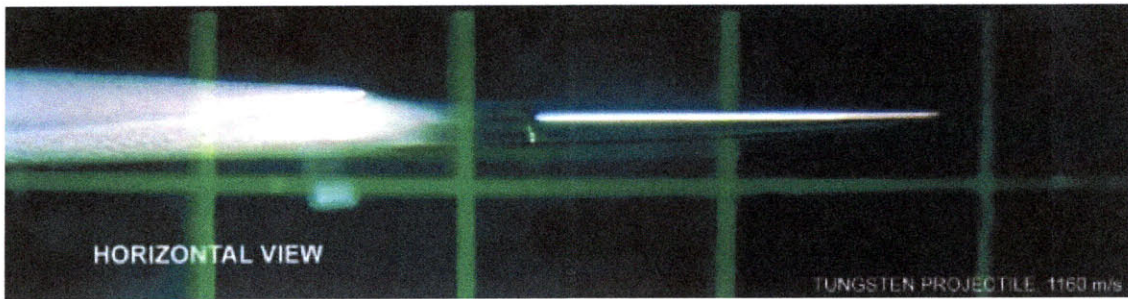
Figure 6-1: a) to c) Series of images taken from a high speed camera showing the water entry of a high speed cavitating underwater projectile [3]. This projectile did not successfully enter the water but ricocheted off the surface. d) image of 0.50 caliber projectile used in images a) to c) bullet length is ~ 8 in. Impact speed is approximately 975 m/s, water entry angle 3.0° . Time between images is unknown.

entry of projectiles such as military ballistics. Projectiles that impact the water at low angles typically do not enter the water, instead they either ricochet off the surface. If they do pierce the surface, they often break up or tumble several meters underwater due to instabilities in their trajectory (see figure 6-1). Reducing these instabilities and increasing the likelihood that they will travel straight and far is important for improving defensive weapon technology.

Objects traveling at high velocities ($Re > 10^6$) underwater can cause the water to cavitate, i.e., change from liquid to vapor. The high velocity reduces the pressure in the fluid; if the pressure is reduced to that of the vapor pressure, cavities of steam will form. As an example, the tip of a propeller is a common place for cavitation to occur because the speed of the tip is so much greater than the speed of the hub. If the leading edge of an object creates enough cavitation, the object can become encompassed by a vapor cavity. This phenomenon is referred to as supercavitation. Projectiles designed to travel inside these cavities are called supercavitating projectiles, as opposed to the super-ventilated cavities torpedos mentioned above. The tips of these projectiles are blunt and present a small surface area into the flow field, which creates cavitation. Their body shape is made to fit inside these small cavities, thus reducing the frictional



(a)



(b)

Figure 6-2: a) Supercavitating torpedo VA-111 Shkval c/o <http://en.wikipedia.org/wiki/VA-111.Shkval>. b) Underwater photograph of a high speed supercavitating projectile [6].

forces associated with underwater travel (see Figure 6-2(b)).

Results from tests performed by a group at the Naval Undersea Warfare Center (NUWC) in Newport, RI reveals that projectiles with flat noses, tapered tips, and high length to diameter ratios (L/D) can pierce the surface at low angles and continue to descend through the water column without ricochet [4, 6] (see figure 6-2(b)). Experiments performed by NUWC [6] and also those presented in chapter 8 reveal that these types of projectiles are stabilized underwater through the hydrodynamic planing of the rear portion of the projectile against the cavity side walls. However, if the body does not fit inside the cavity properly then the projectiles can experience extremely large forces, which may cause break-up, bending (see figure 6-3), or altered



Figure 6-3: Projectile bent during underwater testing of supercavitating bullets [6].

trajectories.

Several experimental studies have looked at vertical air-water impact of high-speed projectiles such as [10, 2] and more recently revisited by [15]. Likely the most complete published study to date was performed by [6], in which they studied a fully developed underwater cavity by firing projectiles underwater, avoiding the free surface interaction, and creating optimal conditions for determining the mechanisms of underwater stability and nearly steady state vapor-cavity size estimates. Several full-scale, shallow-angle, air-to-water studies have been performed by different researcher groups but none have been published to date. Several theoretical cavity models have been developed as well. [8] and [13] have developed analytical models for cavity formation and cavity oscillations based partially on empirical data and mostly on control volume analysis while others such as [14] have focused more on the projectile stability. [5] wrote an entire volume of work on the subject of hydroballistics, which includes a excellent summary of both quantitative and qualitative experimental data taken by Albert May ([10, 11, 9]. More recently [12] used a numerical simulation employing preconditioning to estimate the cavity shape, temperature, shock formation, and pressure inside and outside of the cavity of bullet water entry. [5] comments on the need for experiments that include oblique entry from air to water.

Although the side wall acts to stabilize the bullets underwater, the large L/D

makes them aerodynamically unstable in air. These difficulties have made air-to-water testing quasi-repeatable. In air, projectiles must contend with aerodynamic forces of drag and lift to maintain level flight. To do this, they use gyroscopic and/or fin stabilization techniques. Fins counteract the overturning moment by providing increased lift and drag at the back of the projectile. This moves the aerodynamic center of pressure behind the center of gravity, thus making the projectile inherently stable. Fins are typically used on larger and longer projectiles (e.g. rockets, missiles, etc.), while rotation is typically used for smaller fire arms such as rifles and pistols. Experiments using fin stabilized projectiles aimed at shallow angles to the water surface have flown in air and entered the water. However, once underwater, finned projectiles do not travel in a straight path and tend to break into pieces since their fins often come in contact with the cavity side walls [7].

Gyroscopic stabilization is characterized by an axial spin rate, which provides a gyroscopic righting moment to counteract the aerodynamic pressure or overturning moment. Tests done at Aberdeen, Maryland have shown that gyroscopically stabilized projectiles can travel underwater successfully. However, these tests used rotation rates that are orders of magnitude too small for proper stabilization in-air (as presented in chapter 7) and showed that these types of projectiles still use the cavity walls for stability. Furthermore, NUWC reported that air-to-water tests performed at the same facility showed that rotation can incite the first mode of vibration.

Full scale experiments performed at Aberdeen produced a general understanding of some of the problems associated with these types of water entry. In particular, the cavity shape and validity of the theoretical model was still under scrutiny as it seemed that sometimes the cavities were large enough for the projectiles and other times they were too small. It was also unclear if the cavities were the source of stability or if they were destabilizing the projectiles. Figure 6-4 shows a few frames from high speed videos of the tests performed at NUWC and shows a projectile that successfully entered the water and proceeded downrange to its intended target. Figure 6-5 shows a corresponding underwater camera view of the projectile in figure 6-4. None of the images clearly show the bullet inside the cavity, but do show the trailing cavity and

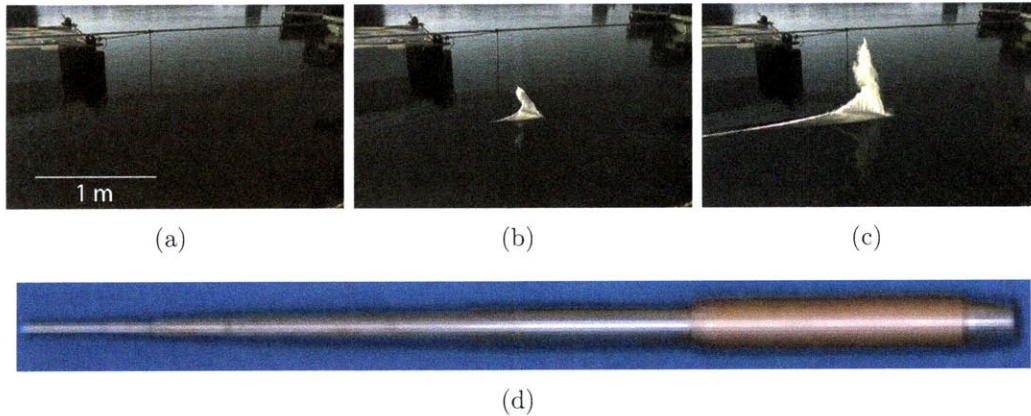


Figure 6-4: a) to c) Series of images taken from a high speed camera showing the water entry of a high speed cavitating underwater projectile [3]. This projectile successfully entered the water. d) image of 0.50 caliber projectile used in images a) to c) bullet length is ~ 8 in. Impact speed is approximately 975 m/s, water entry angle 2.8° . Time between images is unknown.

emphasize the need for more controlled experimentation. Figure 6-1 shows the same projectile type which ricocheted off of the surface yet was under the same initial conditions.

The full scale experiments were performed in a pond at the Aberdeen testing grounds. The pond provided a nearly quiescent flow field in which to perform the experiments. A photograph of the testing grounds is shown in figure 6-6. The nature of the pond and difficulty in placing cameras at points of interest easily demonstrate the need to perform smaller, laboratory scale, controlled experiments presented in chapter 8.

Bibliography

- [1] S. Ashley. Warp drive underwater. *Sci. Amer.*, 284:70–79, 2001.
- [2] David Gilbarg and Robert A. Anderson. Influence of atmospheric pressure on the phenomena accompanying the entry of spheres into water. *Journal of Applied Physics*, 19(2):127–139, 1948.

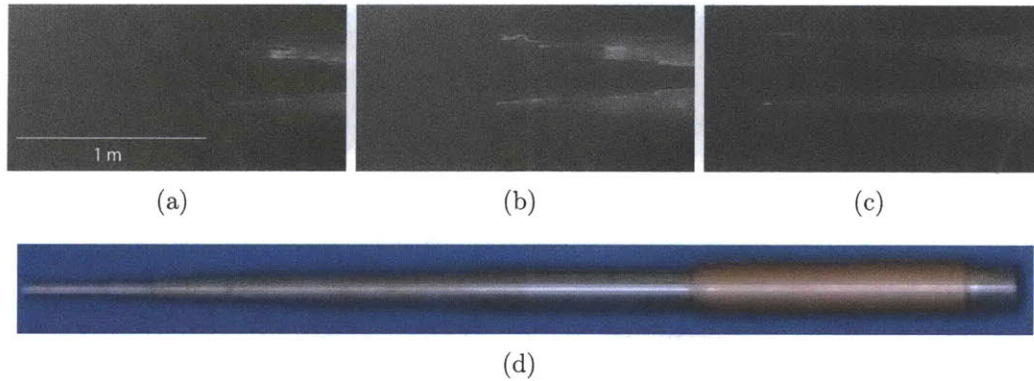


Figure 6-5: Underwater series of images taken of a high speed cavitating projectile [3] (same trial as figure 6-4). This projectile successfully entered the water. d) image of 0.50 caliber projectile used in images a) to c) bullet length is ~ 8 in. Impact speed is approximately 975 m/s, water entry angle 2.8° . Time between images is unknown.

- [3] Jason Gomez and Joseph Miranda. Ahsum. Experiments performed at the Naval Underwater Warfare Center in Newport, RI and Aberdeen, MD., 1999-2007.
- [4] Jason T. Gomez and Arun Shukla. Multiple impact penetration of semi-infinite concrete. *International Journal of Impact Engineering*, 25:965–979, 2001.
- [5] Raymond J. Grady. *Hydroballistics design handbook Volume 1*. Naval Sea Systems command Hydromechanics Committee, January 1979.
- [6] J Dana Hrubes. High-speed imaging of supercavitating underwater projectiles. *Experiments in Fluids*, 30(1):57 – 64, 2001.
- [7] Paul Kocheadorfer. Low cost free flight development testing of a rocket propelled high speed underwater missile. Final report, Naval Undersea warfare center Newport, RI 02841-5047, 1993.
- [8] Georgii Vladimirovich Logvinovich. *Hydrodynamics of free-boundary flows*. Jerusalem, Israel Program for Scientific Translation; [available from the U.S. Dept. of Commerce, National Technical Information Service, Springfield, Va.], 1972.

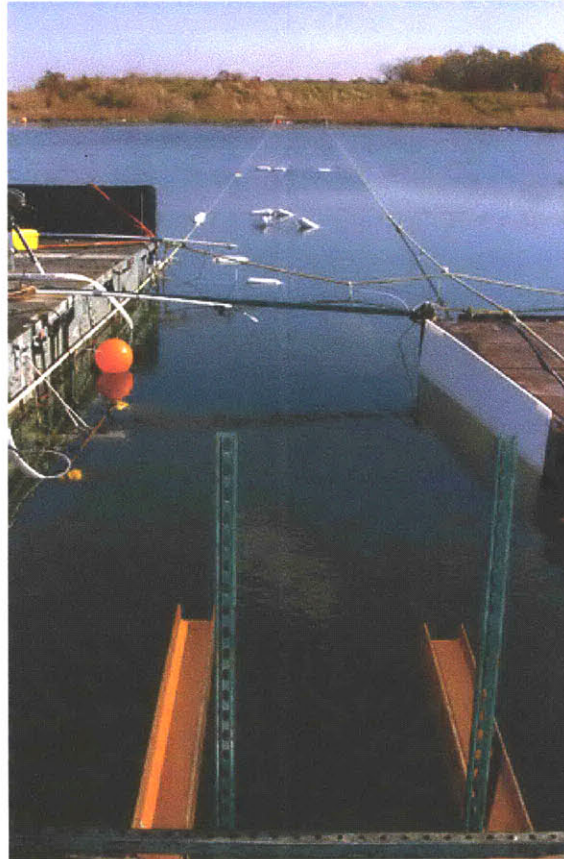


Figure 6-6: Photograph of testing range at Aberdeen Maryland looking downrange from the perspective of the rifle. On the right and left, two barges straddle the testing range and are used to support cameras and equipment. In the foreground two vertical structures hold break screens used to estimate the speed of the projectile before water entry. A large round orange buoy on the left indicates the approximate location of water entry, while three sets of smaller white buoys indicate underwater break screens placed strategically to determine the underwater speed of the bullets downrange.

- [9] A. May. Water entry and the cavity-running behavior of missiles. Technical Report 20910, Naval Surface Weapons Center White Oak Laboratory, 1975.
- [10] Albert May. Vertical entry of missiles into water. *Journal of Applied Physics*, 23(12):1362–1372, 1952.
- [11] Albert May and William R. Hoover. A study of the water-entry cavity. Unclassified NOLTR 63-264, United States Naval Ordnance Laboratory, White Oak, Maryland, 1963.
- [12] Michael Dean Neaves and Jack R. Edwards. All-speed time-accurate underwater projectile calculations using a preconditioning algorithm. *ASME*, 128:284–296, March 2006.
- [13] Emil V. Paryshev. Approximate mathematical models in high speed hydrodynamics. *Journal of Engineering Mathematics*, 55:41–64, 2006.
- [14] Y. Savchenko, V. Semenenko, S. Putilin, V. Savchenko, and Y. Naumova. Theory of stable model motion with ventilated and unventilated supercavities. Review, National Academy of Sciences of Ukraine Institute of Hydromechanics Department of Free Boundary Flows, Kyiv, June 2000.
- [15] Hong-Hui Shi, Motoyuki Itoh, and Takuya Takami. Optical observation of the supercavitation induced by high-speed water entry. *Journal of Fluids Engineering*, 122(4):806–810, 2000.

THIS PAGE INTENTIONALLY LEFT BLANK

Chapter 7

Determination of the minimum spin rate required to keep a bullet stabilized in air.

High speed underwater projectiles use large length to diameter ratios to increase their stability. This increased ratio means that the projectiles are long and narrow and allows them to fit within the underwater cavities that they create. It also decreases the tumbling tendency inside the cavities. The unsteady behavior at the tip of the projectiles has a tendency to cause a pitching or yawing moment. This rotates the back end of the projectile into contact with the side wall, creating a small hydroplaning surface which in turn produces a righting moment forcing the projectile back into the cavity.

In air projectiles must be stabilized by more traditional means such as axial rotation, fins, flaring, etc. Perhaps the simplest and easiest tactic to employ is axial rotation or gyroscopic stabilization. This method consists of spinning a projectile up to rotational speed through the grooving along the rifling of the barrel, or by a motor which spins the projectile inside of a sabot before firing. In either method it is essential to determine the spin rate needed to maintain stable flight in air.

This chapter outlines a first order method of determining the minimum axial spin rate necessary to keep a projectile in stable flight in air. First, a reference to

the gyroscopic stability criterion, and a method of making an estimate of the forces involved with that calculation is presented. Second, a derivation of the criterion using first principles is presented. This chapter was written in an effort to estimate what spin rates are necessary for stability of a given projectile, especially in the development stage, and to help design a series of projectiles that would travel stably in both air and water.

7.1 Introduction

Projectiles traveling at high velocities encounter large aerodynamic forces as they travel through the air. The ability of the projectile to resist axial direction changes (pitch and yaw motion) is important for stable flight. If the projectile begins to yaw it may hit the intended target at an angle, or in worse cases it may veer off in random directions as it precesses, and not impact the target at all. Projectiles can be stabilized by fins or by spinning about the axis of symmetry producing gyroscopic stabilization. A projectile with insufficient spin rates is considered under-stabilized. Conversely, if the projectile has a larger spin rate than is necessary it is considered over-stabilized.

Over stabilization can also be a problem for projectiles. Excessive rates of spin can cause above normal wear inside the barrel, or may tear bullets apart depending on the material. Furthermore, extreme spin rates may cause the accuracy of the bullet to be lessened. As the bullet travels down the barrel the axis of the bullet coincides with the axis of the barrel; however, as it leaves the barrel the projectile axis moves to its center of mass. If the center of mass doesn't line up with the axis of the barrel (aka, radius of gyration) then when the bullet exits the barrel it rotates erratically. This is caused by non-uniform bullet making or voids in the bullet, deformation of the bullet, or undersized bullets in certain rifles. Furthermore, bullets with only a small percentage of their surface area in contact with the barrel can have stability issues. Radius of gyration effects are typically many orders of magnitude smaller than the effects of insufficient spin rates. Therefore, bullets that are over-stabilized

are typically much more accurate than those that are under-stabilized.

7.2 Gyroscopic Stabilization

In air, projectiles must overcome aerodynamic forces of drag and lift to maintain level flight. They use gyroscopic or fin stabilization techniques to overcome these forces. The former is characterized by an axial spin rate in the z -direction (figure 7-3), which provides a righting moment when a force such as a cross wind is applied to the tip. The equations of motion (see section 7.3) are used to derive the non-dimensional gyroscopic stability criterion, which can be represented as,

$$S_g = \frac{I_{zz}^2 \omega^2}{2I \rho A_s D U^2 C_{m\alpha}} = \frac{\text{Rotational effects}}{\text{Aerodynamic effects}} \quad (7.1)$$

where D is the diameter of the projectile, I_{zz} is the axial moment of inertia about the center of mass, I is the transverse moment of inertia about the center of mass, ρ is the density of air, U is the velocity, ω is the angular spin rate, $C_{m\alpha}$ is the overturning moment coefficient, and A_s is projectile reference area (typically $\frac{\pi D^2}{4}$). The criterion compares the force of gyroscopic rotation of the body to the aerodynamic forces externally applied to the body. The comparison shows that if the rotationally induced forces dominate, the aerodynamic forces can be overcome. Conversely, if the aerodynamic forces are greater than the rotational effects, then the projectile will not be able to resist those forces. The criterion requires that S_g must be larger than unity before the projectile is considered stable.

$$S_g > 1 \quad (7.2)$$

A projectile traveling in level flight will encounter small perturbations away from the intended trajectory. If S_g is greater than unity, then the projectile will have a tendency to return to level flight. If S_g is smaller than unity, then it will deviate from its intended course erratically.

From the gyroscopic stability criterion (equation 7.1), a minimum spin rate can be

determined by solving for ω and allowing S_g to equal unity.

$$\omega = \sqrt{\frac{2I\rho A_s D U^2 C_{m\alpha}}{I_{zz}^2}} \quad [rad/s] \quad (7.3)$$

Since the moments of inertia, velocity, projectile shape, and fluid densities are known, the determination of the overturning moment coefficient becomes the leading factor in determining the minimum spin rate. The overturning moment can be difficult to calculate and is typically found by experiment. However, a relatively close estimate can be determined by estimating the aerodynamic drag force on the object (see equation 7.26).

$$F_p = \frac{1}{2}\rho U^2 A = \frac{1}{2}\rho U^2 R h \cos\theta \quad (7.4)$$

Where h is the height of the cone and R is the radius. The overturning moment coefficient can then be determined by multiplying the force F_p by the moment arm and dividing by the force of drag¹.

$$C_{m\alpha} = \frac{F_p l}{\frac{1}{2}\rho U^2 A_s D} \quad (7.5)$$

To determine the range of spin rates desired for a given projectile a plot of the spin rate versus the overturning moment can be plotted for the given conditions. An example plot appears in figure 7-1.

Notice that the magnitude of the required spin rate changes as the square root of the overturning moment. This is good news because a small range of spin rates will have a broader effect on the overturning moment. A 50% increase in overturning moment translates into a 30% increase in spin rate. Of course, a different plot will be generated for each projectile due to geometry and velocity, but the concept remains the same. Therefore as a first order estimate of the required spin rate an estimate of the force using equation 7.4 can be compared to a plot similar to figure 7-1 using the proper geometry and velocities.

Finally, the spin rate can be converted into the required rifling measurement (turns

¹For more information on how this is determined see chapter 2 of reference [1].

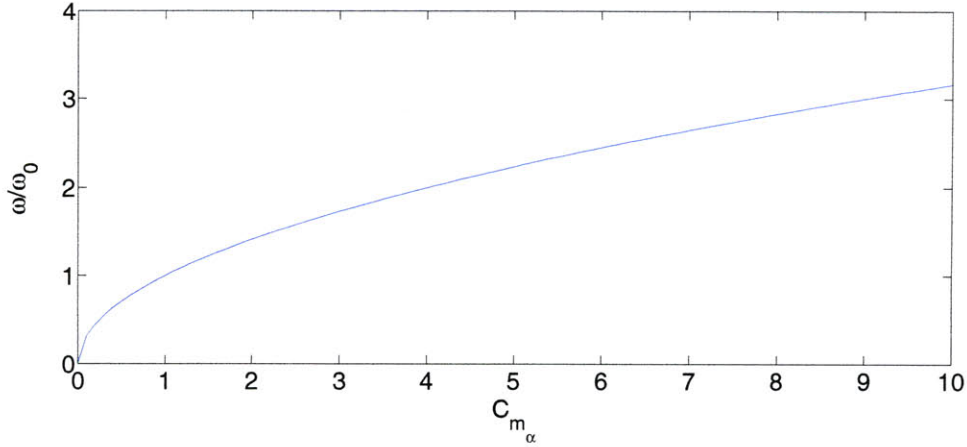


Figure 7-1: Spin rate versus C_{m_α} for $S_g = 1$. In this case ω is scaled by ω_0 . The plot shows that ω scales as the square root of C_{m_α} .

per inch).

$$T_i = \frac{\omega \kappa}{U 2\pi} \left[\frac{\text{turn}}{\text{in}} \right] \quad (7.6)$$

when U is in m/s and $\kappa = 0.0254$ m/in or when U is in ft/s $\kappa = 1/12$ ft/in.

It should be noted that this is a first order approximation, however if one were to expand the coefficient of overturning moment term to

$$C_{m_\alpha} = C_{m_{\alpha 0}} + C_{m_{\alpha 2}} \delta^2 \quad (7.7)$$

where $C_{m_{\alpha 0}}$ is the linear overturning moment coefficient, and $C_{m_{\alpha 2}}$ is the cubic overturning moment coefficient, the criterion can become a more accurate estimate². For a more complete solution non-linear effects and smaller forces involved with projectile motion should also be added. Robert McCoy outlines a numerical solution to the complete set of non-linear equations in his book "Modern Exterior Ballistics"[1].

²For more information on how this is done see chapter 13 of reference [1].

7.3 Generalized equations of motion for a torque free body

When a projectile leaves the barrel of a gun axial torque and forward momentum are no longer supplied. The body is now only under the influence of forces within itself, gravity, and aerodynamic forces. That is to say that no torque is being applied to the body directly. Let the body be defined by a coordinate system xyz fixed to the projectile (see Figure 7-2). Let the axial spin rate be prescribed by $\dot{\psi}$ while xyz is held fixed on the body. The coordinates xyz are then allowed to move about the XYZ coordinate system with angles θ and ϕ . The coordinate XYZ is allowed to travel with the point G but not to spin. Z is the direction of the forward velocity of G , and is also the direction of the precession rate $\dot{\phi}$, which corresponds to a precession of the xyz coordinate system about Z . The angle θ represents the angle between Z and z , and is known as nutation; ϕ represents the angle between X and x , and is known as precession; and ψ is the angle between x and x' (not shown) is known as spin.

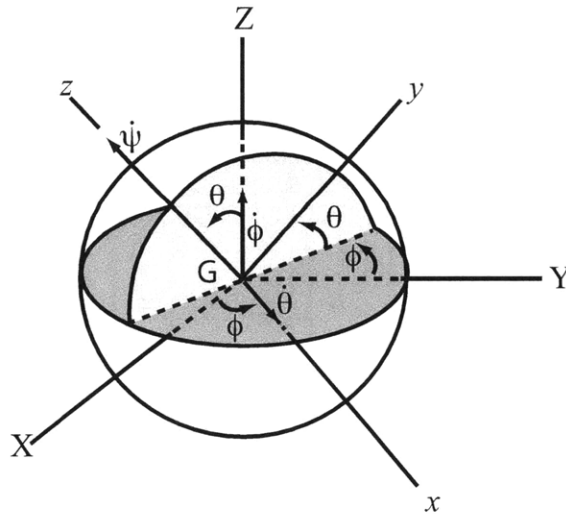


Figure 7-2: Relationship of XYZ and xyz reference frames. Directions of $\dot{\phi}$, $\dot{\psi}$, and $\dot{\theta}$ are shown as positive. G is at the origin.

To determine the equations of motion the relationship between the angles (ϕ, θ, ψ) and the angular velocities $(\vec{\Omega}, \vec{\omega})$ must be defined. Notice that xyz is not allowed to

spin in the $\dot{\psi}$ direction. Therefore, the xyz -reference frame is rotating with $\vec{\Omega}$, and the body-fixed reference is rotating with $\vec{\omega}$, where both are defined as follows.

$$\vec{\Omega} = \dot{\theta}\vec{e}_x + \dot{\phi}\sin(\theta)\vec{e}_y + \dot{\phi}\cos(\theta)\vec{e}_z \quad (7.8)$$

$$\vec{\omega} = \dot{\theta}\vec{e}_x + \dot{\phi}\sin(\theta)\vec{e}_y + (\dot{\psi} + \dot{\phi}\cos(\theta))\vec{e}_z \quad (7.9)$$

The angular momentum of center of mass can be defined as follows.

$$\vec{H}_G = I_G\vec{\omega} \quad (7.10)$$

Where the moment of inertia I_G can be defined as,

$$I_G = \begin{bmatrix} I_{xx} & I_{xy} & I_{xz} \\ & I_{yy} & I_{yz} \\ & & I_{zz} \end{bmatrix} = \begin{bmatrix} I_{xx} & 0 & 0 \\ & I_{yy} & 0 \\ & & I_{zz} \end{bmatrix} \quad (7.11)$$

notice that the products of inertia (I_{xy}, I_{xz}, I_{yz}) become zero when the axis of symmetry falls on the axis z , which reduces the complexity of the problem immensely. The equations of motion can then be found by summing the moment about point G .

$$\sum M = \frac{d}{dt}\vec{H}_G = \vec{H}_G = \vec{H}_G|_{xyz} + \vec{\Omega} \times \vec{H}_G = \vec{r} \times \vec{F} \quad (7.12)$$

Where F is the force of interest and r is the distance from the force to the point at which the moments are taken. The vector $\vec{H}_G|_{xyz}$ represents the derivative of \vec{H}_G in the xyz direction, therefore the derivative of the unit vectors in xyz do not need to be taken, and are encompassed in the term $\vec{\Omega} \times \vec{H}_G$. Since $I_{xx} = I_{yy}$, we will let $I = I_{xx} = I_{yy}$. The angular momentum equation 7.10 then becomes:

$$\vec{H}_G = I\dot{\theta}\vec{e}_x + I\dot{\phi}\sin\theta\vec{e}_y + I_{zz}(\dot{\psi} + \dot{\phi}\cos\theta)\vec{e}_z \quad (7.13)$$

Combining equations 7.12 and 7.13 returns the moment equations in the xyz -reference

frame.

$$\begin{aligned}
\sum M_x &= I\ddot{\theta} + (I_{zz} - I)\dot{\phi}^2 \sin\theta \cos\theta + I_{zz}\dot{\phi}\dot{\psi} \sin\theta \\
\sum M_y &= I\ddot{\phi} \sin\theta + 2I\dot{\phi}\dot{\theta} \cos\theta - I_{zz}\dot{\theta}(\dot{\psi} + \dot{\phi} \cos\theta) \\
\sum M_z &= I_{zz}(\ddot{\psi} + \dot{\phi} \cos\theta - \dot{\phi}\dot{\theta} \sin\theta)
\end{aligned} \tag{7.14}$$

7.4 Minimum axial velocity required to balance the aerodynamic pressure force (first order estimate).

This section outlines a first order approximation of the minimum axial spin rate required for a projectile traveling along a straight path through an air filled medium.

In order to apply the generalized set of equations from section 7.3 to the case of a spinning projectile the following assumptions must be made. The weight of the projectile acts through the center of mass at point G (see figure 7-3). The force F_p acts through a point some distance l along the z -axis. This force represents the aerodynamic pressure associated with travel through the air medium. Like the center of mass, this pressure force can be integrated over the surface of the body to estimate a point at which it acts. For a first order estimate this will be sufficient, but the complexity of the pressure forces on a projectile are more complicated than this assumption. Furthermore, if we assume that the radius of gyration is zero when the projectile leaves the barrel, then we can set up the problem as follows. Figure 7-3 illustrates the coordinates used in analyzing this projectile.

The forces due to F_p can be decomposed into the xyz coordinate system.

$$\vec{F}_p = F_p \cos\theta \vec{e}_z - F_p \sin\theta \vec{e}_y \tag{7.15}$$

Where the initial conditions are

$$\vec{l} = l \vec{e}_z \tag{7.16}$$

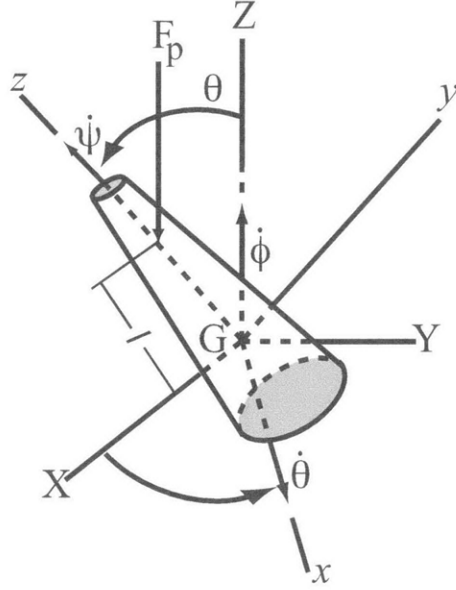


Figure 7-3: Projectile traveling in Z direction. G is center of mass, and F_p is the acting point of the aerodynamic pressure.

$$\begin{aligned}
 \theta = \text{constant} &\rightarrow \dot{\theta} = 0 \\
 \dot{\phi} = \text{constant} &\rightarrow \ddot{\phi} = 0 \\
 \dot{\psi} = \text{constant} &\rightarrow \ddot{\psi} = 0
 \end{aligned} \tag{7.17}$$

Summing the moments about the point G and substituting equations 7.16 and 7.17 into 7.14.

$$\sum M = \vec{l} \times \vec{F}_p \tag{7.18}$$

$$\sum M = F_p l \sin\theta \vec{e}_x = I_{zz} \dot{\phi}^2 \sin\theta \vec{e}_x + I \dot{\phi}^2 \sin\theta \cos\theta + I_{zz} \dot{\phi} \dot{\psi} \sin\theta \tag{7.19}$$

Remembering that $\omega \vec{e}_z = \dot{\psi} + \dot{\phi} \cos\theta$ then equation 7.19 can be rewritten as,

$$\sum M = F_p l \vec{e}_x = I_{zz} \dot{\phi} \omega_z \vec{e}_x - I \dot{\phi}^2 \cos\theta \vec{e}_x \tag{7.20}$$

and solving for $\dot{\phi}$ using the quadratic formula yields the following.

$$\dot{\phi} = \frac{-I_{zz} \omega_z \pm \sqrt{I_{zz}^2 \omega_z^2 - 4 I P l \cos\theta}}{2 I \cos\theta} \tag{7.21}$$

If we look at the term under the square root, we can analyze the critical $\omega_z|_{cr}$ to keep the projectile on a stable path. To keep from taking the negative square root and getting imaginary numbers we see that the left hand term in the square root must be greater than or equal to the one on the right.

$$I_{zz}^2 \omega_z^2 \geq 4IF_p l \cos\theta \quad (7.22)$$

Thus, $\omega_z|_{cr}$ is,

$$\omega_z|_{cr} \geq 2 \frac{\sqrt{IF_p l \cos\theta}}{I_{zz}} \quad (7.23)$$

The moment of inertia of a cone can be expressed as,

$$I_{zz} = \frac{3}{10} m R^2 \quad (7.24)$$

$$I = \frac{3}{80} m (4R^2 + h^2) \quad (7.25)$$

where h is the height of the cone and R is the radius. The force F_p is determined by the drag force acting on the cone, and can be estimated as, where C_D is the drag coefficient.

$$F_p = \frac{1}{2} C_D \rho U^2 A = \frac{1}{2} \rho C_D U^2 R h \cos\theta \quad (7.26)$$

Combining equations 7.23 through 7.26 $\omega_z|_{cr}$ becomes,

$$\omega_z|_{cr} \geq \frac{5hU}{2m^{\frac{1}{2}}R^{\frac{3}{2}}} \left[\frac{\rho}{10} \cos\theta (4R^2 + h^2) \right]^{\frac{1}{2}}. \quad (7.27)$$

Figure 7-4 shows how the critical rate of rotation increases as a function of length to diameter ratio. There is an exponential increase in the spin rate required to maintain stability of a large length to diameter ratio projectile. This explains why most projectiles with length to diameters greater than about 3 have other types of stabilization mainly fins or flaring. For instance, missiles use fins for both stabilization and direction control, while many rockets use flaring and rocket directed thrust to

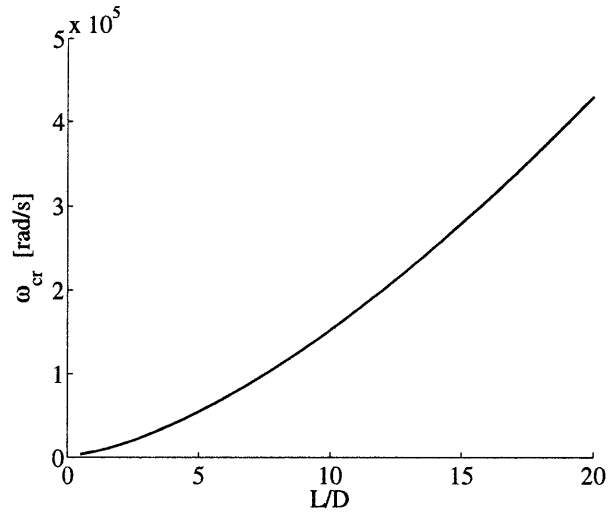


Figure 7-4: Minimum spin rate required as a function of length to diameter ratio (L/D). This particular case had a $D = 0.4$ in, and a varying mass from 1 to 42 grams.

maintain stable flight. For projectiles that will travel underwater the reduction of fins and flares makes gyroscopic stabilization a desirable criterion, but may not be feasible with these excessive spin rates.

7.5 Conclusions

In cooperation with the tests performed in Aberdeen, MD mentioned in chapter 6 projectiles were tested in air at Indian Head, MD in an independent study. The studies at both Aberdeen and Indian Head included non-rotating, rotating, and fin stabilized projectiles. During the Indian Head study it was found that the non-rotating projectiles were just as unstable as the rotating ones. This is likely do to the insufficient spin rates required for gyroscopic stabilization of these long projectiles. The rifles used in Aberdeen and Indian Head had rifling of 1 turn in 15 inches. The projectiles were fired at 3200 ft/s. This translates into a rotation rate of 16085 rad/s. Using equation 7.27 the minimum spin rate is roughly 420000 rad/s, or 26 times more rotation than used in these studies. This translates into 1 turn in 0.56 inches. It is possible that this rifling would be difficult to make, and could require the projectiles to be spun up to speed before being shot through a non-rifled barrel. Furthermore,

if the radius of gyration was not centered about the barrel of the rifle, the bullets could potentially rip themselves apart as they leave the barrel. Obviously, the design of these types of bullets would have to be reconsidered. On the positive side, if these spin rates could be reached the bullets would not require other means of stabilization.

This study emphasizes the excessively large spin rates required to gyroscopically stabilize large length to diameter ratio projectiles in air. This is in contrast to the need for these types of stabilization techniques underwater, where projectiles can be stabilized through contact with the underwater vaporous cavities they inherently create.

7.6 Acknowledgments

I would like to personally thank Brenden Epps for helping me derive these equations from first principles, for spending hours discussing this thesis and many other topics, and for his patience with my often misguided ideas.

Bibliography

- [1] Robert L. McCoy. *Modern Exterior Ballistics*. Schiffer Publishing Ltd., 4880 Lower Valley Road, Atglen, PA 19310, 1999.

Chapter 8

Shallow angle bullet entry

An extended abstract of this chapter has been approved for a full paper submittal to the 7th International Symposium on Cavitation CAV2009 conference in Ann Arbor, MI and will appear as: Tadd T. Truscott, David N. Beal and Alexandra H. Techet, Shallow Angle Water Entry of Ballistic Projectiles, *Proceedings of the 7th International Symposium on Cavitation*. August 17-22, 2009. Ann Arbor, Michigan.

8.1 Introduction

Through the use of high-speed videos, better testing facilities, and increasing performance from computational methods, the ability to predict and design underwater ballistics is progressing. One of the challenges left in determining design criterion is to validate an axisymmetric theoretical model for predicting cavity size and shape. The current model is determined from the tip diameter and forward velocity. Here we present a validation technique using an experimental testing facility built to test 22 caliber projectiles. During the study the cavity model was closely scrutinized and improvements were made that provide a better fitting parameter and a small angular rotation component. The experiments show good agreement with the revised cavity model. They also show the tendency for smaller length to diameter ratios to tumble once underwater, and emphasize the role the cavity plays in stabilizing these projectiles.

The experimental setup provided a more controlled environment in which higher quality and faster frame rate images could be acquired. This was a direct improvement over the full scale tests at Aberdeen which had poor lighting, cloudy water, and relatively slow camera speeds. Here, three high-speed cameras were used to obtain better resolution and higher frame rates of the water-entry phenomena. Thus, the experiments were more controlled, image quality was greatly improved, and motion of the bullet and cavity was captured more quickly. One of the drawbacks of using the facilities at MIT was the limited speed and size of the bullets that could be fired due to safety concerns. Compared to the Aberdeen tests, the projectiles used here have smaller calibers and lower speeds. Therefore, the results may not be completely comparable to the larger speeds and size of the bullets tested in Aberdeen. However, these experiments increase the understanding of high-speed projectile water-entry at shallow angles. In particular, the mechanisms of water-entry are discussed, the cavity size relative to impact speed and tip geometry is shown, the deceleration rates of water-entry are given, the forces associated with water-entry are estimated, and the associated cavity formation is analyzed.

8.2 Experimental details and methods

The high speed nature of these projectiles required a well thought out experiment capable of precise timing and remote triggering. Extensive thought and care was taken to make these experiments simple, elegant, reproducible, and safe. Some of the considerations included: where to perform these experiments, how to make a tank that would allow visualizations but would not shatter if a bullet strayed off course, and timing the impact of the bullets to coincide with the camera frame rates, to name a few. These restraints guided the design, setup, and procedures of this experiment. All tests were approved through the proper authorities before testing could commence, and all systems and procedures were overseen by both the Safety Office and Athletics Department at the Massachusetts Institute of Technology.

8.2.1 Impact tank

The impact tank is made of 0.75 in bullet-proof Lexan to ensure that if a bullet did hit the side of the tank that it would not break and leak water onto the floor. The tank is 6 ft long, 2 ft wide, and 2 ft deep on three sides which only 18 in deep on the bullet entry side. The lower entry side allows the bullet to enter the water at very shallow angles, while the higher sides help keep water inside the tank after bullet entry and allow the cameras to see the action without the visually disturbing line formed by the top of the tank (see figure 8-1). An aluminum frame made of 2-inch square extrusions from 80/20® Inc. was constructed around the tank for support. The entire frame and tank rests on two large dollies for support and transportation. Figure 8-2 shows an image of the tank in place. The back of the tank is protected from bullet impacts by two large 0.5 in steel plates, one of which rests on the bottom of the tank, while the other is inclined at an angle towards the bullet entry direction to deflect bullets down and into the water after impact (see figure 8-1).

By the end of the study a few bullets impacted the tank directly. Although evidence is clearly visible, the tank withstood these impacts without shattering and the glued seams appeared to sustain no damage.

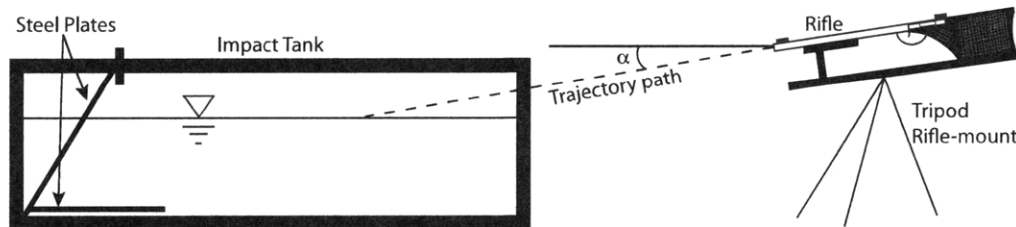


Figure 8-1: Gun and impact tank set up viewed from side. The gun is mounted on a tripod and aimed at a shallow angle (α) to the free surface inside the tank. The trajectory appears to pass through the front side of the tank (right side in image), but in reality the front wall is shorter to accommodate for this. Two steel plates help decrease ricochet and impact with the back of the tank (left side).

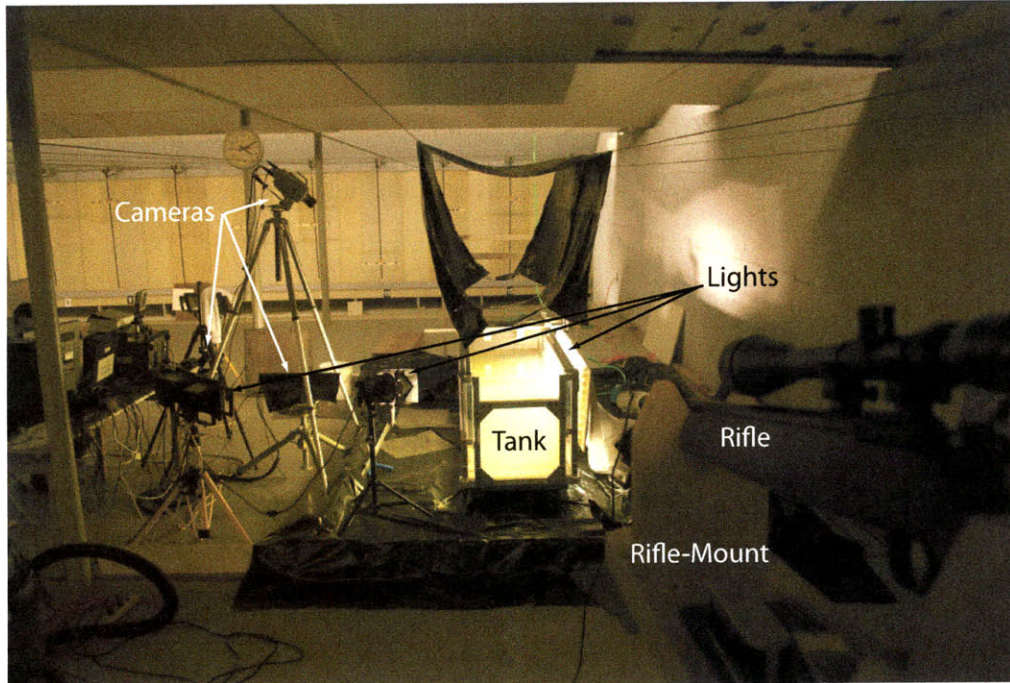


Figure 8-2: Photograph of the experimental setup as seen from a position next to the rifle. The tank is visibly lit from the right hand side by a bank of 32 florescent bulbs. A spot light is seen on the left aimed at the free surface. Three video cameras are also aimed at the surface and are controlled by the computers located on the far left. Plastic placed under the tank and hanging from above prevents water from wetting the floor and ceiling.

8.2.2 Shooting Range

These experiments were performed in the rifle range at MIT. The range is underground with cement walls. The range is 50 ft long with a vented steel backstop. The width of the facility is 50 ft and the ceiling height is 12 ft. All of the supporting equipment took up three full shooting lanes and only about half of the length of the range was needed. Permission to perform the experiments was granted by both the MIT physical fitness faculty and the MIT Chief of Police. Experiments were performed in cooperation with the MIT shooting range faculty, namely Will Hart. All shots were performed by Mr. Hart and his long hours and hard work are much appreciated.

The bullets were fired into the impact tank at a shallow angle, which caused a splash large enough to reach the ceiling of the rifle range. Plastic sheeting was placed

above the impact tank to ensure that the ceiling did not become wet. The tank was placed inside a large containment area comprised of a large plastic sheet (12×12 feet square) inside of a frame with 6 inch sides to ensure that if the tank did leak it would not leak onto the floor.

The gun was mounted in a wooden gun mount attached to a Manfrotto 410 geared head (three axis) and placed on a Bogen tripod. The setup could easily be adjusted to half a degree increments along all three axes. When aiming the gun a laser site was used to help determine the point of impact. A digital level was used to determine the angle the gun was in relation to the free surface. After each shot the gun was checked for alignment and angle. The setup was very reliable; alignment and angle measurements were nearly constant between shots and were only needed when new parameters were introduced.

8.2.3 Bullets

The unusual design required for water entry bullets typically includes high length to diameter ratios and blunt tips. These types of bullets are not common; most bullets have small L/D and ogive tips. In general, standard bullets are designed to split apart or mushroom after impact with a target. Typically, this ensures the most damage upon impact. Since most targets have a high percentage of water contained within, impact with the water surface can cause bullets to break apart. Therefore, custom made bullets were designed with high length to diameter ratios, special tips, and materials strong enough to resist breakup.

The bullet designs were constrained primarily by the weight and size of the 22 caliber rifle barrel. The weight was set to be the same as that of a typical 22 caliber bullet. This was done to ensure that the 22 caliber powder and cap would have a similar accelerating affect on the prototype bullets as the standard manufactured brand. The maximum weight was thus set to 40 grains, which is 2.59 grams, and the maximum diameter set to 0.22 in or 5.5 mm. The bullets were also designed to have the same shoulder length as the standard rounds. The shoulder is the part of the bullet in contact with the rifling (see figure 8-3). The shoulder is also a key

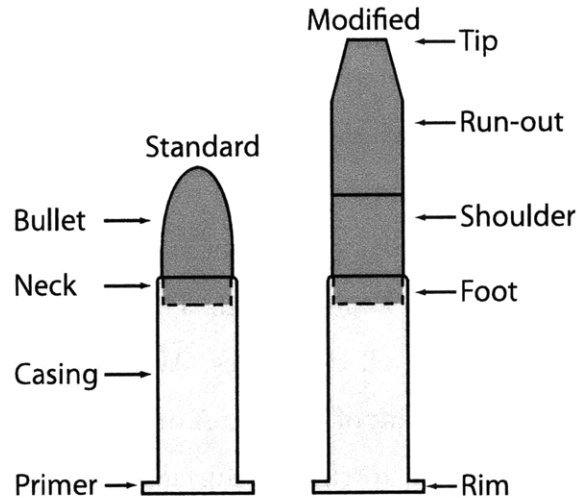
















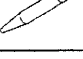
Figure 8-3: Drawing of a standard and modified 22 caliber bullet with the nomenclature used to describe them (not to scale).

factor in producing the same amount of thrust for each bullet. If the shoulder doesn't penetrate as much of the rifling then some of the pressure from firing can leak past the bullet and reduce the back pressure, decreasing the velocity of the bullet down the barrel. It was initially assumed that velocities would be similar if the shoulders were prescribed the same. However, this assumption is somewhat false since it is probable that all of the materials used for the modified bullets could not penetrate as much of the rifling since they were considerably harder than the standard lead bullets. Thus it was expected that the modified bullets would travel at lower speeds than the standard bullets.

A wide range of bullet designs were designed and tested. Three materials were used to make these bullets: Bronze, Steel, and Aluminum. Each material is less dense than the lead bullets used in standard 22 caliber rounds ($11,340 \text{ [kg/m}^3\text{]}$). The lower densities allow the bullets to have larger length to diameter ratios. Table 8.1 highlights the tip design, density, and dimensions of the bullets used. A schematic of the general bullet shape and list of terms can be seen in Figure 8-3.

The foot portion of each bullet was predetermined using the standard 22 caliber bullets as a guide. The foot portion of the bullets rest inside the casing (see figure 8-3). This portion of the bullet must have a diameter large enough to stay inside the

Table 8.1: Bullet types and their respective tip diameters (d_{tip}), density (ρ), and L/d_{tip} ratios. Not all of the bullets in this table were used in the experiment but all were manufactured. Those bullets that were used have a corresponding number associated with them which relates to their association in post processing (see table 8.2).

#	Name	Bullet type	Tip diameter [in]	Density [kg/m ³]	L/d_{tip}
9	12Aluminum		0.12	2700	13.9
	12Steel		0.12	7850	5.3
	12Bronze		0.12	8300	4.9
12	13tipAluminum		0.13	2700	13.3
	13tipSteel		0.13	7850	5.4
	13tipBronze		0.13	8300	4.8
8	15Aluminum		0.15	2700	10.5
	15Steel		0.15	7850	4.0
11	15Bronze		0.15	8300	3.7
7	22Aluminum		0.22	2700	7.2
	22Steel		0.22	7850	2.5
10	22Bronze		0.22	8300	2.4
13	06Aluminumshoulder		0.06	2700	29.5
14	06Aluminumshouldertaper		0.06	2700	29.5
15	06Aluminumtaper		0.06	2700	29.5

shells after being press fit (0.204 in). It is important to ensure a good press fit to gain the best back pressure possible when fired. Back pressure is one consideration when estimating the projectile speed for manufacturers. If the back pressure is too low the bullet will move very slowly, if it is too high it may alter the shape of the projectile or damage it. A balance is required to ensure uniform velocities from projectile to projectile. Therefore, tight tolerances were required to fit the bullet into the casing at the neck. Directly above the foot of each bullet is the shoulder. The shoulder has the largest diameter of the entire bullet. As the bullet passes through the barrel the shoulder engages with the rifling. This ensures that the pressure created after firing remains behind the bullet (not leaking past the sides of the bullet) pushing it through the barrel, and ensures that the bullet rotates about its symmetry axis. Rotation ensures stability of the bullet in air through gyroscopic stabilization (see Chapter 7). This rifle in this study has a turn ratio of 1/16 or one rotation in sixteen inches. Typical speeds of the bullets used here were estimated at the end of the rifle to be ≈ 1200 ft/s, which yields a spin rate of ≈ 5650 rad/s. This rotation rate is not sufficient according to equation 7.27, which should be ≈ 53000 rad/s. This high spin rate translates into a rifling of 1 turn in 1.7 inches. The design and fabrication of a new rifled barrel with these specifications is outside the realm of this study. Therefore, we accepted the 1/16 standard and shot the bullets a maximum of 4 meters from the free surface to decrease the distance the projectiles had to become unstable.

The final design of the bullets is based upon the tip shape. Once the tip shape was known, the bullets could be designed to fit within the desired weight. The cavity shape was determined using a cavity model based on empirical evidence gathered by Logvinovich [1]. The model is derived, explained, and improved in Section 8.4 and is based on the tip diameter and velocity. The cavity shape can be determined using any mathematical solver and plotting function. The bullet can then be designed to fit within the cavity. The run-out of the bullet is lengthened until the bullet mass is equal to 40 grains. The final bullet drawings that were used to manufacture the bullets can be found in Appendix B.

In general, reloading 22 caliber rim fire rounds is not common, nor recommended

by the manufacturer. This procedure requires great care and caution to ensure that no one is hurt and that the rounds are not accidentally fired. Proper eye protection must be worn and the loading should be done in a rifle range. The reloading should be performed while keeping the face and body away from the axis of the bullet and casing. The first step in reloading is to remove the bullets and expose the shell. This was done by placing the bullet in a pre-made 0.5 in thick plate made to fit the bullet snugly using the rim and casing to hold the bullet in place. By placing the assembly on the table and grasping the bullet with vice-grips, the bullet was gently pulled out of the casing. It is essential that caution be used to ensure that the neck is not bent in the process and that the powder is left inside the casing. The bullet was disposed of in a lead recycling bucket. Then the casing was gently placed on a rubber pad and the metal reloading template was placed over the casing. The reloading template is a steel block (3 in x 2 in x 2 in) machined to fit both the casing and the bullet, and is used to press the bullet into the casing. A modified bullet was placed in the top of the reloading template and a bronze rod and a mallet was used to set the modified bullet into the casing. Once the two parts are securely seated the bullet-casing assembly is removed and the bullet is ready for firing.

8.2.4 Image Acquisition and Processing

In this experiment it was very important to obtain high quality images that capture the entry phenomenon. Thus, three different video cameras and two SLR cameras were used. As with all image capture techniques, lighting and event timing were also crucial elements for success. Images were then digitally processed, used to measure various parameters and compared to models for validation.

Hardware

All of the hardware used in this setup was chosen for specific purposes. The first high speed camera of choice was the Shimadzu HyperVision HPV-1 ultra-high-speed video camera, which can take images up to 10^6 frames per second (*fps*) at 312×260

pixel resolution, but can only store 103 images before the buffer must be emptied. This camera was extremely useful and enabled the best close up images of the bullets. Although timing of this camera proved to be a bit difficult, it was easy to use and often captured 100 frames of the bullet entering the field of view, impacting the water surface, and exiting the field of view.

The second camera used was a Phantom 7.3 manufactured by Vision Research. Images were captured at 25×10^3 fps with a resolution of 512×256 pixel resolution. This camera can store up to 8,000 images, which is almost 4 seconds worth of data, making timing of the event trivial. This camera was used to take an overview of the entire event. It was positioned either above looking almost isometrically at the target or from the side looking above and below the surface of the water.

The third camera was an IDT X-Stream VISION XS-3. Images were captured at 2,300 fps with 1280×460 pixel resolution. This camera can store up to 6000 images, allowing it to record for nearly 3 seconds, which is more than enough time to capture these events making timing trivial. The images from this camera had the largest pixel resolution, improving image processing. This camera was also used as an overview of the event and was most often placed to the side of the event with both the water and the air in focus.

A fourth type of camera was used in conjunction with a Discovery Channel shoot done a year after the first study was completed. The cameras used for this shoot were Photron Fastcam S A1, which captured images at 10,000 fps at a resolution of 768×768 pixels. Timing is also trivial with this camera's large 8,000 frame storage capacity and circular triggering mechanism. Two of these cameras were used simultaneously for some of the shots, allowing both a side profile and a head on profile. The head on views were taken by placing a mirror in the tank near the steel plates and angling it so that the camera from the side could see the bullet coming toward the mirror. These shots were valuable in showing both the precession of the bullets in the cavity and the axis-symmetry nature of the impacts.

To gather higher quality images with color and potentially better lighting two single lens reflex (SLR) cameras were used. The entire setup had to be modified to

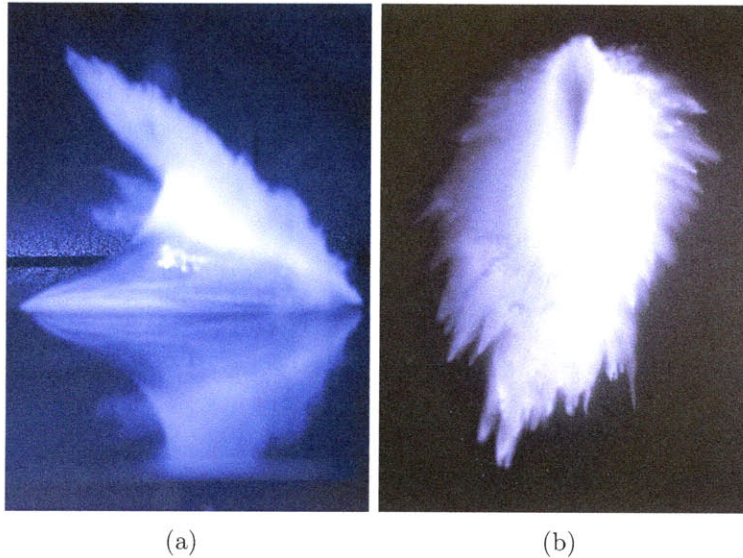


Figure 8-4: a) Photograph of a 0.22 caliber bullet entering the water viewed from the side. Camera settings: 2s exposure, 500 ns flash, F-stop 5.0. b) Photograph of the same bullet and time viewed from above using another camera.

use these cameras and the major goal in using them was simply to gain the highest resolution images possible to highlight this body of work. The setup was modified by placing a wooden frame around the tank ($4 \times 4 \times 16 \text{ ft}^3$). A thick black plastic sheet was stapled in place on top of the framework to create a dark room for the cameras. Each camera aperture was set open by a remote switch just before the bullets were fired, and a second trigger was used to set off the strobe which provided 1000 watts of light for less than 2 millionths of a second. The camera apertures were then closed. One camera was placed to get a view of the impact from the side slightly above the free surface, while the other took images from above by being placed in an aquarium. Figure 8-4 show two of the images obtained using the SLR cameras. The splash from entry is clearly shown from the side while the image from above reveals the axisymmetric nature of water entry.

Lighting consisted of both back lighting and forward lighting. Back lighting was provided by a bank of 32 florescent bulbs next to one another. Foreground lighting was done slightly off angle by a 1000 W spotlight to the right of the images. Lighting is one of the most difficult parts of any image study and this was no exception. The

backlighting was the major key to allowing the images to be processed for cavity size and also letting the bullet be seen within the cavities when the cavities were large enough.

Timing and image acquisition

The short duration of a bullet impact requires precise timing, especially for cameras with short memory and lighting with short durations. However, all cameras had to be externally triggered and therefore a timing system was devised. It consisted of a central electronic timer (TimeMachine by Mumford Micro Systems) and two different types of external triggers (more below). Output cables were manufactured in house to deliver the five volt rise required to alert the high speed video cameras to begin acquiring data. SLR cameras were by the default output of the electronic timing device.

The first trigger used was an infrared (IR) optical sensor. The IR sensor is made of two sensors and two emitters. The emitters emit IR light and the sensors sense the light. When the light stream is broken by a solid object the IR sensor is triggered. The two sensors are placed on a piece of PVC pipe 6 inches apart. The sensor was mounted to the end of the rifle. When the bullet was fired the time between the two IR sensors triggering was used to determine the speed of the bullet. The electronic trigger calculates the speed of the bullet and sends a pulse to the cameras at a time delay based on a known distance to the target entered by the user. This sensor gave sporadic results after the first day of shooting and after the study was complete the manufacturer determined that the unit was broken.

The second trigger was a flat disc sound sensor. This sensor detects both sound and pressure waves when the gun is fired. It was determined early on that if the sensor were mounted to the gun mount that simply touching the gun mount or having ones hand on the gun and talking could set it off. Therefore, placing this sensor downrange helped decrease false triggering. This sensor was used most often.

Once the sensor is working it is important to determine how much time must elapse or delay before the cameras should begin acquiring data. In the case of the

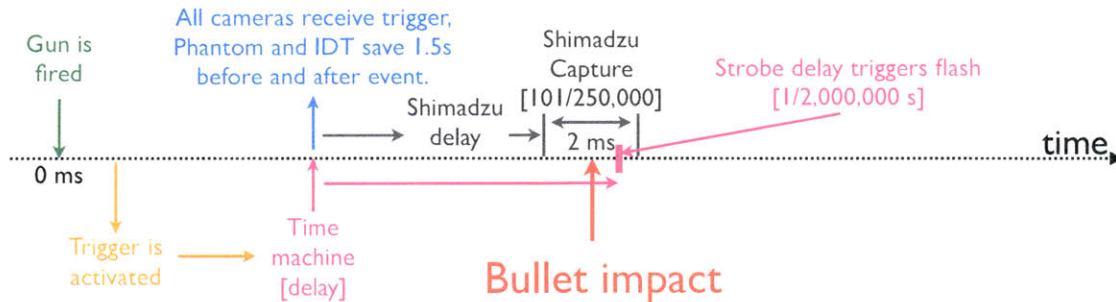


Figure 8-5: Time line diagram depicting how timing mechanisms interact and capture the projectile impact.

IDT, Phantom and Photron cameras there is ample time in the buffer to capture all of the bullet entry in essentially every timing configuration. The Shimadzu and SLR cameras must have a delay set by the electronic trigger. This time delay is crucial to capture the bullet in the field of view.

These types of triggers are often used when photographing bullets. The sound waves from the bullet set off the trigger and the timing switch can delay the moment when the strobe is illuminated. Our particular electronic timing device can only be delayed in increments of 0.0001 seconds which is the time it takes the bullet to travel about 3 cm, which was a fourth the size of the Shimadzu viewing window. In order to get this type of trigger to work with these viewing windows one can adjust the internal digital trigger of the camera itself, which is not always a successful measure nor possible in the case of the SLR cameras. Another alternative is to adjust the trigger by physically moving it a few millimeters closer to or farther from the target of interest. Through trial and error one can find the point where the sound waves from the bullet trigger the event properly. A combination of these two techniques and patience was employed for the photographs and the Shimadzu camera acquisitions. A diagram of the timing issues addressed here is presented in figure 8-5.

Image Processing

The data collected was then processed to determine pertinent pieces of information. The position of the bullet was extracted and used to determine the forces at play

during impact. The cavity shape and splash formations were also extracted in each image. These pieces of information have been used as a method for quantifying the general path and cavity formation for each of the bullet types. They also are also used as an empirical check against the Logvinovich model presented in section 8.4. Most of the data collected required some heavy user input to keep the finding algorithms from gathers too much or too little data. However, computer extraction was the preferred method to keep things consistent from image to image and case to case.

The position of the bullet was determined using two different methods. The first method allows the user to view the image, zoom into the area where the bullet is located and click on the corners or points of interest of the bullet. Using this data the computer then calculates the approximate center of the bullet for the position of the bullet. The second method uses an algorithm built into Matlab that scans the data set for transitions from high valued pixels to low ones (i.e. edge detection). Here we chose the Canny method of edge detection. This method differs from other methods because it uses both a strong and weak edge detector. It uses the weak edge detector results only if the the weaker edge is connected to a stronger one. This method normally yields more edges, making it slower, but more accurately gathering information for the user. The user is then shown an image of the result (see figure 8-6). The user can then click as many of the edges of interest they like. The edges become highlighted and the number corresponding to the selected edge is displayed in the title of the screen. When the user is done they simply click off of the image and the data is combined and saved into a cell. This method works well in determining the bullet edges, but doesn't seem to work as well for the tip and aft portion of the bullet, probably because the thresholding is too high. However, if the thresholding is turned too low then everything is outlined and seeing the bullet becomes too difficult. Nevertheless, the user retains the ability to adjust the thresholding at any point in the program.

The bullet is typically no larger than 9 pixels in diameter in these images. Although this makes data collection easier it becomes difficult to estimate the exact location of the bullets. Furthermore, to get the true center of gravity of the bullets

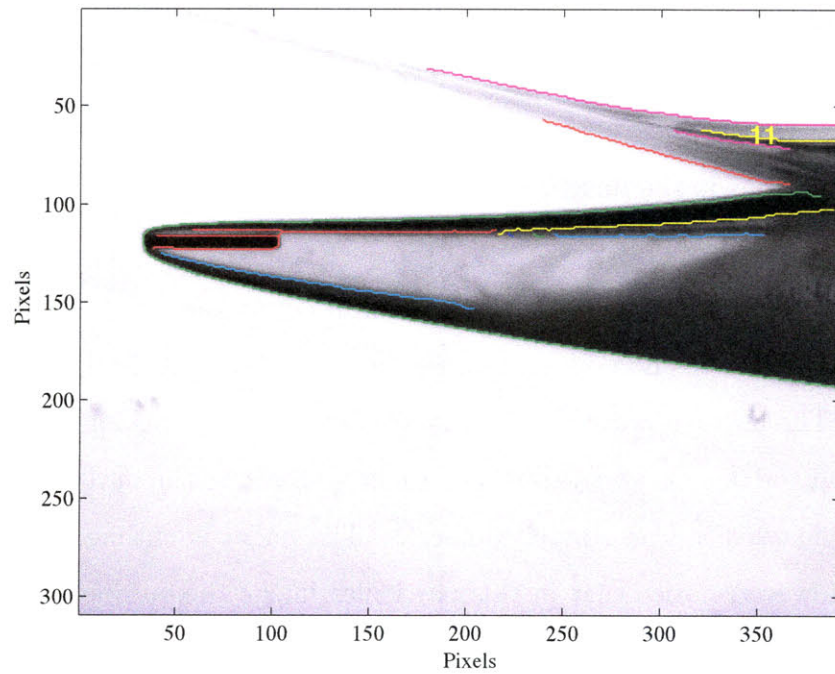


Figure 8-6: Typical output of a bullet impact image that has been zoomed, rotated, and an edge detection (Canny method) has been applied. The numbered outlines indicate edges that were detected. The user is prompted to select edges of interest at this point.

it must be assumed that the bullets are in plane and that if they are rotated around their planar axis their center of gravity can be found. In reality the bullets precess around their axis of symmetry, which causes them to rotate in and out of plane and thus the center of gravity location is not exact. However, a rough estimate of their position and velocity can be made.

The cavity is one of the easiest edges to find in each image. The cavity exhibits a very strong dark outline with lighter shading on either side, making it very detectable. The process of finding the cavity is similar to the second method of finding bullet position. The user is again prompted to pick the relevant portions of the cavity to keep as data. This is done because the edge detection also picks up spurious and unnecessary portions in the image, which would be difficult to sift through later (see figure 8-6).

The outline of the chaotic splash formation is determined in a similar fashion. The user is prompted to choose lines representing the outline of the splash above the free surface. The user chooses the ones they wish to keep by clicking near the edges of interest and the data is saved to a cell. Figure 8-6 shows the outline of the edges of the cavity marked in green by a number 1. The bullet is outlined in red by the number 2. However, notice that in this particular image the outline continues past the bullet and outlines the interior portion of the cavity between $x = 55$ to 225 and $y = 105$ to 120 pixels. The free surface is partially outlined by the green number 4. At this point the user would typically select the boundaries of interest. If more than one contour represents the body of interest then more than one contour can be selected.

Three different cameras were used in this study and required that the image processing codes determine which cameras had pertinent information and only allow the user to work with applicable images. The Shimadzu camera was aimed at the point of impact and data is processed for that camera if it exists. The IDT and Phantom cameras were aimed either above the free surface looking down at impact or aimed directly from the side to get the best possible back lighting and outlined side view of the bullet shot. The side view images are processed while images looking down on the free surface are simply used for visual qualitative evidence as necessary.

During the course of this study over 150 bullets were fired into the water tank. Of those only 99 were captured for data processing. Those not saved were normally not captured properly, or they were bullet types that had already been captured multiple times at a specific impact angle. In total the data sets comprise approximately 9 Gigabits of data. Each data set contains 100 images (on average) that need to be processed. Coupled with the storage of long strings of numbers representing edges of the cavity, bullet, and splash formation stored in memory, the task was daunting. The use of Matlab and heavy dependence on structs to store the data made the task much more bearable. Each case was represented by a struct which was composed of three key numbers; the first number represents the bullet type, the second represents the angle between the gun and the free surface, and the third represents the shot number of that type on that particular day. Table 8.2 shows how each of these three key pieces of information dictates where the data is stored. The data set then includes information ranging from whether or not the bullet skipped off the surface to the position of the bullet in each of the applicable cameras. All of the information gathered is organized into table 8.3.

The structures are filled as the user runs through each of the data sets and each individual image. The user first determines which cameras have applicable data and which images should be processed. Images are then brought on screen and the user is prompted to either determine the edges of the bullet, zoom in on a particular region of interest, or to choose applicable edges that outline cavity, splash, or bullet locations. Once the data is gathered the results can begin to be post-processed. Appendix B contains both the Matlab code used to outline the structure and the Matlab code used to gather the data as outlined.

8.2.5 Forces and moments

One of the most useful measurements made from a study of this nature is a comparison of forces and moments acting on the projectiles as they pass through the water column inside of the cavities they form. The determination of these forces and moments is very similar to the techniques used in chapters 3 & 4. The diagram presented in

Table 8.2: Outline of method used to uniquely store information about each impact case. Three numbers describe each case and correspond to bullet type, angle of attack in degrees, and the shot number at that angle with that bullet.
















#	Bullet Name	Bullet Type	#	Angle of attack [degrees]	Shot number
1	A- CCI Standard velocity Model# 0032 22LR no jacket		1	5.4	1
2	B- CCI Longs Model# 0029 22LR 1215 ft/s copper jacketed		2	5.5	2
3	C- CCI Velocitor Model# 0047 22LR 1435 ft/s, copper plated hollow bullet		3	5.6	3
4	D- CCI Short, high-velocity, Model# 0027 1080 ft/s, copper plated		4	6.1	4
5	E- CCI 17HMR Full metal Jacket, Model# 0055 2375 ft/s, copper jacketed, use different gun H&R 17 HMR sportster model		5	6.1	5
6	G- Eley 22LR Pack WS1130		6	6.2	6
7	22Aluminum		7	7.1	7
8	15Aluminum		8	7.8	8
9	12Aluminum		9	7.9	9
10	22Bronze		10	8.0	10
11	15Bronze		11	8.1	11
12	13TipBronze		12	8.2	12
13	06AluminumShoulder		13	8.3	13
14	06AluminumShoulderTaper		14	10.7	14
15	06AluminumTaper		15	10.8	15
			16	10.9	16
			17	12.3	17
			18	13.5	18
			19	13.8	19
					<i>etc.</i>

Table 8.3: Each case number is designated by a structure that contains the cells specified in this table. Each of the cells contains information that can be extracted to find relevant data. Not all cases have data within each cell. For instance, the Shimadzu camera may not have captured any images for a given run and therefore data regarding that camera will not appear in that particular case number.

Cell name	Description
wt	Weight [grams]
d	Diameter [mm]
spd	Speed of bullet as given by cartridge box.
skip	Skip [1], No-skip [2]
camrate	Camera capture rate [fps]. Given as three values IDT, Phantom, Shimadzu cameras respectively.
wcam	Camera to analyze yes [1], no [2].
img	Images of interest: [First_IDT_Image, Last_IDT_Image, First_Phantom_Image, Last_Phantom_image, First_Shimadzu_Image, Last_Shimadzu_Image].
freesurf	Free surface [unused]
phnimgnum	Phantom camera image number.
phncavity	Phantom camera cavity. This cell contains outlines of the cavity using edge finder for each image number.
phnpos	Phantom camera position. This cell contains points of the corners of the bullet using user designated points for each image number.
phnsplash	Phantom camera splash. This cell contains outlines of the splash formation using edge finder for each image number.
phnbullet	Phantom camera bullet. This cell contains outlines of the bullet using edge finder for each image number.
shmimgnum	Shimadzu camera image number.
shmbullet	Shimadzu camera bullet. This cell contains outlines of the bullet using edge finder for each image number.
shmpos	Shimadzu camera position. This cell contains points of the corners of the bullet using user designated points for each image number.
shmsplash	Shimadzu camera splash. This cell contains outlines of the splash formation using edge finder for each image number.
shm cavity	Shimadzu camera cavity. This cell contains outlines of the cavity using edge finder for each image number.
idtimgnum	IDT camera image number.
idtsplash	IDT camera splash. This cell contains outlines of the splash formation using edge finder for each image number.
idtbullet	IDT camera bullet. This cell contains outlines of the bullet using edge finder for each image number.
idtpos	IDT camera position. This cell contains points of the corners of the bullet using user designated points for each image number.
idtcavity	IDT camera cavity. This cell contains outlines of the cavity using edge finder for each image number.
idt_fs	IDT free surface position.
idtbulletbest	IDT better edge finding of the bullet position. This cell contains outlines of the bullet using edge finder for each image number.
shm_fs	Shimadzu free surface position.
shmbulletbest	Shimadzu better edge finding of the bullet position. This cell contains outlines of the bullet using edge finder for each image number.
phn_fs	Phantom free surface position.
phnbulletbest	Phantom better edge finding of the bullet position. This cell contains outlines of the bullet using edge finder for each image number.

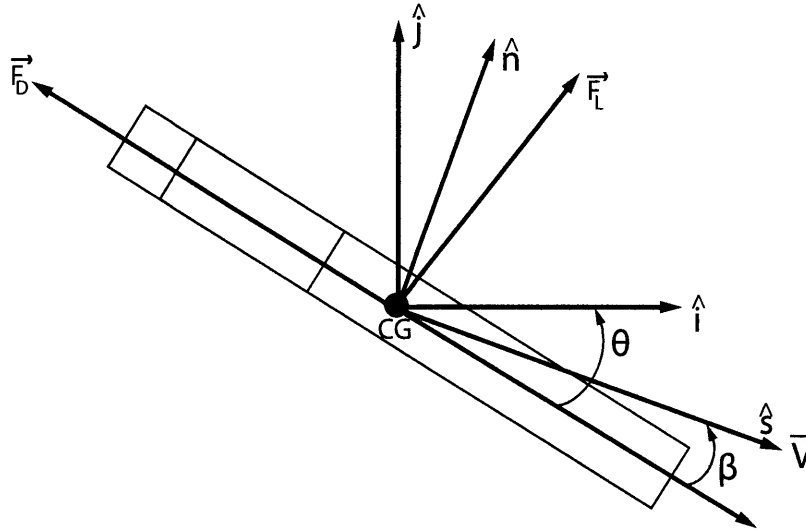


Figure 8-7: Free body diagram of bullet entry. The projectile center of gravity (CG) is traveling in the direction of \vec{V} , but is inclined with angle θ .

figure 8-7 shows how this straightforward formulation is derived. Assuming planar travel the forces of water entry are summed about the center of gravity (CG) and lumped into one term F_H follows (similar to section 4.3.5)

$$F_H \hat{i} + F_H \hat{j} = mg \hat{j} + (m + ma)(\ddot{y} \hat{j} + \ddot{x} \hat{i}) \quad (8.1)$$

where \hat{i} and \hat{j} are unit vectors in x and y respectively. Here, we neglect the forces of surface tension by assuming sizes greater than the capillary length and buoyancy because the projectiles are much denser than the vaporous cavities. The unit vector tangent to the projectile trajectory, \hat{s} , can be written in terms of the x and y components of instantaneous velocity, $\vec{V}(t)$,

$$\hat{s} = \frac{\vec{V}(t)}{|\vec{V}(t)|} = \frac{V_x}{|\vec{V}(t)|} \hat{i} + \frac{V_y}{|\vec{V}(t)|} \hat{j}. \quad (8.2)$$

The unit normal vector, \hat{n} , is defined as the cross product of the unit tangent vector with the unit vector in the z direction, \hat{k} :

$$\hat{n} = \hat{s} \times \hat{k} \quad (8.3)$$

The transverse force (\vec{F}_L) and in-line force of drag (\vec{F}_D) can then be determined as

$$\vec{F}_L = (\vec{F}_H \cdot \hat{n})\hat{n} \quad (8.4)$$

$$\vec{F}_D = (\vec{F}_H \cdot \hat{s})\hat{s} \quad (8.5)$$

Here, we present the transverse force using the subscript L, which is often called lift, however, we recognize that this force is merely orthogonal to the drag force and is not a true lifting force in this case. The coefficient of lift and drag is computed by normalizing these quantities by $\frac{1}{2}\rho|V(t)|^2A$, where A is the frontal area of the projectile.

The moments acting on the sphere are calculated by again assuming planar pitch angles. Evidence from camera angles looking head on at the projectiles show that the projectiles precess in and out of the plane, but in order to interpret the data this assumption must be made. Future work could include a method to resolve the forces in three dimensions. The moment can also be calculated using the moment of inertia about the approximate center of the bullet (CG) and the angular acceleration as

$$\tau = I\ddot{\theta}. \quad (8.6)$$

where $I = \frac{1}{12}m(3R^2 + L^2)$ is the moment of inertia, and R is the radius. The moment coefficient is then computed by normalizing these quantities by $\frac{1}{2}\rho|V(t)|^2Ah$.

8.3 Experimental Results

8.3.1 Ricochet and tumbling

The typical bullet shapes have a tendency to skip out of the water when shot at shallow angles to the free surface. Each set of data was analyzed to determine whether the bullets skipped off the surface. Figure 8-8 shows the relationship between the angle at which the bullets were shot and their tendency to skip off the surface. Notice that most standard bullets would resist skipping when fired above 11° , whereas the modified 22 caliber aluminum bullet #7 in table 8.2 can resist skipping up to 5° . A few other bullet types also resisted skipping at these angles including numbers 8, 9, 13 and 15, all of which are made of aluminum with large L/D values.

Although the 22 caliber bullets did not skip off of the surface at angles above 11° , they did tumble inside their cavities almost immediately after impact. Furthermore, bullet types 10, 11, and 12 (bronze) also tumbled shortly after entry even though they did not skip off of the surface. Part of this is due to the small length to diameter ratio of these bullet types. The larger length to diameter of the 22 aluminum slug style bullet allows it to lean against the cavity as it begins to pitch or yaw, creating a planing force that forces the bullet back into the cavity before it can tumble. This reduces the velocity of the bullet, but allows it to maintain some stability as it passes through the water column.

Although many different bullets were fired and thousands of images were gathered, there are essentially three typical types of bullet impact. First, the case when a standard bullet enters the water and tumbles until it either skips off the free surface, or tumbles to the bottom of the tank (figure 8-8, bullet type 1). Second, a successful water entry of a modified bullet with a large tip, which slows down rapidly and creates a cavity nearly four times larger than the aft portion of the projectile (figure 8-8 bullet type 7). Third, a modified bullet with a smaller tip that successfully enters the water and maintains a large velocity and kinetic energy after impact (figure 8-8 bullet type 15). The following section highlights one case from each of these bullet types. The magnitude of the forces and the different cavity shapes will be discussed.

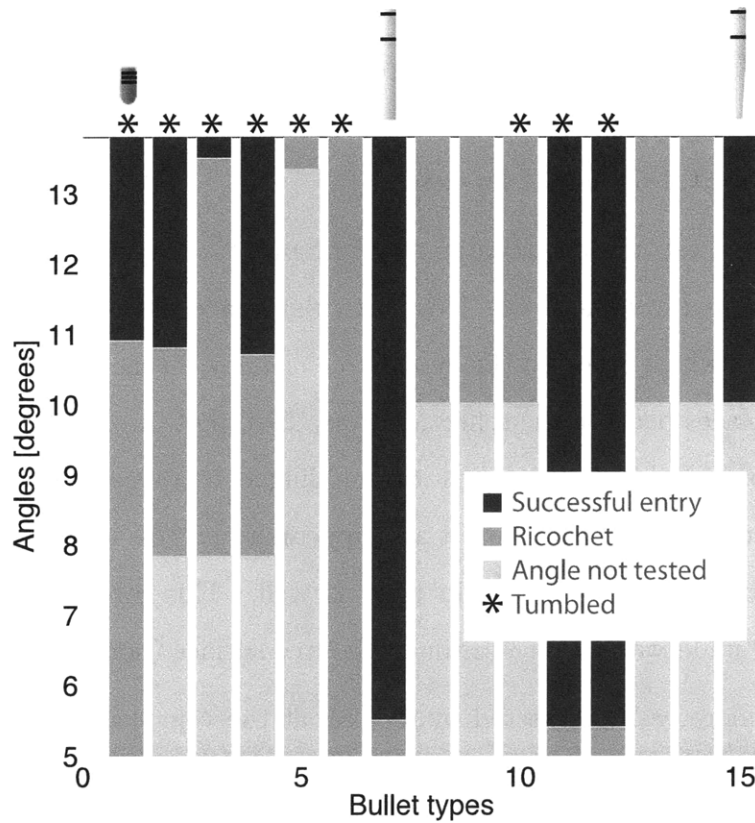


Figure 8-8: Bullet tendency to skip when shot at given angles to the surface. The angles shown here are the angle of the gun to the water surface. Bullet types are given by numbers and correspond to bullet types in table 8.2. Colors and symbols are referenced in the legend. The three bullet types presented in more detail are marked by images above chart, from left, 0.22 standard caliber bullet (type 1), 0.22 aluminum (type 7), 0.06 tapered aluminum (type 15).

8.3.2 0.22 standard projectile

A standard 0.22 bullet was shot into the water at an angle of 10.7° as seen in figure 8-9. The impact shows the sporadic nature of these types of water entry. Even at $t = 0$ ms the projectile is already traveling with a $\theta = 90^\circ$ angle of attack. As the projectile travels through the water it is able to remain under the surface. Bubbles in the wake at $t = 0.4$ ms indicate some sort of forcing event occurring in the cavity. The bullet appears to be tumbling through all times and the non-uniform nature of the cavity is an indicator that this is indeed the case.

Further evidence of tumbling can be seen in figure 8-10 in which the same bullet as figure 8-9 is viewed from head on. This particular image was obtained by placing a mirror in the tank which reflected this image to a camera. In the figure the projectile appears in two places because the reflection from the top of the cavity. At $t = 4.4$ to 13.3 ms it is apparent that the projectile is tumbling as it travels. The projectile not only tumbles from this view point but it also appears to precess as the angle it makes with the horizon appears to change in time as well. This projectile is eventually ejected from the underwater cavity through the free surface (not shown here).

The data is more easily dissected by looking at the velocities and accelerations. Figure 8-11 shows the position, velocity and acceleration of the projectile in figures 8-9 & 8-10. The position in x is fairly constant as the bullet momentum is mainly in this direction, while the position in y becomes more altered as the instabilities in flight affect this direction the most. The position data is approximated using a quintic spline as per the method presented in appendix A and is presented in figure 8-11 as a solid line.

The velocities of this projectile show the dramatic deceleration over this short distance, from 250 m/s to nearly 50 m/s in less than a meter. These large decelerations occur as a result of the large body of fluid that must be moved out of the way the projectile passes through the water column. The accelerations reflect this as they show that the greatest decelerations occur at early times in x -direction but that decelerations in y fluctuate through flight and are an order of magnitude smaller

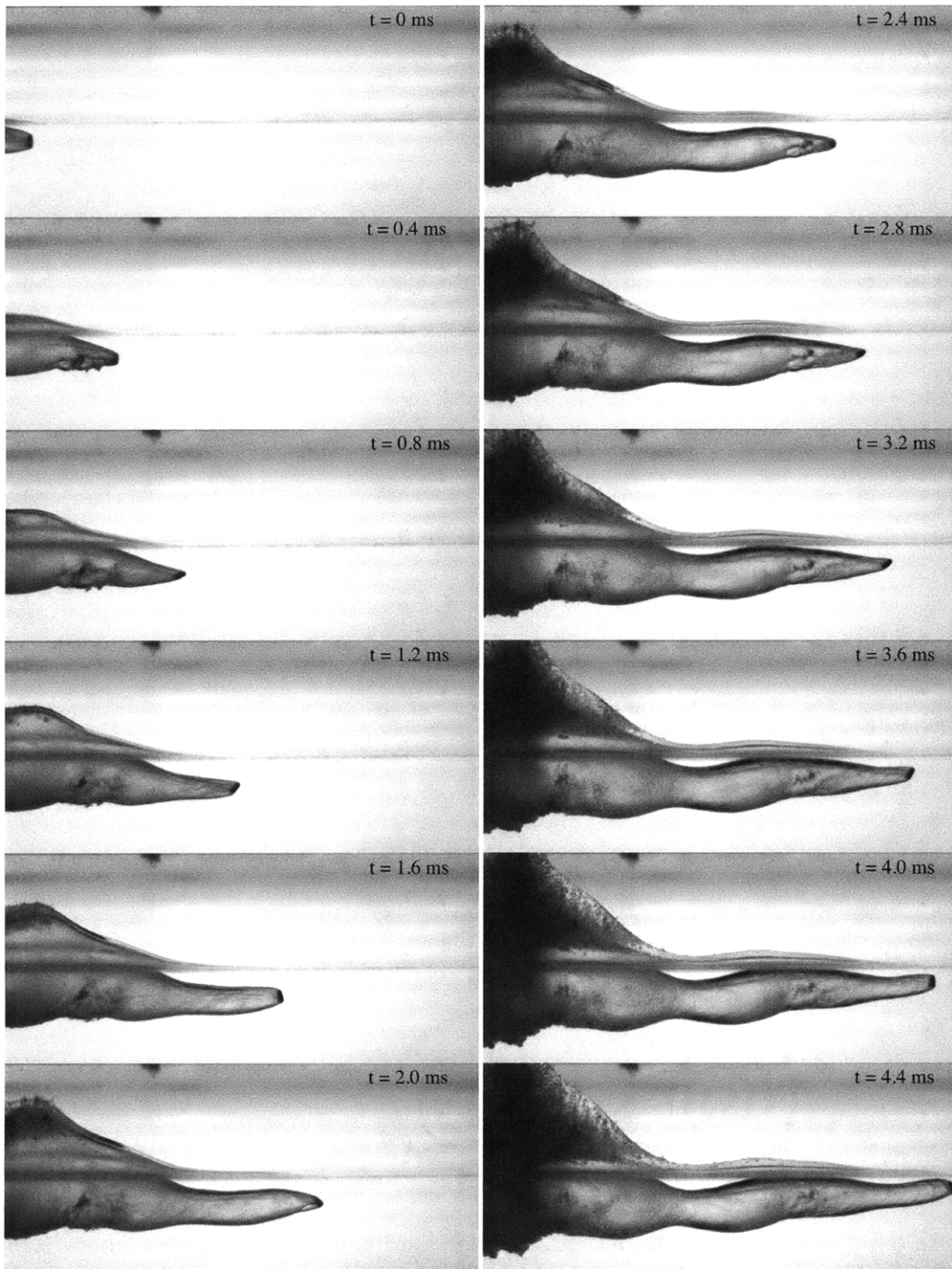


Figure 8-9: Images of a modified 22 caliber aluminum bullet case number (1,14,2). This bullet was fired at 1250 ft/s from the rifle barrel at an angle of 10.7° (see table 8.2). The camera acquired images at 10000 f/s, and every fourth image is shown here.



Figure 8-10: Images of a modified 22 caliber aluminum bullet case number (1,14,2) viewed looking at bullet head on. This bullet type corresponds to bullet name #1 was fired at 1250 ft/s from the rifle barrel at an angle of 10.7° (see table 8.2. The camera acquired images at 2260 f/s, and every image in series is presented here.

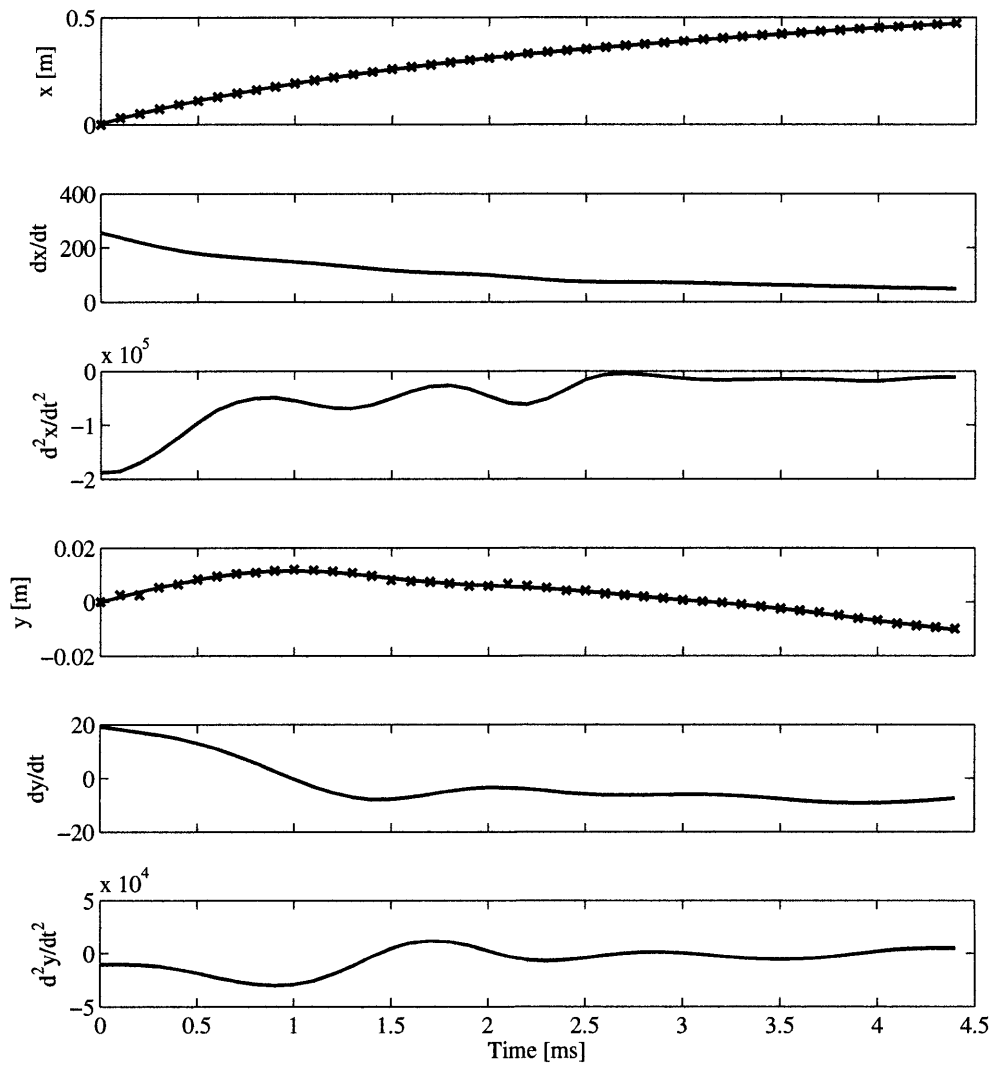


Figure 8-11: Position, velocity, and acceleration in x and y for projectile impact shown in figure 8-9.

than in the x-direction.

The forces associated with water entry are presented in figure 8-12. As expected the drag coefficient is larger than the transverse component and appears to be approximately π rad out of phase with the moment coefficient. The moment coefficient is determined from an estimate of the pitch angle. The forces and moments have an approximate frequency of 1000 Hz. In general, the forces and moments presented here reveal the unsteady nature of this type of water entry.

8.3.3 0.22 modified aluminum projectile

The behavior of the standard projectile can be greatly improved by altering the tip shape and increasing L/D. A modified aluminum 0.22 bullet, characterized as bullet type (7,14,7) in table 8.1, was shot into the water at an angle of 10.7° and is shown in figure 8-13. This projectile forms a cavity that has a more uniform shape which grows both radially and forward through each time step. The projectile can be seen clearly inside the cavity.

As the projectile passes through the water column the cavity grows, and a portion of the cavity splash is entrained into the cavity. It can be seen as a growing gray portion of the cavity on the left hand side of the images. As the projectile continues its downward descent it begins to pitch down. As it does so it eventually comes in contact with the upper portion of the cavity ($t = 2.8$ to 3.6 ms). The contact between the cavity and the tail of the projectile deforms the cavity and leaves evidence of this event in the wake. The projectile is then forced back into the cavity and begins to pitch up ($t = 4.0$ to 4.8 ms).

Contact with the top of the cavity can be seen more closely in figure 8-14 in which the same projectile is viewed from head on with the aid of a mirror as mentioned in the previous section. The images reveal the tendency of these projectiles to pitch up in the fluid. At time $t = 13.3$ ms the projectile is impacting the top of the cavity. The impact with the cavity, seen at the top of the image, is the same event witnessed in the side profile of the event in figure 8-13. The times in this image do not correspond to the same times as in figure 8-13 due to the different arbitrary location of $t = 0$

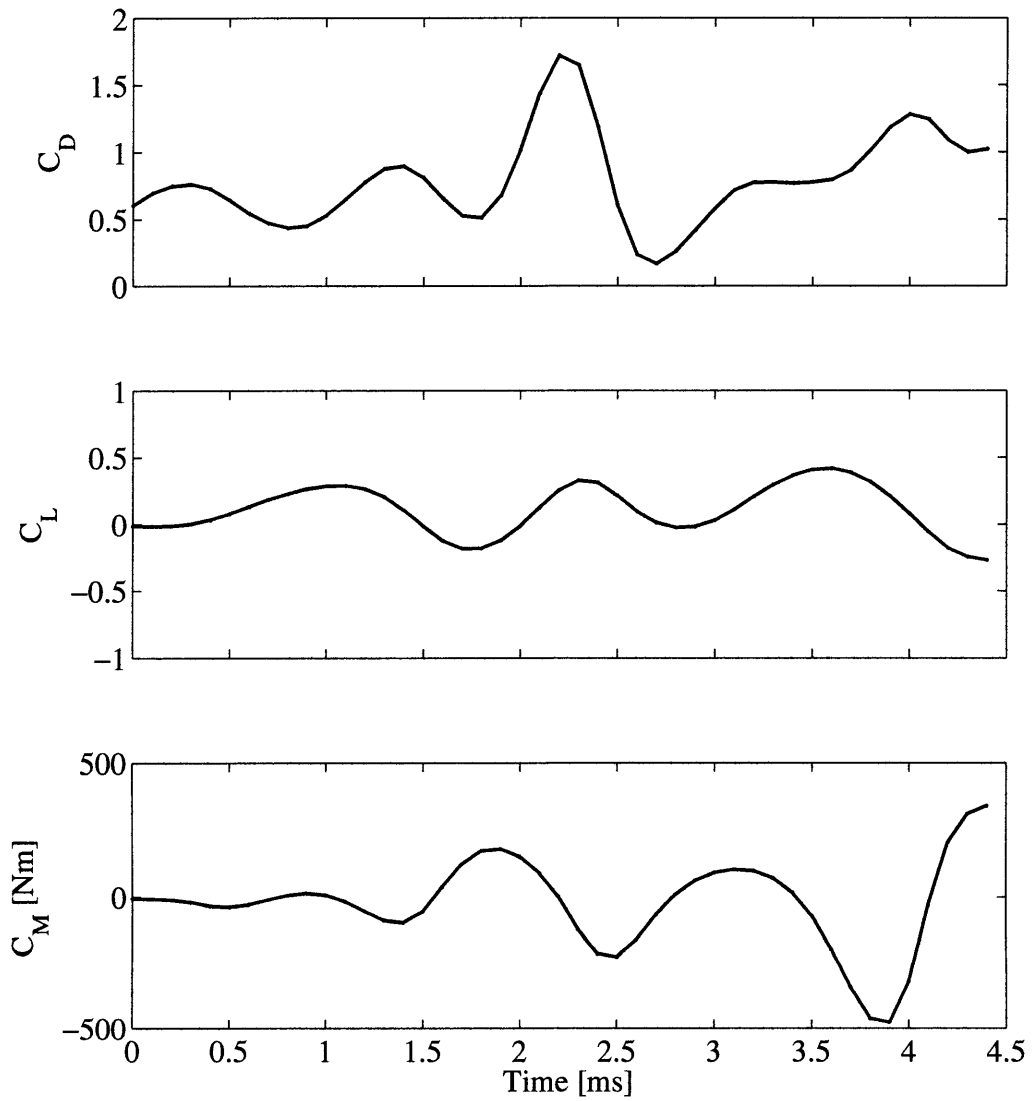


Figure 8-12: Coefficient of drag, lift, and moment for the projectile impact shown in figure 8-9.

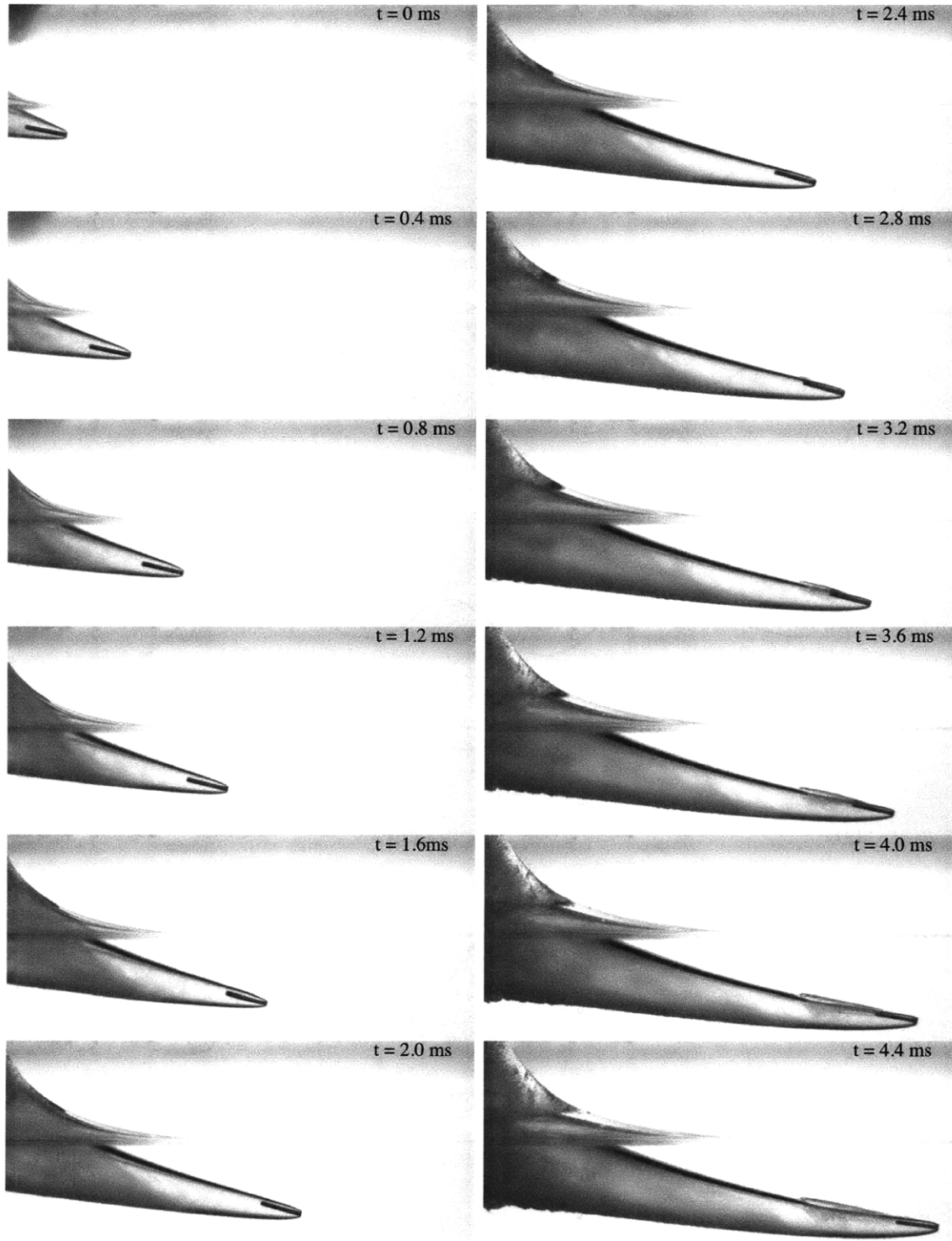


Figure 8-13: Time series of a modified 22 caliber aluminum bullet case number (7,14,7). Images are marked with a timestamp in the upper right hand corner indicating the time from the first image in the series. The darker patch in the upper left hand corner of $t = 0$ ms is a portion of the vaporous splash that is ejected upon impact. The camera acquired images at 10000 f/s, and every fourth image is shown here.

ms. In the side profile images, $t = 0$ corresponds to the moment when the projectile first enters the frame, whereas in the front profile the first image shown is arbitrarily selected as $t = 0$. Since no correlation other than qualitative visualization is used here, no effort to link the two in time was performed.

Looking at the velocities and accelerations it becomes apparent that this projectile is traveling in a much straighter path. Figure 8-15 shows the velocity in the x-direction decreases from approximately the same amount as that of the standard 22 presented above despite the difference in cavity shape. This is likely due to the frontal area of this aluminum case. The standard 22 caliber bullet has an L/D of 2 and at any moment during its flight the frontal area of the projectile is between πR^2 or $8R^2$, since $L = 4R$. For the aluminum case (7,14,7) the frontal area is maximized at πR^2 . These values are very similar and since the impact speeds are nearly identical, we expect the drag coefficients to be similar and the decelerations to also be of a similar magnitude, as is indeed the case in figure 8-15. The y-velocity and acceleration has nearly the same magnitude of the standard 22 case, however, the unsteady oscillations appear smaller.

Coefficients of drag, transverse drag, and torque are presented in figure 8-16. The transverse drag coefficient C_L shows a nearly constant value except for near the end of the field of view. As the projectile slows the pitching motion has a larger effect on the direction the projectile travels, which is apparent in this figure. For drag, the constant force gives way to an unsteady oscillation near the point where the projectile begins to pitch up and tap the cavity wall. The moment coefficient reveals how the projectile travels straight and true through the cavity compared to the standard 22 caliber case (1,14,7). Here, the aluminum projectile slowly alters its pitch angle, changing the value of the moment acting on the projectile, until it gently touches the upper portion of the cavity and is forced back into the cavity. The figure shows that the moments acting on the projectile actually begin to oscillate as the projectile passes through the center line of the cavity. In the future it would be interesting to do this same experiment and be able to see this projectile further downstream to see if the moments are of the same magnitude as the projectile decreases its speed. A

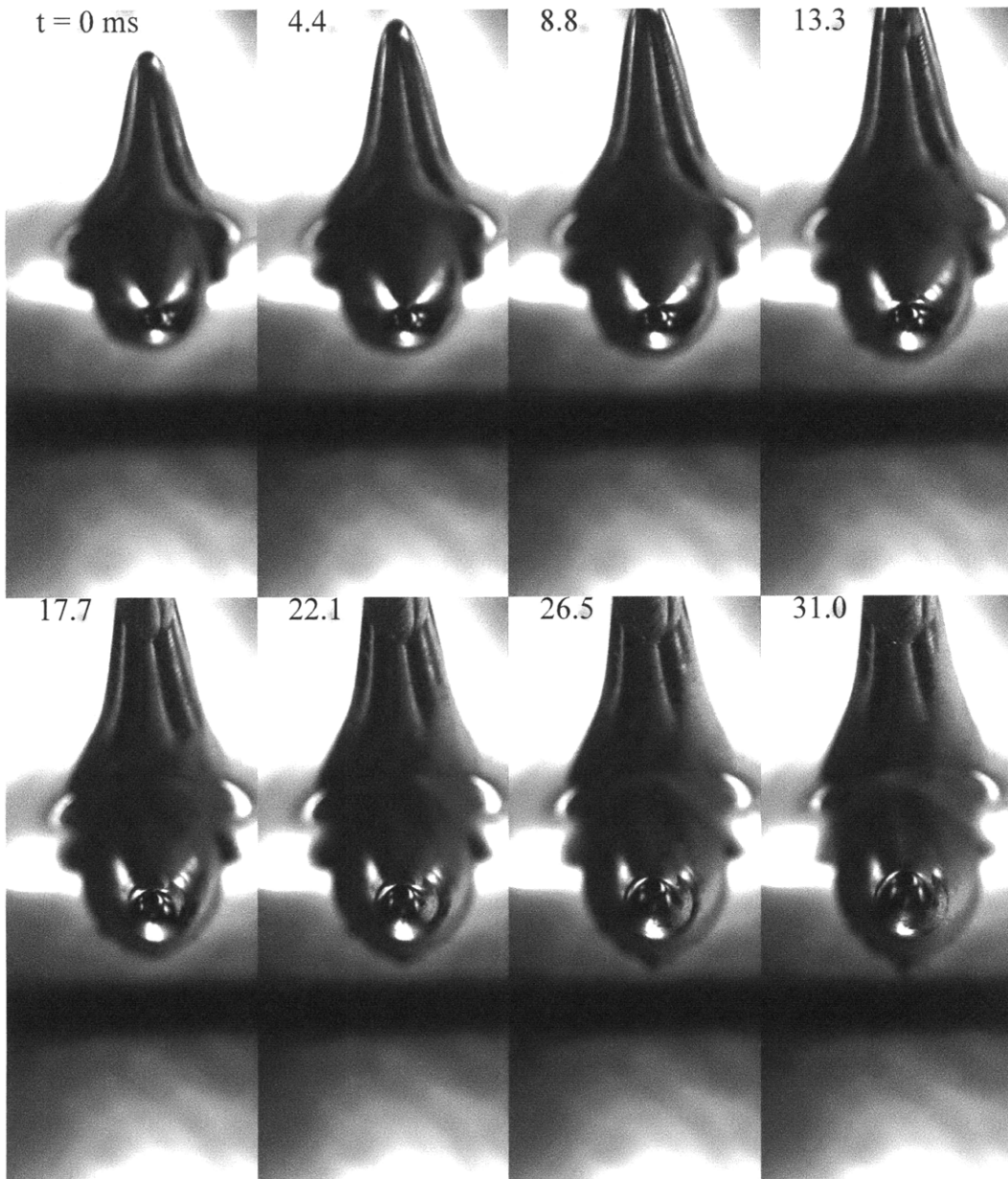


Figure 8-14: Images of a modified 22 caliber aluminum bullet case number (7,14,7) viewed looking at bullet head on. This bullet was fired at 1250 ft/s from the rifle barrel at an angle of 10.7° (see table 8.2). The camera acquired images at 2260 f/s, and every image in series is presented here.

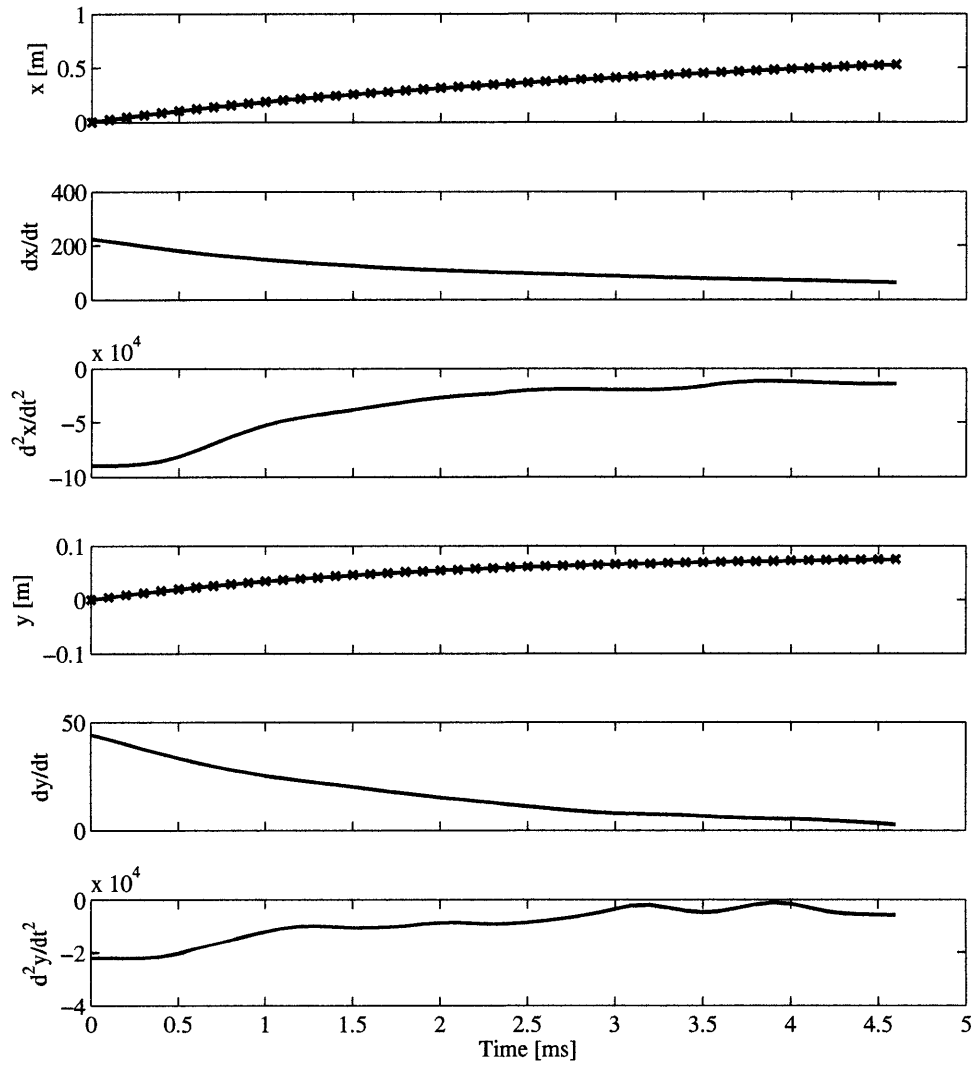


Figure 8-15: Position, velocity, and acceleration in x and y for projectile impact shown in figure 8-13.

critical moment size and forward velocity should be necessary to keep the projectile in the cavity. Overall, the forces and moments reveal that this projectile is able to maintain generally stable and level flight, but also uncovers some of the unsteadiness of the drag force as the projectile slows inside the fluid volume.

8.3.4 0.06 tapered aluminum projectile

The projectile shapes used in the previous sections produce cavities nearly four times larger than the diameter of the projectiles. The straight and level flight achieved by the 22 caliber aluminum projectile could be improved if the projectile were constrained to make a cavity with a diameter comparable to that of the bullet. Furthermore, the velocities the projectiles travel with could be greatly enhanced by decreasing their frontal area in contact with the fluid. Using the cavity model presented in section 8.4, a better projectile was designed that could travel underwater at roughly twice the velocity of the previous projectiles, with a more straight and level flight throughout. This bullet was then built and tested and the results are presented here.

The improved projectile shape behavior can be seen in figure 8-17. The cavity shape is greatly improved and the projectile fills much more of the cavity radially. At time $t = 0.3$ to 0.5 ms the size of the projectile inside the cavity size can be seen. Here the bullet entry point is in the field of view whereas the other projectiles impacted slightly out of the viewable window. This skews the velocity data in favor of this projectile over the previous ones because data above the free surface is available and the actual entry speed can be determined. Furthermore the entry splash can be seen quite easily. The strange v-shaped splash above the projectile from $t = 0.1$ to 0.5 is probably due to the projectile being slightly off-axis during entry, not because of the altered projectile shape.

The projectile appears to lean against the cavity from $t = 0.5$ to 1.1 ms. It is difficult to tell, but it does seem like the projectile is leaning against the cavity throughout this set of images. Ideally, the projectile would not lean against the cavity at all in an effort to keep the drag as low as possible and the trajectory straight. Through improved observations our understanding of how these projectiles behave

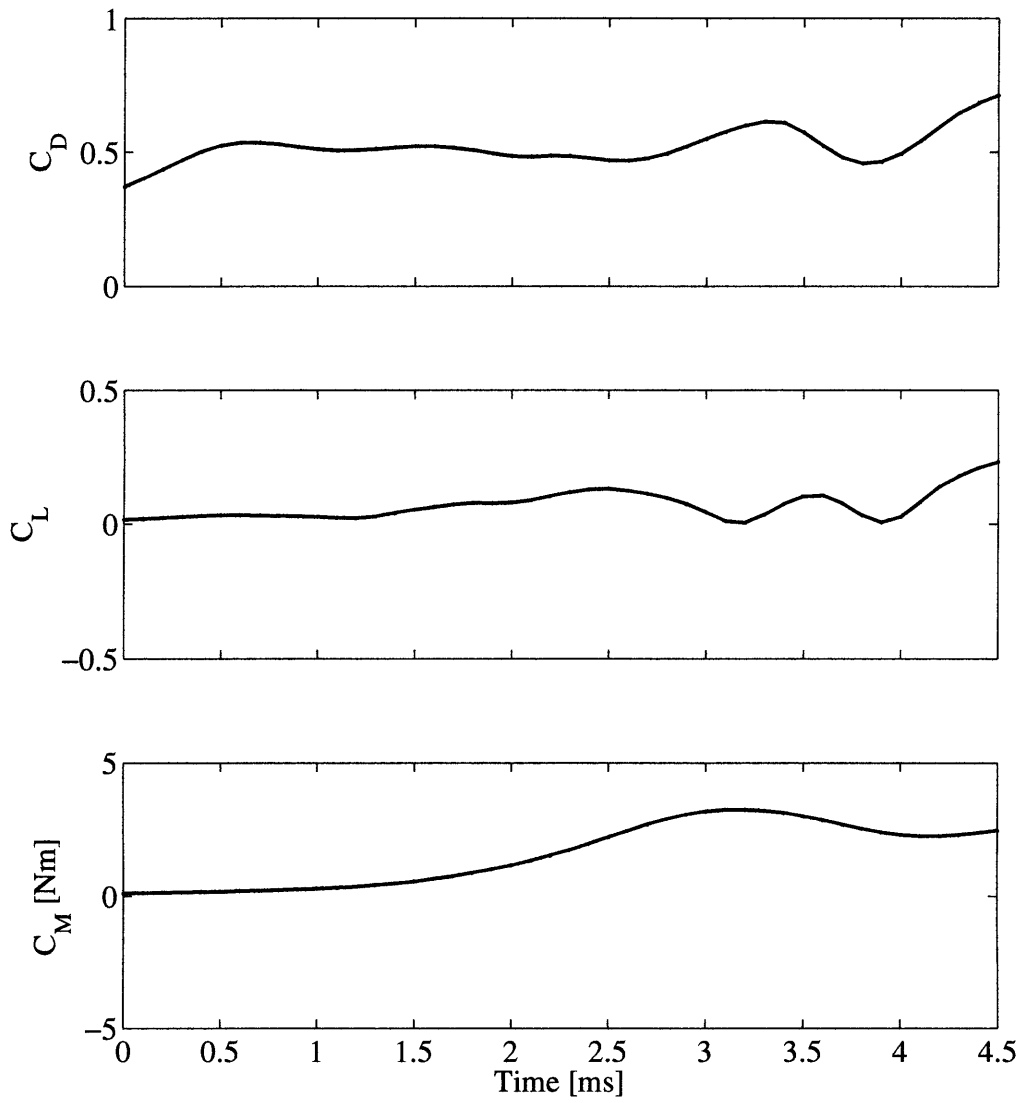


Figure 8-16: Coefficient of drag, lift, and moment for the projectile impact shown in figure 8-13.

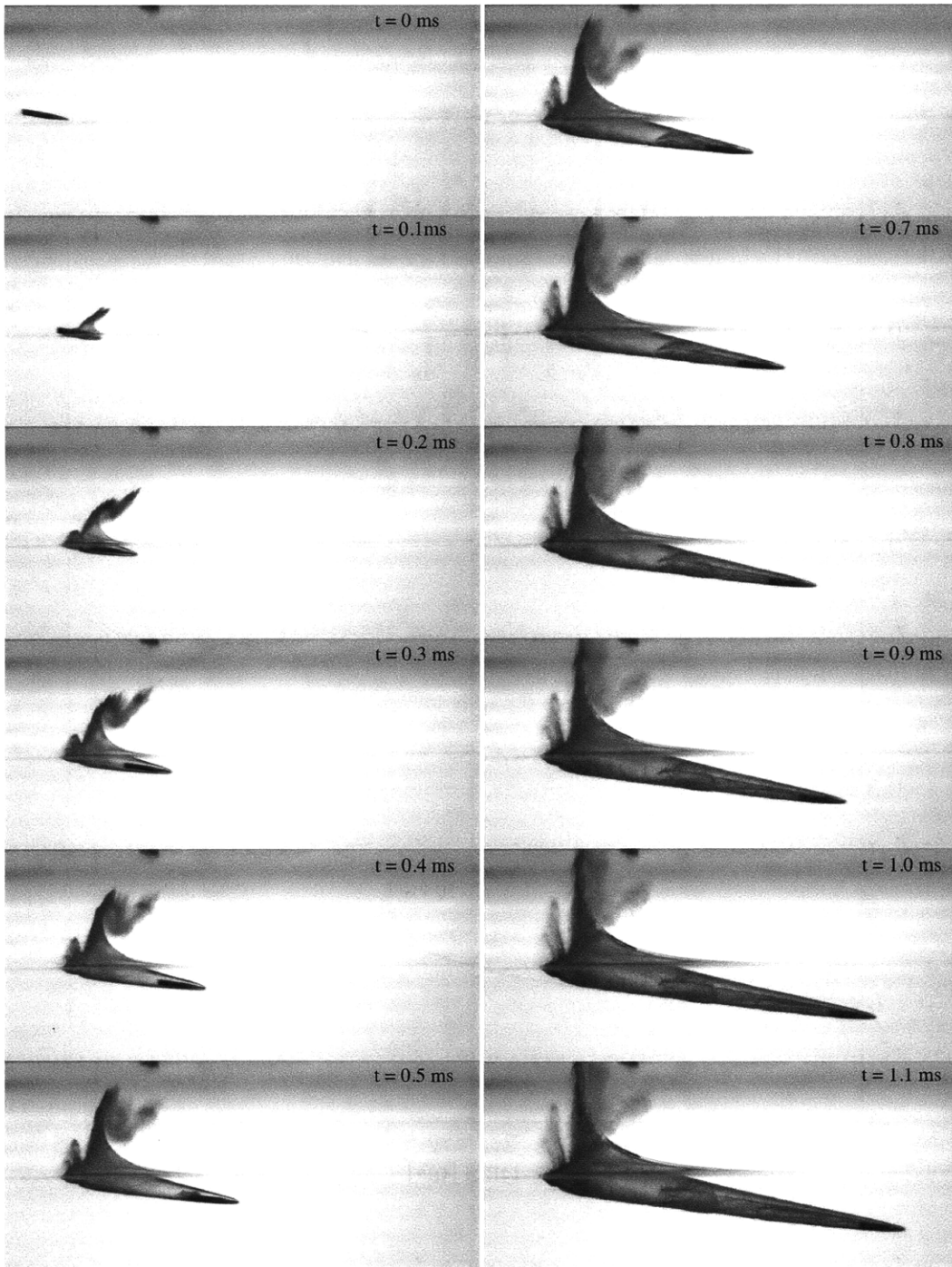


Figure 8-17: Time series of a modified 22 caliber aluminum bullet case number (15,14,10). Images are marked with a time stamp in the upper right hand corner indicating the time from the first image in the series. The darker patch in the upper left hand corner of $t = 0$ ms is a portion of the vaporous splash that is ejected upon impact. The camera acquired images at 10000 f/s, and every image is shown here.

will lead to more efficient designs.

Figure 8-18 shows a front view of the same projectile impact as in figure 8-17. Unfortunately, the projectile goes out of the field of view of the camera before too many details can be observed. It does appear that the projectile is leaning against the cavity wall from $t = 4.4$ to 13.3 ms. This could indicate that this projectile does not oscillate inside the cavity but instead continually leans against the cavity wall. The image also reveals the much smaller cavity size. The short time span that the projectile is in view is also an indicator of an increased velocity. The projectile goes on to break the mirror used to produce this shot just milliseconds after these images were taken (not shown). This is in contrast to the previously highlighted projectiles, which often impacted the mirror and bounced off, but did not break the mirror. That this projectile had enough kinetic energy to break through the mirror adds evidence of its decreased drag and increased velocity.

The velocity and acceleration of this projectile are presented in figure 8-19. The projectile appears to hold a constant velocity for a short time before it begins to decrease more rapidly. This is because a few frames before impact were captured and we get to see the initial moments of entry in which the projectile does not slow down as much. One thing to note in this data series is that only 13 frames of data are available where the projectile is in view. The velocity also shows that these projectiles are traveling at nearly twice the speed of the previous projectiles even at the end of the field of view. Although the field of view here includes the impact zone, whereas the other projectiles had already contacted the free surface, the velocities here are much faster, due to the reduced frontal area of the projectile. The deceleration in x decreases but never really reaches the deceleration rate of case (7,14,7), which is expected.

The coefficients of transverse drag, C_L , shows a generally increasing drag up to about 0.001 in figure 8-20. The drag is negative here due to the acceleration above the free surface. There is likely no acceleration above the free surface after the projectile is released from the rifle. Thus, this data shows the possible magnitude of error associated with these tests. It is difficult to determine the exact center of gravity for

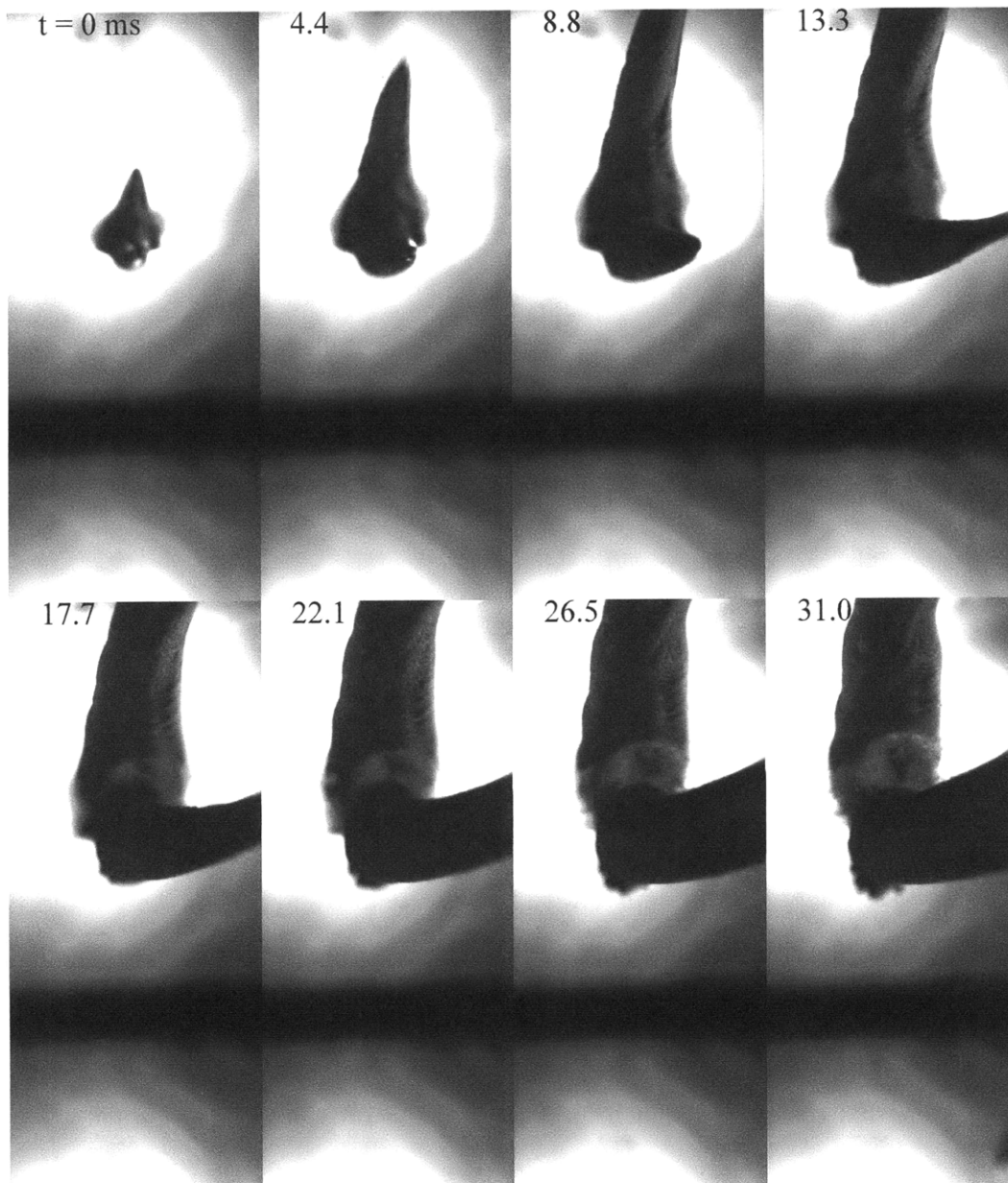


Figure 8-18: Images of a modified 22 caliber aluminum bullet case number (15,14,10) viewed looking at bullet head on. This bullet type corresponds to bullet name #1 was fired at 1250 ft/s from the rifle barrel at an angle of 10.7° (see tale 8.2. The camera acquired images at 2260 f/s, and every image in series is presented here.

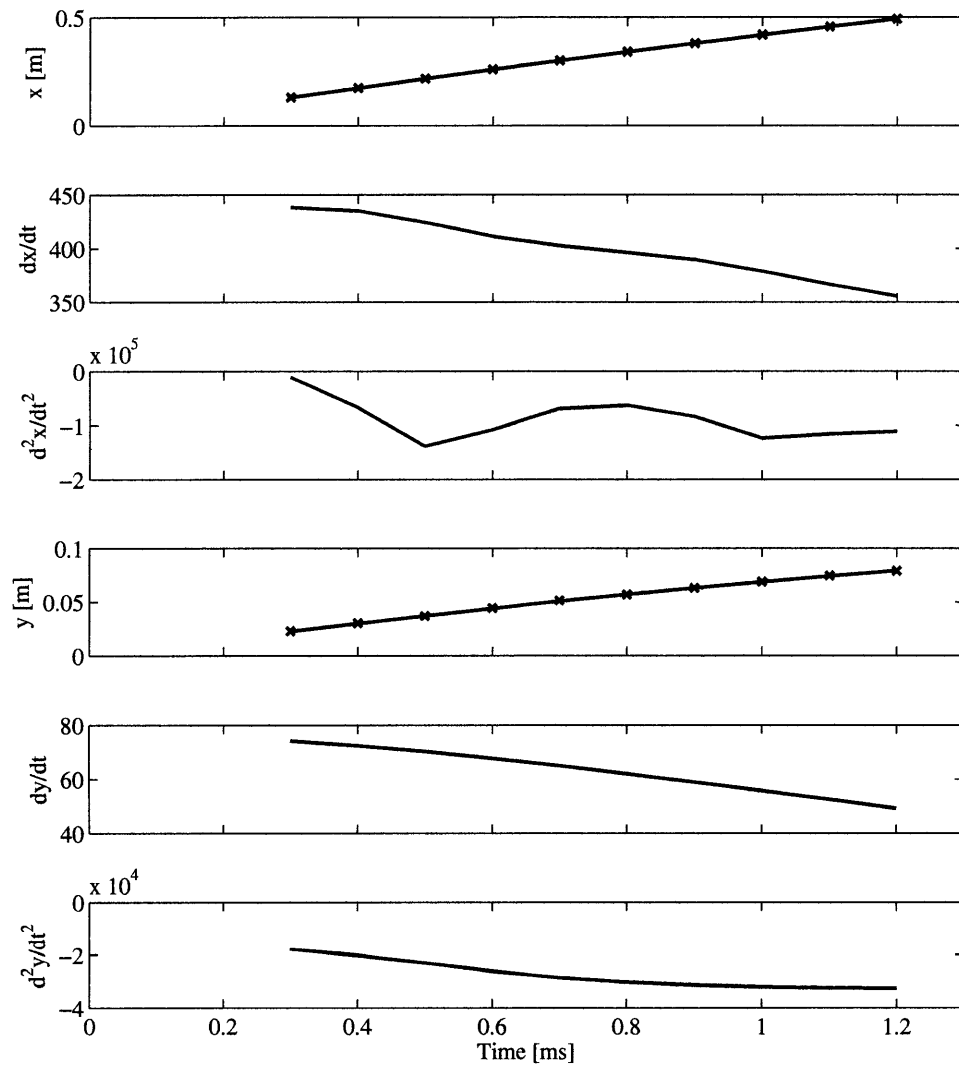


Figure 8-19: Position, velocity, and acceleration in x and y for projectile impact shown in figure 8-17.

each projectile and the exact speeds are uncertain. Here, we present this data in an effort to show the trends involved with these impacts not to authoritatively resolve the accelerations or forces involved.

The coefficient of drag, C_D , shows a dip and then rising value around $t = 0.5$ ms. This is near the point where the projectile impacts the side wall of the cavity. This impact could affect the index of refraction of the cavity and alter the apparent shape of the projectile, making the position values skewed one way or another. The moment coefficient does not show a large change in the torque at that time, which may indicate that the projectile is not being forced back into the cavity, but instead is riding along the cavity wall. Perhaps the contact with the cavity wall causes an increased drag momentarily as the projectile tail pushes through the cavity wall, but is then decreased as the projectile only skims along the surface of the cavity as it rides along inside.

This data set represents the evolution of small caliber high-speed water-entry projectiles from standard bullet shapes to specially designed projectile types. Standard projectiles do not travel well underwater as expected. Modified blunt tip projectiles with large L/D make axially uniform cavities and travel well inside of them. The performance of these projectiles can be greatly improved by decreasing the tip size and adapting the overall shape to fit inside the cavities they form. The design is based on a well formulated theoretical model described in the following section.

8.4 Theoretical Cavity Model

Following the derivation of the Logvinovich cavity model [1] we can find an approximation for the profile of an axisymmetric cavity. The cavity is formed by a disk of radius R_o placed in a uniform flow of V_o . We assume that the flow is ideal and incompressible, which holds true where velocities do not exceed several hundreds of meters per second and temperatures remain below the boiling point. In reality, high-speed videos reveal that the surface of the cavity is mottled with inconsistencies, droplets, and disturbances. However, this approximation assumes that overall the cavity re-

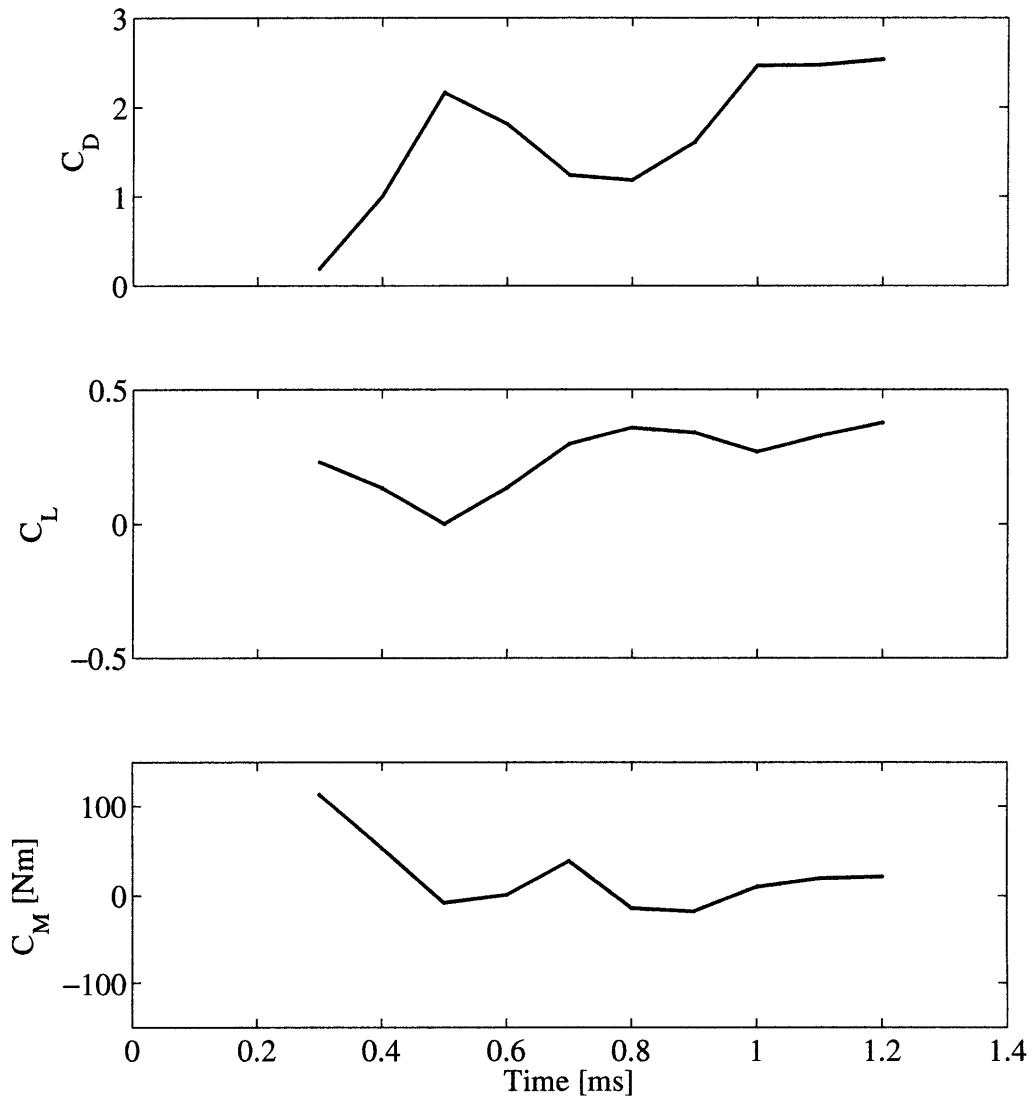


Figure 8-20: Coefficient of drag, lift, and moment for the projectile impact shown in figure 8-17.

tains some ‘macroscopic’ smoothness, thus we ignore these disturbances. Figure 8.4 shows a two dimensional sketch of the disk in the flow field and the associated cavity.

Cavitation occurs when the pressure of the cavity is much smaller than the pressure of the surrounding fluid. The cavitation number is an excellent dimensionless parameter used to characterize the potential of the fluid to cavitate. It is the ratio of the difference between the free stream pressure (P_k) and the vapor pressure of the fluid (P_v) to the kinetic energy per volume ($q = \frac{1}{2}\rho V^2$). The cavitation number is defined as,

$$\sigma = \frac{P_k - P_v}{\frac{1}{2}\rho V^2} \quad (8.7)$$

where fully formed cavities form when $\sigma < 0.1$.

The profile of the cavity can be broken up into two parts. The leading part which extends from the tip of the disk to $\frac{x}{R_o} < 3$ to 5 can be expressed approximately from empirical evidence as

$$R = R_o \left(1 + \frac{3x}{R_o} \right)^{1/3} \quad (8.8)$$

where x is the distance downstream from the disk. This equation is only valid for cavitation numbers below $\sigma < 0.1$

The second part of the profile is determined by applying the momentum theorem. Figure 8.4 is used to apply the cavity profile and points of interest in deriving the momentum theorem. Consider a disk creating a cavity behind it in a free-stream with velocity $V_o \hat{x}$. The plane NN is where the disk is located. The cavity is formed between NN and $N'N'$, and the bubbly foamy flow behind the cavity is ignored. To determine the force of drag W_o acting on the plane AA we introduce six planes of interest to form a control surface enclosing a control volume. The first S_1 is far upstream of the disk in the y-z direction. The second is S_2 which is in the y-z plane and passes through the plane AA. The third, S_3 , and fourth, S_4 , are far away from the x-axis at a distance R_3 . Similarly, S_5 and S_6 are a distance R_3 in the y-direction away from the x-axis but in and out of the plane and not shown in figure 8.4. The force balance of the drag on the body is determined by applying the momentum theorem to the control surface now defined. The momentum theorem states that the summation of the

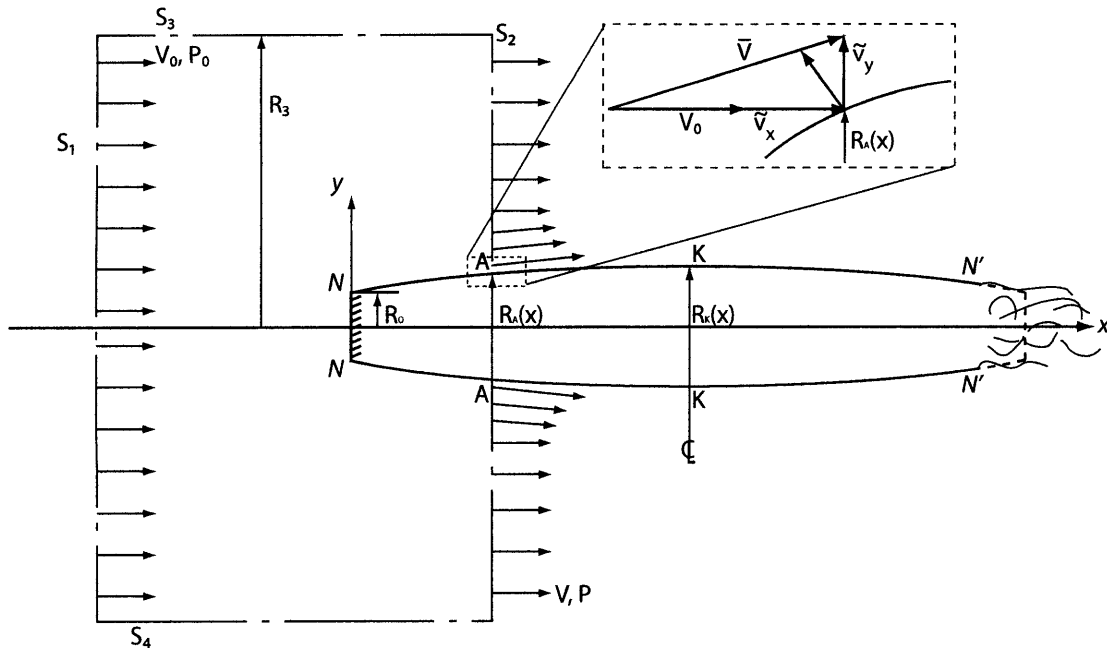


Figure 8-21: Two dimensional sketch of disk NN in a velocity (V_o) and pressure (P_o) field. The control surfaces S_1, S_2, S_3, S_4 define a control volume. The volume includes S_5 , and S_6 (in and out of the plane) but they are not shown here. Along the control surface S_3 the plane AA defines the cavity and the velocity components at the surface of the cavity are shown in the enlarged view. The back of the cavity is cut-off at the plane $N'N'$ due to the chaotic and non-uniform closure typical of these cavities.

pressures and momentum fluxes across the control volume should be zero, assuming the disk is traveling in a steady flow, and has the coordinate system is fixed to it. The momentum flux across S_3 and S_4 is neglected due to the far field assumption. The pressure along S_3 is balanced by the pressure in S_4 , thus no net contribution to the force from either surface. Similarity provides the same explanation for eliminating the momentum flux across surfaces S_5 and S_6 . The summation of forces along the surface S_1 is a function of the incoming velocity and the ambient pressure $\rho V_o^2 + P_o$. Along the surface S_2 , the velocity of the flow field is near zero inside the cavity and only the pressure P_k has an effect at $r < R_A$. Outside the cavity the velocity field is affected by the ambient velocity and the increased velocity due to the presence of the

cavity \bar{V} . The momentum theorem is then defined as

$$F_d = \int_{S_1} (\rho V_o^2 + P_o) dA - \int_{S_2 - \pi R_A^2} (\rho V_x^2 + P) dA - \int_0^{2\pi} \int_0^{R_A} P_k r dr d\theta \quad (8.9)$$

This equation can be further simplified by defining the velocity in the x-direction as $V_x = V_o + \tilde{v}_x$ and in the y-direction by $V_y = \tilde{v}_y$, where \tilde{v}_x and \tilde{v}_y are the perturbed velocities. The determination of this velocity comes by adding the free stream velocity to the velocity in the x-direction of the flow near the cavity wall. The pressure P can be expressed by applying the Bernoulli theorem between S_1 and S_2 as

$$P = P_o + \frac{\rho V_o^2}{2} - \frac{\rho V_x^2}{2} - \frac{\rho V_y^2}{2} \quad (8.10)$$

where $y \geq R_A$. Simplifying the pressure P yields:

$$P = P_o - \rho V_o \tilde{v}_x - \frac{\rho \tilde{v}_x^2}{2} - \frac{\rho \tilde{v}_y^2}{2} \quad (8.11)$$

Substituting the pressure term and velocities into equation 8.9 expands to

$$F_d = S_1(\rho V_o^2 + P_o) - \rho \int_{S_2 - \pi R_A^2} (V_o^2 + 2V_o \tilde{v}_x + \tilde{v}_x^2 + \frac{P_o}{\rho} - V_o \tilde{v}_x - \frac{\tilde{v}_x^2}{2} - \frac{\tilde{v}_y^2}{2}) dA - \pi R_A^2 P_k. \quad (8.12)$$

Simplifying and substituting the area of the cavity at R_A as $S_x = \pi R_A^2$

$$F_d = S_1(\rho V_o^2 + P_o) - S_2(\rho V_o^2 + P_o) + S_x(\rho V_o^2 + P_o) + \rho \int_{S_2 - S_x} (\frac{\tilde{v}_y^2}{2} - \frac{\tilde{v}_x^2}{2} - V_o \tilde{v}_x) dA - S_x P_k. \quad (8.13)$$

The surface S_1 and S_2 are the same size and therefore similar terms cancel. Using the continuity equation for the fluid region bounded by S_1 , S_2 , and S_x of the cavity to define the following

$$S_x V_o = \int_{S_2 - S_x} \tilde{v}_x dA.$$

Substitution then yields

$$F_d = S_x(P_o - P_k) + \int_{S_x}^{\infty} (\frac{\rho \tilde{v}_y^2}{2} - \frac{\rho \tilde{v}_x^2}{2}) dA \quad (8.14)$$

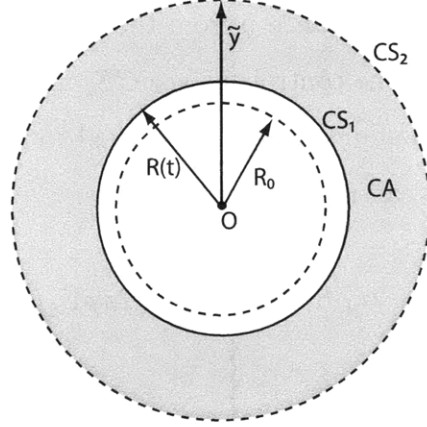


Figure 8-22: Two dimensional sketch of cavity cross section illustrating the control area CA confined by the control surfaces CS_1 and CS_2 .

For a specific value of $P_o - P_k$, equation (8.14) defines the drag F_d for each cross-sectional area of the cavity $S_x = \pi R_A^2$ and the perturbed velocities \tilde{v}_x and \tilde{v}_y within the fluid plane S_2 . Equation (8.14) can be modified further by computing the terms of the integrand. Examining the term $\frac{\rho \tilde{v}_y^2}{2}$, we can replace the velocity \tilde{v}_y with the rate of “cylindrical” expansion as determined from mass conservation around the cavity. A two dimensional slice of the cavity is shown in figure 8.4. The cavity has an initial radius of R_o and a growing radius of $R(t)$. The control surface is defined by the wall made by the cavity at $R(t)$ and the imaginary wall a distance \tilde{y} away from the center. If we assume a small slice of the cavity dx then the conservation of mass equation takes the two-dimensional form:

$$\frac{d}{dt} \left(\int_{CA} \rho dA \right) + \int_{CS_1} \rho (\underline{V}_1 - \underline{V}_{CS_1}) dS + \int_{CS_2} \rho (\underline{V}_2 - \underline{V}_{CS_2}) dS = 0 \quad (8.15)$$

where CA is the control area, CS_1 and CS_2 are the control surfaces, \underline{V} is the velocity of the fluid through the control surface, and \underline{V}_{CS} is the velocity of the control surface. Since ρ is constant, the change in the control area in time can be approximated as the first derivative of the control area $A = \pi(\tilde{y}^2 - R^2(t))$, which is $\frac{dA}{dt} = -2\pi R(t) \frac{dR(t)}{dt}$. Along control surface CS_1 , the velocities of the control surface and the velocity of the fluid are equal, thus they sum up to zero. The velocity of the control surface

CS_2 is zero since it is a fixed distance \tilde{y} from the center of the cavity. Further, the velocity of the fluid through the control surface CS_2 must be non-zero ($\underline{V}_2 \neq 0$) and represents the velocity of the fluid expanding normal to the cavity (\tilde{v}_y) for all values of $\tilde{y} > R(t)$. Equation 8.15 can now be reduced to

$$-2\pi\rho R(t)\frac{dR(t)}{dt} = -2\pi\rho\underline{V}_2\tilde{y} \quad (8.16)$$

which simplifies to

$$\underline{V}_2 = \tilde{v}_y = \frac{R(t)}{\tilde{y}} \frac{dR(t)}{dt} \quad (8.17)$$

The term $\frac{\rho\tilde{v}_y^2}{2}$ in equation 8.14 can now be represented as

$$\int_{S_x}^{\infty} \frac{\rho\tilde{v}_y^2}{2} dA = \int_R^{\infty} \frac{\rho\tilde{v}_y^2}{2} 2\pi\tilde{y}d\tilde{y} = \int_{R(t)}^{\infty} \frac{\rho R(t)}{\tilde{y}} \frac{\partial R(t)}{\partial t} \tilde{v}_y \tilde{y} \pi d\tilde{y} \quad (8.18)$$

This integrand is solved by making two observations. The partial derivative of the surface S_x (related to the S_2 plane) inside the cavity is $\frac{\partial S_x}{\partial t} = \frac{\partial S_x}{\partial x} \frac{\partial x}{\partial t} = \frac{\partial S_x}{\partial x} V_o = 2\pi R \frac{\partial R}{\partial t}$. Further, the velocity potential at the cavity boundary can be defined as

$$\varphi = - \int_R^{\infty} \tilde{v}_y d\tilde{y} \quad (8.19)$$

Applying these relations to the right hand side of equation 8.18 yields the equation

$$\int_R^{\infty} \frac{\rho R \frac{\partial R}{\partial t}}{2\tilde{y}} \tilde{v}_y \tilde{y} 2\pi d\tilde{y} = \frac{1}{2} \rho 2\pi R \frac{\partial R}{\partial t} \int_R^{\infty} \tilde{v}_y d\tilde{y} = -\frac{1}{2} \rho \varphi \frac{\partial S_x}{\partial t}. \quad (8.20)$$

The second term ($\frac{\rho\tilde{v}_x^2}{2}$) inside the integrand of equation (8.14) can be determined by first finding the drag of the cavity at the maximum cross section KK. Here the velocity \tilde{v}_y is zero and the velocity \tilde{v}_x becomes maximum, thus equation (8.14) becomes

$$F_d(K) = S_k \Delta P - \int_{S_k}^{\infty} \frac{\rho\tilde{v}_x^2}{2} dA = S_k \Delta P k$$

$$\int_{S_k}^{\infty} \frac{\rho\tilde{v}_x^2}{2} dA = \Delta P S_k (1 - k) \quad (8.21)$$

where the right hand side describes the total drag as some proportion of the total pressure. This method of solving is useful when empirical data is available to determine k , which can now be defined as

$$k = 1 - \frac{1}{S_k \Delta P} \int_{S_k}^{\infty} \frac{\rho \tilde{v}_x^2}{2} dA. \quad (8.22)$$

In most of the literature the value of k is reported as $0.875 < k < 1.0$, and is used as a correction factor to estimate drag. For any given position x in the cavity past the empirical solution near the tip the value of k_x can be written as $k_x = 1 - \frac{1}{S_x \Delta P} \int_{S_x}^{\infty} \frac{\rho \tilde{v}_x^2}{2} dA$, which becomes k at the maximum cross section of the cavity KK. Because \tilde{v}_x becomes a maximum at the maximum cross section of the cavity it can be assumed that in the central part of the cavity $k_x \approx k$. Since the value of k is near 1.0 then the value of k_x is also near 1.0, thus, $\frac{k_x}{k} = 1$. Dividing equation (8.14) by k and replacing the terms inside the integrand yields

$$\begin{aligned} \frac{F_d}{k} &= \frac{\Delta P S_x(t)}{k} - \frac{1}{2} \rho \varphi \frac{\partial S_x}{\partial t} \frac{1}{k} - \frac{1}{k} \int_{S_k}^{\infty} \frac{\rho v_x^2}{2} dA = \Delta P S_k \\ \frac{F_d}{k} &= \frac{\Delta P S_x(t)}{k} - \frac{1}{2} \rho \varphi \frac{\partial S_x}{\partial t} \frac{1}{k} - \frac{\Delta P S_x(t)(1 - k_x)}{k} = \Delta P S_k \\ \frac{F_d}{k} &= \Delta P S_x(t) - \frac{1}{2} \rho \varphi \frac{\partial S_x}{\partial t} \Phi(t) = \Delta P S_k \end{aligned} \quad (8.23)$$

where $\Phi(t)$ is a correction function introduced to replace the term $\frac{1}{k}$, and $\Delta P S_k$ is the force of drag at the largest cross sectional area KK, where the radial velocity goes to zero.

The potential φ can be determined from the unsteady Bernoulli equation defined here as

$$\frac{\partial \varphi}{\partial t} + \frac{1}{2} v^2 + \frac{\Delta P}{\rho} = 0 \quad (8.24)$$

along a surface contour s_x which is the surface of the cavity, which makes the vapor-fluid interface. The derivative of the potential can be re-written in the form $\frac{\partial \varphi}{\partial t} = \frac{1}{2} \left(\frac{\partial \varphi}{\partial t} + \frac{\partial \varphi}{\partial y} \frac{\partial y}{\partial t} \right)$ where $\frac{\partial \tilde{y}}{\partial t} = \frac{\partial R}{\partial t}$, and $\frac{\partial \varphi}{\partial y} = \tilde{v}_y = \dot{R}$ along the surface of the cavity.

Replacing these quantities in equation 8.24 and solving for $\frac{\partial\varphi}{\partial t}$ yields

$$\frac{\partial\varphi}{\partial t} = \frac{2\Delta P}{\rho} - v^2 - \left(\frac{\partial R}{\partial t}\right)^2, \quad (8.25)$$

and integrating both sides

$$\varphi(t) = \frac{2\Delta P}{\rho}(t_k - t) - \int_{t_k}^t (v^2 + \left(\frac{\partial R}{\partial t}\right)^2) dt. \quad (8.26)$$

The cavity profile can now be determined by evaluating $\varphi(t_k) = 0$ at the maximum cross section of the cavity KK , assuming the cavity is in steady state. The constant of integration is then equal to zero. Rewriting the equation becomes $\varphi(t) = -\frac{2\Delta Pt_x}{\rho}(1 - \frac{t}{t_k})$ and setting the correction factor to a constant $\Phi(t) = \chi$ and replacing terms yields

$$-\chi t_x \left(1 - \frac{t}{t_k}\right) \frac{\partial S_x}{\partial t} = S_x - S_k \quad (8.27)$$

Setting $u = (1 - \frac{t}{t_k})$ and $du = -\frac{1}{t_k} dt$ and noticing that $S_x = \pi R^2$, $S_k = \pi R_k^2$, and $\frac{\partial S_x}{\partial t} = 2\pi R \frac{\partial R}{\partial t} = \frac{\partial(\pi R^2)}{\partial R} \frac{\partial R}{\partial t}$ can reduce the solution to

$$\begin{aligned} \frac{\partial S_x}{\partial t} \frac{1}{(S_x - S_k)} &= -\frac{1}{\chi t_k (1 - \frac{t}{t_k})} \\ \frac{d(R^2)}{(R^2 - R_k^2)} &= \frac{1}{\chi} \frac{du}{u} \end{aligned} \quad (8.28)$$

Integrating both sides when the cavity contour passes through a specified point $R = R_1$ at $t = 0$ gives

$$\frac{R^2 - R_k^2}{R_1^2 - R_k^2} = \left(1 - \frac{t}{t_k}\right)^{1/\chi} \quad (8.29)$$

Solving for R gives the cavity profile up to the point $\frac{t}{t_k} < 1.5$ where the boundaries of the cavity begin to break up and form foam.

Solving for $R(t)$ gives the contour of the cavity radius,

$$R = R_k \sqrt[1/\chi]{1 - \left(1 - \frac{R_1^2}{R_k^2}\right) \left|1 - \frac{t}{t_k}\right|}, \quad (8.30)$$

and taking the derivative yields the cavity growth rate becomes

$$\dot{R} = \frac{R_k \left(1 - \frac{R_1^2}{R_k^2}\right) \left(1 - \frac{t}{t_k}\right)^{\frac{1}{\chi}}}{2t_k \chi \left(1 - \left(1 - \frac{R_1^2}{R_k^2}\right) \left(1 - \frac{t}{t_k}\right)^{\frac{1}{\chi}}\right)^{\frac{1}{2}} \left(1 - \frac{t}{t_k}\right)}. \quad (8.31)$$

The radius of the cavity is now defined and can be solved for. The term R_1 is determined where the empirical result meets the numerical approximation at $x = x_1 = aR_o$ and yields $R = R_o(1 + 3a)^{1/3}$ as defined by equation 8.8. R_k is defined as the maximum cavity radius and is calculated by equation 8.21 at x_k . Solving R_k where $S_k = \pi R_k^2$ and noticing that $F_d = 1/2\rho v^2 \pi R_o^2 C_x$. Experiments show that the drag coefficient for the non-zero cavitation case is approximately $C_x \approx C_{x_o}(1 + \sigma)$ where $C_{x_o} = 0.82$ is the drag coefficient of a disk with a cavitation number of zero. R_k then becomes

$$R_k = R_o \sqrt{\frac{C_{x_o}(1 + \sigma)}{\sigma k}}. \quad (8.32)$$

Equation 8.31 can now be solved at the point where R is defined by the empirical formula in equation 8.8 at the point where $R(x_1) = R_1$, replacing $x = V_o t$ and taking the derivative yields

$$\dot{R}(x_1) = V_o \left(1 + \frac{3V_o t_1}{R_o}\right)^{-\frac{2}{3}}. \quad (8.33)$$

realizing that at R_1 the value of $t_1 = x_1/V_o$ and replacing yields

$$\dot{R} = V_o (1 + 3a)^{-\frac{2}{3}}. \quad (8.34)$$

This is the derivative at the point x_1 . The value of a is given as $a = 2$ herein. It is now possible to calculate the value of t_k . Using equation 8.27 and solving for t_k instead of R gives

$$t_k = \frac{R_k^2 \left(1 - \frac{R^2}{R_k^2}\right)}{2\chi R \frac{\partial R}{\partial t}} + t. \quad (8.35)$$

Reducing this equation by noticing that $t = 0$ at R_1 yields

$$t_k = \frac{R_k^2 \left(1 - \frac{R_1^2}{R_k^2}\right)}{2\chi R_1 \frac{\partial R_1}{\partial t}}. \quad (8.36)$$

8.5 Discussion

The radius of the cavity can now be determined analytically. This method yields cavities that are continuous for all values of x despite the empirical model used near the tip. The original theory of Logvinovich required a lot of adjustment in order to get a continuous cavity near the transition from the empirical to theoretical models. To illustrate this, figure 8-23 shows the discrepancy. Both models have the same input parameters but the Logvinovich model shows a slight jump near $x = 2R_o$, indicating that the newer model is easier to apply and its continuity is more robust than previous models. In order for the Logvinovich model to fit with the new model the value of a must become $a = 11$, which is beyond the accuracy of the empirical results for the near tip geometry. Using $a = 11$ also forces the cavity to be larger than it should be down stream. Both the newer model and the Logvinovich one are based on the same assumptions and as they approach x_k they approach the same R_k value. Section 8.3 discusses further the accuracy of the model with experimental results.

During experiments it was noted that the projectiles have a tendency to pitch and yaw inside the cavity. One way of improving the two dimensional model presented here is to add an angular component to capture this behavior. Figure 8-24 shows a diagram of how this model can be conceived. Assume that the projectile tip can be represented by a two dimensional disk with an angle of δ traveling in the direction of V_o . Assuming small angles, the disc can essentially be remodeled as a disc with a reduced diameter in the plane of rotation angle (δ). The cavity is then created by a disc with a diameter of $D_{xy} = 2R\cos(\delta)$ in the plane of δ , whereas the diameter of the disc normal to this plane is $D_{zy} = 2R$. The upper and lower cavities are then translated to match with the location of the disc edge. The upper cavity translates by $[x'_T = x - R_o\sin(\delta), y'_T = R(x) - R_o\cos(\delta)]$, and the lower cavity translates

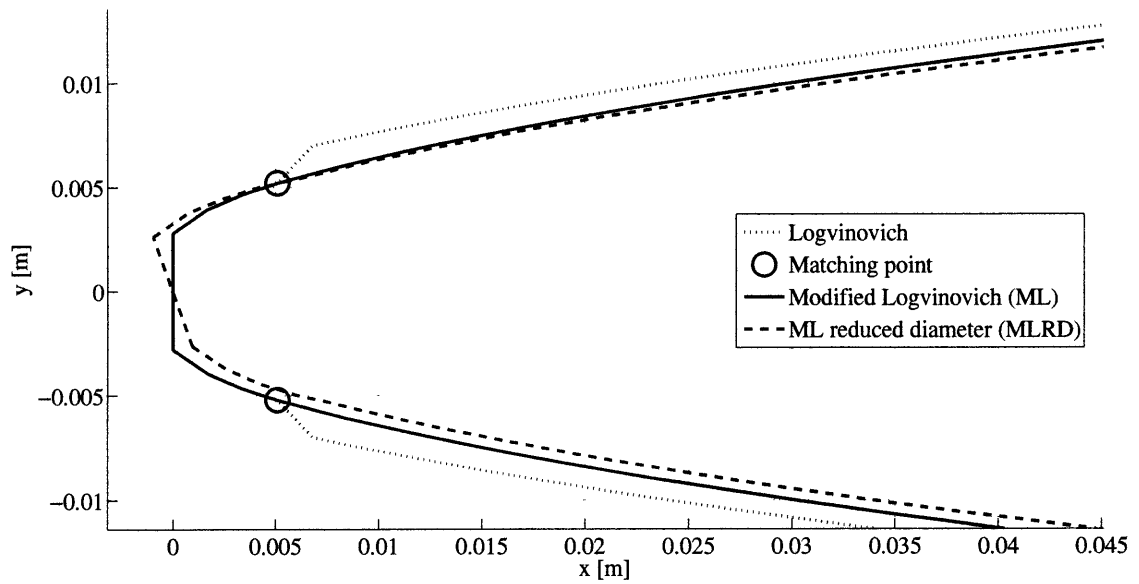


Figure 8-23: Cavity outlines for four different theoretical approaches. (...) represents the cavity formed by the Logvinovich model as discussed in [1]. (○) represents the matching point location for the Logvinovich model. All cases use this point as the transition point from the empirical model at the tip to the analytic model. (—) represents the modified Logvinovich model and (---) represents the same model but uses the altered tip diameter based on the angle (δ) the disc now makes with the vertical.

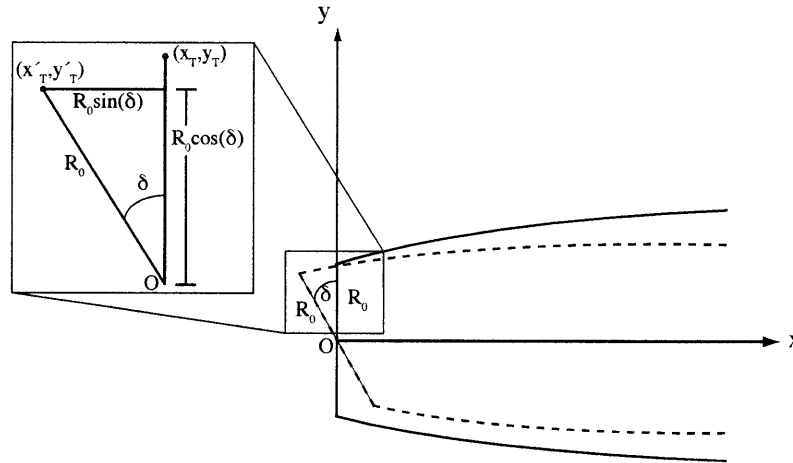


Figure 8-24: Sketch of the cavity near the tip of the disc illustrating how the cavity size is determined when the disc is at an angle (δ) to the incoming flow field. The projected area of the disc tangent to the flow direction is used as the new radius for determining the cavity size. Then the new cavity is moved to align with the edge of the disc, the top portion of the cavity is moved to the position $[x'_T = x - R\sin(\delta), y'_T = R(x) + R\cos(\delta)]$, while the bottom portion is moved to $[x'_B = x + R\sin(\delta), y'_B = R(x) - R\cos(\delta)]$. The inset shows the disk rotated by an angle δ compared to the vertical and shows how the area facing the flow V_o is reduced.

to $[x'_B = x + R\sin(\delta), y'_B = R(x) - R\cos(\delta)]$. A comparison of the Logvinovich model, the modified model, and the modified model with angled disc are shown in figure 8-23.

The theoretical model can be compared to the empirical results by tracing the cavities using an edge detection algorithm. Figure 8-25 shows the results of the comparison for case (7,14,7) and compares with results presented in figures 8-13 to 8-16. Overall, the results show good agreement with the cavity model. The subtleties of the cavity size are difficult to compare. Although the Logvinovich model has been improved, it is not clear from these figures alone whether the improved cavity model explains the cavity shape better than in the past. Preliminary data from NUWC does conclude that the Logvinovich model is generally a bit too large but exact amounts of its discrepancy are not available for comparison at this time. The images also reveal that the cavity is in contact with the free surface and so the upper portion of the cavity is not accurately represented by the steady state model.

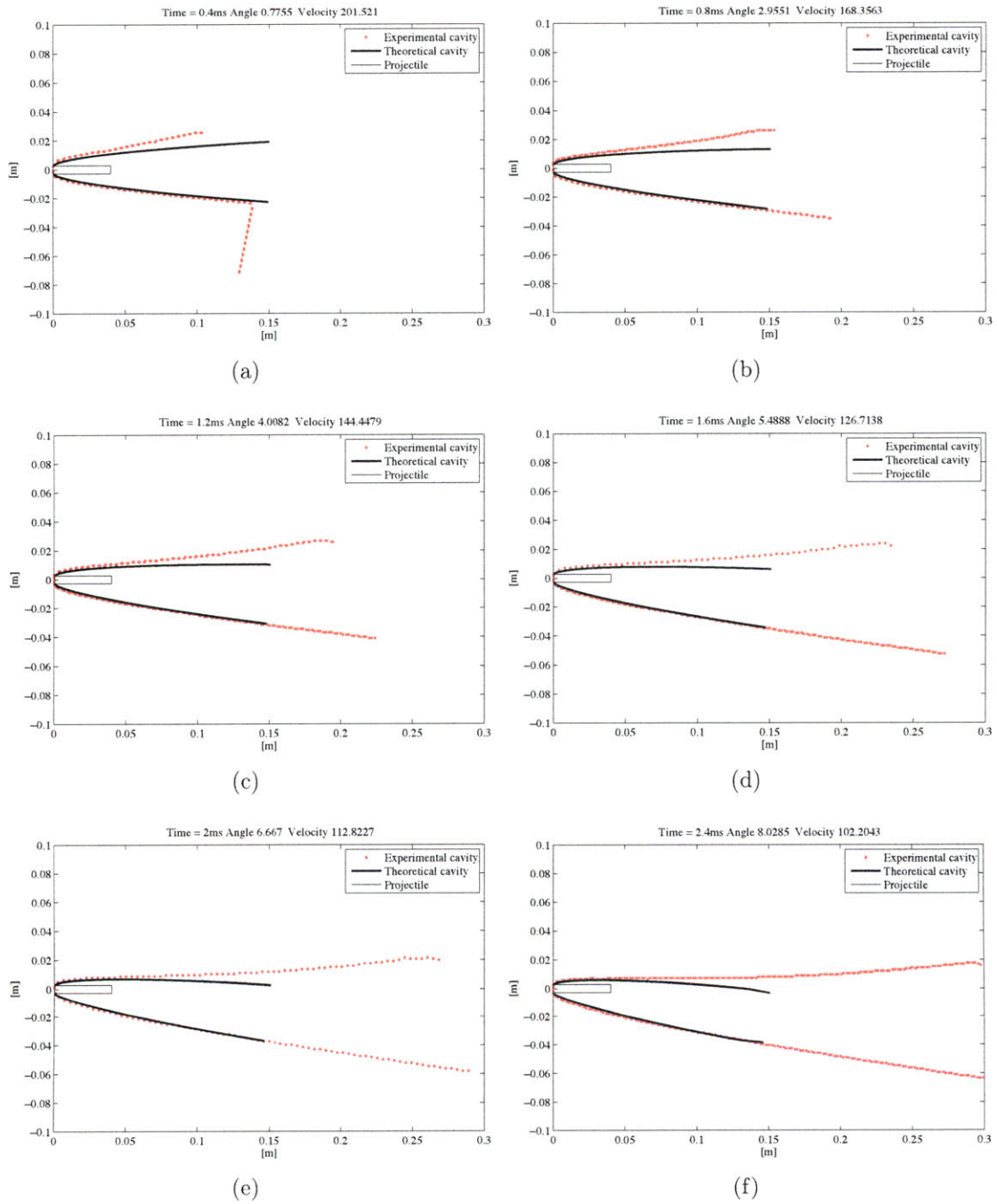


Figure 8-25: Modified Logvinovich model compared to cavity from case (7,14,7). Experimental cavity obtained from images in figure 8-13. Every fifth data point is plotted from the experiment in red, and the cavity model is in black. For ease in processing these images are flipped horizontally from figure 8-13.

Further comparison can be made with case number (15,14,10) in figure 8-26. The projectile presented here corresponds with the data presented in figures 8-17 to 8-20. The figures show good agreement between the model and experiment and emphasize the usefulness in using a theoretical model like this one when designing projectiles for optimum underwater flight.

The data presented in this chapter represents both experimental and theoretical analysis of the water-entry of high speed projectiles. While the data is specific to 0.22 caliber bullets, it can easily be applied to higher speed projectiles. The experimental data shows the evolution of small caliber high-speed projectile water-entry from standard off-the-shelf bullet shapes to specifically designed underwater projectiles. Modified projectiles with blunt tips and large L/D perform significantly better than the ogive tip small L/D counterparts. The design is greatly enhanced through the application of a modified cavity model which accounts for small pitch angles. Using the cavity theory higher performing projectiles were designed and tested and results agree that the model is an accurate representation of the cavities observed.

Further work on the theoretical model including the effects of the free surface, changing from a steady to an unsteady model, and the introduction of the planing force associated with the stability of the projectile. The experimental improvements include higher resolution of the event, along with more down range information in an attempt to gather more steady-state-like data. Further improvements include testing what might occur if there are bubbles of varying sizes in the flow field and determination of how the projectile will behave as it passes through these voids in the medium.

8.6 Acknowledgements

I would to like acknowledge the many organizations and people that supported this project. Because the facilities used were not normally employed for this purpose the timing required the help of many people to get this project off the ground. The MIT safety office, Police, and Rifle Range staff were extremely helpful and encour-

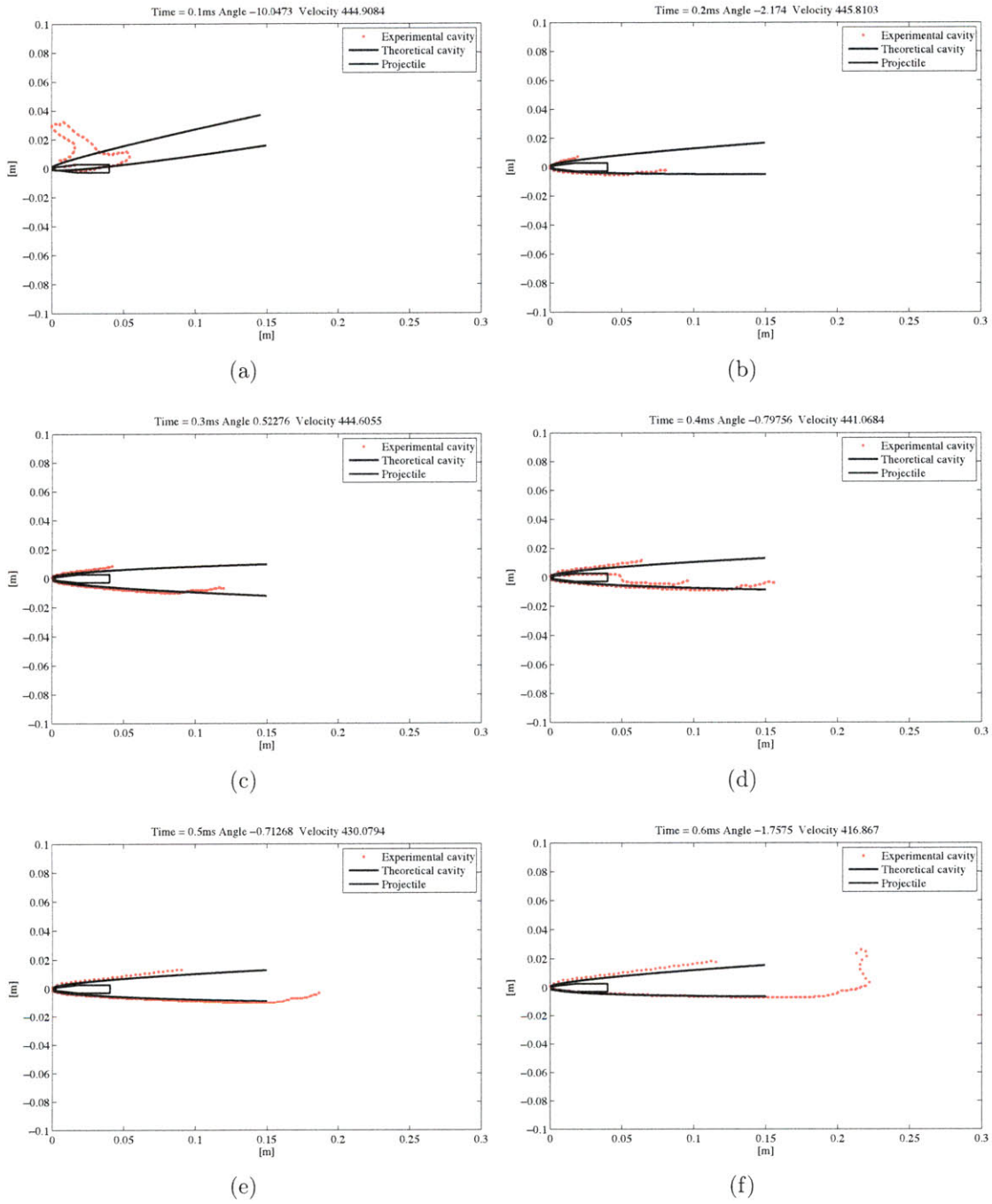


Figure 8-26: Modified Logvinovich model compared to cavity from case (15,14,10). Experimental cavity obtained from images in figure 8-17. Every fifth data point is plotted from the experiment in red, and the cavity model is in black. For ease in processing these images are flipped horizontally from figure 8-17.

aging. Will Hart of the Rifle range was the largest supporter, who stayed with us many days and nights without pay to perform these experiments. Thank you Will. Many graduate students and undergraduates came in to help for many many hours of discussion, setup, and heavy lifting; Roderick LaFoy, Brenden Epps, Jesse Belden, Vera Pavel, Mike Smith-Bronstein, and Ashley Cantieny. The Discovery TimeWarp crew for showing us some tips for better lighting and allowing us to use their cameras for one last shot. Theresa McMullen and the Office of Naval Research University Laboratory Initiative for funding this research. Finally, Dr. David Beal and Prof. Alexandra H. Techet who supported this project from the beginning and helped guide me through every step of the way.

Bibliography

- [1] Georgii Vladimirovich Logvinovich. *Hydrodynamics of free-boundary flows*. Jerusalem, Israel Program for Scientific Translation; [available from the U.S. Dept. of Commerce, National Technical Information Service, Springfield, Va.], 1972.

Chapter 9

Summary and conclusions

In summary, this thesis examines the water entry of spheres and projectiles through the use of high speed imaging. Multiple methods and considerations for improving data obtained from high speed imaging are outlined which attempt to expand our physical understanding of this problem. An overview of the major contributions and conclusions with suggestions for future work are given in this section.

In Part I, quality imaging allowed the positions, velocities, accelerations and forces of spheres impacting the free surface to be resolved from impact to well below pinch-off. Past experimental studies have only measured forces at impact up to one-half a diameter below the free surface. Resolving the forces associated with impact well below the free surface is an important step in improving the numerical and analytical models, especially as it relates to underwater mine deployment, launching of missiles and torpedos, and industrial coating techniques. The determination of the forces acting on the sphere was enhanced through the development of a tool used to determine the best spline fit of position data. In contrast to least squares fitting to position, a spline fit is an analytical solution that matches the position data more accurately, which improves the determination of velocities, accelerations and forces acting on the sphere. Furthermore, the methods developed in this thesis can easily be applied to other imaging problems. The optimized spline fitting tool is especially well suited for use with PIV measurement smoothing in both time and space and is the topic of ongoing study.

The sphere data shows that the forces associated with impact and descent through the fluid column vary dramatically between the cavity forming and non-cavity forming cases. In particular the cavity forming case actually has a lower drag coefficient than the non-cavity forming counterpart. This is potentially counter-intuitive as many have informally commented that the large cavity would appear to create a larger drag on the sphere. PIV results yield evidence that cavity forming spheres have a tendency to inhibit vortex formation in the wake, which makes this argument plausible ($Re = 75,00$ to $300,000$). In the non-cavity forming cases the spheres with lowest mass ratios ($m^* = 1.14$) nearly stop their descent approximately nine diameters below the free surface. PIV data shows that these spheres shed a vortex ring just before this slowing event and the vortex ring grows radially, eventually passing spheres in the vertical direction. For larger mass ratios it does not appear that this happens, which is likely due to the larger inertial forces. PIV data from the cavity forming cases shows near zero vorticity in the flow field, which suggests a potential flow field solution may provide insight . Future work is necessary to apply a potential flow model to the cavity forming spheres in an effort to accurately determine the unsteady nature of the forces on the spheres presented.

Emphasis on the general mechanisms that can alter the dynamics of cavity formation including surface treatment and transverse rotation have been presented. The dynamic effects of rotation can mimic the effects of altered surface treatment. In particular, coating a sphere half in a hydrophobic coating and half cleaned to be hydrophilic will alter the cavity shape to resemble that of a rotating hydrophobic sphere with sufficient spin rate. These two effects alter the cavity shape of the sphere and form a wedge of fluid that crosses the cavity, which is described and quantified for the first time here. Rotation also adds a component of lift, which is presented in the context of lift and drag coefficients on a transversely spinning sphere impacting the free surface, and this is the first time these components are presented to the general community.

Interestingly, the trajectory of the half uncoated and half coated spheres move away from the cavity forming side of the sphere until the pinch-off, after which the

spheres begin a more vertical descent. Similarly, the spinning spheres experience a lifting force due to the coupled forward and rotational velocities, which cause deviations in their vertical trajectory that continue well after deep seal. An obvious extension of this work includes the effect of roughness on cavity formation. Future work could also examine the physical behavior of the air-water-solid interface as the sphere moves dynamically through the free surface.

Finally, for all of the cavity forming spheres tested, regardless of spin rate, mass ratio and diameter, the non-dimensional time to deep seal ($\tau = t\sqrt{2g/D} = 1.726 \pm 0.0688$) remains constant, similar to results of previous studies [1, 2, 3]. Here we also note that the depth of the sphere at deep seal can be scaled by the Froude number $F_r = V/\sqrt{gD}$ and mass ratio as $F_r(m^*)^{1/2}$. This is a direct application to industrial and naval applications that need to know where deep seal occurs for materials used in underwater applications that vary in density from steel to kevlar. Because τ is constant, all theoretical work related to determining the deep seal location and times can be nearly approximated by a third order polynomial fit to position, even though this experimental work emphasizes that this is an approximation and more precise spline fitting should be used for numerical methods. Ongoing work in this area includes an analytical model that describes the deceleration of spheres of varying mass ratio as it relates to deep seal location. This method is currently in preparation. Efforts are also being made to determine a physical model that explains the unsteady forces from impact to approximately 10 diameters below the free surface for both cavity and non-cavity forming spheres.

High speed (≥ 300 m/s) projectile studies shown herein emphasize the need for laboratory conditions in order to improve our understanding of these phenomena. Through a full scale laboratory experiment, measurements of the forces, moments and cavity shapes were performed and show that projectiles that travel underwater do indeed use the vaporous cavity side walls they form for stability. Although these bullets are stable underwater, further work in determining optimal methods of stabilization in air is required. An emphasis on gyroscopic stabilization is presented and describes the minimum spin rate needed for gyroscopic stabilization as a function of

L/D . An existing theoretical cavity model is improved and a small-angle rotational component is added that improves the cavity size estimates and agrees well with the data. Using the improved model, a modified bullet shape is proposed and successfully tested, which shows excellent down range velocity and smaller cavity shape improvement over the initial design.

Overall, this thesis represents an experimental step towards a full understanding of the problem of water entry. The major contributions can be summarized in two categories: experimental methods and physical insights.

In the area of experimental methods, major contributions of this thesis include:

- High speed imaging of fluid-structure interactions using technically advanced lighting, image acquisition timing, and imaging concepts to obtain high quality, high-resolution images.
- The application of advanced image processing techniques to improve object tracking algorithms, including sub-pixel position resolution, accurate determination of angular rotation, and optimized spline fitting to accurately infer object accelerations and forces.
- Experimental facilities for the testing of spinning and non-spinning sphere water entry, as well as bullets at shallow water entry angles.

This thesis marks the first time that the problem of water entry by spinning spheres has been addressed in the literature and several novel features of cavity formation were observed. Major physical insights presented in this thesis include:

- Significant curvature of the water entry cavity under the influence of spin-induced lift
- The formation of a fluid wedge for spinning spheres during water entry
- The effect of surface coating on cavity dynamics for both spinning and non-spinning spheres

- Empirical force model for prediction of forces acting on objects from water entry to beyond the point of cavity collapse
- Reporting time resolved drag and lift forces
- Consistent trends in cavity collapse: non-dimensional time to deep seal remains constant across all geometric and kinematic parameters investigated and the depth to deep seal is not constant for varying mass ratios but can be scaled as $F_r(m^*)^{1/2}$
- The minimum spin rate required for stability versus L/D was determined for ballistic projectiles with axial spin, and confirmation that supercavitating projectiles can use contact with cavity side walls for stabilization
- An improved cavity model for high speed projectile impact with an added pitch component that can be used to design modified bullets geometries which exhibit enhanced performance underwater

Although these contributions are significant aids in improving theoretical models and physical understanding of free surface interactions, there are many questions left unanswered that warrant further investigation. In addition to developing an analytical model that describes the deceleration of varying mass ratio spheres as it relates to deep seal location, which is currently in preparation, several suggestions for continuing work in this field include

- Developing a potential flow model using the empirical cavity shape as a boundary condition to determine the unsteady forces acting on the spheres
- Exploring the effect of roughness on cavity formation
- Examining the physical behavior of the air-water-solid interface as the sphere moves dynamically through the free surface
- Improving cavity models to include unsteady effects

- Developing a coupled model for ballistic projectile stability in air and underwater
- Further optimizing projectile design using improved cavity model
- Determining how a bubbly flow field might affect projectile stability

Advances in digital high speed-imaging continue to improve time and spatial resolution while reducing costs; making the exploration of high speed events more and more accessible to the world at large. As improved observation continues, scientific inquiry and discovery will enhance our current understanding and capacity to manipulate our environment. Within the realm of fluid mechanics these discoveries could lead to things once thought impossible such as walking on water or constraining fluids to a volume without a solid interface. Whether or not these extreme phenomena are ever reproduced or the Navier-Stokes equations are ever fully solved, our fascination with the fluids that surround us will continue to be the topic of visually stunning photography and scientific curiosity for eons.

Bibliography

- [1] David Gilbarg and Robert A. Anderson. Influence of atmospheric pressure on the phenomena accompanying the entry of spheres into water. *Journal of Applied Physics*, 19(2):127–139, 1948.
- [2] J. W. Glasheen and T. A. McMahon. Vertical water entry of disks at low Froude numbers. *Physics of Fluids*, 8(8):2078–2083, 1996.
- [3] Tadd T. Truscott and Alexandra H. Tchet. Water entry of spinning spheres. *J. Fluid Mech.*, 625:135–165, 2009.

Appendix A

A robust method for curve fitting and evaluating derivatives of experimental data using smoothing splines

This appendix is in preparation for submission to Measurement Science and Technology as: Brenden P. Epps, Tadd T. Truscott and Alexandra H. Techet, A robust method for curve fitting and evaluating derivatives of experimental data using smoothing splines, *Meas. Sci. Technol.* In preparation.

Abstract

It is well known that performing data regression using *smoothing splines* is the best method for predicting instantaneous derivatives of noisy experimental data. This paper presents a novel and robust method for choosing the best spline fit.

Typically, a smoothing spline is fit by choosing the value of a smoothing parameter that controls the tradeoff between *error* to the data and *roughness* of the spline. This method is unreliable, because a poor choice of the smoothing parameter drastically degrades the spline fit. An alternate view of the problem is to choose an *error tolerance* and to find the spline with the least roughness possible, given that the error must be less than this tolerance.

In this paper, we systematically explore the relationship between error tolerance and the minimum possible roughness of smoothing splines. We find that there exists

a *critical error tolerance*, corresponding to the spline that has the minimum error to the data possible, without also having roughness due to the noise in the data. We present a method to find this critical error tolerance and show that this in fact yields the best spline fit.

A.1 Introduction

Finding the rate of change of a measured quantity is a ubiquitous experimental task. Consider experimental measurements

$$\tilde{y}_i = y(t_i) + \tilde{\epsilon}_i \tag{A.1}$$

made at times, t_1, \dots, t_N , where $y(t_i)$ is the true value of some smoothly-changing quantity and $\tilde{\epsilon}_i$ is the measurement error¹. The goal of the present work is to examine experimental $\tilde{y}(t_i)$ data and find the true function it represents, as well as its first few derivatives

$$y(t), \frac{dy(t)}{dt}, \frac{d^2y(t)}{dt^2}, \frac{d^3y(t)}{dt^3}$$

Typically in experimental work, the true function is either unknown or too complex to be represented by a simple parameterized model (e.g. a single polynomial with unknown coefficients). In this case, the appropriate way to represent the unknown function is to fit the data with a *smoothing spline*. This spline does not require any knowledge about the true function (aside from assuming that it is somewhat smooth), and derivatives of this spline can be computed exactly.

A smoothing spline can be formed by a piecewise polynomial of degree n , with $n - 1$ continuous derivatives at each break point. Typically, cubic ($n = 3$) or quintic ($n = 5$) polynomials are used. A particular spline, $s(t)$, can be characterized by its

¹Assume for all examples in this paper that the time at which each measurement took place can itself be measured exactly. Also note, the curve fitting procedure discussed herein is not restricted to functions of time. Semantically, ‘rate of change...’ implies ‘... in time’, so examples in which time is the independent variable are given herein.

error

$$\bar{E}(s) = \int_{t_1}^{t_N} |\tilde{y}_i - s(t_i)|^2 dt \quad (\text{A.2})$$

and *roughness*, which is defined for cubic and quintic splines as follows

$$R_2(s) = \int_{t_1}^{t_N} \left| \frac{d^2 s}{dt^2} \right|^2 dt \quad (\text{cubic spline}) \quad (\text{A.3})$$

$$R_3(s) = \int_{t_1}^{t_N} \left| \frac{d^3 s}{dt^3} \right|^2 dt \quad (\text{quintic spline}) \quad (\text{A.4})$$

Further background can be found in references [5, 11, 15].

In the vast majority of the smoothing spline literature, researchers try to find the ‘best’ smoothing spline fit by minimizing the quantity

$$J(s) = p\bar{E}(s) + (1 - p)R(s)$$

where the *smoothing parameter*, p , controls the amount of smoothing. Note that p must be chosen a-priori. If you pick $p = 1$, then minimizing $J(s)$ requires minimizing $\bar{E}(s)$, which happens when the spline passes through every data point. If you pick $p = 0$, then minimizing $J(s)$ requires minimizing $R(s)$; roughness is zero for a cubic spline that is composed of linear segments (and zero for a quintic spline composed of quadratic segments). For any $p \in [0, 1]$, there exists a unique spline that minimizes $J(s)$ [5]. Let us call this problem of identifying the best p and minimizing $J(s)$ the ‘deBoor formulation’.

Several researchers have developed numerical procedures to identify the ‘best’ smoothing parameter for a given data set (e.g. [14], [3] [2], [16], [7], [9], [6], [17], [12]). However, to the author’s knowledge, none of the codes developed therein have been implemented in MATLAB, which is widely-used for experimental data post-processing and analysis.

One freely-available tool is an implementation of one of deBoor’s codes in the MATLAB function `csaps(t, y)`, which attempts to choose the optimum p and then

determine the spline which minimizes $J(s)$. The solution of the deBoor problem in `csaps` requires solving a linear system of equations whose coefficient matrix has the form $p \cdot \mathbf{A} + (1 - p) \cdot \mathbf{B}$, where the matrices \mathbf{A} and \mathbf{B} depend on the data. The default value of the smoothing parameter in `csaps` is chosen such that $p \cdot \text{trace}(\mathbf{A}) = (1 - p) \cdot \text{trace}(\mathbf{B})$ [4]. This ad-hoc method for selecting p often results in inadequate smoothing.

This paper is motivated by the poor performance of `csaps` and the lack of any alternative implemented and freely-available for use in MATLAB. The implementation of the method described herein has been done in MATLAB, but the theoretical results and methodology can be implemented in any other programming language, if researchers desire to do so.

Our approach to the spline fitting problem follows Reinsch [10]: We choose an *error tolerance*, E , and find the spline with the least roughness, given that the error must be less than or equal to this error tolerance:

$$\begin{aligned} & \text{minimize } R(s) \\ & \text{requiring } \bar{E}(s) \leq E \end{aligned}$$

One can show that this roughness minimization problem, hereafter referred to as the ‘Reinsch formulation’, is equivalent to minimizing $J(s)$ in the above ‘deBoor formulation’ [5]. Note that $E = 0$ in the Reinsch formulation is equivalent to $p = 1$ in the deBoor formulation, and $E \rightarrow \infty$ in the Reinsch formulation is equivalent to $p = 0$ in the deBoor formulation. An implementation of the Reinsch formulation is available in MATLAB; the function `spaps(t, \tilde{y}, E)` returns the smoothing spline, $s(t)$, that has the least roughness possible, given that the error must be less than or equal to the given tolerance, E . The problem now is to choose the ‘best’ error tolerance, E , for a given data set.

The Reinsch problem, as implemented in `spaps`, provides a relationship between minimum roughness and error tolerance, $R(E)$. One could evaluate `spaps(t, \tilde{y}, E)` for several values of the error tolerance and compute the roughness of each resulting

spline. In doing so, one would generate an ‘efficient frontier’ of smoothing splines that are viable candidates for the best fit. For any given error tolerance, splines exist with more roughness than the one on the $R(E)$ frontier, but these are undesirable.

We find that there exists a critical error tolerance, E_{cr} , which can be used to identify the ‘best fit’ spline. For error tolerances greater than E_{cr} , a spline fit to noisy data will still be smooth. For error tolerances less than E_{cr} , the minimum-roughness spline is still very rough, since it must follow very closely to the error-ridden data points.

In this paper, we present a method for selecting the ‘best’ smoothing spline by identifying the critical error tolerance on the $R(E)$ frontier. This ‘best’ spline fit is the one that most closely follows the true function, $y(t)$; it has the minimum error possible and as much of the roughness of $y(t)$ as possible, without capturing any roughness due to the noise in the data.

The remainder of the paper is parsed into four sections: analytical example, algorithm summary, experimental example, and conclusions. The algorithm described herein has been implemented in MATLAB, and the code is available from the first author.

A.2 Analytic example

The solution of the Reinsch problem for several error tolerances produces an efficient frontier of smoothing spline choices. For a given error tolerance, no spline exists with less roughness than the spline represented by the point on this frontier. In this section, we consider an analytic example, and we examine the efficient frontier of roughness versus error tolerance. The shape of this frontier will allow us to determine the best smoothing spline. Since the true function is known in this example, we can compare our spline fits to the true function.

Consider noisy “experimental” data constructed using the function $y(t) = e^{-t} \cdot \sin(t)$ and normally-distributed “measurement error” with zero mean and standard

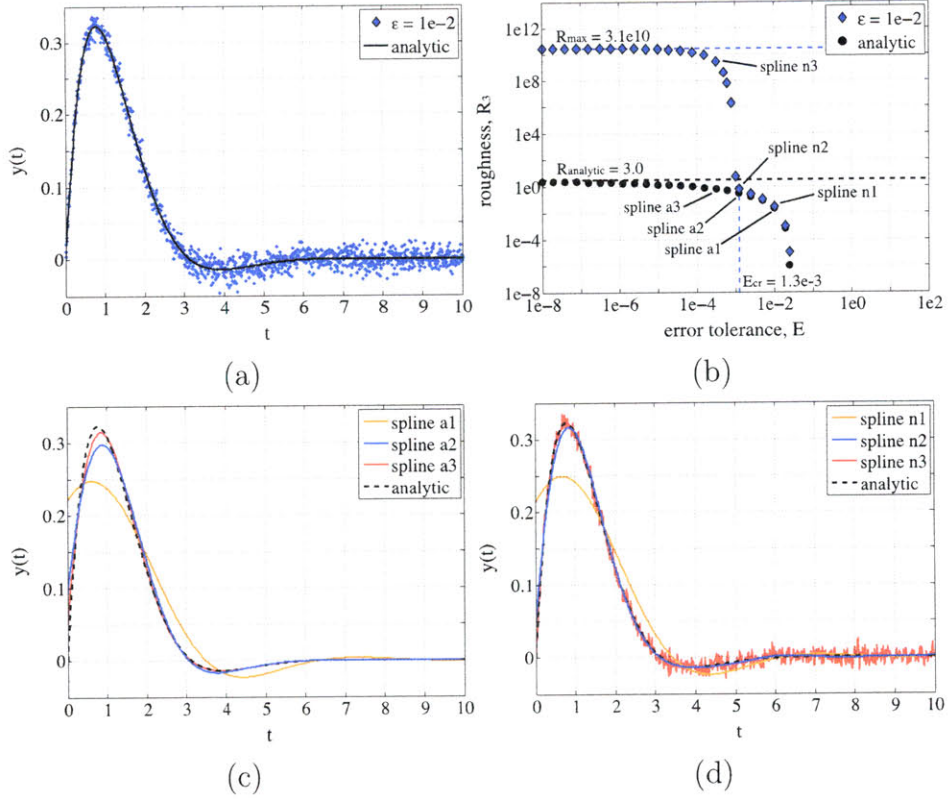


Figure A-1: (a) Example analytic function $y(t) = e^{-t} \cdot \sin(t)$ and noisy ‘data’ $\tilde{y}(t) = y(t) + \mathcal{N}(0, \epsilon^2)$ with $\epsilon = 10^{-2}$. (b) Roughness, R_3 , versus error tolerance, E , of quintic splines found by solving the Reinsch problem. Note: each point represents a particular spline fit. The roughnesses of the spline fits to the analytic data, ‘•’, asymptotically reach the analytically-computed roughness of $y(t)$, whereas the roughnesses of the spline fits to the noisy data, ‘♦’, follow this trend for E larger than a critical error tolerance, E_{cr} , but increase several orders of magnitude for $E < E_{\text{cr}}$. (c) Selected splines fit to the analytic data. (d) Selected splines fit to the noisy data. Spline n2 is the fit with the smallest error tolerance that still mimics its corresponding spline fit to the analytic data.

deviation, ϵ . That is,

$$\tilde{y}(t_i) = e^{-t_i} \cdot \sin(t_i) + \mathcal{N}(0, \epsilon^2) \quad (\text{A.5})$$

with $t_i = i \cdot \Delta t$ and $i = 1 \dots N$. These data are shown in figure A-1a, with $\epsilon = 10^{-2}$, $\Delta t = 10^{-2}$, and $N = 10^3$.

By evaluating $\text{spaps}(t, \tilde{y}, E)$ for several error tolerances, one can determine the relationship between R and E for the frontier of least-roughness quintic smoothing splines. Two such frontiers are shown in figure A-1b, one corresponding to splines fit

to the noisy $\epsilon = 10^{-2}$ data ('♦'), and one corresponding to splines fit to the analytic $y(t_i)$ data ('●'). One striking feature of the $\epsilon = 10^{-2}$ frontier is that there is a kink at $E = 1.3 \cdot 10^{-3}$.

There are three interesting regions of the $R(E)$ frontiers in this example, namely $E > 2.5 \cdot 10^{-2}$, $1.3 \cdot 10^{-3} < E < 2.5 \cdot 10^{-2}$, and $E < 1.3 \cdot 10^{-3}$. For $E > 2.5 \cdot 10^{-2}$, roughness is zero, since the smoothing spline is allowed such a large error that it can be composed of segments which have no roughness. As E is decreased from $2.5 \cdot 10^{-2}$ to $1.3 \cdot 10^{-3}$, the resulting smoothing splines are required to pass more closely to the given data. In doing so, each successive spline captures more of the roughness of the true function. This is illustrated by splines a1 and a2 in figure A-1c and splines n1 and n2 in figure A-1d. Note the similarity between the spline fits to the analytic data versus the noisy data; splines a1 and n1 look virtually identical, and splines a2 and n2 look quite similar as well. These figures show that for error tolerances larger than the critical error tolerance ($E_{\text{cr}} = 1.3 \cdot 10^{-3}$ in this example), a spline fit to noisy data is quite comparable to a spline fit to the analytic data.

For error tolerances less than the critical value (i.e. in the region $E < 1.3 \cdot 10^{-3}$), a smoothing spline fit to noisy data is now required to follow the data so closely that the measurement error is captured by the smoothing spline. In other words, the spline is not permitted enough error tolerance to ignore the measurement error. Consequently, many wiggles are introduced into the spline fit, and the roughness increases by ten orders of magnitude over a relatively small range of E . Splines a3 and n3 (shown in figures A-1c and A-1d) were computed for an error tolerance just less than that of E_{cr} . Note that spline a3 follows the analytic $y(t)$ function more closely than spline a2, whereas spline n3 is quite noisy, because it is attempting to follow the noisy data.

Smoothing spline n2, as well as its first three derivatives, are compared to the analytic function in figure A-2. The spline fit itself lays nearly on top of the analytic function in figure A-2a, and the first two derivatives are also quite accurate. The second derivative does not capture the nature of the analytic function near time $t = 0$, because the third derivative of the analytic function is non-zero at that time, and one requirement of the quintic spline fitting procedure is that the third derivative

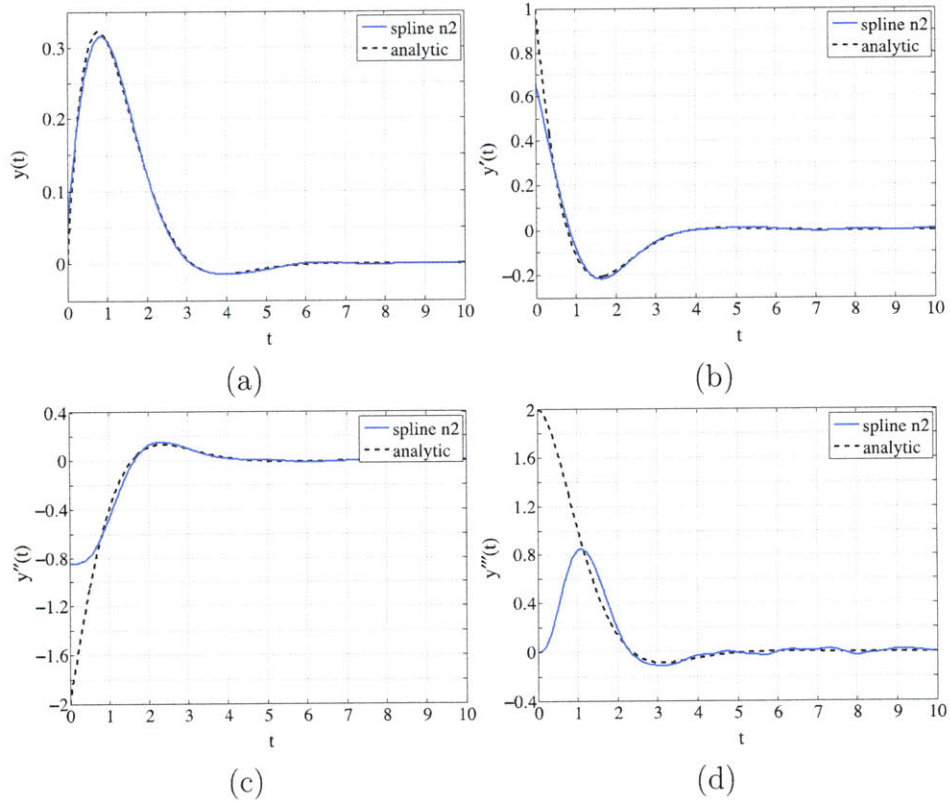


Figure A-2: Comparison of the analytic function $y(t) = e^{-t} \cdot \sin(t)$ and spline fit n2 (see figure A-1), as well as their first three derivatives with respect to time.

is zero at the endpoints. If one desires to accurately represent the third derivative at the endpoints, a spline of higher degree than quintic must be used.

The results shown in figures A-1 and A-2 indicate that the ‘best’ smoothing spline corresponds to the one for which $E = E_{\text{cr}}$. This spline has the minimum error tolerance, without the introduction of much roughness due to measurement error. We define E_{cr} as the error tolerance for which the $R(E)$ frontier has its maximum positive curvature; this definition allows one to automate the process of determining E_{cr} , as will be discussed in section A.3.

A.2.1 Roughness and Error scaling

Why, in this example, is the critical error tolerance $E_{\text{cr}} = 1.3 \cdot 10^{-3}$, and why is the maximum roughness $R_{3,\text{max}} = 3.1 \cdot 10^{10}$? What would happen if we had ‘measurement

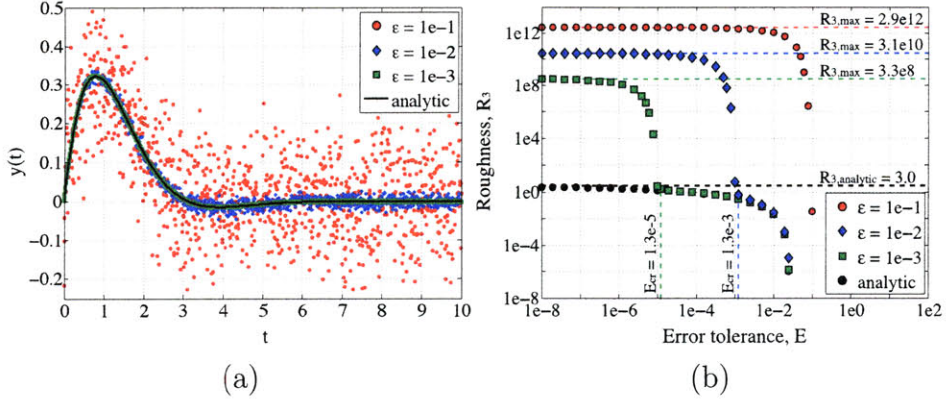


Figure A-3: (a) Example analytic function $y(t) = e^{-t} \cdot \sin(t)$ and noisy ‘data’ $\tilde{y}(t) = y(t) + \mathcal{N}(0, \epsilon^2)$ with $\epsilon = \{10^{-1}, 10^{-2}, 10^{-3}\}$. (b) Roughness of quintic splines, R_3 , versus error tolerance, E .

error’ with standard deviation, say $\epsilon = 10^{-3}$ or 10^{-1} ?

Example data with measurement error, $\epsilon = \{10^{-1}, 10^{-2}, 10^{-3}\}$, and their corresponding $R(E)$ frontiers are shown in figures A-3a and A-3b, respectively. The $\epsilon = 10^{-2}$ data is the same as figure A-1. The $\epsilon = 10^{-3}$ data have a lower critical error tolerance than the $\epsilon = 10^{-2}$ data, as shown in figure A-3b. The $\epsilon = 10^{-3}$ data more accurately represent the analytic function than the $\epsilon = 10^{-2}$ data, and as a result, the spline fit to the $\epsilon = 10^{-3}$ data at its critical error tolerance more accurately represents the analytic function than the spline fit to the $\epsilon = 10^{-2}$ data at its critical error tolerance. The $R(E)$ frontier corresponding to the $\epsilon = 10^{-1}$ data has no kink, since the noise level is so large that the analytic function cannot be resolved from these data.

To develop scaling arguments for the critical error tolerance and maximum roughness, consider a hypothetical data set, $\tilde{y}(t_i) = (-1)^i \cdot \epsilon$ with $t_i = i \cdot \Delta t$ and $i = 1 \dots N$, as if the true function were $y(t) = 0$ and this data set represents measurement noise in an average sense.

The critical error tolerance is the minimum error with which the spline still represents the true function (i.e. $s(t) \approx 0$). Thus, the critical error tolerance scales as

$$E_{cr} \sim \int_{t_1}^{t_N} |\tilde{y}(t_i) - 0|^2 dt \sim N \epsilon^2 \Delta t \quad (\text{A.6})$$

In our analytical example, $N = 10^3$, $\epsilon = 10^{-2}$, and $\Delta t = 10^{-2}$, so by (A.6), $E_{\text{cr}} \sim 10^3 \cdot 10^{-4} \cdot 10^{-2} = 10^{-3}$, which agrees with the computed value of $E_{\text{cr}} = 1.3 \cdot 10^{-3}$ up to an $O(1)$ constant. Note that for the $\epsilon = 10^{-3}$ data, (A.6) predicts $E_{\text{cr}} \sim 10^{-5}$, which also agrees with the computed value of $E_{\text{cr}} = 1.3 \cdot 10^{-5}$ shown in figure A-3.

The maximum roughness occurs when the spline passes through every data point. To scale the maximum roughness, we need to scale the second and third derivatives, which we can do using the forward divided difference formulae on our hypothetical error data set

$$\frac{d^2 s(t_i)}{dt^2} = \frac{s_{i+2} - 2s_{i+1} + s_i}{\Delta t} \sim \frac{4\epsilon}{\Delta t^2} \quad (\text{A.7})$$

$$\frac{d^3 s(t_i)}{dt^3} = \frac{s_{i+3} - 3s_{i+2} + 3s_{i+1} - s_i}{\Delta t} \sim \frac{8\epsilon}{\Delta t^3} \quad (\text{A.8})$$

Thus, the maximum roughness scales by

$$R_{2,\text{max}} = \int_{t_1}^{t_N} \left| \frac{d^2 s}{dt^2} \right|^2 dt \sim N \left(\frac{4\epsilon}{\Delta t^2} \right)^2 \Delta t = 16N\Delta t^{-3}\epsilon^2 \quad (\text{A.9})$$

$$R_{3,\text{max}} = \int_{t_1}^{t_N} \left| \frac{d^3 s}{dt^3} \right|^2 dt \sim N \left(\frac{8\epsilon}{\Delta t^3} \right)^2 \Delta t = 64N\Delta t^{-5}\epsilon^2 \quad (\text{A.10})$$

For our example $\epsilon = 10^{-2}$ data, (A.10) predicts $R_{3,\text{max}} \sim 64 \cdot 10^3 \cdot 10^{10} \cdot 10^{-4} = 6.4 \cdot 10^{10}$, which agrees with the computed value of $R_{3,\text{max}} = 3.1 \cdot 10^{10}$ up to an $O(1)$ constant.

To improve upon the roughness scaling formulae (A.9) and (A.10), consider the following Monte Carlo experiment. Create a data set of Gaussian noise, where $\tilde{y}(t_i) = \mathcal{N}(0, \epsilon^2)$, again $t_i = i \cdot \Delta t$ and $i = 1 \dots N$, and the true function is $y(t) = 0$, as with our scaling arguments. Now, fit a natural interpolating spline through that data ($E = 0$), and compute its roughness. By repeating this procedure several times, with several different N , ϵ , and Δt , we observe that on average

$$R_{2,\text{max}} \approx 36N\Delta t^{-3}\epsilon^2 \quad (\text{cubic spline}) \quad (\text{A.11})$$

$$R_{3,\text{max}} \approx 31N\Delta t^{-5}\epsilon^2 \quad (\text{quintic spline}) \quad (\text{A.12})$$

Surprisingly, the front-factors in formulae (A.11) and (A.12) appear to be insensitive

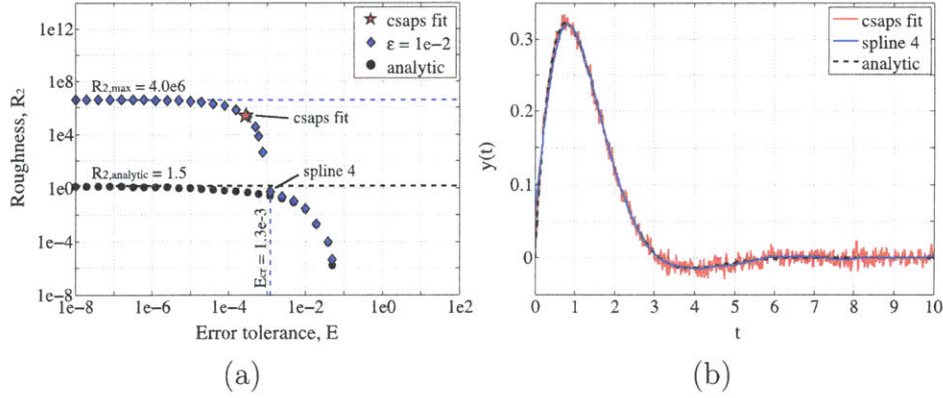


Figure A-4: (a) Roughness, R_2 , versus error tolerance, E , of cubic splines fit to the example $\epsilon = 10^{-2}$ data. The spline fit by csaps has $E = 2.9 \cdot 10^{-4}$ and $R_2 = 2.5 \cdot 10^5$. (b) The spline fit by csaps is quite rough, whereas spline 4 smoothly approximates the analytic function.

to probability distribution. To show this, one may repeat this computational experiment, this time drawing the random numbers from a uniform distribution on the range $\sqrt{3}\epsilon \cdot [-1, 1]$. (The front factor, $\sqrt{3}\epsilon$, makes this probability distribution have a standard deviation of ϵ , which is equivalent to the above normal distribution.) If one repeats the Monte Carlo experiment with the uniform distribution, one finds that the roughness formulae (A.11) and (A.12) still hold true. The fact that the front-factors in (A.11) and (A.12) are insensitive to error probability distribution means that no matter how error actually is distributed, (A.11) and (A.12) still give a good estimate of the maximum roughness of the data. More importantly, since $R_{2,\max}$ and $R_{3,\max}$ can be computed for an experimental data set, equations (A.11) and (A.12) can be used to estimate the measurement error!

A.2.2 Comparison between csaps and the present method

An efficient frontier of minimum roughness cubic splines (fit to the $\epsilon = 10^{-2}$ data) versus error tolerance is shown in figure A-4a. It exhibits a kink at, $E_{cr} = 1.3 \cdot 10^{-3}$, which is the same critical error tolerance as with the quintic smoothing splines (see figure A-1b). This is to be expected, since the critical error tolerance scaling equation (A.6) does not depend on fit type. This kink allows one to select ‘spline 4’ as the

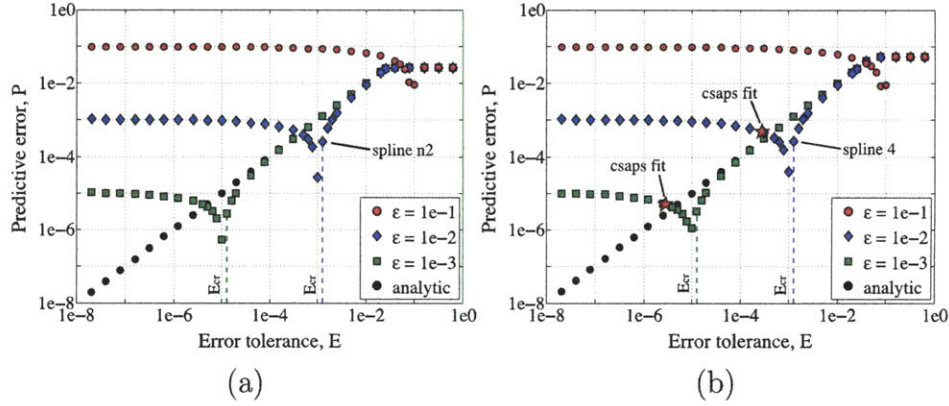


Figure A-5: (a) Predictive error, P , versus error tolerance, E , of *quintic* splines fit to the example $\epsilon = \{10^{-1}, 10^{-2}, 10^{-3}\}$ data. (b) Predictive error versus error tolerance of *cubic* splines. The spline fit by csaps to the $\epsilon = 10^{-2}$ data has $E = 2.9 \cdot 10^{-4}$ and $P = 4.8 \cdot 10^{-4}$, and spline 4 has $E = 1.3 \cdot 10^{-3}$ and $P = 2.7 \cdot 10^{-4}$.

best fit to the data using cubic smoothing splines, which yields a smooth curve in figure A-4b.

Figure A-4 illustrates that our method fits a smooth spline to the noisy data, whereas the present implementation of the MATLAB function, csaps, does not. In this case, the smoothing parameter selected by csaps corresponds to an error tolerance lower than the critical value, which is why the csaps fit does not smooth the data adequately.

On a side note, the maximum roughness predicted by (A.11) is $R_{2,\max} \approx 36 \cdot 10^3 \cdot 10^6 \cdot 10^{-4} = 3.6 \cdot 10^6$, whereas the maximum roughness of these cubic spline fits to our noisy ($\epsilon = 10^{-2}$) data is $R_{2,\max} = 4.0 \cdot 10^6$, which is about 10% larger than the predicted value.

A.2.3 Predictive error

Let us now turn our attention to the spline *predictive error*, P , which is defined as the integral of the squared deviation between the smoothing spline and the true function:

$$P(s) = \int_{t_1}^{t_N} |y(t) - s(t)|^2 dt \quad (\text{A.13})$$

Since we know the true function in our analytical example, we can compute P for each spline on the $R(E)$ frontier. Plots of P versus E for the example analytic data with three noise levels, $\epsilon = \{10^{-1}, 10^{-2}, 10^{-3}\}$, are shown in figure A-5. These plots show that, for both noise levels, $\epsilon = \{10^{-2}, 10^{-3}\}$, and for both cubic and quintic splines, the spline with the critical error tolerance has nearly the minimum predictive error. The spline with the minimum P has slightly more roughness than the spline corresponding to E_{cr} ; thus, our definition of E_{cr} strikes a balance between minimizing predictive error and minimizing roughness.

These figures show that the ‘best’ spline fit, which is the one that balances both having the minimum predictive error and having the minimum roughness, is indeed the spline fit given by solving the Reinsch problem with an error tolerance of E_{cr} . In the next section, we describe a method for automating the process of determining E_{cr} and finding the best fit spline for a given data set.

A.3 Algorithm

The ‘best’ smoothing spline is the one generated by solving the Reinsch problem with $E = E_{\text{cr}}$, which corresponds to the point on the $R(E)$ frontier that has the maximum positive curvature in log-log space. To find this point of maximum curvature, we employ a procedure inspired by the ‘bisection method’ of root finding. The general idea is to create a stencil of trial E values, solve the Reinsch problem for each E in the stencil, compute the roughness of each resulting spline, use these roughness values to estimate the curvature of the $R(E)$ frontier, select the stencil point with the maximum positive curvature, refine the resolution of the stencil in the neighborhood of the selected point, and iterate until the stencil becomes acceptably fine.

In order to have three choices for the point on the $R(E)$ frontier that has maximum positive curvature, we employ a five-point stencil. The endpoints of this stencil must bound E_{cr} , and the central point of the stencil should be at an educated initial guess for E_{cr} . We can make such a guess by combining equation (A.6) with (A.11) or (A.12)

to yield

$$E_{\text{cr,guess}} = \frac{R_{2,\text{max}}}{36\Delta t^{-4}} \quad (\text{cubic spline}) \quad (\text{A.14})$$

$$E_{\text{cr,guess}} = \frac{R_{3,\text{max}}}{31\Delta t^{-6}} \quad (\text{quintic spline}) \quad (\text{A.15})$$

where $R_{2,\text{max}}$ or $R_{3,\text{max}}$ is found by computing the roughness of the natural interpolating spline fit through the data.

In order to determine the endpoints of the initial E stencil, we must bound error tolerance. The lower bound for E is, of course, zero. However, it is more practical to implement a finite value, say 10^{-14} , which is two orders of magnitude larger than the typical machine zero and yields stable behavior. An upper bound for the error tolerance, E_{ub} , in the cubic/quintic case is the error tolerance that allows spaps to fit the data using linear/quadratic piecewise polynomials, which have zero second/third derivative and hence zero roughness. Since it is possible to fit data with less error using piecewise linear/quadratic polynomials rather than using a single linear/quadratic polynomial fit to the entire data set, the single polynomial can be used to compute an upper bound for the error tolerance. Thus, E_{ub} is found by performing a linear/quadratic least squares fit to the entire data set and computing the error of that curve.

Using the upper and lower bounds as the endpoints of the initial E stencil, a five-point stencil is generated with

$$\begin{aligned} E_1^1 &= 10^{-14} \\ E_2^1 &= \sqrt{10^{-14} \cdot E_{\text{cr,guess}}} \\ E_3^1 &= E_{\text{cr,guess}} \\ E_4^1 &= \sqrt{E_{\text{cr,guess}} \cdot E_{\text{ub}}} \\ E_5^1 &= E_{\text{ub}} \end{aligned}$$

where the superscript indicates iteration number and the subscript indicates stencil point number. The value of E_2^1 is set such that $\log_{10} E_2^1 = \frac{1}{2}(\log_{10} E_1^1 + \log_{10} E_3^1)$ (i.e.

$\log_{10} E_2^1$ bisects its neighbors).

The five points on the $R(E)$ frontier corresponding to this initial stencil are computed as follows: for each E_j^1 ($j = 1, \dots, 5$), find the corresponding smoothing spline using $\text{spaps}(t, \tilde{y}, E_j^1)$, compute its derivatives, and compute the roughness, R_j^1 . The curvatures (in log-log space) at points $j = 2, 3$, and 4 are estimated using divided differences

$$\left[\frac{d(\log_{10} R)}{d(\log_{10} E)} \right]_{E=E_j^1} = \frac{\frac{\log_{10}(R_{j+1}^1) - \log_{10}(R_j^1)}{\log_{10}(E_{j+1}^1) - \log_{10}(E_j^1)} - \frac{\log_{10}(R_j^1) - \log_{10}(R_{j-1}^1)}{\log_{10}(E_j^1) - \log_{10}(E_{j-1}^1)}}{\frac{1}{2}(\log_{10}(E_{j+1}^1) - \log_{10}(E_{j-1}^1))} \quad (\text{A.16})$$

The stencil is then refined in the neighborhood of the point that has the maximum curvature. If the maximum curvature lay at point p in the k^{th} iteration, then the stencil for the $(k+1)^{\text{th}}$ iteration would be:

$$\begin{aligned} E_1^{k+1} &= E_{p-1}^k \\ E_2^{k+1} &= \sqrt{E_{p-1}^k \cdot E_p^k} \\ E_3^{k+1} &= E_p^k \\ E_4^{k+1} &= \sqrt{E_p^k \cdot E_{p+1}^k} \\ E_5^{k+1} &= E_{p+1}^k \end{aligned}$$

Such that point E_p^k becomes the center of the new stencil, and points E_2^{k+1} and E_4^{k+1} bisect points from the previous stencil in log space.

In the bisection method, a three-point stencil is refined by bisecting one of the two stencil intervals. In the present method, our five-point stencil is refined by bisection two of the intervals: since we perform two bisections during each stencil refinement, we call this the *double-bisection method*.

The double-bisection procedure iterates until the stencil is deemed fine enough. In the present implementation, when the criterion

$$\left| \frac{\log_{10} E_3^k - \log_{10} E_4^k}{\log_{10} E_4^k} \right| < 1\%$$

is satisfied, E_4^k is selected as the error tolerance corresponding to the ‘best’ fit smoothing spline. For $N \sim O(10^3)$ and $\epsilon \sim O(10^{-2})$, this typically requires less than ten double-bisection iterations, which corresponds to solving the spaps problem for less than 25 smoothing splines in total. Evaluating spaps is computationally-intensive and accounts for most of the computing time of the algorithm. In the double-bisection algorithm, three of the points from the previous stencil carry over, so only two new smoothing splines need to be determined during each iteration.

Using the present double bisection procedure automates curve fitting process. Of course, if a researcher were to fit a smoothing spline manually, it would be prudent to compute the entire $R(E)$ frontier and to manually choose a spline near the kink in the curve.

One final note: A less aggressive method for choosing the smoothing spline would be to choose the spline at which the $R(E)$ frontier has zero curvature. Since the $R(E)$ frontier should have negative curvature for the entire time it follows the true function, if the experimental data $R(E)$ frontier had zero curvature, this would indicate a departure from the true $R(E)$ frontier. Practically speaking, automating this method may be less stable than the ‘maximum curvature’ method above, and this is one point of ongoing work.

A.4 Experimental example

To demonstrate the utility of the present spline fitting method, consider a laboratory experiment in which a billiard ball falls into a quiescent pool of water, as shown in figure A-6. In this prototypical problem, we need to determine the velocity and acceleration of the ball using position data collected during the experiment. In this case, the velocity and acceleration are complicated functions of time, so simple time-averaged rates of change do not represent the data adequately. Instead, we must fit a curve to the position data in order to determine the instantaneous rates of change.

The goal of the experiment is to compute the force coefficient (i.e. the net hydro-

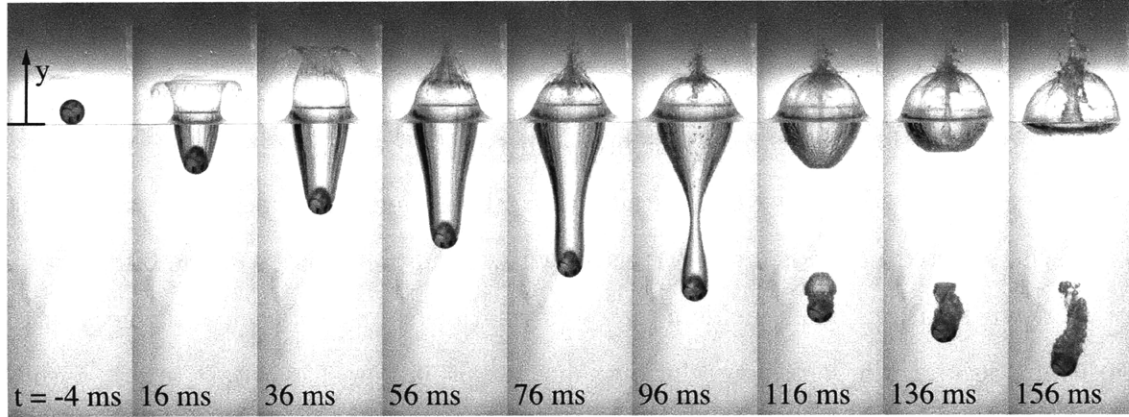


Figure A-6: A billiard ball falls into a quiescent pool of water. Position, y , is measured in each timestep, t , by inspection of the images.

dynamic force, normalized by the dynamic pressure force [8])

$$C_F(t) = \frac{F(t)}{\frac{1}{2}\rho[V(t)]^2 A} \quad (\text{A.17})$$

where $F(t) = ma(t) + mg$ is the net force on the billiard ball, $m = 0.17$ kg is the ball mass, $a(t) = \frac{d^2\tilde{y}(t)}{dt^2}$ is the instantaneous acceleration of the ball, $g = 9.8$ m/s² is the acceleration due to gravity, $\rho = 1000$ kg/m³ is the density of water, $V(t) = \frac{d\tilde{y}(t)}{dt}$ is the instantaneous velocity of the ball, $A = \pi \left(\frac{d}{2}\right)^2 = 0.0026$ m² is the cross-sectional area of the ball, and $d = 0.057$ m = 2.25 inches is the ball diameter.

In order to compute the force coefficient accurately, one must accurately evaluate the first and second derivatives of the $\tilde{y}(t)$ position data. This physics problem demonstrates the utility of the present curve fitting methodology.

A.4.1 Experimental details

In the present experiment, a high-speed digital camera acquired $N = 230$ still images at 1000 frames per second ($\Delta t = 0.001$ s) as the ball plunged into the basin.

The position of the center of the billiard ball, $y(t)$, is measured in meters above the quiescent free surface, and time, t , is measured in seconds after impact (i.e. $t = 0$ when the *center* of the billiard ball is at the quiescent free surface height). Note that

the timing of the camera and thus, the time of the measurement, is assumed to be exact.

The following is a summary of the procedure used to acquire the $\tilde{y}(t)$ position data from the images with sub-pixel accuracy; this procedure is explained in detail in [13]. First, the selected image is cross-correlated with a template image of the billiard ball in a known location. This yields a ‘cross-correlation value’ for each possible y -pixel position. Second, the ‘cross-correlation value vs. y -pixel position’ data are fit with a Gaussian curve², and the peak of this Gaussian is assumed to lie at the \tilde{y} position of the ball. Finally, the \tilde{y} data are normalized by the optical zoom (0.762 mm per pixel) to give measurements in physical units.

The experimental $\tilde{y}(t)$ position data are shown in figure A-7a. (Note that the abscissa represents *time*, so this is the trajectory of the ball in time. The ball falls nearly straight down in space.) The data are very well resolved in time and evolve smoothly; every fifth data point is shown.

A.4.2 Application of the present spline fitting method

The present spline fitting method is now used to determine the velocity and acceleration from the position data. The minimum roughness versus error tolerance frontier is shown in figure A-7b for quintic splines. Quintic splines must be used in order to obtain a smooth second derivative (i.e. acceleration). This chart shows a kink at critical error tolerance $E_{\text{cr}} = 2.5 \cdot 10^{-9}$. The roughness increases six orders of magnitude as E is decreased below E_{cr} . The maximum roughness, which corresponds to the interpolating spline ($E = 0$), is $R_{3,\text{max}} = 1.7 \cdot 10^{10}$. It is expected that the smoothing spline corresponding to the critical error tolerance contains little of the noise due to the measurement error and best captures the true $y(t)$ curve.

The maximum roughness equation (A.12) and critical error tolerance equation (A.6) can be used to derive estimates of the error in our experimental measurement

²Here, we know that the cross-correlation procedure should produce a Gaussian ‘cross-correlation value vs. y -position’ curve, so it is appropriate to choose the form of the curve fit.

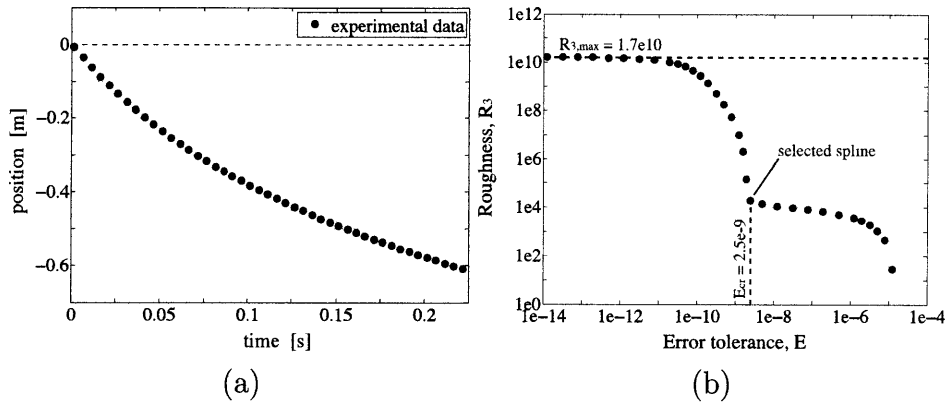


Figure A-7: (a) Position of the billiard ball as a function of time, $\tilde{y}(t)$. Every fifth data point is shown. (b) Roughness of quintic smoothing splines, R_3 , versus error tolerance, E . The kink in this $R(E)$ frontier is at critical error tolerance, $E_{cr} = 2.5 \cdot 10^{-9}$.

of ball position.

$$\epsilon \approx \sqrt{\frac{R_{3,\max}}{31N\Delta t^{-5}}} = 0.048 \text{ mm}$$

$$\epsilon \approx \sqrt{\frac{E_{cr}}{N\Delta t}} = 0.11 \text{ mm}$$

These estimates agree up to the $O(1)$ scaling factor in (A.6) and are equivalent to about 0.1% of the ball diameter. Also note that $0.11 \text{ mm} = 0.14 \text{ px}$, so this estimate agrees with the assertion that our experimental procedure has sub-pixel accuracy.

The selected spline fit and its derivatives are shown in figure A-8. Note that y position is defined positive upwards: The ball falls downwards, so its velocity is less than zero, and it decelerates downwards (i.e. it accelerates upwards), so its acceleration is greater than zero. The smoothing spline, as well as its three derivatives, all evolve smoothly in time, which is expected in a physical system which evolves smoothly. The only physically unrealistic feature of these curves is the slope of the acceleration at time $t = 0$ (and therefore, also the value of $s'''(t = 0)$). This implies physically that the net force is unchanging at the moment of impact, which is obviously not true. This result occurred because the quintic spline fitting procedure requires that $s'''(t) = 0$ at the endpoints. Therefore, these portions of the $s''(t)$ and

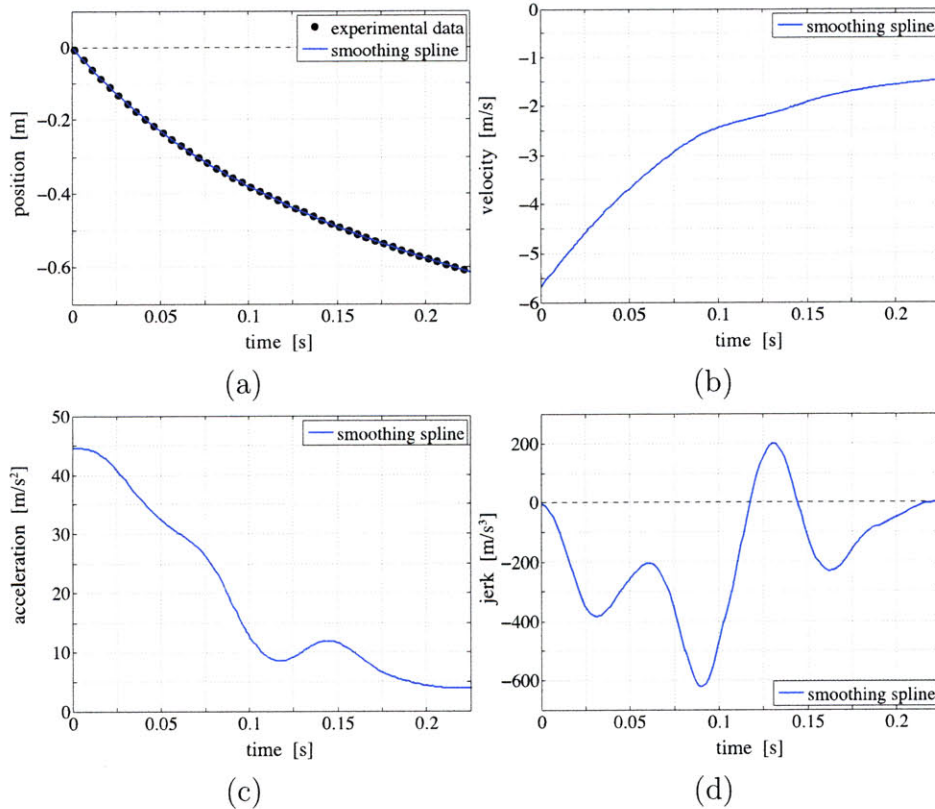


Figure A-8: The selected smoothing spline fit, $s(t)$, and its derivatives $s'(t)$, $s''(t)$, and $s'''(t)$. Note that the ball experiences more than $4g = 39 \text{ m/s}^2$ acceleration at impact: An aggressive roller coaster may subject its passengers to $4g$ at the bottom of the first drop [1].

$s'''(t)$ curves are simply ignored. The velocity and acceleration can now be used to compute the net hydrodynamic force on the billiard ball.

Figure A-9 shows the force coefficient during the water entry event³. For reference, the force coefficient for a ball of the size and speed in this experiment, when immersed in a free stream of steadily-flowing water, is about 0.2 - 0.5 [8]. The data in figure A-9 show that the force coefficient increases from initial water impact until time $t = 83 \text{ ms}$. Between 83 ms and 113 ms, the force coefficient drops dramatically during the cavity pinch-off process; cavity pinch-off occurs at $t = 98 \text{ ms}$ (just after the sixth image

³It is misleading to examine the force directly, because as the ball slows down during the course of the experiment, the expected force decreases. Thus, a lower force at later times during the experiment (when the ball is going slower) does not necessarily imply that the ball is 'more streamlined' then. The astute reader will note that force is linearly related to acceleration, so graphs of these two quantities have the same form.

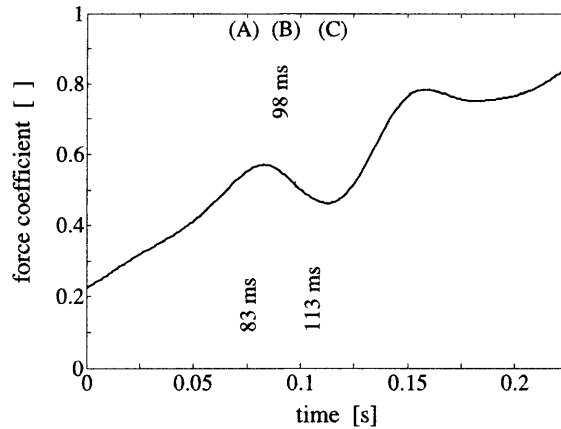


Figure A-9: Force coefficient versus time for the billiard ball water entry experiment: (A) local maximum force coefficient; (B) pinch-off; and (C) local minimum force coefficient.

shown in figure A-6). A local minimum of force coefficient occurs at $t = 113$ ms, as the lower cavity sheds from the sphere and begins to disintegrate into bubbles. Further discussion of the fluid dynamics can be found in [13].

To the authors' knowledge, this is the first published data of force coefficient during cavity impact for times when the ball is deeper than one radius below the surface. Using the present spline fitting method was critical in obtaining reliable velocity and acceleration data, which made these force coefficient predictions possible.

A.4.3 A check for the derivatives $s'(t)$, $s''(t)$, and $s'''(t)$

It is desirable to perform a check on the derivatives of the smoothing spline, which we can do by comparing them to estimates made from the noisy experimental data. For this, we need a regression technique which behaves like a non-parametric model -- one in which the fitting parameters are free to change along the length of the curve.

As a check of the first derivative, a line may be fit to a small window of data using least squares regression. The slope of this line represents the 'slope' of the data at the center of the window⁴. Mathematically speaking, to find the first derivative of $\tilde{y}(t)$ data at time, t_i , one can fit a line $(a_1t + a_2)$ to the data within the window $[t_{i-w}, t_{i+w}]$.

⁴This is equivalent to performing a Taylor series expansion about the center of the data window.

Table A.1: Windowed least squares estimates of the first, second, and third derivatives of noisy $\tilde{y}(t)$ data.

windowed least squares fit	derivative estimate
linear: $a_1 t + a_2$	$y'_{\text{wls}}(t) \approx a_1$
quadratic: $a_1 t^2 + a_2 t + a_3$	$y''_{\text{wls}}(t) \approx 2 \cdot a_1$
cubic: $a_1 t^3 + a_2 t^2 + a_3 t + a_4$	$y'''_{\text{wls}}(t) \approx 3 \cdot 2 \cdot a_1$

The width of the window is $2w+1$ data points, where a larger w yields more smoothing of the data but a less localized estimate. The first derivative of this linear polynomial (namely a_1) is the estimate of the first derivative of the data at time, t_i . This process would be repeated with the window centered at each $t_{w+1} \leq t_i \leq t_{N-w}$ to obtain the derivative estimate for each time. Since this procedure involves performing a least squares fit to a small window of data, we call this the *windowed least squares* (WLS) method.

Higher order derivatives can also be estimated using windowed least squares. At each discrete time, a least squares linear polynomial fit gives an estimate of the first derivative at that time, a quadratic polynomial fit gives an estimate of the second derivative, a cubic polynomial fit gives an estimate of the third derivative at that time, and so on. The windowed least squares fit types and derivative estimates are summarized in table A.1, and the estimates of the first and second derivatives are shown in figure A-10. These data agree quite well with the derivatives of the smoothing spline, as expected.

The estimates of the second and third derivatives obtained using windowed least squares can also be used as a check of the roughness of the true function:

$$R_{2,\text{wls}}(s) = \sum_{i=1+w}^{N-w} |y''_{\text{wls}}(t_i)|^2 \Delta t \quad (\text{cubic spline}) \quad (\text{A.18})$$

$$R_{3,\text{wls}}(s) = \sum_{i=1+w}^{N-w} |y'''_{\text{wls}}(t_i)|^2 \Delta t \quad (\text{quintic spline}) \quad (\text{A.19})$$

It is expected that the roughness of the true function and hence, the roughness of the

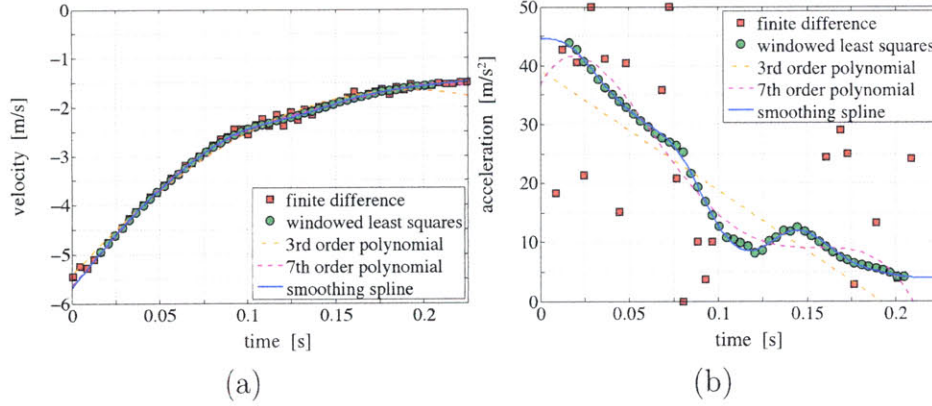


Figure A-10: Velocity, $y'(t)$, and acceleration, $y''(t)$, computed by: finite difference; windowed least squares; third-order polynomial least squares fit to the entire data set; seventh-order polynomial least squares fit to the entire data set; and the selected smoothing spline, for which $E = E_{\text{cr}}$.

best fit smoothing spline, would be approximately equal to the value given by (A.18) or (A.19).

The windowed least squares method provides a good estimate of the derivatives of the function, because the general trend of the data surrounding each point is captured by the least squares regression technique. However, this method does not ensure that the derivative is a smooth function as the window is moved along the data set. It also fails to predict the derivative near the ends of the data interval ($t_i < t_{w+1}$ and $t_i > t_{N-w}$), since the window would then extend beyond the interval of available data.

Two questionable methods for estimating the derivatives are also shown in figure A-10: least squares regression to the entire data set, and finite differences.

The derivatives of a least squares regression to all the data are inherently questionable, because the fitting parameters depend on the entire data set. Clearly, one cannot assume that the dynamics of our billiard ball during early times (e.g. during cavity formation) are the same as the dynamics during later times (e.g. after cavity collapse). Fitting a single polynomial to all of the data implicitly demands that the physics at all times be the same, which is clearly not true in this experiment.

It would be appropriate to fit a polynomial to all of the data (using least squares) if the physics were the same throughout the experiment and the form of the true

function is known (e.g. a quadratic polynomial fit to position data of a ball falling in a vacuum). However, if the form of the true function is unknown (which is usually the case in scientific research), then this method can give misleading results. For example, both 3rd-order and 7th-order polynomials fit well to all of the position data in the billiard ball example problem. However, their second derivatives are quite different, and neither agrees with the smoothing spline prediction or windowed least squares estimate (see figure A-10b).

Finite difference methods amplify measurement noise, yielding poor estimates of derivatives. For example, the central divided difference formula predicts

$$\begin{aligned}
 \frac{d\tilde{y}(t_i)}{dt} &= \frac{\tilde{y}_{i+1} - \tilde{y}_{i-1}}{2\Delta t} + O(\Delta t^2) \\
 &= \frac{y(t_{i+1}) - y(t_{i-1})}{2\Delta t} + \frac{\tilde{\epsilon}_{i+1} - \tilde{\epsilon}_{i-1}}{2\Delta t} + O(\Delta t^2) \\
 &= \frac{dy(t_i)}{dt} + O\left(\frac{\epsilon}{\Delta t}\right) + O(\Delta t^2)
 \end{aligned} \tag{A.20}$$

where $O(\)$ denotes the order of magnitude of the error in the prediction. For a small timestep, $\Delta t \ll 1$, the measurement error, ϵ , is amplified. The noise is amplified again upon taking each successive derivative, yielding derivatives with unsatisfactorily-large error on the order of

$$\frac{d\tilde{y}}{dt} \sim O\left(\frac{\epsilon}{\Delta t}\right), \quad \frac{d^2\tilde{y}}{dt^2} \sim O\left(\frac{\epsilon}{\Delta t^2}\right), \quad \frac{d^3\tilde{y}}{dt^3} \sim O\left(\frac{\epsilon}{\Delta t^3}\right), \quad \dots$$

Similarly, all finite difference methods amplify measurement noise, even when a larger time step is used⁵. This error amplification is quite noticeable in the acceleration estimates in figure A-10b.

⁵Even if n timesteps are skipped on either side of the data point, the central difference formula predicts

$$\frac{dy(\tilde{t}_i)}{dt} = \frac{y(t_{i+n}) - y(t_{i-n})}{2n\Delta t} + O\left(\frac{\epsilon}{n\Delta t}\right) + O(n^2\Delta t^2)$$

which may never have satisfactorily-small error.

A.5 Conclusions

We have shown that performing data regression using smoothing splines is the best method for predicting the derivatives of noisy experimental data. It agrees well with the windowed least squares method, which is a good means to approximate the instantaneous derivatives. Other methods, such as finite differences or fitting a polynomial to the entire data set yield poor estimates of the derivatives.

Finding the derivative of noisy data amounts to fitting a curve which captures most of the behavior of the true function that the data represents. The `spaps(t, \tilde{y}, E)` function, available in the MATLAB Spline Toolbox, fits a smoothing spline to the given $\tilde{y}(t)$ data, with error at most equal to E . The method described herein is a procedure for selecting the E value which produces the ‘best’ spline fit, one which follows the roughness of the true function but does not introduce roughness due to the measurement error.

The present computational tool is based on two critical insights. First, by systematically exploring the $R(E)$ relationship implicit in the Reinsch problem, we discovered that the $R(E)$ frontier has a kink at a critical error tolerance, E_{cr} . Second, we showed both graphically and with scaling arguments that E_{cr} corresponds to the spline with the minimum error to the data possible without introducing roughness due to the noise in the data. In our analytical example, we also showed that the spline corresponding to E_{cr} has nearly the minimum possible predictive error, P , which supports our claim that $E = E_{\text{cr}}$ produces the best possible smoothing spline.

The critical error tolerance corresponds to the point on the $R(E)$ frontier with the maximum positive curvature (in log space). The present computational tool works by finding this critical error tolerance for a given data set, using the double-bisection procedure developed herein. For many experimental measurements, with high-precision (small ϵ) and high-resolution (large N), the present method robustly smoothes the data and yields the desired instantaneous derivatives.

A.6 Appendix

A.6.1 Non-dimensional equations

Readers who prefer to consider the arguments made herein using non-dimensional quantities may normalize the data as follows:

$$\hat{y} = \frac{y}{Y} \quad \tilde{y} = \frac{\tilde{y}}{Y} \quad \hat{\epsilon} = \frac{\epsilon}{Y} \quad \hat{t} = \frac{t - t_1}{T}$$

where Y is a reference length scale (such as the total distance traveled by the billiard ball) and $T = t_N - t_1$ is the duration of the measurement times.

In non-dimensional form, the experimental data are

$$\hat{y}_i = \hat{y}(\hat{t}_i) + \hat{\epsilon}_i \quad (\text{eqn. A.1})$$

The non-dimensional error tolerance and roughness are

$$\hat{E} = \frac{E}{Y^2 T} \geq \int_0^1 |\hat{y}_i - \hat{s}(\hat{t}_i)|^2 d\hat{t} \quad (\text{eqn. A.2})$$

$$\hat{R}_2 = \frac{R_2 T^3}{Y^2} = \int_0^1 \left| \frac{d^2 \hat{s}}{d\hat{t}^2} \right|^2 d\hat{t} \quad (\text{eqn. A.3})$$

$$\hat{R}_3 = \frac{R_3 T^5}{Y^2} = \int_0^1 \left| \frac{d^3 \hat{s}}{d\hat{t}^3} \right|^3 d\hat{t} \quad (\text{eqn. A.4})$$

and the non-dimensional critical error tolerance and maximum roughness are

$$\hat{E}_{\text{cr}} = \frac{E_{\text{cr}}}{Y^2 T} \sim \hat{\epsilon}^2 \quad (\text{eqn. A.6})$$

$$\hat{R}_{2,\text{max}} = \frac{R_{2,\text{max}} T^3}{Y^2} \approx 36 N^4 \hat{\epsilon}^2 \quad (\text{eqn. A.11})$$

$$\hat{R}_{3,\text{max}} = \frac{R_{3,\text{max}} T^5}{Y^2} \approx 31 N^6 \hat{\epsilon}^2 \quad (\text{eqn. A.12})$$

These roughness formulae indicate that the total time interval, T , does not affect the prominence of the kink in the $R(E)$ curve; rather, the number of data points, N , and the non-dimensional error, $\hat{\epsilon}$, affect the prominence of the maximum roughness due

to measurement error, versus the roughness of the true function itself.

We can also show that, in non-dimensional terms, error is amplified when estimating derivatives by finite difference schemes. The measured data have error on the order of $O(\hat{\epsilon})$. The central difference formula predicts

$$\frac{d\hat{y}(\hat{t}_i)}{d\hat{t}} = \frac{\hat{y}(\hat{t}_{i+1}) - \hat{y}(\hat{t}_{i-1})}{2\Delta\hat{t}} + O\left(\frac{\hat{\epsilon}}{\Delta\hat{t}}\right) + O(\Delta\hat{t}^2)$$

Since the non-dimensional time step is small, $\Delta\hat{t} = \frac{\Delta t}{T} = \frac{1}{N} \ll 1$, measurement noise is amplified by the finite difference procedure, $O\left(\frac{\hat{\epsilon}}{\Delta\hat{t}}\right)$.

These non-dimensional equations show that as the temporal resolution of the measurements increases (i.e. as N increases) and as the measurement precision increases (i.e. as $\hat{\epsilon}$ decreases), the smoothing spline fitting procedure described herein becomes more accurate.

Bibliography

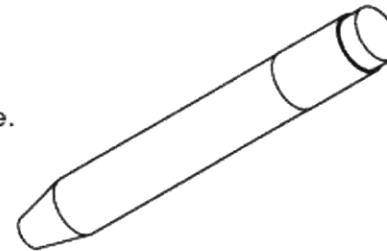
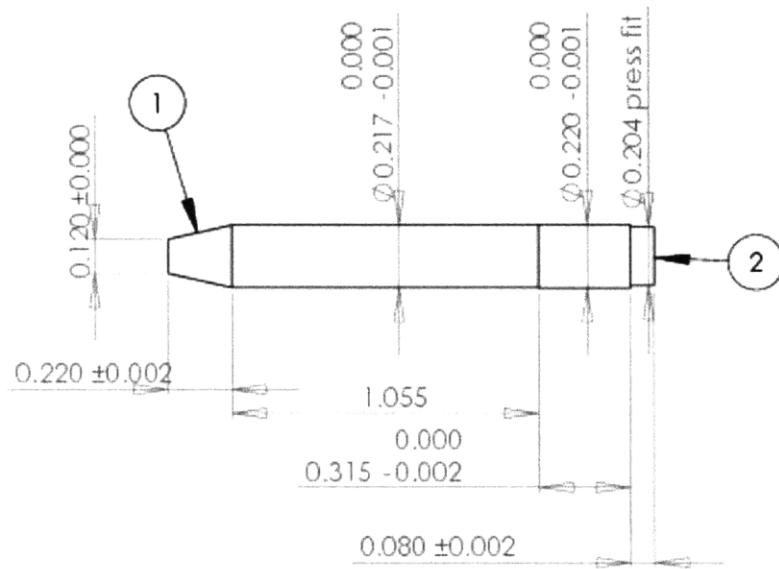
- [1] George Bibel. *Beyond the Black Box: the Forensics of Airplane Crashes*. John Hopkins University Press, 2008.
- [2] Won L. Chung. Automatic curve fitting using an adaptive local algorithm. *ACM Transactions on Mathematical Software*, 6(1):45–57, 1980.
- [3] Peter Craven and Grace Wahba. Smoothing noisy data with spline functions: Estimating the correct degree of smoothing by the method of generalized cross-validation. *Numerische Mathematik*, 31:377–403, 1979.
- [4] Carl de Boor. *MATLAB Spline Toolbox 3: User's Guide*. The MathWorks.
- [5] Carl de Boor. *A Practical Guide to Splines*. Springer, 1978.
- [6] Clifford M. Hurvich and Jeffrey S. Simonoff. Smoothing parameter selection in nonparametric regression using an improved akaike information criterion. *J. R. Statist. Soc. B*, 60(2):271–293, 1998.
- [7] Robert Kohn and Craig F. Ansley. A new algorithm for spline smoothing based on smoothing a stochastic process. *SIAM J. Sci. Stat. Comput.*, 8(1):33–48, 1987.
- [8] Pijush K. Kundu and Ira M. Cohen. *Fluid Mechanics*, volume Third Edition. Elsevier Academic Press, 2004.

- [9] S. B. Pope and R. Gadh. Fitting noisy data using cross-validated cubic smoothing splines. *Communications in Statistics - Simulation and Computation*, 17(2):349–376, 1988.
- [10] Christian H. Reinsch. Smoothing by spline functions. *Numerische Mathematik*, 10:177–183, 1967.
- [11] B. W. Silverman. Some aspects of the spline smoothing approach to non-parametric regression curve fitting. *J. R. Statist. Soc. B*, 47(1), 1985.
- [12] Nicholas A. Teanby. Constrained smoothing of noisy data using splines in tension. *Math Geol*, 39:41–434, 2007.
- [13] Tadd T. Truscott, Brenden P. Epps, and Alexandra H. Techet. Unsteady forces on spheres during water entry. *in preparation*, 2009.
- [14] G. Wahba and S. Wold. A completely automatic french curve: Fitting spline functions by cross validation. *Communications in Statistics - Simulation and Computation*, 4(1):1–17, 1975.
- [15] Grace Wahba. *Spline Models for Observable Data*. SIAM, 1990.
- [16] W. Wecker and C. Ansley. The signal extraction approach to non-linear regression and spline smoothing. *Journal of the American Statistical Association*, 78:81–89, 1983.
- [17] S. N. Wood. Modelling and smoothing parameter estimation with multiple quadratic penalties. *J. R. Statist. Soc. B*, 62(2):413–428, 2000.

Appendix B

Bullet designs

This appendix includes all of the drawings for the individual bullet types that were used in the bullet study.



- 1.) Can be shorter or longer to make the weight as close to 40 grains as possible.
- 2.) Machined to fit blunt end inside 0.22 caliber LR cartridge

Made of Aluminium

Weight ~ 40 grains = 2.592 grams

PROPRIETARY AND CONFIDENTIAL
 THE INFORMATION CONTAINED IN THIS
 DRAWING IS THE SOLE PROPERTY OF
 BICEST COMPANY HAVE HERE. ANY
 REPRODUCTION IN PART OR AS A WHOLE
 WITHOUT THE WRITTEN PERMISSION OF
 BICEST COMPANY HAVE HERE IS
 PROHIBITED.

NEXT ASSY USED ON

APPLICATION

UNLESS OTHERWISE SPECIFIED:

DIMENSIONS ARE IN INCHES
 TOLERANCES:
 FRACTIONAL:
 ANGULAR: MACH: BEND:
 TWO PLACE DECIMAL
 THREE PLACE DECIMAL

INTERPRET GEOMETRIC
 TOLERANCING PER:
 MATERIAL

FR424

DO NOT SCALE DRAWING

NAME DATE

DRAWN
 CHECKED
 ENG APPR.
 MFG APPR.

Q.A.
 COMMENTS:

TITLE:

SIZE DWG. NO. REV
A12aluminium

SCALE: 2:1 WEIGHT: SHEET 1 OF 1

5

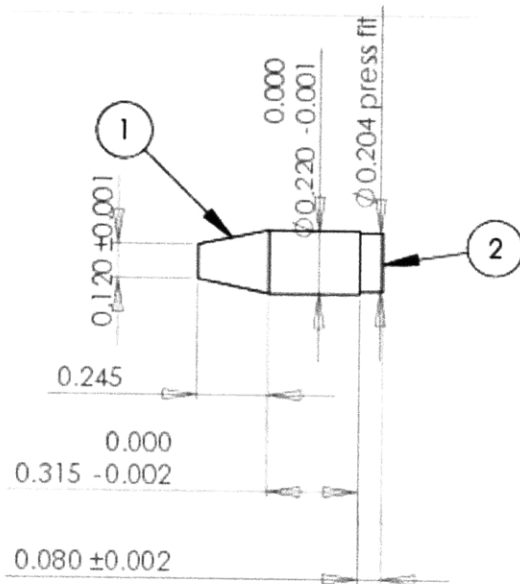
4

3

2

1

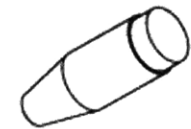
Figure B-1: Aluminum 0.12 in tip with 0.22 in angled shoulder.



- 1.) Can be shorter or longer to make the weight as close to 40 grains as possible.
- 2.) Machined to fit blunt end inside 0.22 caliber LR cartridge

Made of Steel

Weight ~ 40 grains = 2.592 grams



<p>UNLESS OTHERWISE SPECIFIED:</p> <p>DIMENSIONS ARE IN INCHES</p> <p>TOLERANCES:</p> <p>FRACTIONAL: ±</p> <p>ANGULAR: MACH: ±</p> <p>TWO PLACE DECIMAL: ±</p> <p>THREE PLACE DECIMAL: ±</p> <p>INTERPRET GEOMETRIC TOLERANCING PER: ASME Y14.5</p> <p>MATERIAL: 304</p> <p>FINISH: POLISHED</p>		<p>NAME: _____</p> <p>DATE: _____</p>	<p>DRAWN: _____</p> <p>CHECKED: _____</p> <p>ENG APPR: _____</p> <p>MFG APPR: _____</p> <p>Q.A.: _____</p> <p>COMMENTS: _____</p>	<p>TITLE: _____</p>
<p>5 PROPRIETARY AND CONFIDENTIAL</p> <p>THE INFORMATION CONTAINED IN THIS DRAWING IS THE SOLE PROPERTY OF [INSERT COMPANY NAME HERE]. ANY REPRODUCTION IN PART OR AS A WHOLE WITHOUT THE WRITTEN PERMISSION OF [INSERT COMPANY NAME HERE] IS PROHIBITED.</p>	<p>4 NEXT ASSY USED ON</p>	<p>3 APPLICATION</p>	<p>2 DO NOT SCALE DRAWING</p>	<p>1</p>
<p>SIZE DWG. NO. REV</p> <p>A 12steel</p>			<p>SCALE: 2:1 WEIGHT: SHEET 1 OF 1</p>	

Figure B-2: Steel 0.12 in tip with 0.245 in angled shoulder.

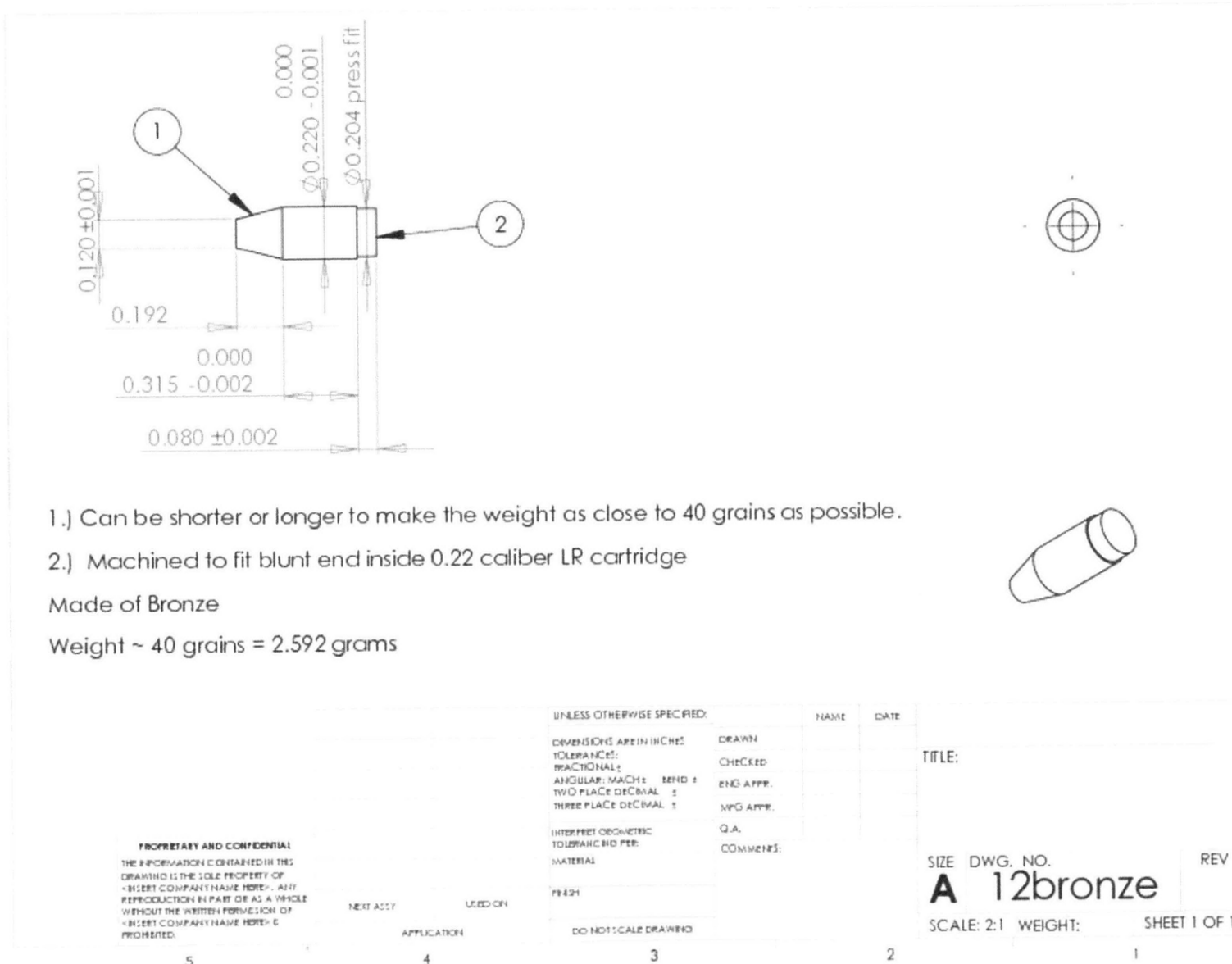
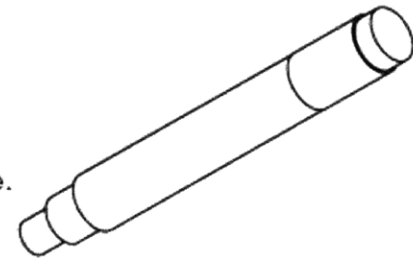
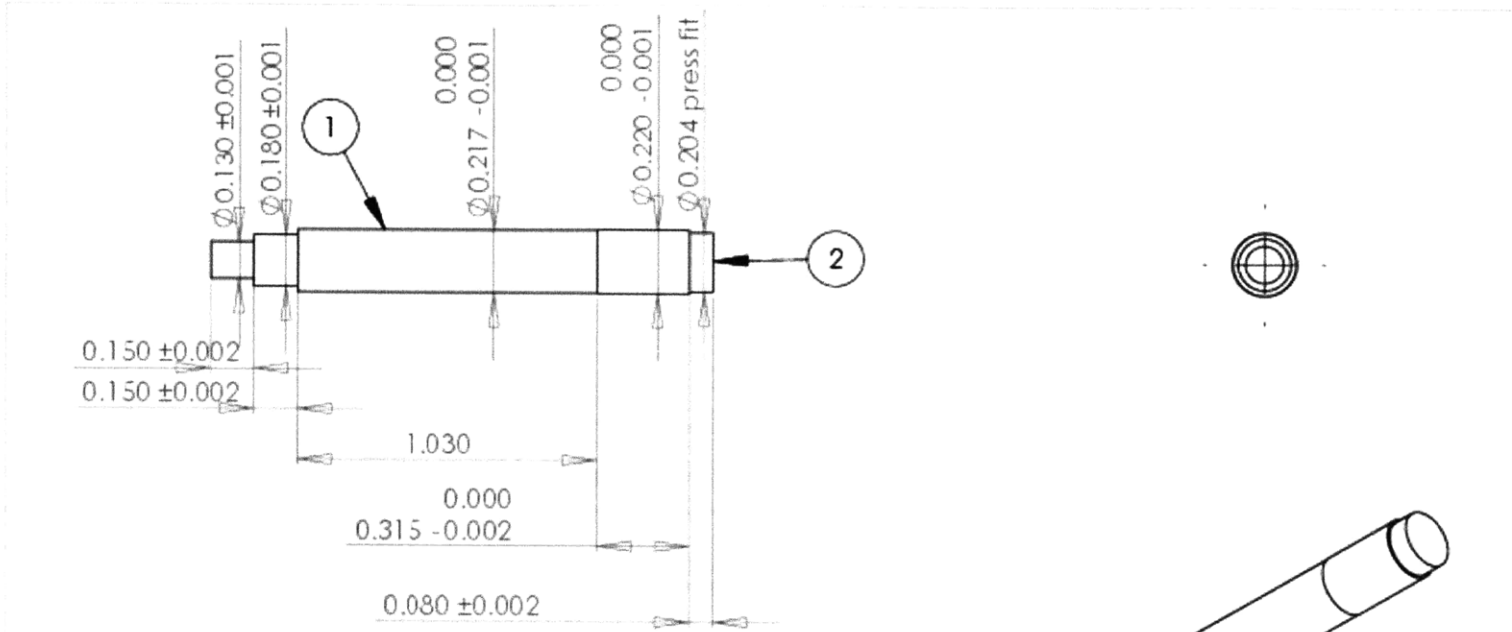


Figure B-3: Bronze 0.12 in tip with 0.192 in angled shoulder.



1.) Can be shorter or longer to make the weight as close to 40 grains as possible.

2.) Machined to fit blunt end inside 0.22 caliber LR cartridge

Made of Aluminium

Weight ~ 40 grains = 2.592 grams

PROPRIETARY AND CONFIDENTIAL
 THE INFORMATION CONTAINED IN THIS
 DRAWING IS THE SOLE PROPERTY OF
 <INSERT COMPANY NAME HERE>. ANY
 REPRODUCTION IN PART OR AS A WHOLE
 WITHOUT THE WRITTEN PERMISSION OF
 <INSERT COMPANY NAME HERE> IS
 PROHIBITED.

UNLESS OTHERWISE SPECIFIED:		NAME	DATE
DIMENSIONS ARE IN INCHES	DRAWN		
TOLERANCES:	CHECKED		
FRACTIONALS	ENG APPR.		
ANGULAR: MACH ±	WPG APPR.		
TWO PLACE DECIMAL ±	Q.A.		
THREE PLACE DECIMAL ±	COMMENTS:		
INTERPRET GEOMETRIC TOLERANCING PER MATERIAL			
FR421			
NEXT ASSY	USED ON		
APPLICATION	DO NOT SCALE DRAWING		

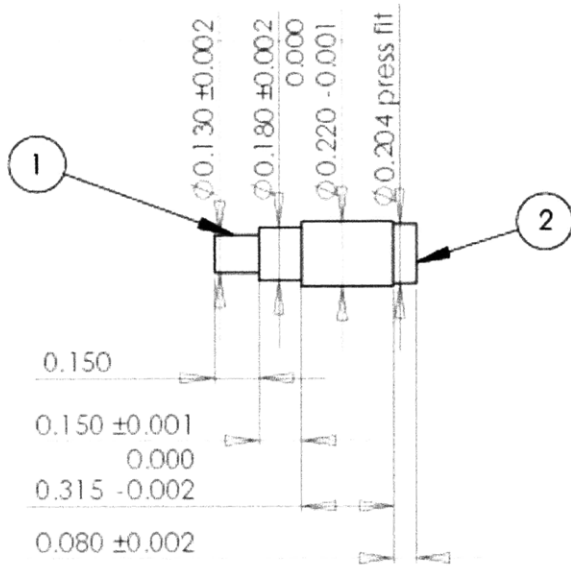
TITLE:

SIZE DWG. NO. REV

13tip_aluminium

SCALE: 2:1 WEIGHT: SHEET 1 OF 1

Figure B-4: Aluminum 0.13 in modified tip with two steps 0.15 in long.

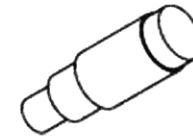


1.) Can be shorter or longer to make the weight as close to 40 grains as possible.

2.) Machined to fit blunt end inside 0.22 caliber LR cartridge

Made of Steel

Weight ~ 40 grains = 2.592 grams



PROPRIETARY AND CONFIDENTIAL
 THE INFORMATION CONTAINED IN THIS DRAWING IS THE SOLE PROPERTY OF «BIEERT COMPANY NAME HERE». ANY REPRODUCTION IN PART OR AS A WHOLE WITHOUT THE WRITTEN PERMISSION OF «BIEERT COMPANY NAME HERE» IS PROHIBITED.

NEXT ACTY USED ON

APPLICATION

5

4

UNLESS OTHERWISE SPECIFIED:

DIMENSIONS ARE IN INCHES

TOLERANCES:

FRACTIONAL ±

ANGULAR: MACH ± BEND ±

TWO PLACE DECIMAL ±

THREE PLACE DECIMAL ±

INTERPRET GEOMETRIC TOLERANCES PER:

MATERIAL

PER 421

DO NOT SCALE DRAWING

3

NAME DATE

DRAWN

CHECKED

ENG APPR.

MFG APPR.

Q.A.

COMMENTS:

2

TITLE:

SIZE DWG. NO.

A 13tip_steel

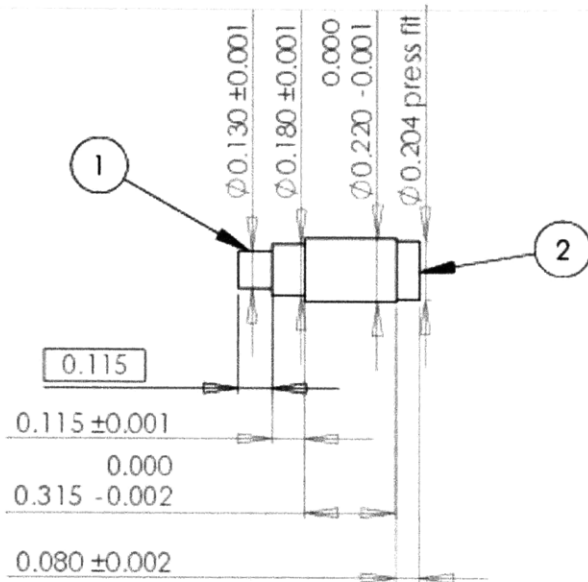
REV

SCALE: 2:1 WEIGHT:

SHEET 1 OF 1

1

Figure B-5: Steel 0.13 in modified tip with two steps 0.15 in long.



1.) Can be shorter or longer to make the weight as close to 40 grains as possible.

2.) Machined to fit blunt end inside 0.22 caliber LR cartridge

Made of Bronze

Weight ~ 40 grains = 2.592 grams



PROPRIETARY AND CONFIDENTIAL
 THE INFORMATION CONTAINED IN THIS
 DRAWING IS THE SOLE PROPERTY OF
 <INSERT COMPANY NAME HERE>. ANY
 REPRODUCTION IN PART OR AS A WHOLE
 WITHOUT THE WRITTEN PERMISSION OF
 <INSERT COMPANY NAME HERE> IS
 PROHIBITED.

NEXT ASSY

USED ON

APPLICATION

FR421

DO NOT SCALE DRAWING

UNLESS OTHERWISE SPECIFIED:

DIMENSIONS ARE IN INCHES
 TOLERANCES:
 FRACTIONAL ±
 ANGULAR: MACH ± 1/2°
 TWO PLACE DECIMAL ±
 THREE PLACE DECIMAL ±

INTERPRET GEOMETRIC
 TOLERANCING PER
 MATERIAL

NAME DATE

DRAWN

CHECKED

ENG APPR.

MFG APPR.

Q.A.

COMMENTS:

TITLE:

SIZE DWG. NO.

A13tip_bronze

REV

SCALE: 2:1 WEIGHT:

SHEET 1 OF 1

5

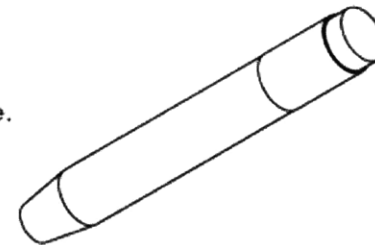
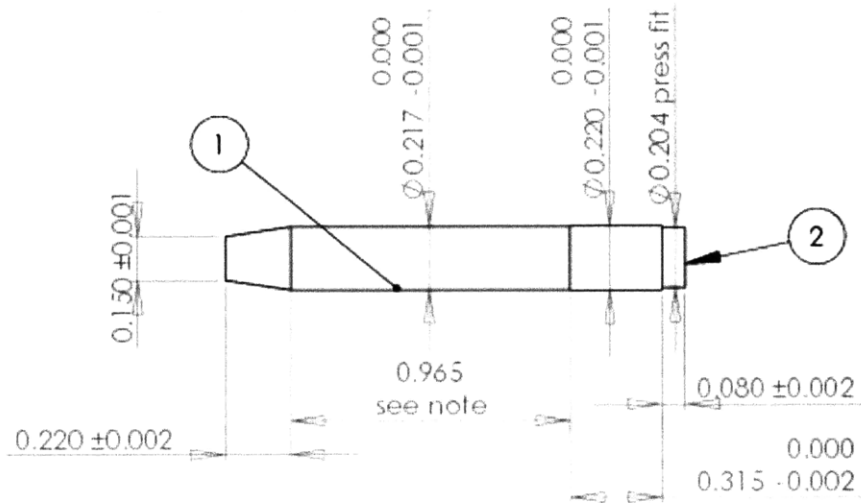
4

3

2

1

Figure B-6: Bronze 0.13 in modified tip with two steps 0.115 in long.



- 1.) Can be shorter or longer to make the weight as close to 40 grains as possible.
 - 2.) Machined to fit blunt end inside 0.22 caliber LR cartridge
- Made of Aluminium
 Weight ~ 40 grains = 2.592 grams

PROPRIETARY AND CONFIDENTIAL
 THE INFORMATION CONTAINED IN THIS DRAWING IS THE SOLE PROPERTY OF
 <INSERT COMPANY NAME HERE>. ANY
 REPRODUCTION IN PART OR AS A WHOLE
 WITHOUT THE WRITTEN PERMISSION OF
 <INSERT COMPANY NAME HERE> IS
 PROHIBITED.

NEXT ASSY

USED ON

APPLICATION

DO NOT SCALE DRAWING

UNLESS OTHERWISE SPECIFIED:

DIMENSIONS ARE IN INCHES

TOLERANCES:

FRACTIONAL ±

ANGULAR: MACH ±

TWO PLACE DECIMAL ±

THREE PLACE DECIMAL ±

INTERPRET OBSCURE

TOLERANCE PER:

MATERIAL

FINISH

DRAWN

CHECKED

ENG APPR.

MFG APPR.

Q.A.

COMMENTS:

NAME

DATE

TITLE:

SIZE DWG. NO.

REV

A15aluminium

SCALE: 2:1 WEIGHT:

SHEET 1 OF 1

5

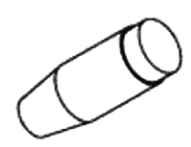
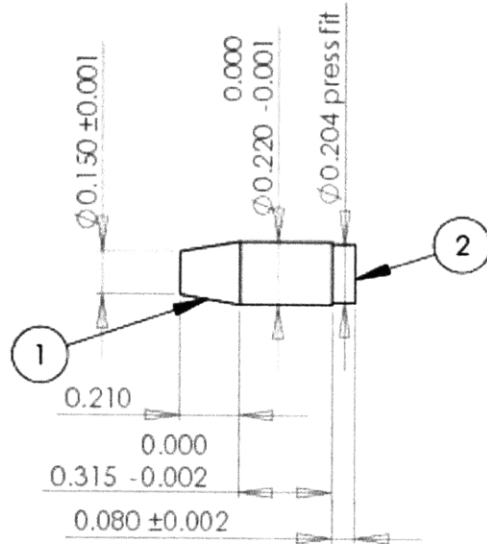
4

3

2

1

Figure B-7: Aluminum 0.15 in tip with 0.22 in shoulder.



- 1.) Can be shorter or longer to make the weight as close to 40 grains as possible.
 - 2.) Machined to fit blunt end inside 0.22 caliber LR cartridge
- Made of Steel

Weight ~ 40 grains = 2.592 grams

PROPRIETARY AND CONFIDENTIAL
 THE INFORMATION CONTAINED IN THIS DRAWING IS THE SOLE PROPERTY OF <INSERT COMPANY NAME HERE>. ANY REPRODUCTION IN PART OR AS A WHOLE WITHOUT THE WRITTEN PERMISSION OF <INSERT COMPANY NAME HERE> IS PROHIBITED.

UNLESS OTHERWISE SPECIFIED:

DIMENSIONS ARE IN INCHES
 TOLERANCES:
 FRACTIONAL:
 ANGULAR: MACHINE BEND ±
 TWO PLACE DECIMAL ±
 THREE PLACE DECIMAL ±

INTERPRET GEOMETRIC TOLERANCES PER: MATERIAL

FRESH

DO NOT SCALE DRAWING

NAME DATE

DRAWN
 CHECKED
 ENG APPR.
 MFG APPR.
 Q.A.
 COMMENTS:

TITLE:

SIZE DWG. NO.

A 15steel

REV

SCALE: 2:1 WEIGHT:

SHEET 1 OF 1

5

4

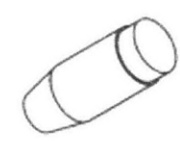
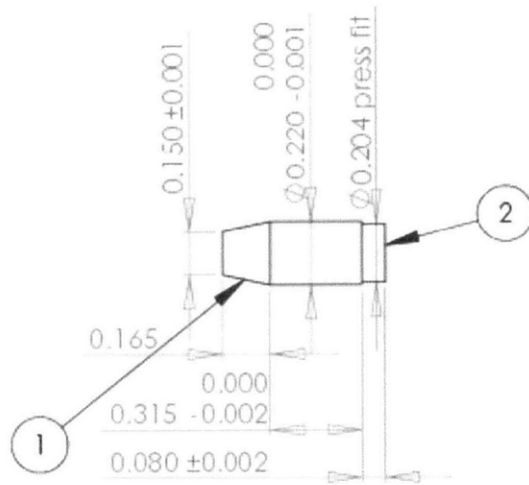
4

3

2

1

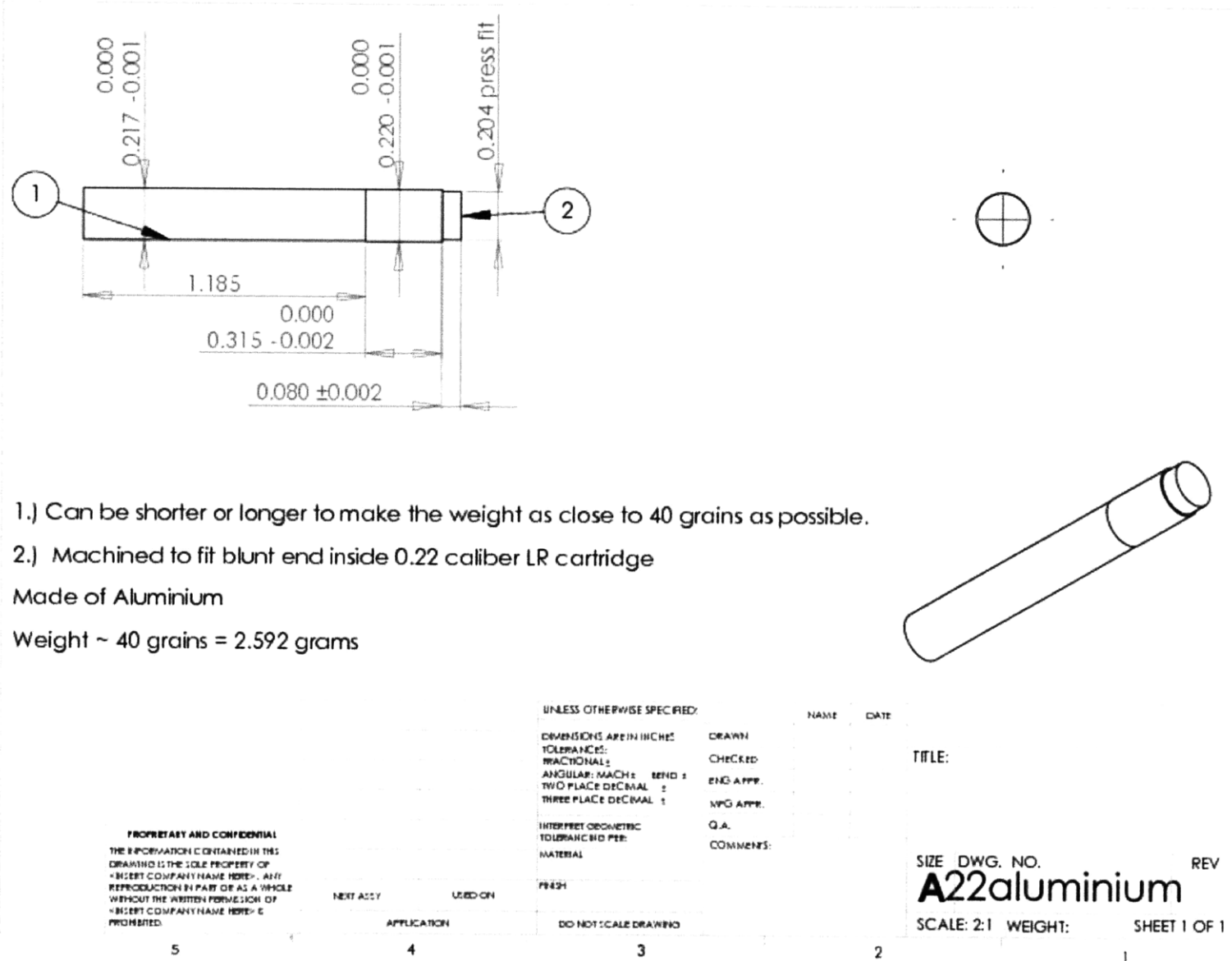
Figure B-8: Steel 0.15 in tip with 0.21 in shoulder.



- 1.) Can be shorter or longer to make the weight as close to 40 grains as possible.
 - 2.) Machined to fit blunt end inside 0.22 caliber LR cartridge
- Made of Bronze
 Weight ~ 40 grains = 2.592 grams

<p>PROPRIETARY AND CONFIDENTIAL THE INFORMATION CONTAINED IN THIS DRAWING IS THE SOLE PROPERTY OF <BEEET COMPANY NAME HERE>. ANY REPRODUCTION IN PART OR AS A WHOLE WITHOUT THE WRITTEN PERMISSION OF <BEEET COMPANY NAME HERE> IS PROHIBITED.</p>	NEXT ASSY 5	USED ON 4	APPLICATION 4	UNLESS OTHERWISE SPECIFIED: DIMENSIONS ARE IN INCHES TOLERANCES: FRACTIONAL ± ANGULAR: MACH ± BEND ± TWO PLACE DECIMAL ± THREE PLACE DECIMAL ± INTERPRET GEOMETRIC TOLERANCING PER: MATERIAL FINISH DO NOT SCALE DRAWING	NAME DATE DRAWN CHECKED ENG APPR. MFG APPR. Q.A. COMMENTS:	TITLE: SIZE DWG. NO. A 15bronze SCALE: 2:1 WEIGHT: SHEET 1 OF 1	REV 1
--	----------------	--------------	------------------	---	---	---	----------

Figure B-9: Bronze 0.15 in tip with 0.165 in shoulder.



- 1.) Can be shorter or longer to make the weight as close to 40 grains as possible.
 - 2.) Machined to fit blunt end inside 0.22 caliber LR cartridge
- Made of Aluminium
 Weight ~ 40 grains = 2.592 grams

PROPRIETARY AND CONFIDENTIAL
 THE INFORMATION CONTAINED IN THIS DRAWING IS THE SOLE PROPERTY OF [INSERT COMPANY NAME HERE]. ANY REPRODUCTION IN PART OR AS A WHOLE WITHOUT THE WRITTEN PERMISSION OF [INSERT COMPANY NAME HERE] IS PROHIBITED.

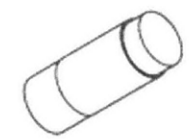
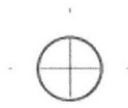
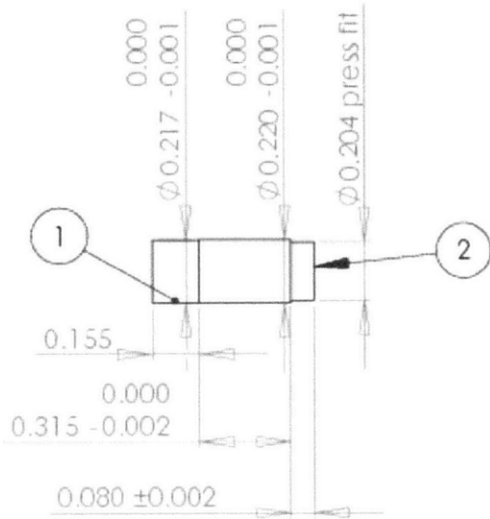
UNLESS OTHERWISE SPECIFIED:		NAME	DATE
5	4		
3	2		
1			

DIMENSIONS ARE IN INCHES
 TOLERANCES:
 FRACTIONALS:
 ANGULAR: MACH ± BEND ±
 TWO PLACE DECIMAL ±
 THREE PLACE DECIMAL ±
 INTERPRET GEOMETRIC TOLERANCE BIDD PER MATERIAL
 FRESH
 DO NOT SCALE DRAWING

TITLE:

SIZE DWG. NO. **A22aluminium** REV

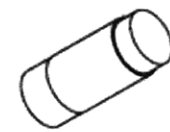
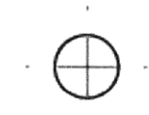
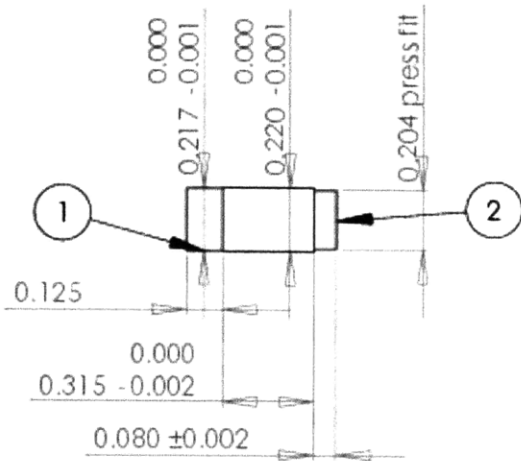
SCALE: 2:1 WEIGHT: SHEET 1 OF 1



- 1.) Can be shorter or longer to make the weight as close to 40 grains as possible.
 - 2.) Machined to fit blunt end inside 0.22 caliber LR cartridge
- Made of Aluminium
 Weight ~ 40 grains = 2.592 grams

<p>PROPRIETARY AND CONFIDENTIAL THE INFORMATION CONTAINED IN THIS DRAWING IS THE SOLE PROPERTY OF <INSERT COMPANY NAME HERE>. ANY REPRODUCTION IN PART OR AS A WHOLE WITHOUT THE WRITTEN PERMISSION OF <INSERT COMPANY NAME HERE> IS PROHIBITED.</p>	5	4	3	2	1	
	<p>UNLESS OTHERWISE SPECIFIED: DIMENSIONS ARE IN INCHES TOLERANCES: FRACTIONAL ± ANGULAR: MACH ± BEND ± TWO PLACE DECIMAL ± THREE PLACE DECIMAL ±</p>	<p>INTERPRET GEOMETRIC TOLERANCING PER: MATERIAL</p>	<p>FRZM</p> <p>DO NOT SCALE DRAWING</p>	<p>DRAWN CHECKED ENG APPR. MFG APPR. Q.A. COMMENTS:</p>	<p>NAME</p> <p>DATE</p>	<p>TITLE:</p>
	<p>NEXT ASSY</p>	<p>USED ON</p>	<p>APPLICATION</p>	<p>SCALE: 2:1</p>	<p>WEIGHT:</p>	<p>SIZE DWG. NO. A 22steel</p>
	<p>REV</p>	<p>SHEET 1 OF 1</p>	<p>SCALE: 2:1</p>	<p>WEIGHT:</p>	<p>REV</p>	<p>SHEET 1 OF 1</p>
	<p>APPLICATION</p>	<p>USED ON</p>	<p>FRZM</p>	<p>SCALE: 2:1</p>	<p>WEIGHT:</p>	<p>REV</p>

Figure B-11: Stee 0.22 in tip with no shoulder.



- 1.) Can be shorter or longer to make the weight as close to 40 grains as possible.
- 2.) Machined to fit blunt end inside 0.22 caliber LR cartridge

Made of Bronze

Weight ~ 40 grains = 2.592 grams

PROPRIETARY AND CONFIDENTIAL
 THE INFORMATION CONTAINED IN THIS DRAWING IS THE SOLE PROPERTY OF <BISERT COMPANY NAME HERE>. ANY REPRODUCTION IN PART OR AS A WHOLE WITHOUT THE WRITTEN PERMISSION OF <BISERT COMPANY NAME HERE> IS PROHIBITED.

UNLESS OTHERWISE SPECIFIED:

DIMENSIONS ARE IN INCHES
 TOLERANCES:
 FRACTIONALS ±
 ANGULAR: MATCH ±
 HOLE: TWO PLACE DECIMAL ±
 HOLE: THREE PLACE DECIMAL ±

INTERPRET GEOMETRIC TOLERANCES PER: MATERIAL

NAME DATE

DRAWN
 CHECKED
 ENG APPR.
 MFG APPR.
 Q.A.
 COMMENTS:

TITLE:

SIZE DWG. NO. REV
A 22bronze

SCALE: 2:1 WEIGHT: SHEET 1 OF 1

NEXT ASSY USED ON PART
 APPLICATION DO NOT SCALE DRAWING

5

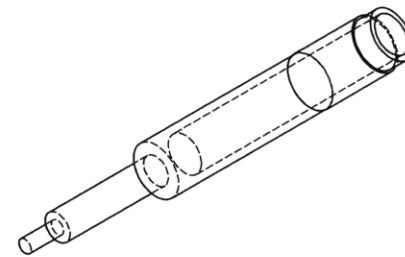
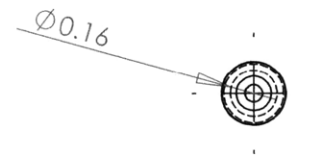
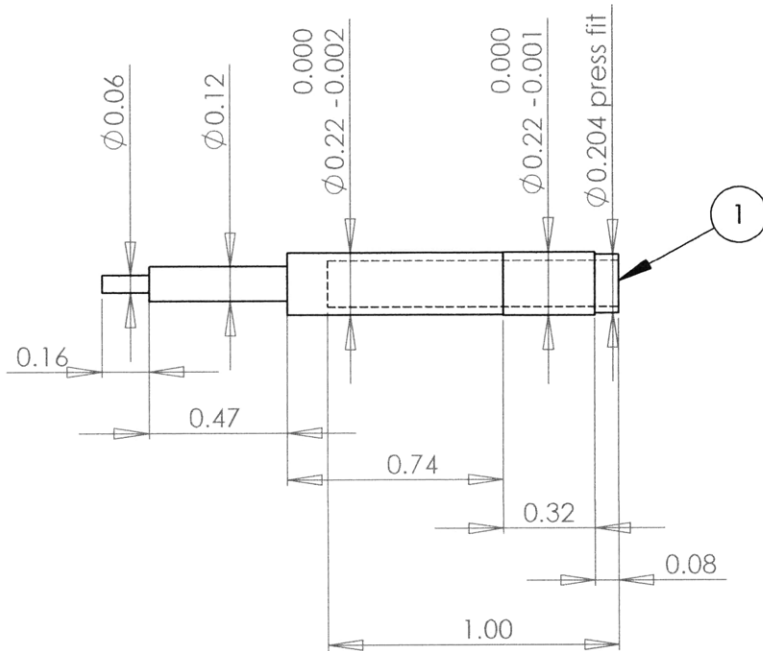
4

3

2

1

Figure B-12: Bronze 0.22 in tip with no shoulder.



1.) Machined to fit blunt end inside 0.22 caliber LR cartridge

Made of Aluminium

Weight ~ 40 grains = 2.592 grams

PROPRIETARY AND CONFIDENTIAL
 THE INFORMATION CONTAINED IN THIS DRAWING IS THE SOLE PROPERTY OF <INSERT COMPANY NAME HERE>. ANY REPRODUCTION IN PART OR AS A WHOLE WITHOUT THE WRITTEN PERMISSION OF <INSERT COMPANY NAME HERE> IS PROHIBITED.

		UNLESS OTHERWISE SPECIFIED:	NAME	DATE	
		DIMENSIONS ARE IN INCHES	DRAWN		TITLE:
		TOLERANCES:	CHECKED		
		FRACTIONAL ±	ENG APPR.		
		ANGULAR: MACH ± BEND ±	MFG APPR.		
		TWO PLACE DECIMAL ±	Q.A.		
		THREE PLACE DECIMAL ±	COMMENTS:		
		INTERPRET GEOMETRIC TOLERANCING PER:			SIZE DWG. NO. REV
		MATERIAL			06 Aluminum shoulder
		FINISH			SCALE: 2:1 WEIGHT: SHEET 1 OF 1
	NEXT ASSY	USED ON			
	APPLICATION	DO NOT SCALE DRAWING			

5

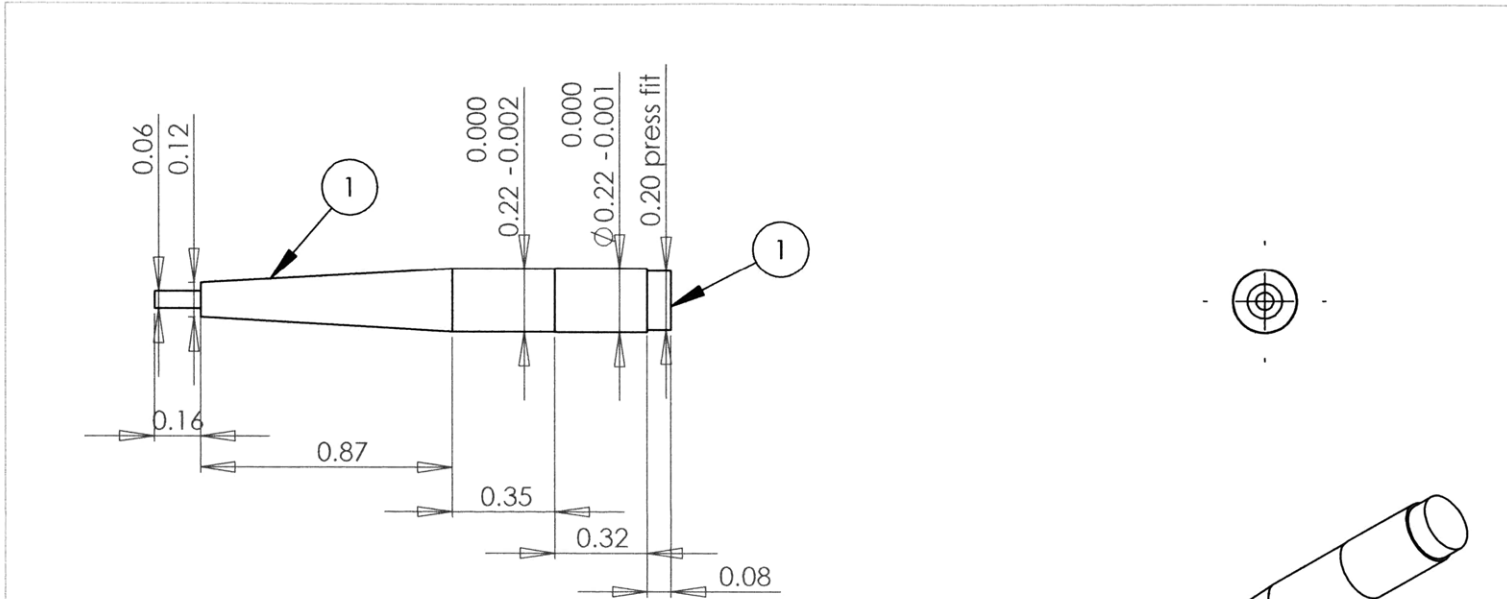
4

3

2

1

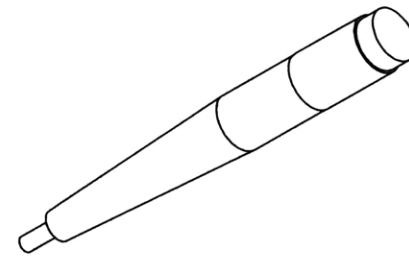
Figure B-13: Aluminum 0.06 in tip with no two shoulders.



- 1.) Angle is ~6.5 degrees.
- 2.) Machined to fit blunt end inside 0.22 caliber LR cartridge

Made of Aluminium

Weight ~ 40 grains = 2.592 grams



PROPRIETARY AND CONFIDENTIAL
 THE INFORMATION CONTAINED IN THIS DRAWING IS THE SOLE PROPERTY OF <INSERT COMPANY NAME HERE>. ANY REPRODUCTION IN PART OR AS A WHOLE WITHOUT THE WRITTEN PERMISSION OF <INSERT COMPANY NAME HERE> IS PROHIBITED.

		UNLESS OTHERWISE SPECIFIED:		NAME	DATE		
		DIMENSIONS ARE IN INCHES		DRAWN		TITLE:	
		TOLERANCES:		CHECKED			
		FRACTIONAL ±		ENG APPR.			
		ANGULAR: MACH ± BEND ±		MFG APPR.			
		TWO PLACE DECIMAL ±		Q.A.			
		THREE PLACE DECIMAL ±		COMMENTS:			
		INTERPRET GEOMETRIC TOLERANCING PER:				SIZE	DWG. NO.
		MATERIAL					REV
		FINISH				06aluminumshouldertape	
NEXT ASSY	USED ON					SCALE: 2:1	WEIGHT:
APPLICATION		DO NOT SCALE DRAWING				SHEET 1 OF 1	

5

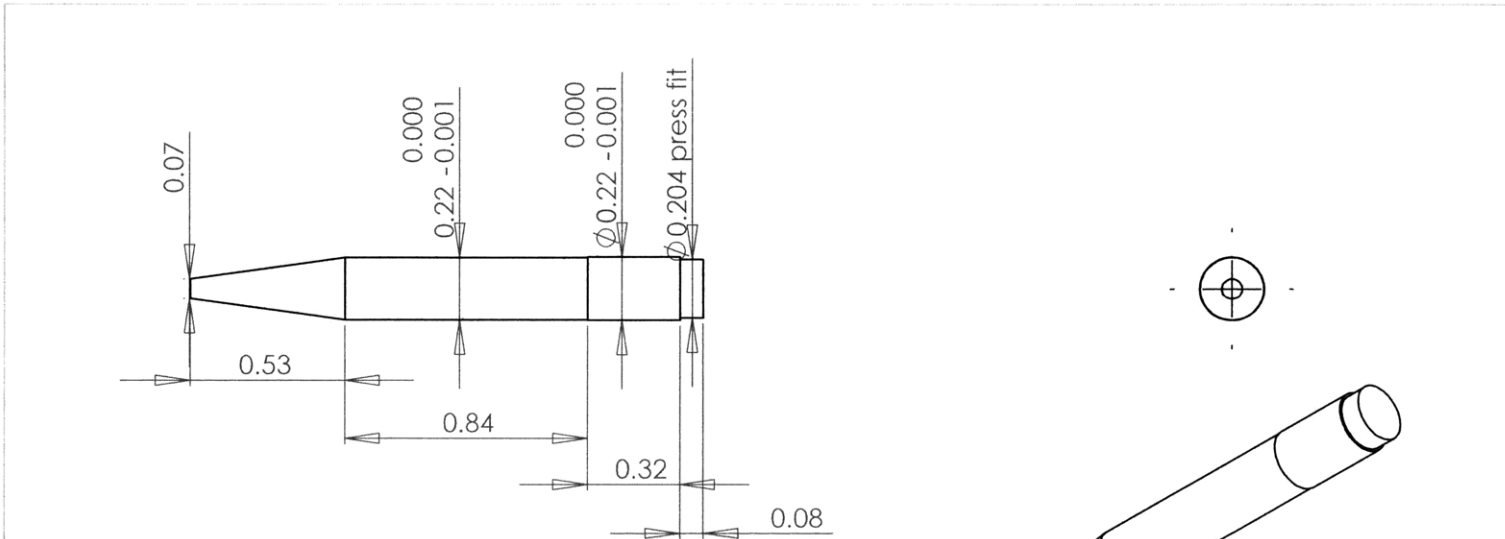
4

3

2

1

Figure B-14: Bronze 0.06 in tip with shoulder and taper.



- 1.) Angle is ~15.8 degrees.
 - 2.) Machined to fit blunt end inside 0.22 caliber LR cartridge
- Made of Aluminium
 Weight ~ 40 grains = 2.592 grams

<p>PROPRIETARY AND CONFIDENTIAL THE INFORMATION CONTAINED IN THIS DRAWING IS THE SOLE PROPERTY OF <INSERT COMPANY NAME HERE>. ANY REPRODUCTION IN PART OR AS A WHOLE WITHOUT THE WRITTEN PERMISSION OF <INSERT COMPANY NAME HERE> IS PROHIBITED.</p>				UNLESS OTHERWISE SPECIFIED:	NAME	DATE	TITLE:
				DIMENSIONS ARE IN INCHES TOLERANCES: FRACTIONAL ± ANGULAR: MACH ± BEND ± TWO PLACE DECIMAL ± THREE PLACE DECIMAL ±	DRAWN		
				INTERPRET GEOMETRIC TOLERANCING PER:	CHECKED		SIZE DWG. NO. REV 00 Aluminum taper
				MATERIAL	ENG APPR.		
				FINISH	MFG APPR.		SCALE: 2:1 WEIGHT: SHEET 1 OF 1
		NEXT ASSY	USED ON		Q.A.		
		APPLICATION		DO NOT SCALE DRAWING	COMMENTS:		

Figure B-15: Bronze 0.07 in tip with taper only.